

# Electro-Optical Bunch Length Measurements at the ANKA Storage Ring

Zur Erlangung des akademischen Grades eines  
DOKTORS DER NATURWISSENSCHAFTEN

von der Fakultät für Physik  
des Karlsruher Institutes für Technologie (KIT)

genehmigte  
DISSERTATION  
von

Dipl.-Phys.  
**Nicole Hiller**  
aus Backnang

Tag der mündlichen Prüfung: 6. Dezember 2013  
Referent: **Prof. Dr. Anke-Susanne Müller**  
Korreferent: **Prof. Dr. Günter Quast**

---





**A scientist in his laboratory is not only a technician: he is also a child placed before natural phenomena which impress him like a fairy tale.**

— *Marie Curie*

From: <http://abstrusegoose.com/430>





# Contents

<b>1</b>	<b>Introduction</b>	<b>1</b>
<b>2</b>	<b>Short Bunch Operation in Storage Rings</b>	<b>5</b>
2.1	Storage Rings . . . . .	6
2.1.1	Optics and Beam Dynamics . . . . .	7
2.1.2	Short Bunch Operation at ANKA . . . . .	12
2.2	Radiation from Charged Particles . . . . .	14
2.2.1	Near-Field - Coulomb Regime . . . . .	15
2.2.2	Far-Field - Synchrotron Radiation (SR) & Coherent SR (CSR) . . . . .	15
2.3	Microbunching Instability . . . . .	20
<b>3</b>	<b>Techniques for Longitudinal Beam Diagnostics</b>	<b>23</b>
3.1	Introduction to Longitudinal Diagnostics . . . . .	23
3.2	Streak Camera . . . . .	25
3.3	Electro-Optical Techniques . . . . .	28
3.3.1	The Pockels Effect & Phase Modulation . . . . .	28
3.3.2	Detection Scheme . . . . .	30
3.3.3	Electro-Optical Sampling (EOS) . . . . .	32
3.3.4	Electro-Optical Spectral Decoding (EOSD) . . . . .	34
3.3.5	History of Electro-Optical Bunch Length Measurements . . . . .	35
<b>4</b>	<b>Streak Camera Measurements</b>	<b>37</b>
4.1	Streak Camera Setup at ANKA . . . . .	37
4.1.1	Visible Light Diagnostics Beamline . . . . .	38
4.1.2	Streak Camera Optical Setup . . . . .	39
4.2	Characterization . . . . .	39
4.2.1	Streak Camera Data Analysis . . . . .	40
4.2.2	Benchmarking of the Diagnostics Beam Port . . . . .	42
4.2.3	Calibration Measurements with a fs-Laser System . . . . .	42
4.2.4	Single-Shot Measurements with the Streak Camera . . . . .	43
<b>5</b>	<b>Electro-Optical Setup at ANKA</b>	<b>45</b>
5.1	Design Considerations . . . . .	45
5.2	Laser System . . . . .	47
5.2.1	Laser Oscillator . . . . .	47
5.2.2	Synchronization Unit . . . . .	49



5.2.3	Amplifier System . . . . .	50
5.2.4	Control System . . . . .	52
5.3	Near-Field Setup . . . . .	55
5.3.1	EO-Monitor . . . . .	55
5.3.2	Temporal overlap . . . . .	58
5.3.3	Loss Rate Monitor . . . . .	59
5.4	Laser Detection System . . . . .	61
5.4.1	Temporal Detection for EOS . . . . .	61
5.4.2	Spectral Detection for EOSD . . . . .	61
<b>6</b>	<b>Systematic Studies with the EO Setup at ANKA</b>	<b>65</b>
6.1	Characterization of the Electro-Optical Sampling (EOS) Setup . . . . .	65
6.1.1	Data Readout for EOS . . . . .	66
6.1.2	Data Processing for EOS . . . . .	67
6.1.3	Wave Plate Settings . . . . .	68
6.2	Characterization of Electro-Optical Spectral Decoding (EOSD) Measurements	73
6.2.1	Data Recording for EOSD . . . . .	73
6.2.2	Data Processing for EOSD . . . . .	78
6.2.3	Calibration Measurements for EOSD . . . . .	81
6.2.3.1	Intensity correction . . . . .	81
6.2.3.2	Phase calibration . . . . .	83
6.2.3.2.1	Phase Calibration Measurement . . . . .	83
6.2.3.2.2	Systematic Studies for the Phase Calibration . . .	87
6.2.3.3	Time calibration . . . . .	100
6.2.4	Resolution and Sensitivity of EOSD Measurements . . . . .	105
6.3	Wake-Field Induced Heat Load . . . . .	112
<b>7</b>	<b>Beam Studies with Longitudinal Diagnostics at ANKA</b>	<b>117</b>
7.1	Low- $\alpha_c$ -Mode Characterization . . . . .	117
7.1.1	Bunch Length in Dependence of Current for Different Values of the Momentum Compaction Factor $\alpha_c$ . . . . .	118
7.1.2	Bunch Length in Dependence of Current for Different RF Values . .	120
7.1.3	Studies of Bunch Length Fluctuations . . . . .	121
7.1.4	Average Bunch Shapes for Different Currents . . . . .	123
7.1.5	Single-Shot Bunch Length and Shape Measurements . . . . .	125
7.2	Studies of Long Range Wake-Fields . . . . .	131
7.2.1	Current Dependence of Wake-Fields . . . . .	131
7.2.2	Distance Dependence of Wake-Fields . . . . .	133
7.2.3	Maschine Parameter Dependence of Wake-Fields . . . . .	135
7.2.4	Wake-Fields Influencing Following Bunches . . . . .	137
7.3	Bunch Length Measurements During the Energy Ramp . . . . .	139
7.4	Influences of the Cavity Cooling Loop on the Bunch Arrival Time . . . . .	140
<b>8</b>	<b>Summary</b>	<b>141</b>



---

<b>9 Appendix</b>	<b>145</b>
A Mathematical Description of the Pockels Effect . . . . .	145
B Correlations Between Fit Parameters . . . . .	151
<b>Acronyms</b>	<b>153</b>
<b>Bibliography</b>	<b>155</b>
<b>Acknowledgments</b>	<b>165</b>







# 1. Introduction

Since its first experimental observation more than half a century ago, in 1947 [1], synchrotron radiation (SR) has proven to be a unique tool for studies in many fields of science such as condensed matter physics, materials science, biology, medicine and many more.

Prior to experimental observation, it had been predicted by various researchers nearly simultaneously that relativistic particles that are deflected in a magnetic field would emit large quantities of radiation - synchrotron radiation<sup>1</sup> [2–5]. In the following years to come, its characteristics were studied, and first user experiments were carried out parasitically at various accelerators that were originally only dedicated to high energy or nuclear physics experiments.

The early experiments with SR consisted mostly of spectroscopy in the ultra-violet range, especially the absorption spectra of noble gases revealed a large number of previously unobserved resonances, caused by inner-shell and electron excitations [6]. When high energy physics pushed the development of synchrotrons to higher beam energies. Like at DORIS , for example, a former synchrotron at Deutsches Elektronen-Synchrotron (DESY) in Hamburg, operating at 4.4 GeV, photons with even shorter wavelengths ranging down to 0.1 Å became available, allowing for absorption measurements of metals at their K shells [6].

It took until 1968 before the first dedicated storage ring for the production of SR had been built at the synchrotron radiation center in Wisconsin (USA), which was a user facility with 10 experimental stations, quite like the concept of modern facilities [7].

The continuous spectrum of the synchrotron radiation generated from highly relativistic, light particles (typically electrons) ranges from the far infrared into the hard X-ray range. Especially in the X-ray range, SR distinguishes itself most from standard lab sources, such as X-ray tubes by the fact that its highly collimated beam offers not only an enormous brilliance<sup>2</sup>, leading to a degree of spatial coherence, which allows for phase reconstruction. The time structure of the emitted SR resembles that of the electron beam. Typically

---

<sup>1</sup>The radiation was named synchrotron radiation because of its first observation at a synchrotron, a type of particle accelerator.

<sup>2</sup>Brilliance gives a measure to compare photon sources, its unit is: photons/s/mm<sup>2</sup>/mrad<sup>2</sup>/0.1%BW



the electron beams in synchrotrons are bunched with bunch lengths in the order of a few millimeters, so that the radiation pulses have a length in the range of tens of picoseconds. Due to the growing number of applications for SR, nowadays, more than 60 synchrotron radiation centers are operational world-wide offering measurement stations - called beam-lines - to users from all over the world [8].

While the shape of the spectrum of normal SR does not depend upon the spatial (temporal) charge distribution of the electrons<sup>3</sup>, radiation losses due to the emission of coherent synchrotron radiation (CSR) were predicted in 1954 [9]. It was stated that for wavelengths that are longer than the length of the bunches, the SR emitted from the many millions of electrons within one bunch could interfere constructively, causing a great increase in radiation power. Because the length of typical electron bunches in synchrotrons is in the range of tens of picoseconds, the frequency range of this CSR would lie in the low GHz range. Radiation in this frequency range is heavily damped inside electron beam pipes, with characteristic dimensions of just a few centimeters of diameter, used for electron and SR beam transport. Nevertheless first hints of CSR were reported early at the SRS in Daresbury (UK) [10].

The first definite experimental validation of CSR was at linear accelerators, where the bunch length was only about 5 ps RMS<sup>4</sup>, thus moving the spectrum of the CSR towards shorter wavelengths which can propagate more easily through the beam pipe [11, 12]. First this radiation was mostly undesired. The discoverers of the CSR already proposed how to shield it to get rid of it again [13]. Over the years, however, ideas grew to compress the electron bunches to lengths short enough that the spectrum of the CSR could be moved into the THz range. This range is not easily accessible by any lab sources, especially, if one seeks high intensities and brilliances. Additionally, the reduced bunch length would of course also mean that the length of the normal SR pulses would be decreased, allowing for time-resolved studies, such as pump-probe experiments, on a shorter time scale.

In 2004, BESSY II in Berlin was the first synchrotron lightsource to offer a dedicated short-bunch operation, called low- $\alpha_c$ -mode<sup>5</sup> to users. The Ångström Source Karlsruhe (ANKA), the synchrotron radiation facility of the Karlsruhe Institute of Technology (KIT), where this work has been carried out, soon followed in 2005 [14].

Several ring accelerators published that they observed a beam-current-dependent bunch-lengthening effect and even a bursting behavior of the emitted CSR [15–19]. A first theory for this so-called microbunching instability was then given by Stupakov and Heifets in [20] and by Venturini and Warnock in [21]. First experiments validated the predictions by these theories [22]. The microbunching model assumes that the interaction of the beam with its own SR creates substructures in the longitudinal density profile of the bunch,

---

<sup>3</sup>It is an incoherent addition of the spectra for single electrons within the bunch.

<sup>4</sup>In accelerator physics, typically all dimensions concerning the electron bunches are denoted with the standard deviations of their distributions.

<sup>5</sup>Named after the momentum compaction factor  $\alpha_c$ , which is proportional to the square of the bunch length.



called microbunches. This microbunching then amplifies itself via the coherent emission of CSR. Because the spectrum of the CSR is linked to the longitudinal bunch profile, even small changes of the longitudinal charge density profile can result in rather large changes of the emitted CSR power. The growth and decay of the microbunching instability then causes a series of periodic or quasi-periodic bursts of CSR. It should also be mentioned that the microbunching instability limits the achievable bunch compression that can be achieved, because it leads to a current-depending bunch lengthening effect. Consequently, it does not only make the emission of CSR hard to predict and unstable, but also makes the bunches longer than desired.

New machines for the generation of synchrotron radiation (e. g. ultra-low-emittance rings) and even for high energy physics (e. g. damping rings) all operate with electron beam optics that highly compress the electron bunches in all directions, so instabilities due to CSR will pose great challenges for all of them. The deeper understanding of this bursting behavior, which is limiting the low- $\alpha_c$ -operation, is not an easy task, as it is influenced by many factors. The measurement of the temporal and spectral characteristics of the bursts together with measurements of the longitudinal bunch profiles can aid to improve the modeling and find ways to control the emission of CSR. Especially the control of the emission would greatly help to make CSR more applicable to user experiments, which might be perturbed by a bursting behavior of the radiation.

To resolve the dynamic changes to the bunch profiles, single-shot measurements with a sub-ps resolution are required. Averaging techniques will not be able to detect the formation and evolution of a burst because the dynamic changes of the substructure happen on short time scales and can change from turn to turn<sup>6</sup>. The single-shot capabilities of current methods for longitudinal bunch profile measurements at synchrotron storage rings are limited. The reason for that is that initially ring accelerators were designed to offer very stable and reproducible beam parameters, so not much emphasis was put onto resolving dynamics on a turn-by-turn basis.

So, for this thesis, the search went on for a technique, which would allow for single-shot bunch profile measurements at a ring machine. The choice fell onto the electro-optical (EO) method of electro-optical spectral decoding (EOSD). EOSD is a technique that has, in recent years, found its way from laser physics into the field of accelerator physics where it allows direct imaging of Coulomb fields. Thus far, it has mostly been used at linear accelerators (e. g. [23–27]).

Its working principle is the following: The electric field of the electron bunch, induces a birefringence inside an EO crystal (Pockels effect), this birefringence is then probed with a laser pulse, which is afterwards analyzed. If a femtosecond laser pulse is temporally stretched with a known relation between laser wavelength and time delay within the pulse, the whole temporal profile of a single electron bunch can be encoded as intensity modulation onto the temporal and thus spectral profile of a single laser pulse. This laser pulse is then subsequently detected with a single-shot spectrometer. From the known relation

---

<sup>6</sup>The revolution of one bunch at ANKA takes 368 ns.

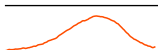


between wavelength and time delay, the spectral profile can be transformed back into a temporal profile and we obtain a single-shot measurement of the longitudinal bunch profile.

In the framework of this thesis, an EOSD setup allowing for single-shot bunch profile measurements has been adapted for the operation at a storage ring and has been successfully installed into the ultra-high vacuum (UHV) system of ANKA. My work included the assembly of the laser system, which had to be physically altered, and the design, fabrication, alignment and installation of the optical setup including the in-vacuum components. This setup allowed, for the first time at a ring machine, to resolve dynamic substructures on compressed electron bunches.

Extensive systematic studies of the complex setup have been performed during the commissioning at ANKA and the results are compared to measurements with a streak camera, a well established diagnostics device, with only limited single-shot capabilities.

The work is structured in the following way: Chapter 2 gives an introduction to storage rings and the characteristics of the radiation generated by relativistic charged particles. The methods used for the bunch length measurements in this thesis are explained in Chapter 3. While Chapter 4 describes the experimental setup and the characterization of the streak camera measurements, Chapter 5 introduces the EO setup, followed by Chapter 6, which shows the results of extensive characterization measurements with the setup. Results of the beam studies performed with the two methods are then presented in Chapter 7. The thesis concludes with a summary in Chapter 8.



## 2. Short Bunch Operation in Storage Rings

A synchrotron storage ring is a specific type of particle accelerator that is designed to keep a bunched beam of charged particles efficiently stored inside an evacuated beam pipe for several hours. Most commonly, storage rings are used as lightsources for the generation of synchrotron radiation, which is emitted when highly relativistic particles - typically electrons - are deflected inside magnetic fields. Some storage rings are operated additionally in a short-bunch mode of operation, the so called low- $\alpha_c$ -operation, which is typically used to generate coherent synchrotron radiation (CSR) in the THz range or generally very short X-ray pulses.

This chapter is motivated by three points that need to be understood to follow the measurements of the longitudinal bunch profiles - the topic of this thesis.

First, the measurement of the shape of short bunches is crucial to the understanding and eventually control of the short bunch beam dynamics. Second, it needs to be shown that measuring the electric field in the near-field of a relativistic electron bunch gives its longitudinal bunch profile. This is what we do with electro-optical (EO) bunch length measurements, which will be discussed later on (see Ch. 6 & 7).

Third, it needs to be made clear that the intensity profile of the emitted SR pulses also corresponds to the longitudinal bunch profile. This is required in order to understand the working principle of the streak camera (SC), a detector we use as comparative method to the new technique of EO bunch length measurements (see Ch. 4).

The first Section (2.1) will give a brief introduction to storage rings, introducing the mathematical description and the common terminology used to describe the various beam parameters. This will then lead to a description of the short-bunch operation, which will be explained at the example of ANKA, the synchrotron radiation facility of the KIT at which the experiments presented in this thesis were carried out.

The characteristics of the radiation emitted from relativistic electron bunches will be ex-



plained in Chapter 2.2, there the near-field (Coulomb regime) and the far-field (radiation regime) are treated separately in more detail. The treatment of the near-field will show the second point - that the electric field in the near field resembles the longitudinal charge density - and the treatment of the far-field will show the third point - that the intensity profile of the SR also holds the longitudinal charge density.

While the second and the third point are rather straight forward to show, point one - the general motivation for longitudinal bunch profile measurements - requires a thorough understanding of longitudinal beam dynamics. It cannot be fully comprehended without first understanding the basic concepts of accelerator physics, especially during the short-bunch operation, and synchrotron radiation. So after introducing all those concepts in the following parts of this chapter, Section 2.3 will conclude the chapter with a brief introduction of the microbunching instability, which plays an important role during the low- $\alpha_c$ -operation, leading to the full motivation for the measurements carried out for this work.

## 2.1 Storage Rings

The operating principle of a storage ring is based on that of a synchrotron, which keeps a particle beam on a constant orbit by synchronously increasing the magnetic field with the particle energy. If the energy and the orbit are kept constant, one speaks of a synchrotron storage ring. The beam's path inside the beam pipe is guided by magnetic fields. The path itself is not technically a circle, but consists of straight and curved parts. For each curved part, a dipole magnet is used to deflect the beam of charged particles according to the Lorentz force. To store such a particle beam in a stable way over several hours, quadrupole magnets, acting as magnetic lenses, are used to focus the beam and prevent it from diverging inside the beam pipe. As with optical lenses, which exhibit chromatic aberration for non-monochromatic light, quadrupole magnets introduce similar effects, shifting their focal lengths in dependence of the exact particle momentum. In order to compensate for those chromatic effects, sextupole magnets are used for correction. To ensure that the losses due to scattering with rest gas are low, the beam pipe is evacuated down to  $10^{-9}$  mbar. The acceleration itself is achieved by a sinusoidal electric field inside radio frequency (RF) cavities.

Because free electromagnetic waves do not have field components in the direction of propagation, they are not suited for particle acceleration. If, however, certain boundary conditions are introduced, plane electromagnetic waves can exhibit longitudinal field components. RF cavities are resonators that are designed in a way to exhibit those boundary conditions, leading to a  $TM_{010}$ -mode<sup>1</sup> of the field that can then be used for the acceleration of charged particles [28].

---

<sup>1</sup>TM stands for transverse magnetic and denotes the fact that the magnetic field components are only along the transverse direction. The indices  $TM_{npq}$  denote the azimuthal, radial and longitudinal periodicity, so the mode  $TM_{010}$ , which is used in RF cavities has no longitudinal and azimuthal periodicity, but has a node in radial direction to fulfill the boundary condition that the electric field at the wall of the cavity must be zero.



The energy gain  $\Delta E$  inside such a sinusoidal electric field is given by:

$$\Delta E = qV_0 \sin \Psi_s, \quad (2.1)$$

where  $q$  is the charge of the particle,  $V_0$  the amplitude of the voltage and  $\Psi_s$  the stable phase at which the particle travels through the field. So when using sinusoidal electric fields, the particles arriving at the right time can always gain energy independently of their current energy. The alternating nature of the field, however, makes it impossible to accelerate a continuous particle beam and leads to a bunched beam with the length of the bunches being considerably shorter than the period length of the field inside the RF cavity.

The next Subsection will first give a very brief introduction to the physics of particle accelerators with the focus on a synchrotron storage ring (see Ch. 2.1.1), explaining the basics of beam optics and beam dynamics. Then a description of the short bunch operation, the low- $\alpha_c$ -mode, which is a specific operation mode designated to the reduction of the length of the bunches, is given with respect to ANKA. This mode of operation is typically used to generate coherent synchrotron radiation (CSR) in the THz range or picosecond long X-ray pulses for time resolved measurements (see Chapter 2.2 for the treatment of the emitted radiation).

### 2.1.1 Optics and Beam Dynamics

For the mathematical description of ring accelerators it is most convenient to work in a **co-moving coordinate system**, which moves along the reference trajectory of a particle having the nominal momentum  $p = p_0$ . Figure 2.1 illustrates this coordinate system.

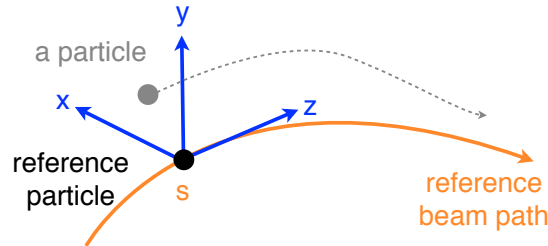


**Figure 2.1:** Co-moving coordinate system. A reference particle with  $p = p_0$ , moves along  $s$  with the velocity  $v$ .  $x$ ,  $y$  and  $z$  are used to describe the particle's offsets from the reference beam path, also called reference orbit.

The reference particle travels along  $s$  with the velocity  $v$ . For every position  $s$  around the ring,  $x$ ,  $y$  and  $z$  are used to describe the particle's position relative to that of the reference particle. The particle, at a position  $s$ , can be fully characterized by the 6d **phase space**:  $x, x', y, y', z, \delta$ . Here, the momenta  $x'$  and  $y'$  represent the position change with respect to the longitudinal coordinate  $z$ :  $x' = \frac{dx}{ds}$ ,  $y' = \frac{dy}{ds}$  and the relative momentum deviation  $\delta$  is given by:  $\delta = \frac{p-p_0}{p_0} = \frac{\Delta p}{p_0}$ .

From the equality of Lorentz and centripetal force

$$\frac{1}{R(x, y, s)} = \frac{q}{p} B_y(x, y, s) \quad (2.2)$$



we can see that to keep the radius of curvature  $R$  constant, for an increasing particle momentum  $p$ , the magnetic field  $B$  needs to be increased as well.

For the further treatment of the magnetic fields in a ring accelerator, which consist of many individual magnets, it makes sense to expand the right hand side of Eq. 2.2 into a Taylor series around the ideal orbit  $x = 0$  to split the magnetic fields into separate multipole components:

$$\frac{q}{p}B_y(x) = \frac{q}{p} \left( B_{y,0} + \frac{dB_y}{dx} \cdot x + \frac{d^2B_y}{2!dx^2} \cdot x^2 + \dots \right) \quad (2.3)$$

$$= \underbrace{\frac{1}{R}}_{\text{Dipole term}} + \underbrace{kx}_{\text{Quadrupole term}} + \underbrace{\frac{1}{2}mx^2}_{\text{Sextupole term}} + \dots \quad (2.4)$$

An analogous expansion can then also be made for the horizontal component  $B_x(y)$ .

A compact **Matrix notation** is convenient for an accelerator with periodic structures. Matrices for all the single components along the beam path (e. g. dipole magnets, quadrupole magnets, drift spaces, ...) in an accelerator, can then give a transfer matrix  $\mathbf{M}$  for a particle traveling from  $s_0$  to  $s$ .

$$\begin{pmatrix} x \\ x' \\ y \\ y' \\ z \\ \delta \end{pmatrix}_s = \mathbf{M}(s/s_0) \begin{pmatrix} x \\ x' \\ y \\ y' \\ z \\ \delta \end{pmatrix}_{s_0} \quad (2.5)$$

Considering only the effects of dipoles and quadrupoles, and assuming there is no coupling between the horizontal and vertical plane, we obtain the following **equations of motion** for the particles [29]:

$$x''(s) = \left( \frac{1}{R^2(s)} - k(s) \right) x(s) = \frac{1}{R(s)} \frac{\Delta p}{p_0} \quad (2.6)$$

$$y''(s) + k(s) \cdot y(s) = 0 \quad (2.7)$$

$\frac{1}{R^2(s)}$  is dipole strength and  $k(s)$  quadrupole strength.

Assuming  $\frac{\Delta p}{p} = 0$  on a circular orbit ( $R \neq 0$ ), the differential equations shorten to the so called **Hill's equations** :

$$u''(s) + K(s) \cdot u(s) = 0, \quad K(s) = \begin{cases} \frac{1}{R^2(s)-k(s)} & \text{for } u(s) = x(s) \\ k(s) & \text{for } u(s) = y(s) \end{cases} \quad (2.8)$$

For a circular accelerator  $K(s)$  has to be periodic in  $s$  because the orbit is a closed curve with length  $L_0$ , so  $K(s + L_0) = K(s)$ . This leads to the general solution of the type:

$$u(s) = A(s) \cos(\Psi_u(s) + \phi) \quad (2.9)$$

Here, the amplitude function  $A(s)$  is also periodic with  $L_0$ . The oscillation is referred to as betatron oscillation with the horizontal and vertical frequencies  $f_x$  and  $f_y$ . The solutions





for different phases  $\Psi_u$ , which correspond to different times  $t$ , lie on an ellipsoid in phase space. Typically, the ellipses are treated separately for the different planes of phase space, e. g.  $(x, x')$ ,  $(y, y')$ , and  $(z, \delta)$ . Following Liouville's Theorem, such a phase space ellipse has a constant area  $F$  in a conservative system [30].  $F$  is used to define the **emittance**  $\epsilon$  of a beam with  $\epsilon = F\pi$ . The amplitude function  $A(s)$  can be expressed as:

$$A(s) = \sqrt{\epsilon\beta(s)} \quad (2.10)$$

Where,  $\beta(s)$  is the so-called **beta function**. The phase changes  $\Delta\Psi$  for one revolution  $s \rightarrow s + L_0$  are referred to as horizontal and vertical **tunes**  $Q_x$  and  $Q_y$ , which are easily given by ratios between horizontal and vertical betatron frequencies to the revolution frequency of the synchronous particle  $f_{rev}$ :

$$Q_x = \frac{f_x}{f_{rev}} \quad \text{and} \quad Q_y = \frac{f_y}{f_{rev}}. \quad (2.11)$$

For a given beta function, the tunes can also be calculated with the following equation:

$$Q = \frac{1}{2\pi} \oint \frac{ds}{\beta(s)}. \quad (2.12)$$

The horizontal and vertical tune define the working point of an accelerator. For the optics to be stable, the working point should not lie on a resonance line, otherwise the amplitudes of the betatron oscillations can get amplified and lead to the beam being lost. The resonance conditions are given by the following equations [31]:

$$mQ_x = p, \quad (2.13)$$

$$nQ_y = p, \quad (2.14)$$

$$mQ_x + nQ_y = p \quad (2.15)$$

Here  $m, n, p \in \mathbb{Z}$  and  $|m|+|n|$  gives the order of the resonance. For electron accelerators it is typically enough to consider resonances up to the 4th order, when choosing a working point.

So far we have assumed  $p = p_0$ , but if we now to the case that  $\frac{\Delta p}{p_0} \neq 0$ , look back to Eq. 2.6 and define the **dispersion**  $D(s)$  as horizontal displacement relative to the momentum deviation,

$$D(s) = \frac{x(s)}{\Delta p/p_0}, \quad (2.16)$$

the solutions to the differential equations, which consist of the homogenous and the particular solution, lead to offsets in the particle positions

$$x(s) = x_{p=p_0}(s) + D(s) \frac{\Delta p}{p_0} \quad (2.17)$$

$$= \sqrt{\epsilon\beta(s)} \cos(\Psi_u(s) + \phi) + D(s) \frac{\Delta p}{p_0} \quad (2.18)$$

Since the momentum deviation just causes an off-set of beam position if a curvature is present, only elements with a dipole moment are considered. This means that usually in a storage ring, dispersion is only considered along  $x$  as a first approach. The dispersion  $D$

together with the beta functions  $\beta_x$  and  $\beta_y$  are typically referred to as **optics functions** of an accelerator.

The horizontal and vertical tunes vary slightly for particles with a different momentum. This is caused by the fact that the effective focal lengths of the quadrupoles also changes with the particle momentum, likewise to the effect of chromatic aberration in optics. A measure for this effect is the so-called **chromaticity**  $Q'$ , which is defined as the change in tune with momentum:

$$Q' = \frac{\Delta Q}{\Delta p/p_0} \quad (2.19)$$

Without the presence of sextupoles, we would measure the natural chromaticity of a given set of optics, which typically is in the negative range. As mentioned before, sextupole magnets are used to correct the natural chromaticity to a small positive value.

The **lattice** of an accelerator is given by the geometrical placement of the different magnets and cannot be altered easily without major changes to the machines. The magnet settings, however that determine the strength of the different multipole components can be changed; we then call this a different set of **beam optics**. If the strength of the dipole magnets is changed, this will inevitably result in a change of beam energy, but for the quadrupole and sextupole magnets, different stable optics can be found for a constant beam energy.

So far we have not given much thought about the **longitudinal movements**. The particles in the accelerator lose a certain amount of energy every revolution, the main contributing factor to this is the emission of synchrotron radiation (SR), which will be explained in detail in Ch. 2.2.2. When operating a synchrotron as storage ring, this energy loss needs to be compensated, otherwise the particles will be lost quickly. Typically the energy loss is rather low compared to the total energy of the particles. For ANKA, for example, it is around 600 keV per revolution for a beam energy of 2.5 GeV. In Eq. 2.1 on p. 7, the energy gain introduced by RF cavities was already briefly stated to be:

$$\Delta E = qV_0 \sin \Psi_s, \quad (2.20)$$

with  $q$  as charge of the particle,  $V_0$  the amplitude of the voltage and  $\Psi_s$  the stable phase at which the particle travels through the field.

While for the transverse directions, quadrupole magnets focus the beam, in the longitudinal direction phase focusing is achieved by the sinusoidal RF field, an effect which is illustrated in Fig. 2.2.

Particles with a momentum that is smaller than the nominal momentum, are deflected on a different path inside the dipole magnets. If the momentum compaction factor (see Eq. 2.23) is positive, which is the standard case, this leads to them traveling on a slightly shorter orbit than particles with a slightly higher momentum. If traveling on a shorter orbit, they arrive earlier at the RF cavity, when the field is higher, and thus they gain more energy. Vice versa, if they have a too high momentum, they arrive later and gain less energy. The overall effect is a focusing of the electron beam in longitudinal direction.



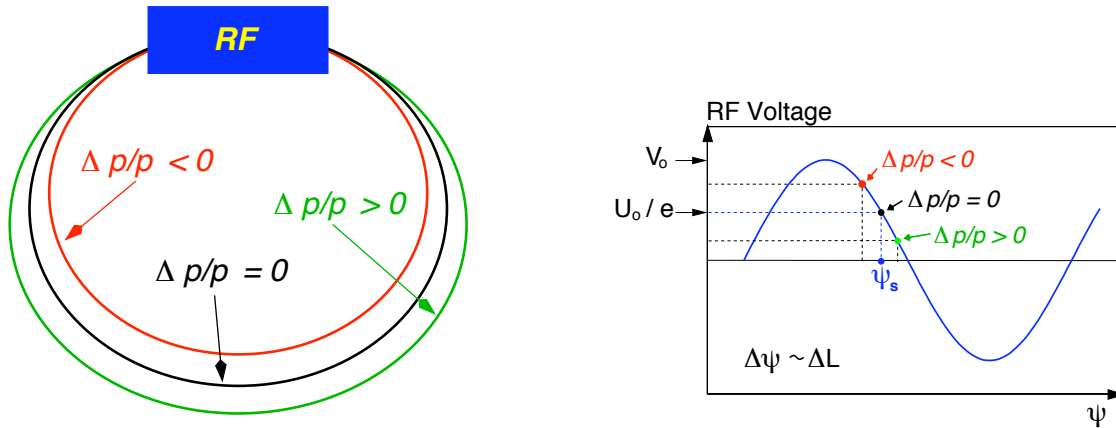


**Figure 2.2:** Particles with a momentum, which is smaller than the nominal momentum travel on a slightly shorter orbit than particles with a higher momentum. Because the particles are highly relativistic, a shorter orbit will cause them to arrive at the RF-cavity at an earlier phase which will result in them being affected by a higher field. This means, they will get a higher energy gain than particles with a too low momentum, which arrive later. This effect is called phase focusing. Illustration courtesy of A.-S. Müller.

For this to work out, the revolution frequency  $f_{rev}$  needs to be a subharmonic of the RF frequency  $f_{RF}$ .

$$f_{RF} = h \cdot f_{rev} \quad (2.21)$$

Here  $h$  is called the **harmonic number** of the accelerator. For ANKA,  $h$  is 184 and the RF frequency is slightly below 500 MHz (period length  $2 \text{ ns}$ )<sup>2</sup>, leading to a total circumference of the accelerator of 110.4 m.

If we neglect any changes of the energy loss due to small momentum deviations and assume that the energy loss is constant over the whole revolution time, the equation of motion for the momentum deviation coordinate  $\delta$  is solved by a harmonic oscillation, the synchrotron oscillation, with a frequency  $f_s$  (see e. g. [32, p. 15 ff]). Similar to the tunes in transverse direction, a tune in longitudinal direction can be computed by dividing the **synchrotron frequency**  $f_s$  by the revolution frequency.

$$Q_s = \frac{f_s}{f_{rev}}. \quad (2.22)$$

Bunches in accelerators typically have large numbers of particles ( $n > 10^6$ ), so it is convenient to describe the particles in a bunch as **ensemble** and find a common solution for the whole ensemble. The particle beam is then characterized by a particle distribution in phase space, usually a Gaussian distribution can be assumed with different RMS widths  $\sigma$  along the different directions ( $\sigma_x, \sigma_{x'}, \sigma_y, \sigma_{y'}, \sigma_z, \sigma_\delta$ ). Assuming that there is no interaction between the particles, the solution for the ensemble can be deduced straight from the solutions for single particles. Here, every accelerator has a certain acceptance, which

<sup>2</sup>The exact frequency is adapted in the range of typically 499.69 to 499.73 MHz by mechanically changing the resonance frequencies of the cavities.

determines for which areas in the phase space, the particles can be stored. In transverse directions, this acceptance is mainly determined by the geometry of the beam pipe and the energy acceptance in the longitudinal plane is determined mostly by the RF frequency that dictates longitudinal buckets, referred to as RF buckets inside which particles can be stored in the accelerator. Particles outside of this acceptance are lost after a few revolutions.

Now that the basic concepts of accelerator physics for storage rings have been introduced, the next section takes a closer look at the special short-bunch operation, which aims at the reduction of the bunch length  $\sigma_z$ .

### 2.1.2 Short Bunch Operation at ANKA

During a short-bunch operation, the main goal is to reduce the longitudinal beam size, the bunch length  $\sigma_z$ . As you will see later in Chapter 2.2.2, this will not only lead to a reduction of the length of the SR pulses, but also give a significant increase to the radiation power in the THz frequency range.

The coupling between transverse and longitudinal beam optics is caused by the dispersion  $D$  which leads to a momentum dependent change in orbit length, which can be described with the **momentum compaction factor**  $\alpha_c$

$$\alpha_c = \frac{\Delta L/L_0}{\Delta p/p} = \frac{1}{L_0} \oint \frac{D(s)}{R(s)} ds \quad (2.23)$$

So the momentum compaction factor  $\alpha_c$  gives a measure for the longitudinal compression for a given set of optics functions. The bunch length  $\sigma_{z,0}$  is then given by

$$\sigma_{z,0} = \frac{c\sigma_\delta|\alpha_c|}{2\pi f_s} \quad (2.24)$$

for the case of highly relativistic particles [33].

The synchrotron frequency  $f_s$  can be computed by the following equation [33]:

$$f_s = f_{\text{rev}} \sqrt{\frac{\alpha_c h}{2\pi E} \sqrt{(g \cdot e \cdot V_{\text{RF}})^2 - (U_0 + k)^2}} \quad (2.25)$$

Where  $h$  is the harmonic number,  $E$  is the beam energy,  $e$  the electron charge,  $g$  a voltage calibration factor,  $U_0$  the losses in the dipoles and  $k$  the losses due to multipoles and impedances. Thus is  $\sigma_z \sim \sqrt{\alpha_c} \sim f_s$  and approximately also  $\sigma_z \sim V_{\text{RF}}^{-1/2}$ .

The easiest way to decrease the bunch length is by simply increasing the RF voltage  $V_{\text{RF}}$ , this, however, is limited by the fields the cavities in the storage ring can achieve. To decrease the bunch length further, we can decrease the integral over the dispersion function, which will decrease  $\alpha_c$  and thus the bunch length  $\sigma_z$ . The decrease in the integral over the dispersion function is achieved by changing the strengths of the quadrupole and sextupole magnets in a way that the dispersion becomes negative in the parts where it used to have values around zero for the uncompressed optics. Figure 2.3 shows the optical functions  $\beta_x$ ,  $\beta_y$  and  $D$  for uncompressed beam optics (left) and for compressed optics (right).



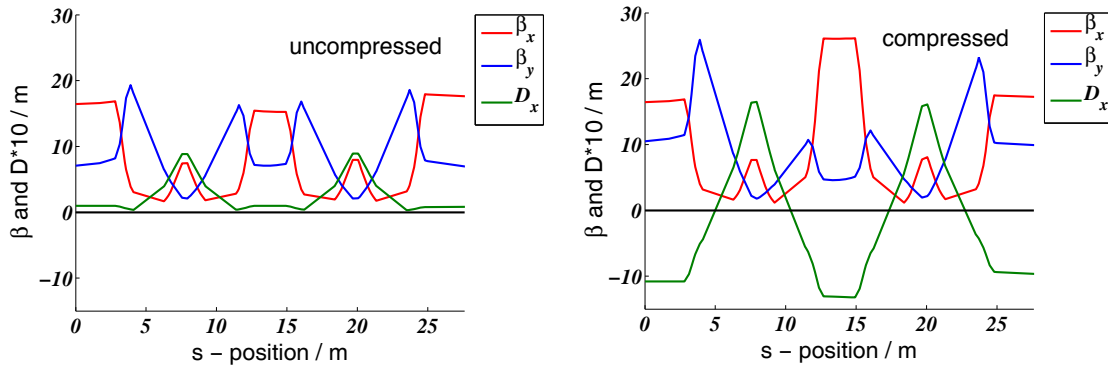


**Figure 2.3:** Optics functions for the uncompressed standard optics at 1.3 GeV (left) and for the compressed low- $\alpha_c$ -optics (right) at ANKA, shown for one sector. Compared to the uncompressed optics, the dispersion for the compressed optics is negative in some parts of the ring, decreasing the integral over the dispersion, thus decreasing  $\alpha_c$ . The slightly larger beta functions are accepted. Courtesy of M. Klein, model published in [34].

The procedure to change the optics to the low- $\alpha_c$ -optics is referred to as “squeeze”. It is achieved with a step-wise change of the magnet strengths (quadrupole, sextupole, and corrector magnets) going from the normal (uncompressed) optics to low- $\alpha_c$ -optics and so a continuous decrease of  $\alpha_c$  can be achieved.

## 2.2 Radiation from Charged Particles

This Section covers the radiation emitted from charged particles. Depending on how close an observer is to the electron bunch, we differentiate between the near-field or “direct” field (Coulomb regime), where we speak of the Coulomb field of the particles (Sec. 2.2.1) and the far-field (radiation regime), in which we speak of synchrotron radiation (SR) or coherent synchrotron radiation (CSR) (Sec. 2.2.2). Typically, in electro-dynamics, the near-field term is  $\sim \frac{1}{R^2}$  and the far-field term  $\sim \frac{1}{R}$  in the equation describing the electric field[35], but for the description used here it is more suitable to separate the fields into the Coulomb regime, which is seen by an observer close to the electron bunch and the synchrotron radiation observed far away from the electron bunch.

The near-field radiation is dominated by the Coulomb field of the relativistic charge distribution and can be understood as a constant electric field, the particle beam drags along itself while propagating around the ring at nearly the speed of light. Because the EO bunch length and shape measurements carried out for this work have been performed in the near-field regime, the temporal field characteristics in the near-field are shown in the first subsection. There it will be shown that the temporal field profile of the radiation in the near-field resembles the longitudinal charge density.

Storage rings are designed to generate a lot of SR from many different source points around the ring, the radiation is then guided to various experimental stations around the ring, where the actual user experiments (e. g. spectroscopy) can take place simultaneously. Unlike the Coulomb field, SR is only emitted when the particles are accelerated, predominantly when the acceleration is perpendicular to the direction of propagation as it occurs when the particles are deflected inside a magnetic dipole field. Storage rings offer the unique possibility to generate collimated beams of SR which offer an effectively continuous spectrum over a large wavelength range spanning from microwaves up to hard X-rays. Especially in the X-ray range, the beam quality is far superior to that of lab sources like X-ray tubes, because the SR beam is highly collimated.

The emitted SR propagates inside an evacuated beam pipe into the beamlines, which are measurement stations a few meters away from the source points inside the dipole magnets. The radiation can be used for various experiments, depending on the specialization of the corresponding beamline. Typically, at a synchrotron storage ring, most dipole magnets are equipped with at least one beamline which is designed for a designated application. Even though, the radiation itself has a very wide spectral range, usually only a smaller part of this huge spectral range is used at a specific beamline. Because the temporal intensity profile of the emitted SR resembles the longitudinal charge density of the electron bunch - a fact which will be shown in Ch. 2.2.1 - the radiation itself can be used to diagnose the electron beam. This feature was exploited by the streak camera measurements carried out for this work.



### 2.2.1 Near-Field - Coulomb Regime

For a highly relativistic electron, the longitudinal component of the Coulomb field  $E_z$  is contracted by a factor of  $1/\gamma$  with respect to its radial components, where  $\gamma$  is the relativistic Lorentz factor. The radial component of the electric field of a relativistic point charge  $Q$  moving at a constant velocity of  $v = \beta c$  along the  $z$ -axis is given in cylindrical components by (p. 559 in [35]):

$$E_r(r, t) = \frac{Q}{4\pi\epsilon_0} \cdot \frac{\gamma \cdot r}{(r^2 + \gamma^2 v^2 t^2)^{3/2}} \quad (2.26)$$

where  $z = 0$  for  $t = 0$ . For a highly relativistic electron with  $\gamma \gg 1$ , the temporal behavior of the radial component becomes a very short spike. If we now want to know the temporal field for a line charge density  $Q(t)$  moving along  $z$ , we need to convolute the charge density with the field for a point charge from Eq. 2.26.

$$E_{r,Q}(r, t) = (E_r * Q)(r, t) \quad (2.27)$$

$$= \int_{-\infty}^{+\infty} E_r(r, t - t') Q(t) dt' \quad (2.28)$$

During the low- $\alpha_c$ -operation at ANKA, the electron beam energy is typically 1.3 GeV, which results in a Lorentz factor of  $\gamma = 2544$ . Evaluating Eq. 2.26 for a distance of 10 mm, and  $\gamma = 2544$  yields a very narrow spike with a width of just 20 fs FWHM. This is the electric field for a relativistic point charge. Compared to the actual bunch length which is  $\sigma_z > 1$  ps,  $E_r(10 \text{ mm}, t)$  can be taken as  $\delta$  function, so the convolution does not alter the shape of  $Q(t)$ . Only for bunch lengths  $< 100$  fs (or substructures on the bunch on such a time scale) and at a distance of 10 mm, the electric field starts to smear out slightly. Figure 2.4 shows the computed curves corresponding to those parameters.

### 2.2.2 Far-Field - Synchrotron Radiation (SR) & Coherent SR (CSR)

This section covers the far-field regime, which is seen by an observer far away from the charge. In the far-field regime, we speak of synchrotron radiation (SR), whose generation is the main purpose of any synchrotron lightsource. In addition to the “normal” SR, coherent synchrotron radiation (CSR) is emitted during the short-bunch operation.

While the full mathematical deduction of the spectral, temporal and angular properties of SR is rather lengthy and can be found in standard literature like [36], here just its characteristics are shown. Furthermore, it is illustrated how the the properties of the CSR depend on the longitudinal bunch profile.

Figure 2.5 illustrates the emission of the SR inside a bending magnet. The radiation is emitted inside a narrow cone in the vertical direction. The opening angle of the cone is proportional to  $\gamma^{-1}$ , so for a highly relativistic electron beam with  $\gamma \gg 1$ , this will produce a very collimated beam. In horizontal direction the radiation will fan out over the whole range of the deflection inside the dipole magnet, but typically, only a narrow part of this fan is detected inside the beamlines because the aperture inside the beam pipe is limited at some point. The radiation is polarized horizontally in the orbit plane. Outside of this plane, it shows a circular polarization, which swaps handedness between above and below



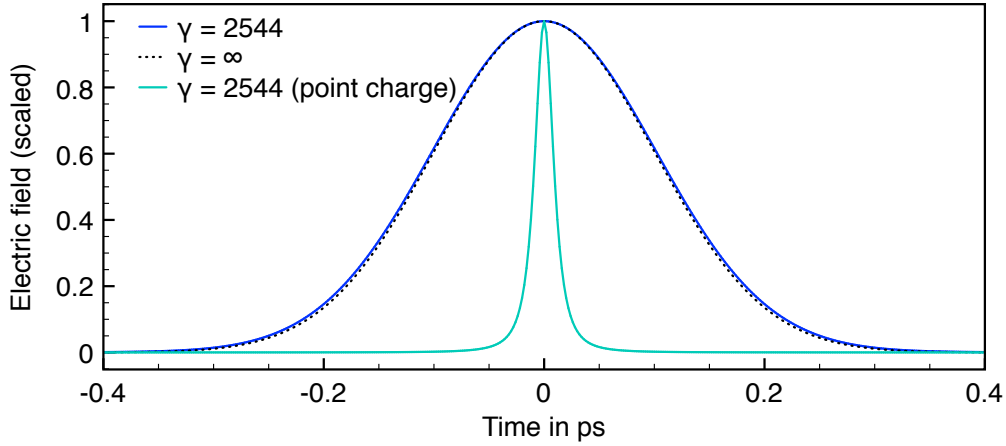


**Figure 2.4:** Radial components of the electric fields for relativistic electron bunches following Eq. 2.27 for  $\gamma = 2544$  (blue, solid curve) and  $\gamma = \infty$  (dashed black line), both computed for an initial width of  $\sigma_z = 100$  fs seen at a radial distance of 10 mm away from the direction of propagation. In addition to that, the field for a point charge following Eq. 2.26 is shown for  $\gamma = 2544$  (light blue solid line). The FWHM width of the curve is 20 fs. The effect of the very slight broadening due to the convolution of the charge density with the electric field of a point charge can be seen very slightly when comparing the curves for  $\gamma = 2544$ , with the one for  $\gamma = \infty$  for which this effect does not occur.

the orbit plane.

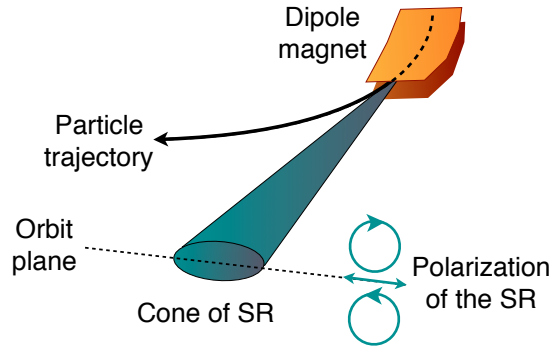


**Figure 2.5:** The synchrotron radiation (SR) is emitted in a cone tangential to the trajectory when the electrons are deflected inside a dipole magnet. The direction of polarization is horizontal in the orbit plane and circular above and below the orbit plane. According to the illustration in [27].

The total power of the emitted SR for a single particle is given by [29]:

$$P_s = \frac{e^2 c}{6\pi\epsilon_0(m_0c^2)^4} \frac{E^4}{R^2} \quad (2.29)$$

The fact that  $P_s \sim m_0^{-4}$  explains why preferably light particles, like electrons, are used for the generation of SR. To increase the radiation power, the energy can be increased and due to  $P_s \sim E^4$ , the scaling is enormous.



In the top of Fig. 2.6, the calculated spectrum of the SR emitted at ANKA is shown in dependence of the beam energy. One can clearly see that the low frequency part of the spectrum is not affected by the change in beam energy, but the high frequency part extends to higher frequencies.

In the low frequency part, the flux gradually decreases, the increase below 0.03 THz, however, is caused by the coherent component of the SR, the CSR. Unlike the normal SR, whose spectrum for many electrons does not differ from the spectrum for one single electron, the spectrum of the CSR is highly dependent upon the longitudinal bunch shape and will be discussed further down.

The length of the SR radiation pulse emitted from a single electron, observed in the far-field (e. g. at a beamline) has a finite length  $\delta t$ , which is caused by the electrons traveling at a slightly lower velocity than the emitted photons. So the observer sees photons coming from a small angle, which causes the finite length to the observer [36]:

$$\delta t = \frac{4R}{3c\gamma^3} \quad (2.30)$$

With R being the bending radius, c the speed of light and  $\gamma$  the relativistic gamma factor. For highly relativistic electrons, where  $\gamma > 10^3$  and with typical bending radii being in the order of a few meters,  $\delta t$  is in the order of several tens of attoseconds ( $10^{-17}$  s).

The temporal characteristic of the SR pulse from a whole electron bunch, is then just given by the convolution of the longitudinal bunch profile and the pulse emitted from one electron. Because the pulse from a single electron can be assumed to be a delta pulse compared to the longitudinal bunch profile ( $\sigma_z \approx 10^{-12}$  s), the intensity profile of the SR pulse resembles the longitudinal bunch profile perfectly. An important fact, which makes it possible to perform non-invasive longitudinal beam diagnostics by analyzing the temporal characteristics of the emitted SR.

Coming back to the coherent part of the emitted SR:

The time-averaged spectral power density for  $N_e$  electrons inside a beam with current I, is given by [37]:

$$\begin{aligned} \frac{dP}{d\omega} &= \frac{9R}{16\pi^3 c \gamma^2} \left( \frac{\omega}{\omega_c} \right)^2 P_{\text{total}} ((1 - \mathcal{F}) + N_e \mathcal{F}) \\ &\times \phi_{\text{max}} \int_0^{\theta_{\text{max}}/2} d\theta (1 + \gamma^2 \theta^2)^2 \left[ K_{2/3}^2(G) + \frac{\gamma^2 \theta^2}{1 + \gamma^2 \theta^2} K_{1/3}^2(G) \right] \end{aligned} \quad (2.31)$$

Here R is the radius of curvature of the electron trajectory. The critical photon frequency  $\omega_c = \frac{3c\gamma^3}{2R}$ . G, the argument of the modified Bessel functions  $K_{1/3}$  and  $K_{2/3}$  is given by  $G = \frac{\omega}{2\omega_c(1+\gamma^2\theta^2)^{3/2}}$  and  $P_{\text{total}} = \frac{e\gamma^4 I}{3\epsilon_0 R} = 88.46 \frac{E^{AI/A}}{R/m}$ . The number of electrons  $N_e = \frac{IC}{ec}$ , with C being the circumference of the whole ring. And  $\theta_{\text{max}}$  and  $\phi_{\text{max}}$  give the aperture of the port where the radiation is observed.

$\mathcal{F}$  is the so-called, form factor

$$\mathcal{F}(\omega) = \left| \int d\mathbf{r} Q(\mathbf{r}) e^{i(\omega/c)\hat{\mathbf{n}}\mathbf{r}} \right| \quad (2.32)$$



The integral goes over the full 3d charge distribution  $Q(\mathbf{r})$  and  $\hat{n}$  is the unity vector from the observer to the charge. Because the emission is strongly peaked in the forward direction, we can simplify the integral to a one-dimensional integral over the line charge density of the electron bunch. For a Gaussian charge distribution, with  $\sigma_z$ , we obtain [37]

$$\mathcal{F}(\omega) = e^{-\left(\frac{\sigma_z \omega}{c}\right)^2} \quad (2.33)$$

For wavelengths  $\lambda = 2\pi c/\omega$ , which are shorter than the bunch length  $\sigma_z$ , the form factor drops rapidly, reducing Eq. 2.31 to the expression for incoherent emission of radiation (i.e. the standard SR spectrum). For wavelengths which are equal or longer than the bunch length, however, the coherent term becomes the dominant one. This results in an enormous boost of the radiation power in that region with a factor of  $N_e$ , which typically is in the order of  $10^9 > N_e > 10^6$ . Coming back to Fig. 2.6, in the bottom the full spectrum following Eq. 2.31 is shown for the parameters present at ANKA. Spectra are depicted for different bunch lengths during the low- $\alpha_e$ -operation. By decreasing the bunch length down into the low picosecond range, the spectrum of the emitted CSR can be shifted into the low THz range. Radiation in this frequency range is still comparably hard to come by with lab sources, especially when a wide spectral range or single-cycle characteristics of the emitted THz pulses are required. This is the reason why some storage rings offer a dedicated short-bunch mode of operation to users, which are interested in the THz range.



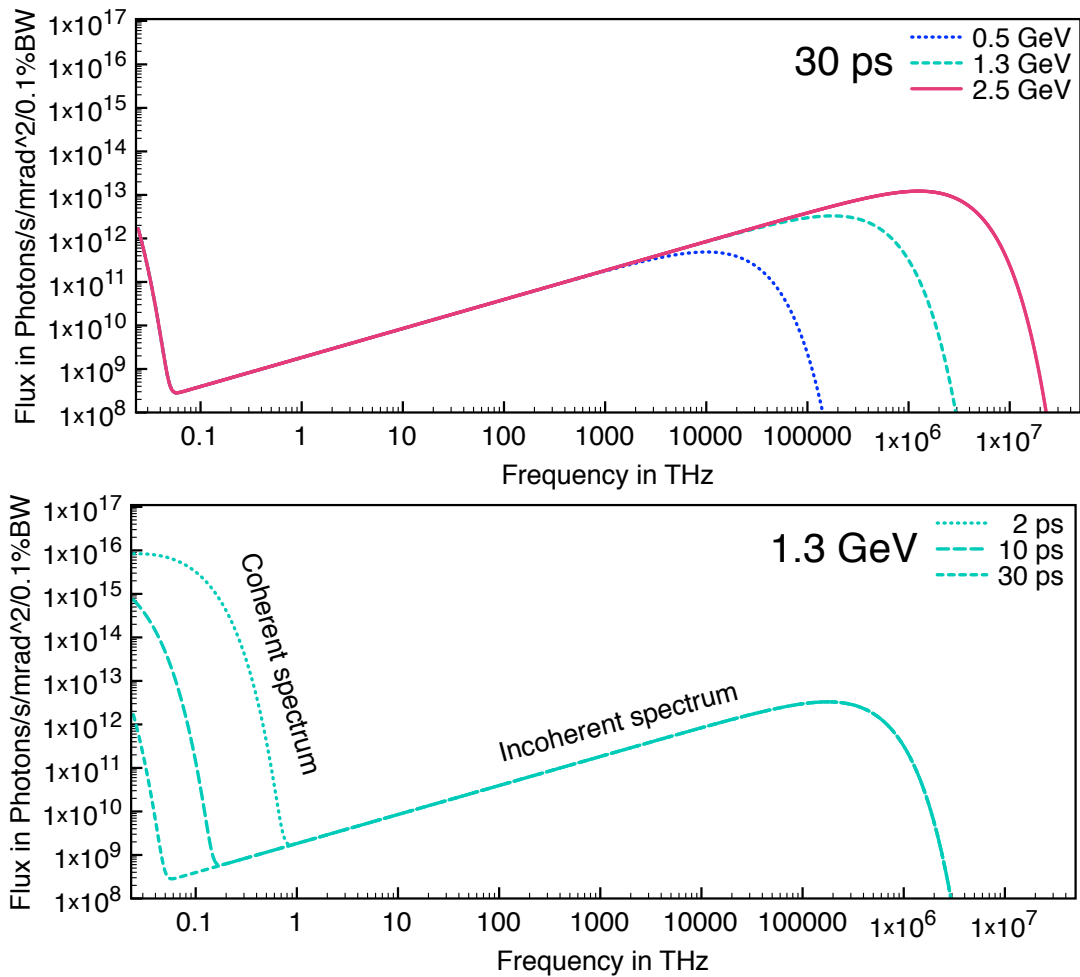


**Figure 2.6:** Calculated full synchrotron radiation flux spectra (coherent and incoherent) for  $10^8$  electrons in one Gaussian bunch at ANKA. While the frequency components between 1 and  $10^4$  THz remain constant for the beam parameters at ANKA, the range  $> 10^4$  THz is dominated by the beam energy, and the low frequency range  $< 1$  THz is by CSR for which the defining parameter is the bunch length. Top: Spectra for different beam energies and a fixed bunch length, here only the incoherent part shifts to higher frequencies for higher beam energies. Bottom: Spectra for different bunch lengths for a fixed energy, here the CSR contribution extends to higher frequencies for shorter bunch lengths. Code to calculate the spectra, courtesy of V. Judin.

## 2.3 Microbunching Instability

All the derivations of the bunch length in Section 2.1.2 do not take into account any kind of particle-particle interactions, this is only a good assumption for comparably low charge densities inside the bunches. For higher charge densities, which typically are reached a lot quicker during the low- $\alpha_c$ -operation, because the bunches are compressed longitudinally, those interactions lead to an increase in bunch length and the originally Gaussian distribution distorts with the longitudinal profile leaning slightly forward (profiles will be shown later on e. g. Fig. 4.5 on p. 42). In the case of very high bunch compressions, the bunch length is not constant, but starts to show dynamic substructures. We have learned in the previous Section that changes to the form factor (see Eq. 2.32 & 2.33), which can be imagined as Fourier transform of the temporal bunch profile, change the spectrum of the emitted CSR (shorter bunches  $\leftrightarrow$  wider spectrum; substructures  $\leftrightarrow$  components with a higher frequency). So if the bunch becomes shorter and longer due to some beating effect, or if a time dependent substructure will form upon it, it will greatly alter the detected CSR intensity.

Several ring accelerators published that they observed a beam current dependent bunch lengthening effect and even a bursting behavior of the emitted CSR [15–19]. This led to the development of a first theory to describe this so-called microbunching instability by [20] and [21].

First experiments validated the predictions by the model [22]. In the microbunching model, the interaction of the beam with its own SR creates substructures in the longitudinal density profile of the bunch, called microbunches, within the bunch. This microbunching then amplifies itself via the coherent emission of CSR. The growth and decay of the microbunching instability then causes a series of sometimes even periodic bursts of CSR. Furthermore, the microbunching instability limits the bunch compression that can be achieved, because it leads to a current depending bunch lengthening effect. So it does not only make the emission of CSR hard to predict and unstable, but also makes the bunches on average longer than desired.

Figure 2.7 shows temporal observations of the emitted THz signal from a single bunch over many revolutions around the ring. The intensity of the emitted CSR clearly shows a bursting behavior which changes modes for different bunch currents. A detailed study of the bursting behavior at ANKA can be found in [38].

Over the years, the theoretical predictions have been improved, but their refinement is still ongoing work within a few theory groups world-wide [40–42].

Predictions of the longitudinal phase space from [41] are shown in Fig. 2.8. There, the longitudinal phase space is simulated for compressed bunches. The projection of the longitudinal phase space onto the z-coordinate gives the longitudinal bunch profile, which for the simulations, clearly shows substructures. The exact shape of the longitudinal phase space and the formation of the sub-structures is not only dependent on the bunch charge, but also differs for different machine optics.

The formation and the temporal evolution of those substructures are a very interesting



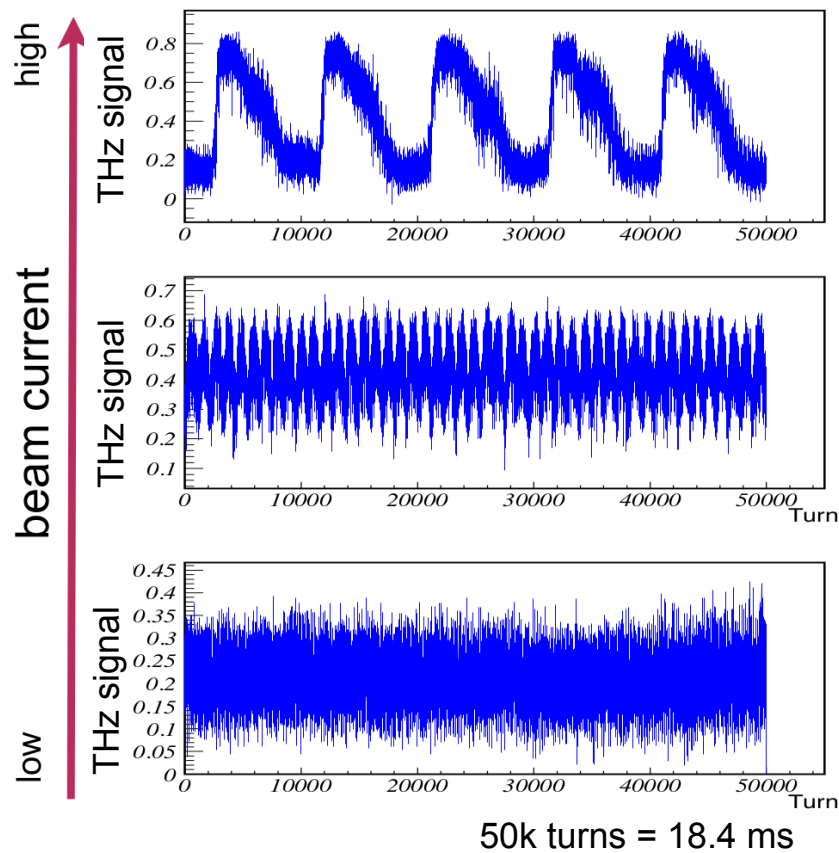


**Figure 2.7:** Measurements of the peak signal of the emitted CSR over 50k revolutions at ANKA for different currents. Top: For a high beam current, the CSR is emitted in burst of radiation with a periodicity in the order of 300 Hz. Middle: For intermediate bunch currents, the frequency of the CSR bursts seems to increase. Bottom: For a very low bunch current, the signal seems to become dominated by white noise. Courtesy of V. Judin, data published in [39].

field of current research and motivated the measurements of longitudinal bunch profiles performed for this thesis.

However, the measurement of the longitudinal phase space is not an easy task and especially the detection of any dynamic changes of the longitudinal bunch profile requires not only a sup-ps resolution, but also single-shot measurements. The next Chapter will give an overview over measurement techniques which allow us to detect the longitudinal bunch shape in great detail.

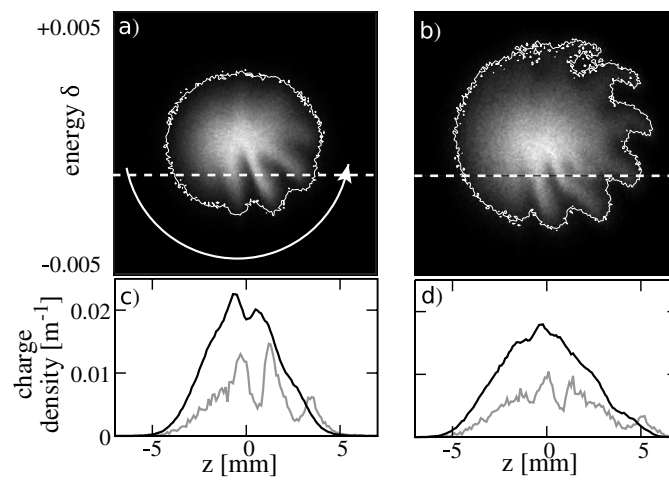


**Figure 2.8:** Simulations of the typical longitudinal phase-space ( $z, \delta$ ) at the storage ring SOLEIL (France) for a current of 0.5 mA (a) and 1.0 mA (b). In c and d the corresponding projections along the longitudinal coordinate are shown. While the black lines are the projections over the whole energy range, the grey lines present the projections around the white dashed lines in a and b. The formation of finger-like structures in the longitudinal phase space will lead to substructures on the longitudinal bunch profile. Courtesy of C. Evain, published in [41].

# 3. Techniques for Longitudinal Beam Diagnostics

This chapter will give a very basic introduction to longitudinal beam diagnostics, focusing mainly on the detection techniques which were used for the measurements presented in this work. The first section - Section 3.1 - will give a short overview of longitudinal beam diagnostics and motivate why they play an important role. The focus will be put on diagnostics for electron storage rings - such as ANKA - which offers a special short bunch operation - the low- $\alpha_e$ -operation. Then the two main diagnostics methods, which were used for the measurements shown further along this thesis, are discussed in detail. The first one is the streak camera (SC) - in Chapter 3.2 - which is a very common diagnostics device used at many accelerators world-wide [43]. The second method is based on using the electro-optical effect to modulate the longitudinal bunch profile onto a laser pulse. It is a technique which has recently found its way from laser physics into the world of accelerator physics. At ANKA, this technique has now been used for single-shot near-field bunch profile measurements for the first time at a ring machine. Its history with respect to accelerator physics and its working principles are explained in Chapter 3.3.

## 3.1 Introduction to Longitudinal Diagnostics

Longitudinal diagnostics groups diagnostic devices which resolve the time dependent particle density distribution in an accelerator. Whether the diagnostics aim to resolve the temporal behavior in the range down to femtoseconds or up to seconds highly depends on the type of accelerator. This thesis is about bunch length measurements at an electron storage ring therefore the main focus of this chapter will be to introduce the working principles of the longitudinal diagnostics present at ANKA.

Most parameters of the ANKA storage ring have already been introduced along the way in Chapter 2.1, here just the parameters with relevance for longitudinal diagnostics are given:



- Revolution time: 368 ns
- Minimum bunch spacing: 2 ns
- Bunch length: 45 ps RMS (normal user operation), down to 2 ps RMS (low- $\alpha_c$ -operation)

The revolution time states how long it takes for a single electron bunch to revolve around the accelerator. The minimum bunch spacing is given by the period length of the RF to which the cavities are tuned. In our case, the RF frequency is approximately 500 MHz which leads to a minimum bunch spacing of 2 ns. The length of the electron bunches is usually stated as RMS value of the longitudinal distribution.

In contrast to linear accelerators, all diagnostics at a storage ring has to be non-invasive to the electron beam. There are several diagnostics devices which can resolve individual bunches, and give information about how many electrons are inside those bunches. This is usually referred to as measurements of the filling pattern. An example for such a device would be an annular electrode or a stripline detector, both work in a way that a bypassing electron bunch induces a signal which is then read out by a fast digitizer like an oscilloscope. Because the synchrotron radiation has practically the same temporal characteristics as the electron density distribution, it is possible to use diagnostics which detect the synchrotron radiation pulses rather than obtaining an electrical signal from the electron bunches.

There are also indirect methods such as time-correlated single photon counting (TCSPC) which allow for a very precise measurement of the filling pattern. It is achieved by measuring time delays between a revolution trigger signal and the events generated by single photons hitting an avalanche photodiode. There is a diploma thesis about filling pattern measurements at ANKA by B. Kehrer which covers different detectors for filling pattern monitors in great detail[44].

What filling pattern monitors typically cannot resolve is the bunch length. This is because all those devices are limited by the bandwidth, either the bandwidth of the detector itself or the bandwidth of the readout electronics, which determine their temporal resolution. For example an oscilloscope with a bandwidth of 20 GHz, only gives a temporal resolution of 50 ps.

At the time this thesis was written, leading oscilloscope manufacturers had high end oscilloscopes with a bandwidth of 60 GHz on the market and first direct electron bunch length measurements had been undertaken at ANKA by a group from the Institute of Micro- und Nanoelectronic Systems (IMS) within KIT who have developed a very fast THz-detector[45]. They managed to detect a signal with a length of just 17 ps FWHM, the bandwidth limit of the oscilloscope. Independent bunch length measurements with our streak camera could confirm, that this length agreed with the length of the electron bunches for the machine conditions present.

To resolve the temporal shape of an electron bunch, an even better resolution down to the sub-ps range is desired. At the moment, this can only be achieved with indirect measure-





ments that translate the fast temporal information in either spatial or spectral information.

For storage rings, the most common detector to measure the longitudinal bunch profile is a streak camera, which translates the fast temporal information of a synchrotron light pulse into a spatial information which can then be detected from a fluorescent screen. While a streak camera is a very powerful tool to measure the averaged bunch profile with a very high precision<sup>1</sup>, it is not sensitive enough to allow for single-shot bunch profile measurements which could reveal any kind of dynamic substructure on the electron bunches. The detailed working principle of streak cameras will be discussed in Chapter 3.2.

Several measurements in the time domain during the low- $\alpha_c$ -operation at ANKA and elsewhere have revealed a bursting behavior of the emitted CSR (see Chapter 2.3), which is believed to be caused by dynamic changes of the longitudinal electron distribution. To understand these effects, we searched for a non-destructive detection technique which would allow the measurements of single-shot bunch profiles. Our choice fell onto the non-destructive EO techniques which make use of the EO effect to modulate the electric field of an electron bunch onto a laser pulse which is then analyzed. Chapter 3.3 will explore the working principle of EO techniques in more detail.

## 3.2 Streak Camera

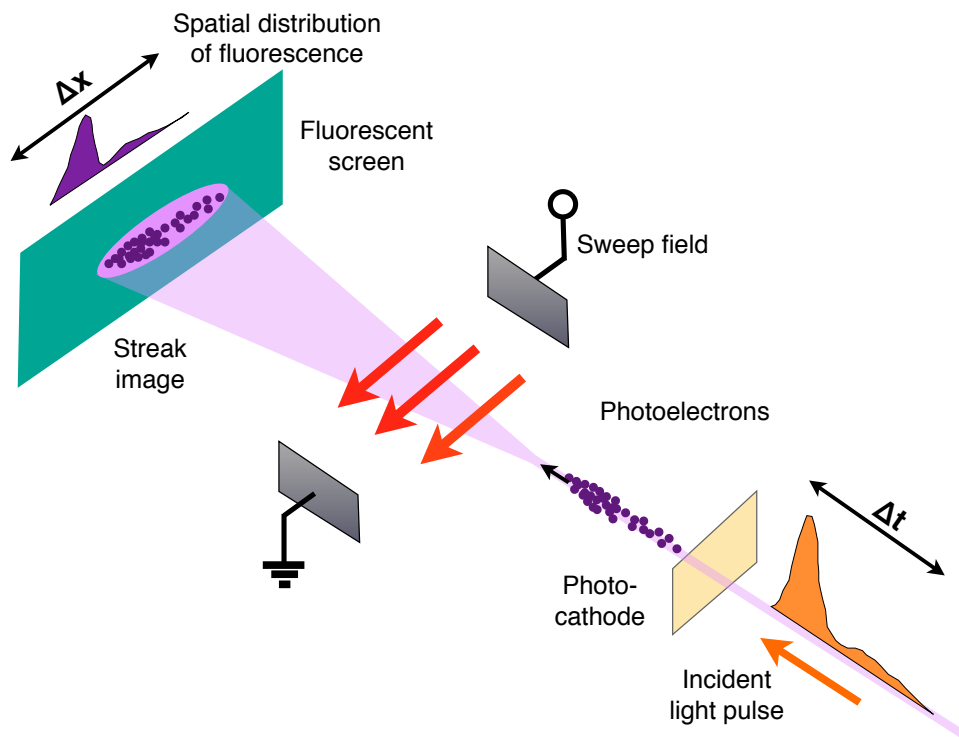


**Figure 3.1:** Illustration showing the working principle of a SC following the illustration in [46].

<sup>1</sup>400 fs resolution and a minimum detection limit of 1.7 ps FWHM for our model

A streak camera is a detector which allows us to measure the longitudinal bunch profile. It measures the temporal intensity distribution of SR pulses - typically in the visible range<sup>2</sup> by transferring the temporal distribution to a spatial one. The working principle of a streak camera is depicted in Fig. 3.1. An incident SR pulse is sent to a photocathode which in turn emits photoelectrons. The time distribution of those photoelectrons is equal to that of the incident light pulse. The photoelectrons are then directed towards a fluorescent screen. On their way to the fluorescent screen they have to pass a time-varying high voltage field between two metal plates, usually referred to as sweep field. The sweep field will be set in a way that electrons arriving earlier will see a different field than electrons arriving later. As a consequence, they will hit the fluorescent screen at a different location. There is an electron multiplier<sup>3</sup> right before the fluorescent screen to amplify the signal (not drawn). The streak image will have a spatial distribution along the screen that corresponds to the time distribution of the incident light pulse. A CCD camera is used to capture an image of the fluorescent screen to allow evaluation of the data. With this setup not only the pulse length, but also the full time characteristics of the pulse can be extracted from the CCD image.

The synchrotron radiation has an intensity distribution which corresponds to the charge distribution within the accelerator (see Ch. 2.2.2). For ANKA it was already mentioned that this can vary between a bunch-train structure with usually three trains consisting of around 30 bunches each or just a single bunch every revolution<sup>4</sup>. In particular during the multi-bunch operation it is of great interest to not only measure the length and shape of bunches, but also the time structure for one complete revolution. This, however, brings another challenge with it: The bunches themselves are very short (ps) compared to the distance between two bunches (2 ns). To measure the filling pattern a time scale of several hundred nanoseconds is required, but to measure the individual pulse shapes, a fine picosecond-resolution is needed. This can be achieved by adding a second sweep unit with a field perpendicular to the first one, so the two dimensional fluorescent screen can be filled not only in x-direction, but also in y-direction. This second unit then sweeps at a different speed, thus allowing us to have a slow and a fast time axis on the screen.

For the streak camera<sup>5</sup> in use at ANKA the fast time axis can be varied between 190 ps and 800 ps in four steps, the slow time axis can be varied between 100 ns and several milliseconds.

The horizontal and vertical size of the light beam which is focussed onto the slit opening of the streak camera is one of the factors limiting the resolution along the axes. Schematically, this effect can be seen in Fig. 3.1, where the image on the screen is already two dimensional without having a deflection in the y-direction.

The scale along the fast time axis is between 190 to 800 ps, as stated above, but the actual pulse length of the synchrotron radiation pulses is below 100 ps, and can be even as low as a few picoseconds during the low- $\alpha_c$ -operation. This means there is quite some unused

---

<sup>2</sup>There are also models which work with X-ray pulses.

<sup>3</sup>typically a multi-channel plate (MCP)

<sup>4</sup>Time for one revolution: 368 ns

<sup>5</sup>Model C5680 by Hamamatsu with a synchroscan plugin and dual time base extender.



space along the fast axis, whereas the time resolution along the slow time axis - which can only go as low as 100 ns over the 640 pixels - is barely enough to tell two bunches apart. In particular when smearing because of the transverse beam size is taken into account. A convenient way to solve this is to have two neighboring bunches detected with a spatial displacement along the fast time axis, so the odd bunches are for example shown in the bottom half of the screen and the even bunches in the top half (or the other way around, depending on the delay time chosen).

The fast sweep needs to be driven by a RF frequency which is synchronous to the bunches, e. g., the 500 MHz RF clock, this ensures that the signals from consecutive bunch revolutions will be aligned at the same starting time of the fast sweep along the slow axis. If we now want to picture the signal from two consecutive bunches at different spots on the screen, a 250 MHz sine wave signal is used ( $\frac{1}{2} \cdot f_{RF}$ ) to control the fast sweeping unit rather than sweeping at the full 500 MHz. This sine signal is generated by a so called “Countdown Unit” which is fed by the 500 MHz RF clock signal and divides the frequency by two. An illustration of this working principle can be seen in Fig. 3.2.

The delay time which controls the delay of the sweep unit is adjusted so that, out of two neighboring bunches, one lies on the rising slope of the trigger signal and one on the falling slope. Changing the phase of the sinusoidal sweep voltage relative to the SR pulses allows us to move the bunches further apart along the fast time axis.

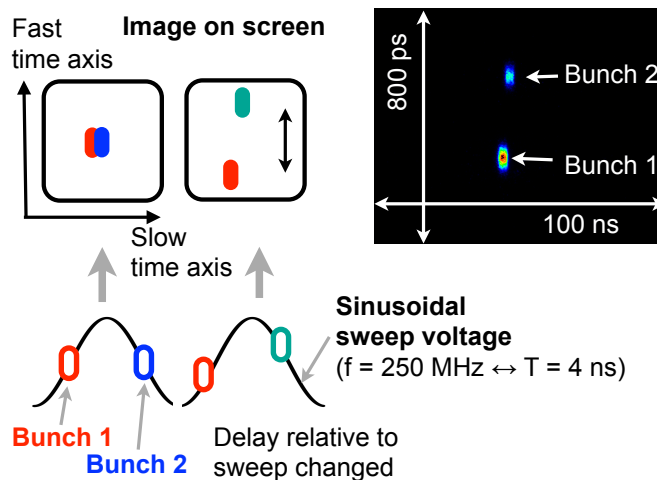


**Figure 3.2:** Left: Schematic drawing to illustrate how consecutive bunches (bunch spacing 2 ns) can be depicted with a SC when the delay time relative to the sinusoidal sweep frequency of 250 MHz is changed. Right: Actual averaged image recorded with the SC at ANKA, showing two bunches.

By decreasing the horizontal and vertical aperture of the streak camera, the time resolution can be improved, however, at the cost of intensity. With a lower intensity, the image on the screen is less bright, this makes the evaluation of the data from one bunch for one revolution very noisy (see Ch. 4.2.4). Thus averaging is required.

However, if we would just simply average the signal, fluctuations or oscillations of the arrival time of the bunches smear out the longitudinal profiles. So we record sequences of individual images, which enables us to detect the averaged arrival time over a shorter time range. This works, because the main contribution to changes in the arrival time of

the bunches are synchrotron oscillations with a frequency in the low kHz-range. Typically, the synchrotron frequency,  $f_s$  is between 4 - 40 kHz depending on the machine settings. This results in period lengths of one oscillation between 250 and 33  $\mu\text{s}$ . When recording sequences, the range of the slow time axis has to be set to several  $\mu\text{s}$  (usually around 100 - 500  $\mu\text{s}$ ) to obtain a sufficiently high signal to allow for an evaluation of the bunch profile for this image. Over this range, the individual synchrotron oscillations can be resolved easily and the averaged profile can be corrected for them. Even for slower deflections in the order of a few ms, this is possible. The post-processing algorithm, which is used to correct for the arrival time fluctuations is explained in more detail in Chapter 4.2.1.

Compared to the bunch spacing of 2 ns or the bunch revolution time of 368 ns, the slow deflection with several hundreds of  $\mu\text{s}$  is rather slow. Thus the signal from all bunches is depicted for many hundreds to thousands of revolutions<sup>6</sup> over the range of 640 pixels, which makes it impossible to tell which signal came from which bunch for which revolution. The electrons created by photons from different bunches and different bunch revolutions overlap slightly along the direction of the slow sweep. This leads to a broadening of the extracted pulse length if longitudinal oscillations with different phases for the individual bunches are present, or the bunch lengths for the individual bunches are significantly different. Typically this can be the case when the bunch currents differ greatly or longitudinal instabilities are present. This effect is decreased significantly during single- or double-bunch operation, because there the signal of only one individual bunch will overlap for several revolutions. So during single- or double-bunch operation we can study the temporal behavior of one bunch for several hundreds to thousands of revolutions. An example of a single image from such a sequence can be found in Figure 4.3 in Chapter 4.2.1.

### 3.3 Electro-Optical Techniques

Techniques for EO bunch length measurements utilize a linear EO effect - the so called Pockels effect (see Section 3.3.1). This effect can lead to a phase modulation of a laser pulse passing through an electro-optically active material in the presence of an external electric field. A suitable detection scheme (see Section 3.3.2) can then transform this induced phase modulation into an intensity modulation. This intensity modulation can finally be detected with the methods of electro-optical sampling (EOS) - Sec. 3.3.3 or electro-optical spectral decoding (EOSD) - Sec. 3.3.4.

Last, but not least, Section 3.3.5 gives a brief overview of the historical evolution of the field of EO bunch length measurements.

#### 3.3.1 The Pockels Effect & Phase Modulation

An EO effect describes the change in optical properties of a material in response to an external electric field. In the special case of EO bunch length measurements, we are interested in a change in refractive index which is linearly proportional to the external electric

---

<sup>6</sup>More than 1300 revolutions for a time range of 500  $\mu\text{s}$



field - the Pockels effect. A more detailed mathematical description of the Pockels effect has been moved to the Appendix A, here just a brief description of the effect without any derivations is given.

The Pockels effect generates a birefringence inside an electro-optically active crystal material - in our case gallium phosphide (GaP). Typical materials for EO bunch length measurements are GaP and zinc telluride (ZnTe), both are isotropic without the presence of an electric field, this means that the index of refraction  $n_0$  does not depend upon direction of propagation. But when an electric field is present, the refractive indices  $n$  along two of the crystal axes will become a function of the electric field. One of them will increase and the other one will decrease. They are referred to as the “slow”-axis with the refractive index  $n_s$  and the “fast”-axis with  $n_f$ . The induced difference in refractive index is directly proportional to the electric field. For our setup we have chosen GaP because it exhibits excellent phase matching between the electric field and the laser wavelength (1030 nm), so a relatively thick crystal can be used to yield a higher signal (see Eq. 3.1 ) [27].

The electric field which induces the modulation can be either the Coulomb field (near-field, see Chapter 2.2.1) or the field of the CSR (far-field, see Chapter 2.2.2).

For near-field EO bunch length measurements, the crystal has to be brought inside the UHV system of the electron beam pipe. Here the distance between the electron beam and crystal is only a few millimeters.

For the far-field variant, CSR - e. g. at a beamline - supplies the modulating field when it is focused and sent directly through the crystal.

The EO bunch length measurements carried out for this work have all been performed in the near-field, which had never been done before at any storage ring. But it should be mentioned that the first far-field measurements using CSR at a storage ring had also been carried out at ANKA, in 2009 [47].

To probe the field induced birefringence, a laser pulse is sent through the crystal at the same time as the modulating field. Because the response of the Pockels effect is very prompt, the temporal profile of electric field will be modulated onto the phase of the laser pulse, which will, in turn, result in a phase retardation of the laser pulse.

In the Appendix A it is shown that the phase modulation (phase retardation)  $\Gamma$ , which the laser pulse undergoes is directly proportional to the modulating electric field  $E$ .

$$\Gamma = \frac{\omega d}{c} n_0^3 r_{41} E. \quad (3.1)$$

Here  $\omega$  is the laser frequency (not the repetition rate),  $d$  the thickness of the crystal and  $r_{41}$  the Pockels coefficient of GaP. However, for this equation to hold, certain criteria concerning the crystal orientation and the directions of propagation and polarizations of the laser pulse and the modulating field need to be fulfilled. Figure 3.3 illustrates this alignment. The electric fields travel through the crystal perpendicular to the (110)-plane along which the crystal is cut. Their polarizations lie along the (-110)-axis which will maximize the

phase retardation for a given electric field.

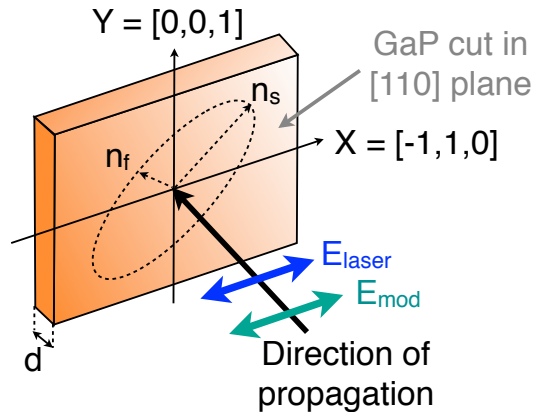


**Figure 3.3:** Illustration showing the alignment of the directions of propagation and the polarizations for the laser  $E_{\text{laser}}$  and the modulating electric field  $E_{\text{mod}}$  with respect to the GaP crystal (thickness  $d$ ) which is cut along its (110)-plane. The direction of propagation for the electric fields is perpendicular to the (110)-plane with their directions of polarization being parallel to the (-110)-axis X. The refractive indices of the fast and slow axis  $n_f$  and  $n_s$  which will change magnitude in dependence of  $E_{\text{mod}}$  are also indicated. Without the presence of a modulating field  $n_s = n_f = n_0$ .

To turn the phase retardation into a detectable intensity modulation a suitable detection scheme has to be applied which is explained in the following section.

### 3.3.2 Detection Scheme

There are various EO detection schemes, such as the “crossed polarizer scheme”, “the balanced detection scheme” or the “near crossed polarizer scheme” which can be used to detect the field induced phase retardation. In [26], a thorough mathematical description of the different schemes can be found.

Here, only the “near crossed polarizer scheme”, which we use for the EO bunch length measurements at ANKA is discussed.

With the near crossed polarizer scheme, we want to turn the phase retardation into a detectable intensity modulation. The advantages of this method are that the intensity of the detected signal can be adapted to the dynamic range of the detectors and the EO signal is already nearly linearly proportional to the field strength of the modulating field.

For this setup several optical components need to be placed along the beam path and Fig. 3.4 shows an illustration of the placement.

The laser pulse is first sent through a polarizer to ensure that it reaches the EO crystal with a linear polarization. After its modulation inside the crystal it passes through a quarter-wave plate (QWP), which is used to compensate any intrinsic birefringence the crystal might already exhibit (e.g. due to mechanical stress or defects inside the crystal). The half-wave plate (HWP) is then used to rotate the polarization by a small angle with

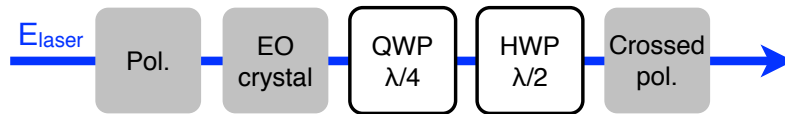


**Figure 3.4:** Near crossed polarizer scheme. The laser first goes through a polarizer to ensure its linear polarization when it passes the subsequent EO crystal. The modulated laser pulse then passes a quarter-wave plate (QWP) to correct for any intrinsic birefringence of the crystal and then a half-wave plate (HWP) which can rotate the direction of polarization to adjust the intensity that passes through the following polarizer which is in crossed position with respect to the first polarizer. While the orientations of the polarizers and the EO crystal are fixed, the QWP and HWP can be rotated to adapt the setup.

respect to the crossed polarizer.

The detectable laser intensity at the end of the setup can be calculated using Jones calculus (see e. g. [48]). For Jones calculus, the optical components are represented by transformation matrices. The matrices for the different optical components are simply multiplied to obtain a transformation matrix for the whole optical setup. The calculations for the near crossed polarizer setup as we use it at ANKA are shown in detail in [27], here just the result is presented.

$$I_{\text{final}} = \frac{1}{2} I_{\text{laser}} (1 - \cos(\Gamma - 4\Theta)) \quad (3.2)$$

Where  $I_{\text{final}}$  is the laser intensity at the end of the setup and  $I_{\text{laser}}$  the intensity at the start of the setup.  $\Gamma$  is the phase retardation from Eq. 3.1 and  $\Theta$  the angle of the HWP, where an angle of 0 would result in maximum signal suppression through the optical setup. The angle of the QWP is assumed to be 0, which would leave the beam unaltered in the absence of any external influences.

Figure 3.5 illustrates the behavior of the detected laser intensity in dependence of  $\Gamma$  for fixed angles of  $\Theta$ . While for lower angles of  $\Theta$ , the absolute laser signal is lower (left of Fig. 3.5), the change in signal relative to the signal without any modulation (relative modulation) is rather large, but the cosine behavior shows strongly (right of Fig. 3.5). And vice versa, for higher  $\Theta$ , the absolute signal increases, but the change in relative modulation becomes smaller, but also more linear. The final choice of angle is determined experimentally according to the dynamic ranges of the detectors. An angle  $\Theta$  of about  $5^\circ$  has proven to be most suitable for our setup and its detectors, but the details of this will be discussed in Chapters 6.1.3 and 6.2.3.2.

So far we have not yet looked at the time dependence of the modulating electric field. It was shown in Chapter 2.2.1 that the temporal profile of the Coulomb field of a relativistic line charge represents the line charge density. So by measuring the time dependent Coulomb field, we can measure the longitudinal bunch profile.

The following two sections go into detail of the detection methods of EOS and EOSD,

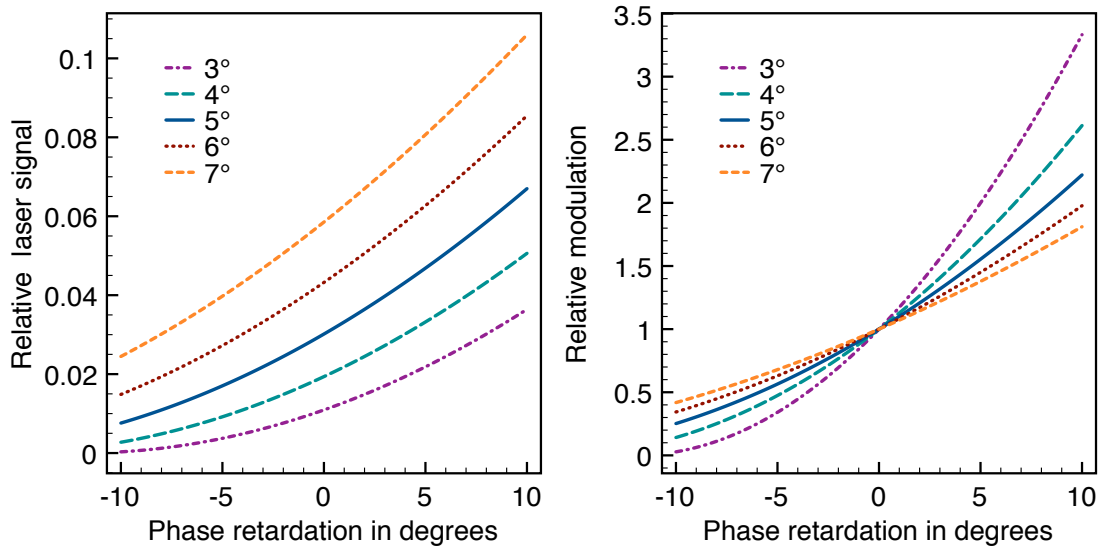


**Figure 3.5:** Left: Showing the laser intensity relative to the initial intensity versus the phase retardation induced by the EO crystal. The different curves are for different angles of the HWP. Right: Here the laser signal is shown relative to the signal at a phase retardation of 0.

showing how the field induced intensity modulation of a laser can be used to actually measure bunch lengths.

### 3.3.3 Electro-Optical Sampling (EOS)

A comparatively easy method to detect the laser intensity which is modulated by the Coulomb field is achieved with electro-optical sampling (EOS). Its working principle is illustrated in Fig. 3.6. The time dependence of the Coulomb field is sampled by a short laser pulse for which the delay with respect to the electron bunch is changed step-wise. A fast photodiode (PD) can then be used to measure the peak signal in dependence of the delay.

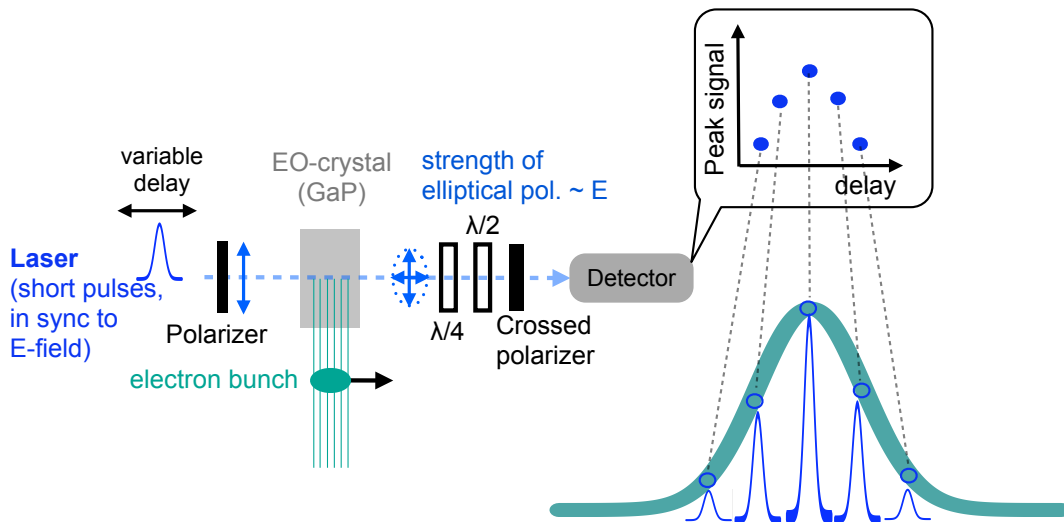


**Figure 3.6:** Illustration showing the working principle of EOS with a near-crossed polarizer setup.



This technique is a convenient and easy way to scan the electric field and find the delay at which the laser pulse and the electron bunch have full temporal overlap inside the crystal. With it the shape wake-fields which trail the Coulomb field of the electron bunch can also be studied.

As this technique is not a single-shot technique, but requires a scan of the delay over several minutes, its resolution depends highly upon the stability of the different components over this time. While it is comparably easy to delay a laser pulse in precise steps (e. g. with an optical delay stage, or electronically by delaying via its synchronization unit), the synchronization between the laser pulse and the actual electron bunches is only as good as the longitudinal stability of the arrival time of the electron bunches. In the case of the bunches oscillating longitudinally or their shape changing over the course of the measurement, the measured bunch profiles will smear out. Of course, the length of the laser pulses also limits the resolution, as we are only measuring the peak signal of the laser, we will obtain a convolution of the laser pulse length with the electric field.

Assuming Gaussian distributions of the different components the measured result is elongated in the following way:

$$\sigma_{\text{meas}}^2 = \sigma_{\text{bunch}}^2 + \sigma_{\text{laser}}^2 + \sigma_{\text{jitter, laser}}^2 + \sigma_{\text{jitter, bunch}}^2 \quad (3.3)$$

For the setup in use at ANKA, the resolution is mainly limited by the laser pulse length being in the order of 10 ps RMS because we require it to be long for EOSD measurements, which will be discussed in the next Section.



### 3.3.4 Electro-Optical Spectral Decoding (EOSD)

EOSD provides the possibility to measure the temporal profile of the Coulomb field with a single shot. The principle is shown in Fig. 3.7. The laser pulse is stretched in time with a chirp<sup>7</sup>, this means that the relation between arrival time and wavelength inside the laser pulse is continuous (ideally linear). The different wavelengths inside the laser pulse then pass the crystal at different times, because the Pockels effect is nearly instantaneous, the bunch profile is modulated onto the temporal profile of the laser. The laser pulse is then analyzed with a single-shot spectrometer. Because the relation between the spectral and the time domain of the laser is known (requires calibration measurement), from the measured spectral modulation the bunch profile can be extracted.

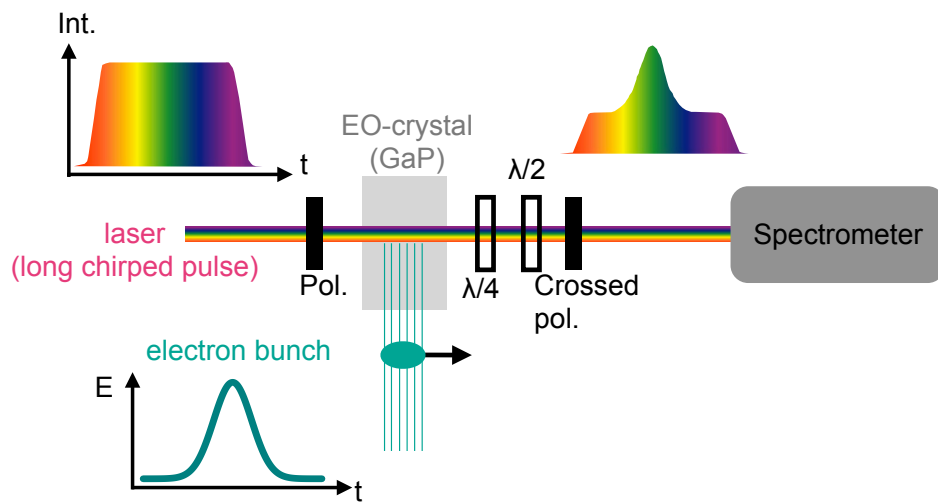


**Figure 3.7:** Illustration showing the working principle of EOSD with a near-crossed polarizer setup.

The limitations of this technique lie in the fact that, even though the measurement is single-shot, it can only measure the bunch profile within a certain time window with one shot. To increase this time window means to stretch the pulse further in time, which in turn, due to the resolution of the spectrometer, will decrease the temporal resolution within the time window.

Additionally, there is a further limitation introduced by the modulating electric field - frequency mixing. For very rapid changes of the electric field, the modulation blurs the wavelength of the laser spectrum. The mathematical description of this effect can be found in [49] and numerical simulations for bunch lengths in the order of a few hundred femtoseconds have been made in [27]. The length of the electron bunches at ANKA, is  $> 2$  ps RMS and even the scale of the expected substructures on the longitudinal bunch profile is  $> 100$  fs. This does not put us at the lower edge of the detection limit.

For us, the main limiting factor is given by the resolution of the spectrometer and quality of the linear relation between wavelength and time within the laser pulse, which is discussed in more detail in Chapter 6.2.4.

<sup>7</sup>In Dispersive media, the refractive index is a function of wavelength  $n(\lambda)$ . In media with normal dispersion  $n$  decreases with wavelength thus leading to the longer wavelengths traveling at a higher velocity than the shorter wavelengths. This correlation between wavelength and time is referred to as chirp.

### 3.3.5 History of Electro-Optical Bunch Length Measurements

Now that the basic working principle of the rather complex electro-optical (EO) bunch length measurements has been introduced in the previous parts of this Chapter, this final Subsection tries to give an overview of the history of EO measurements. To tell the story of how the different EO techniques, which had first been used to characterize laser based THz sources has found its way from laser physics into the world of accelerator physics.

First EOS measurements date back to 1982 [50, 51] when they were used to characterize fast electrical transients. Single-shot EOSD was first used in 1998 [52] when they measured the electric field of a laser generated THz pulse.

First EO measurements at an accelerator were performed at FELIX (Nijmegen, Netherlands) between 1999 - 2002. There they achieved a sub-ps resolution and tested various different detection techniques and even performed single-shot measurements [23] [24]. Around the same time, EO measurements were performed at ATF (Brookhaven National Laboratory, USA) in 2001 [53] and at the Fermilab photoinjector (Fermilab, Batavia, USA) in 2001 [54].

Over the years, many other measurements at different machines followed, establishing EO bunch length measurements into the world of longitudinal beam diagnostics. Measurements were performed at machines like the SDL (NSLS, Brookhaven National Laboratory, USA) in 2003 [55], at the SLS injector linac at PSI (far-field) in 2004 [56], at VUV-FEL (DESY, Hamburg, Germany) in 2005 [57], at the SLAC linac (Menlo Park, USA) in 2005 [25] and then at FLASH (DESY) [26].

Until then all measurements were performed at linear accelerators, either measuring in the near-field or in the far-field using coherent transition radiation (CTR).

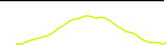
In 2009, first far-field measurements at a synchrotron light source using CSR during the low- $\alpha_c$ -operation were performed at ANKA (Karlsruhe, Germany) [47] and an image of one of the EOS traces is shown in Fig. 3.8. In 2011, first far-field EOSD measurements during a femto-slicing operation at a synchrotron light source were performed at the SLS [27]. At the UVSOR II (Japan) similar measurements were also performed around the same time during femto-slicing operation [58]. In 2012, EOS measurements were performed at ELBE at HZDR (Rossendorf, Germany) [59].

And for this thesis, first single-shot near-field EOSD measurements were performed at a storage ring during low- $\alpha_c$ -operation.

Current research topics aim to improve the temporal resolution, the sensitivity, and to explore the capabilities of new organic crystal materials, or even to try out new techniques which make use of the non-linear effects which would otherwise limit the techniques for shorter bunch lengths [60–62].

At ANKA the research will be driven towards a turn-by-turn detection of single-shot bunch profiles, for which the readout speed has to be increased greatly - up to 2.7 MHz, the revolution frequency of the ring.

In addition to that, for our new accelerator project FLUTE we also plan to have EO



techniques implemented [63]. The design layout and considerations for a system to reach even better temporal resolutions are currently being carried out by A. Borysenko.

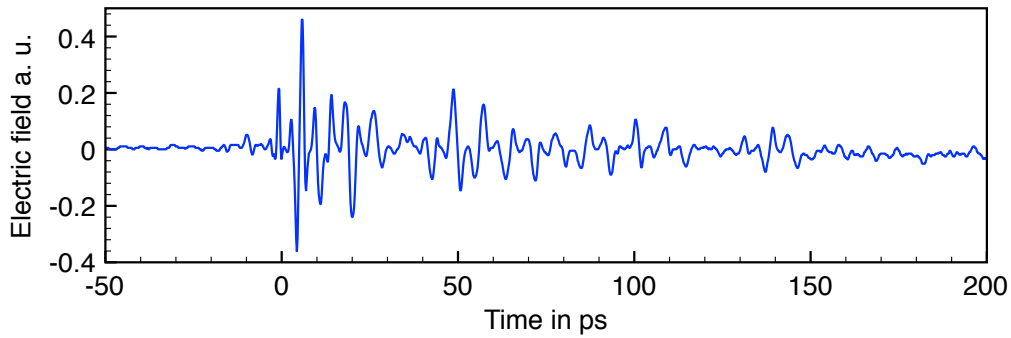


**Figure 3.8:** Measurement of the electric field of the CSR, averaged over 100 bunches and many revolutions (100s integration time). Recorded at the IR1 beamline at ANKA via asynchronous electro-optical sampling (EOS). Courtesy of A. Plech, data published in [47].

## 4. Streak Camera Measurements

When introducing a new measurement technique, such as electro-optical measurements are for ring machines, it is crucial to have means of cross-calibration and comparison with existing state of the art diagnostics. Whereas for linear machines a deflecting cavity would be such a tool, for electron storage rings, a streak camera (SC) is such a state of the art detector which allows insight into the longitudinal beam dynamics. However, as all techniques it has its virtues and its limits (see Ch. 3.2 for a general introduction to the working principle of a SC).

This chapter gives a summary of the experimental setup and characterization measurements performed with the SC setup at ANKA in the framework of this thesis. The first part covers the SC setup for which a new dedicated visible light diagnostics beamline has been set up during the scope of this work. In the second part, characterization measurements and a calibration measurement with a fs-laser system are presented.

Actual electron beam studies performed with the SC and other longitudinal diagnostics at ANKA, are shown in Chapter 7.

### 4.1 Streak Camera Setup at ANKA

As the SC works with the visible part of the synchrotron radiation (SR) spectrum, experiments need to be carried out in a location where this part of the spectrum is coupled out. ANKA currently has two IR beamlines, IR1 and IR2, both offering sufficient photon flux also in the visible range. Whereas IR1, as one of the first beamlines at ANKA, has been operational throughout the early days of low- $\alpha_c$ -operation at ANKA, IR2 saw first beam in 2009 [64, 65]. All beam diagnostics requiring visible light like SC measurements [66] and TCSPC measurements [67] had to be performed first at the IR1 and later also at the IR2 beamline. This brought a few disadvantages such as the relatively low optical power in the visible range due to gold mirrors; the measurement equipment had to be set up each time for the measurement since the IR beamlines are only available when there are no users scheduled for experiments, so those measurements could not easily be done para-



sitically. So a dedicated visible light diagnostics beamline has been designed and became operational in October 2010.

#### 4.1.1 Visible Light Diagnostics Beamline

The visible light diagnostics beamline makes use of an existing front end at a 5°-port<sup>1</sup> off a bending magnet at ANKA. For this front end with its given aperture we simulated the photon flux along the beam path with Synchrotron Radiation Workshop (SRW)<sup>2</sup> [68].

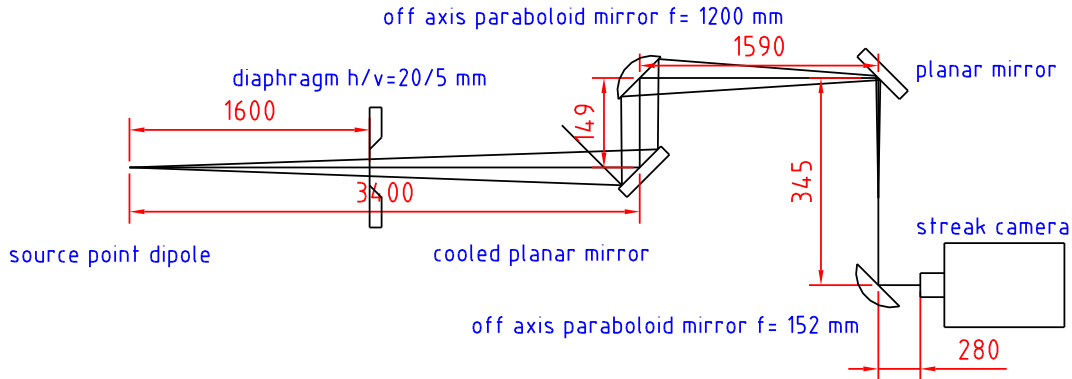


**Figure 4.1:** Beam path from the source point inside the bend to the streak camera with the distances shown in mm.

A sketch of the beam path can be seen in Fig. 4.1. The distance from the source point to the first mirror (cooled planar mirror) is 3400 mm, the beam is then deflected upwards<sup>3</sup> and passes through a Quartz glass vacuum viewport. From this point onwards the beam path is through air. It then reaches an off-axis paraboloid mirror with a focal length of 1200 mm which collimates the beam and also deflects it by 90°, so it can safely be transported through a small hole in ANKA’s radiation protection wall. On the other side of the radiation protection wall, the beam is deflected downwards by a planar dichroic mirror. This dichroic mirror<sup>4</sup> transmits light with wavelengths between 600 nm and 725 nm towards an avalanche photodiode which is used for the TCSPC setup allowing us to measure the bunch purity and the filling pattern with a dynamic range of  $10^4$  [67].

Light with wavelengths below 600 nm is reflected towards the last mirror before the SC which is an off-axis paraboloid mirror with an effective focal length of 152 mm. It focuses the light onto the entrance slit of the streak camera. Between the last mirror and the SC there is room for a 40 nm bandpass filter<sup>5</sup> centered around a central wavelength of 550 nm which is used for standard streak camera measurements to avoid any pulse lengthening effects due to dispersion.

The photon flux limiting effect of the fixed aperture / diaphragm (20 mm horizontally by 5 mm vertically) after the source point was simulated with SRW based on ANKA machine

<sup>1</sup>The total deflection angle of a single bending magnet at ANKA is 22.5°. For space reasons every bending magnet can accommodate a maximum of 2-3 beamlines. They can be placed under different angles of 0° (edge port), 5°, or 11.25°

<sup>2</sup> <http://www.esrf.eu/Accelerators/Groups/InsertionDevices/Software/SRW>

<sup>3</sup>For radiation safety reasons it is not desired to drill any holes into the radiation protection wall in the orbit plane.

<sup>4</sup>Thorlabs DMLP605

<sup>5</sup>Thorlabs FB550-40

parameters<sup>6</sup> (2.5 GeV electron energy, 200 mA beam current). The dimensions of the aperture had to be accepted and could not be changed because this part of the beamline was already present. The vertical photon flux profile for a photon energy of 2 eV (620 nm) can be seen in Fig. 4.2 in the left. Roughly 60% of the intensity of the light in the visible range is cut off by the narrow aperture. In the right of Fig. 4.2 the flux at the SC's entrance slit position is visualized.

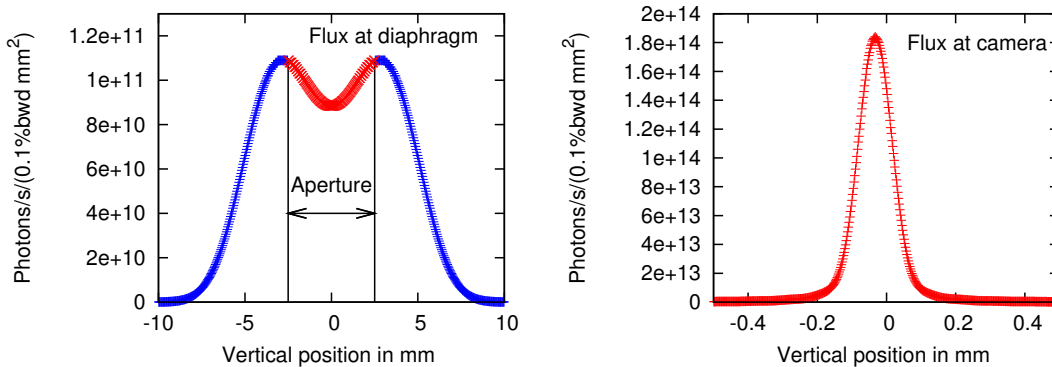


**Figure 4.2:** Left: Simulated photon flux at the diaphragm in dependence of vertical position. The part marked in red between -2.5 and 2.5 mm can pass through the aperture, the rest is absorbed. Right: Simulated photon flux at the focus point where the streak camera is placed.

### 4.1.2 Streak Camera Optical Setup

The SC setup at ANKA consists of a Hamamatsu C5680 streak camera that is extended with a synchroscan plugin and a dual time base extender (double sweep unit). The synchroscan unit operates at half the frequency of the RF system, so signals from bunches in odd and even RF buckets can be separated. There is an active feedback loop to correct for any temperature dependent drifts of the fast deflection phase due to heating up of the camera unit. For all measurements during the low- $\alpha_c$ -mode the fastest deflection was used with a resolution of 190 ps / 512 pixels = 370 fs per pixel. The blanking amplitude - slow deflection, which allows us to see the signal from many consecutive revolutions - was varied between 100  $\mu$ s ( $\approx$  270 ANKA revolutions) and 2 ms ( $\approx$  5400 ANKA revolutions), depending on the signal strength.

## 4.2 Characterization

The raw data obtained with the SC needs to be post-processed in order to obtain longitudinal bunch profiles. The detailed steps of the analysis algorithm are explained in the following section. This is followed by measurements to compare the performance of the new diagnostics beam port to previous measurements at the infrared (IR) beamlines.

<sup>6</sup>other SRW input parameters: // name, dE/E, h-emit, v-emit, h-beta, v-beta, h-alpha, v-alpha, h-disp, h-disp'

SrwElecThick("E\_ebm",0.001,50,0.5,1.06,8.17,0.66,-2.3,0.21,-0.18)



### 4.2.1 Streak Camera Data Analysis

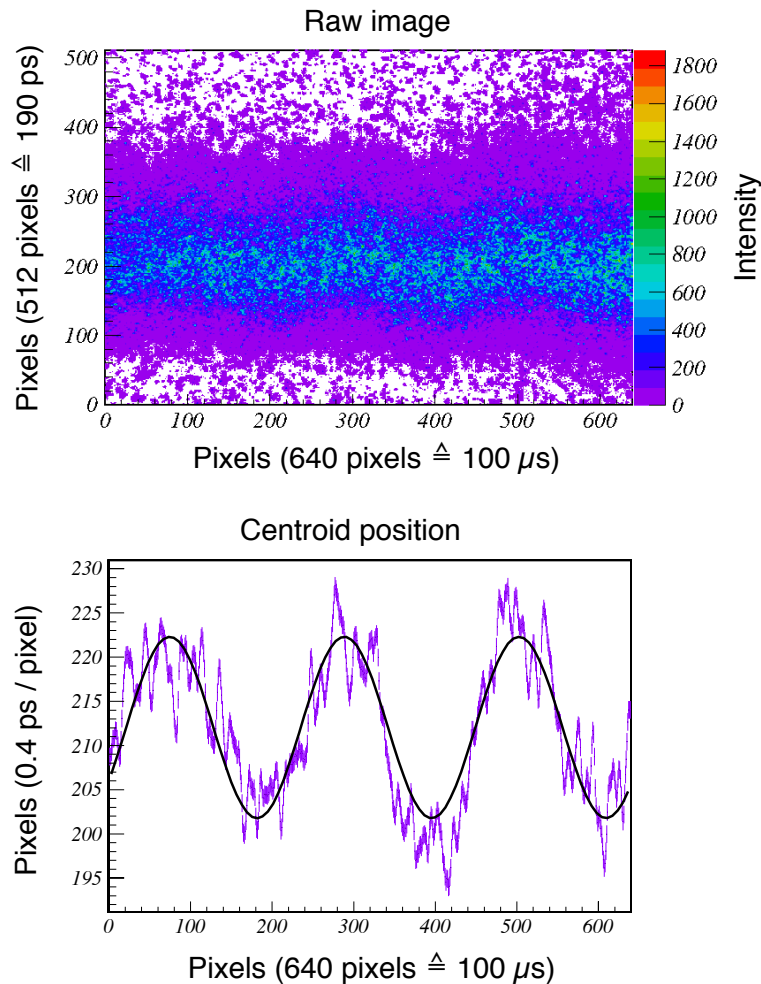
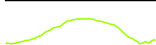


**Figure 4.3:** Top: Single streak camera image of a sequence of 500 consecutive images; recorded in dual-sweep mode. The synchrotron frequency for this measurement was 30.8 kHz which corresponds to a period length of roughly 33  $\mu$ s. Bottom: CoM calculated for 5-pixel-wide slices. The sinusoidal fit to the data matches the synchrotron frequency well.

Figure 4.3 shows in the top a single streak camera image. To obtain an averaged bunch profile, one needs to project the data onto the y-axis. One can clearly see that there is an oscillation along the x-axis which would smear out the projection. This oscillation which is caused by the bunches undergoing longitudinal (synchrotron) oscillations can be seen more clearly in the bottom of Figure 4.3, where just the motion of the centre of mass from the raw image in the top is drawn. As there was no longitudinal feedback system at ANKA when those measurements had been performed<sup>7</sup>, synchrotron oscillations with amplitudes in the order of a few ps are visible quite clearly for most machine settings. In order to minimize this effect, we apply a post-processing algorithm (flow-diagram shown in Fig. 4.4) to the acquired images.

For the evaluation we normalized the bunch profiles to a unit area to allow an easy comparison of profiles for different bunch currents or different machine settings. The bunch

<sup>7</sup>In October 2013, a 3d fast orbit feedback system has been installed.





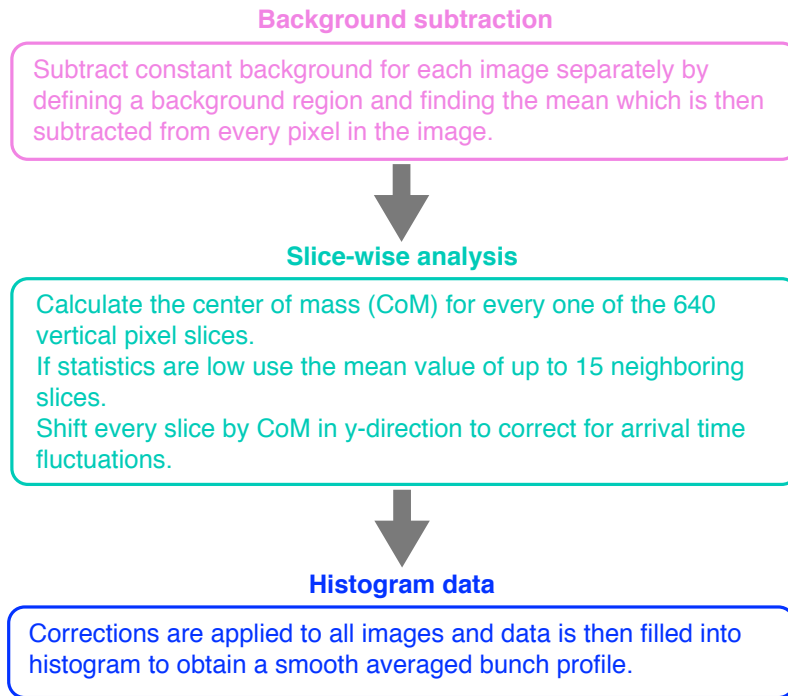


**Figure 4.4:** Sketch of the main steps for the SC data processing

lengths have been extracted from the bunch profiles by determining the full width at half maximum (FWHM). To deconvolute the data with the measured point spread function (PSF), we quadratically subtract the resolution/jitter contribution of 4.1 ps. Details of the measurement of the PSF will be discussed in detail in section 4.2.3. As last step, we calculated a RMS-equivalent value for a Gaussian profile<sup>8</sup>. An example for post-processed bunch profiles is shown in Fig. 4.5.

This algorithm has meanwhile been slightly altered and automated to allow for a semi-real-time analysis of bunch length measurements [69].

<sup>8</sup> $\sigma = \text{FWHM} / 2.35$  for a Gaussian distribution



### 4.2.2 Benchmarking of the Diagnostics Beam Port

To benchmark the performance of the diagnostics beam port, we measured the bunch length in dependence of the single bunch current<sup>9</sup> as done previously at the IR beamline [66]. The same evaluation method as above including the correction of longitudinal oscillations was applied.

Now the light intensity at a bunch current of 40  $\mu\text{A}$  (15 pC) is still more than sufficient to measure bunch profiles that allow for correction of synchrotron oscillations. An example of such bunch profiles can be seen in Fig. 4.5.

At the IR beamline about 170  $\mu\text{A}$  were required to obtain a comparable signal. For measurements with more compressed bunches even below 20  $\mu\text{A}$  a sufficient signal strength was achieved which can be seen in Figure 7.3 further down in Section 7.1.

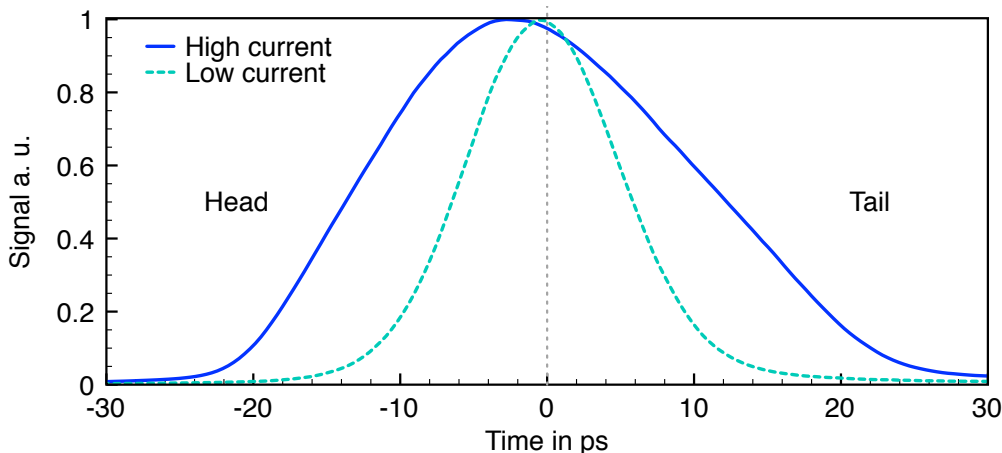


**Figure 4.5:** Bunchprofiles recorded during the low- $\alpha_c$ -mode (Fill 3667, 1.6 GeV,  $f_s = 7.383$  kHz,  $V_{RF} = 1.0$  MV) for high and low current (2.01 mA & 0.05 mA). The one for high current is not only wider (11.2 ps & 5.4 ps) but also shows a stronger deformation. For better comparison, the amplitudes have been scaled to 1. Published in [70].

### 4.2.3 Calibration Measurements with a fs-Laser System

The resolution of the SC is not only limited by the spot size of the focal point on the cathode (image without any deflections), but also the quality of the fast deflection which is continuously on during the synchroscan mode. To characterize those effects and obtain a PSF to deconvolute the data with, calibration measurements with a titanium-sapphire (Ti:Sa)-50-fs-laser system (central wavelength 800 nm) which is also synchronized to the 500 MHz storage ring RF-system, were performed. For this, the laser beam was attenuated and measured with the SC as if it was synchrotron radiation (no band pass filter was used as the laser's intrinsic spectral width is small enough). The same data-analysis as for normal SC measurements was performed on the data. A background- and oscillation-corrected laser profile can be seen in Fig. 4.6. The width of this profile (FWHM of  $11 \pm 1$  pixels ;  $4.1 \pm 0.37$  ps) is taken as PSF for the data analysis of all our SC measurements. For various parameter settings the measured pulse length did not change more than  $\pm 1$  pixel which it also does statistically for many consecutive measurements with the same settings.

<sup>9</sup>0.1 mA  $\cong$  37 pC for ANKA

To make sure that the laser pulse length can be considered short enough and does not influence the measurement, a block of acrylic glass was inserted to stretch the laser pulse due to dispersion, but no significant effect on the measured temporal profile could be observed.

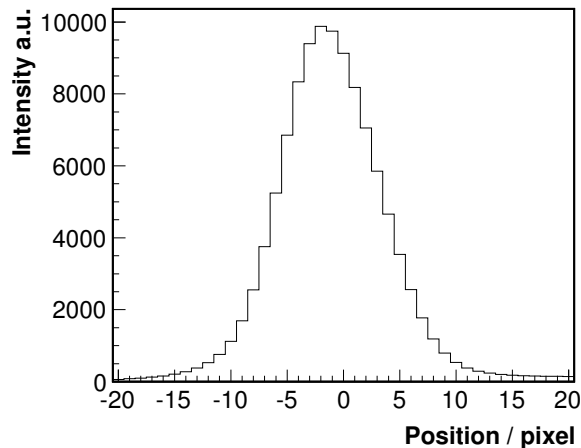


**Figure 4.6:** Background- and oscillation-corrected longitudinal profile of a fs-laser pulse from a Ti:Sa laser measured with our SC. The FWHM is 11 pixels which corresponds to 4.1 ps.

#### 4.2.4 Single-Shot Measurements with the Streak Camera

The SC is an excellent tool for longitudinal beam diagnostics that allows us to measure averaged bunch profiles with a very high accuracy and even down to very low bunch charges. Furthermore, it gives the possibility to study longitudinal oscillations over the course of a single revolution to several thousand revolutions. However, its capabilities to measure actual single-shot bunch profiles are rather limited.

The signal intensity from just a single revolution of a single bunch is rather low for the SC, even when the V-shaped slit which limits the time resolution along the slow time axis is opened considerably further than during normal SC operation, the profiles shown in Fig. 4.7 are dominated by low photon statistics. Depicted are two sets of single-shot bunch profiles recorded with the SC during single-bunch operation. In black, the averaged profiles are also shown. For the profiles in the left, the optical band pass filter which we typically use to limit the effects of dispersion inside the camera has been removed to increase the signal, for the data sets in the right it has been inserted again, decreasing the intensity by slightly more than a factor of 10. The fluctuations of bunch shape we observe for this measurement are mostly caused by by statistical fluctuations (Poisson noise), which has been shown with Monte Carlo simulations in [71].

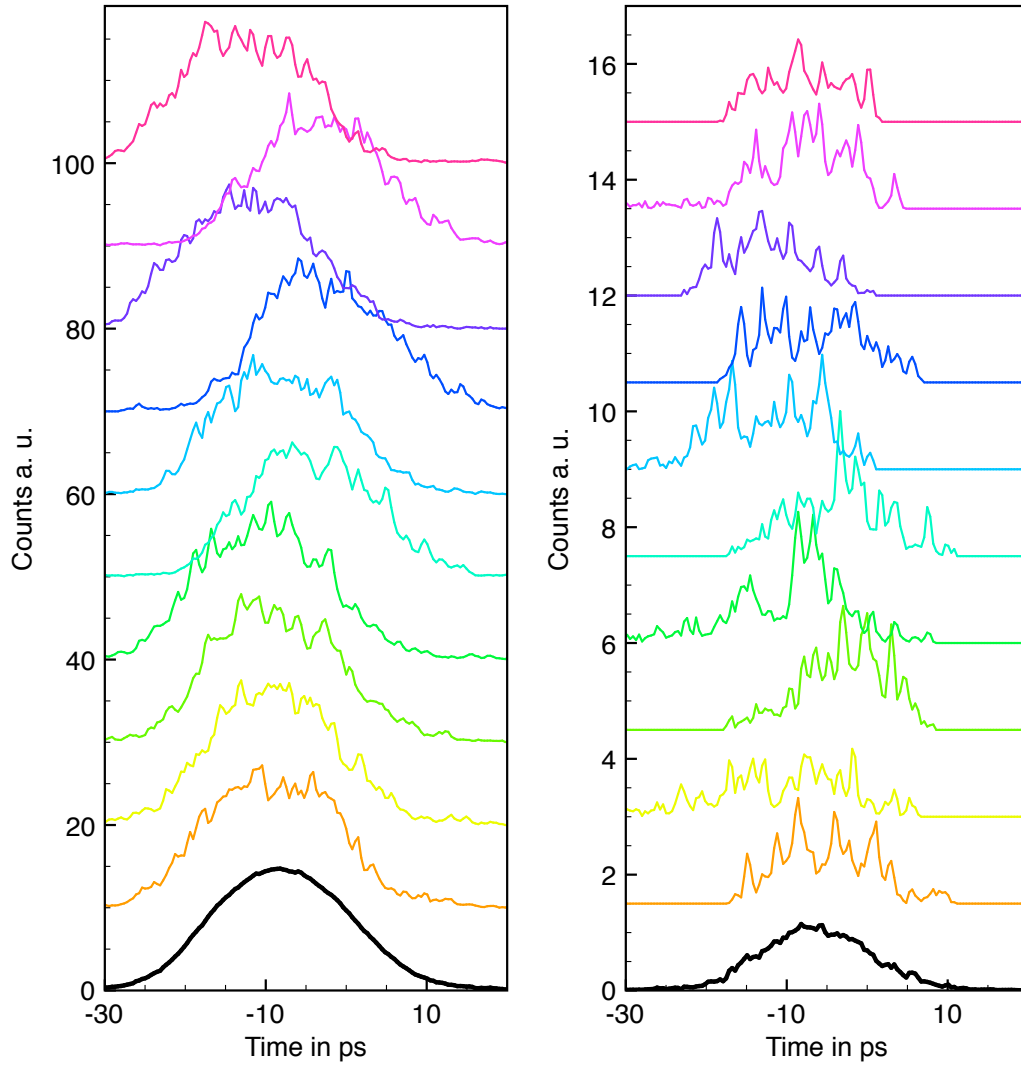


**Figure 4.7:** Two sets of single-shot profiles recorded with the streak camera. The averaged profiles (averaged over 271 single shots) are shown as thick black lines. Left: Without any optical filters in the beam path, to have maximum light intensity. Right: With a 550 nm bandpass filter (40 nm width), which we normally use for measurements to avoid dispersion. The counts for the images have been scaled by the same constant factor to make to allow for the comparison of the intensities relative to each other. Electron beam parameters: Fill 4855; beam current of 0.3 mA; 23k steps;  $f_s = 12.8$  kHz; 300 kV / cavity. The spikes on the SC signal are caused by the low count rate and can be attributed to Poisson noise rather than actual sub-structure on the bunches. For better visibility, the profiles have been displaced in y-direction. Data kindly post-processed by P. Schönfeldt.

## 5. Electro-Optical Setup at ANKA

The main part of this thesis was to specify, build and commission a single-shot near-field EO setup at ANKA and then perform first systematic studies and measurements with it. This chapter goes into detail of the experimental setup layout and challenges of this technique to work at a storage ring opposed to linear accelerators, where it had been used up to now.

Every setup for EO bunch length measurements requires a laser, an optical setup and a detection system.

The requirements upon the laser system to perform both multi-shot EOS and single-shot EOSD measurements are very stringent and require careful planning, a topic that will be discussed in the following section along with design considerations for the other parts of the setup.

In Section 5.2 a detailed description of the chosen laser system is given. Section 5.3 then describes the near-field setup and Sec. 5.4 the detection system.

### 5.1 Design Considerations

The laser system needs to supply laser pulses with a pulse energy in the order of a few nJ at a repetition rate of ideally the storage ring's revolution frequency or a subharmonic of it.

This is necessary to assure that the passage of each laser through the EO crystal (modulation) coincides with the arrival of one electron bunch.

The synchronization between the laser pulses and the RF system of the storage ring needs to have a femtosecond accuracy, which can only be achieved by an active synchronization loop which gives a direct feedback to the laser cavity. The revolution frequency of ANKA is around 2.7 MHz. Typically, laser cavities of femtosecond fiber or titanium sapphire lasers (the standard choices for EO measurements) do not operate in the low MHz repetition rate range, but rather at frequencies in the order of 50 - 500 MHz. So the synchronization



is achieved for the laser oscillator and then pulse picking and subsequent pulse amplification is required to obtain the desired synchronized laser pulses at the low MHz repetition frequency. This however means that the repetition frequency of the laser oscillator needs to be a harmonic of the storage ring repetition rate, and for synchronization purposes also a subharmonic of the storage ring RF system which is 500 MHz for ANKA. Those restrictions narrow down the possible repetition rates of the laser oscillator greatly and, in our case, made the use of an off-the-shelf commercial laser system not possible.

The laser wavelength spectrum needs to cover a range in the order of 60 - 100 nm FWHM to allow for single-shot EOSD measurements. This rather wide spectral range can conveniently be achieved by laser oscillators generating ultra-short laser pulses<sup>1</sup>. The most common laser systems which can offer this, are titanium sapphire lasers operating at a central wavelength in the order of 800 nm, and fiber laser systems operating around 1000 nm. Both types of systems are used for EO measurements around the world. Both systems have their respective advantages and disadvantages. The laser pulses for EOSD measurements need to be stretched in the time domain to lengths greater than that of the electron bunches. For the operation at ANKA this means to stretch them to values in the order of 20 - 60 ps FWHM.

As we could not use an off-the-shelf commercial solution for a laser system, a team from Paul Scherrer Institute (PSI) developing a modular fiber laser system - specifically designed and optimized for EO measurements at accelerators[72] - very kindly offered aid to build a custom laser system with the specific needs for operation at ANKA.

The optical setup required to bring the correctly conditioned laser pulses into the UHV system was based on designs used at PSI and DESY, but had to be slightly altered to match the requirements for the use at a storage ring. The main point of this was to find a way of ensuring that the beam quality during normal user operation at ANKA would not be decreased due to impedance effects from the modified vacuum chamber.

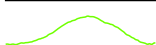
The detection system needs to be able to detect the modulated laser pulses in the time domain for EOS measurements and in the frequency domain for EOSD measurements. For the latter, it also needs to provide single-shot spectral detection capabilities.

The EO setup finally chosen for ANKA consists of three main parts which are discussed below:

1. An Ytterbium-doped fiber laser system consisting of an oscillator synchronized to the RF-system and a pulse picker followed by a single-pass fiber amplifier allowing the reduction of the repetition rate.
2. A compact fiber-coupled near-field setup that allows the coupling of the laser pulses into the UHV-system where the field-induced laser modulation occurs inside an EO-crystal which is brought close to the electron beam.

---

<sup>1</sup>As the time-bandwidth product of lasers is limited by the Heisenberg principle, very short laser pulses produce a wide spectrum.



3. A detection system to detect the modulated and unmodulated laser signal both temporally with a fast photodiode and and spectrally with a grating spectrometer including a line detector.

This chapter follows the division of the setup into these three parts: The next part describes the laser system itself (Section 5.2), then follows the description of the near-field setup (Section 5.3) and the chapter is concluded by the illustration of the detection system (Section 5.4).

## 5.2 Laser System

The laser system consists of an Ytterbium-doped fiber oscillator operating at 62.5 MHz with a central wavelength of 1030 nm and an active synchronization unit that locks its repetition rate to the storage ring RF master oscillator at 500 MHz. In addition to that it is equipped with a pulse picker and a subsequent single-pass fiber amplifier, which lowers the repetition rate below 31 MHz (typically 0.9 - 2.7 MHz) and slightly broadens the spectrum while shifting its central wavelength to around 1050 nm.

The laser system itself was originally developed at PSI specifically for EO bunch diagnostics at SwissFEL and the European X-FEL [27, 72]. The repetition rate in this oscillator then needed to be increased for the use at ANKA and the control system had to be adapted to integrate with our system.

During the scope of this work, I spent three months at PSI for the assembly and commissioning of the laser system and to gain valuable “hands-on” experience in the operation of the laser.

### 5.2.1 Laser Oscillator

A sketch of the laser oscillator can be seen in Fig. 5.1. The laser oscillator itself consists of a fiber- and a free-space-part with the active medium being an Ytterbium-doped fiber. It is pumped optically with a commercial laser diode operating at 980 nm. The laser pulses are coupled out of the circular resonator with a polarizing beam splitter. In order to achieve passive mode-locking (ultra-short pulse operation with a constant repetition rate) a non-linear effect inside the laser oscillator is required which makes it energetically more beneficial for the laser pulses inside the resonator to be very short with a high peak intensity. This is achieved by making the losses for long laser pulses (or even CW laser radiation) very large. The repetition rate of the laser is then determined by the round-trip time inside the resonator [73].

For our laser, the passive mode-locking is achieved with non-linear polarization evolution (NPE), a common technique making use of the Kerr-effect causing a non-linear polarization rotation inside fibers which acts as a kind of intensity dependent HWP [27]. A schematic drawing of the NPE can be found in Fig. 5.2. The mode-locking can be controlled by changing the angles of three remote controllable wave plates (two QWPs and one HWP) inside the oscillator which are shown in Fig. 5.1.



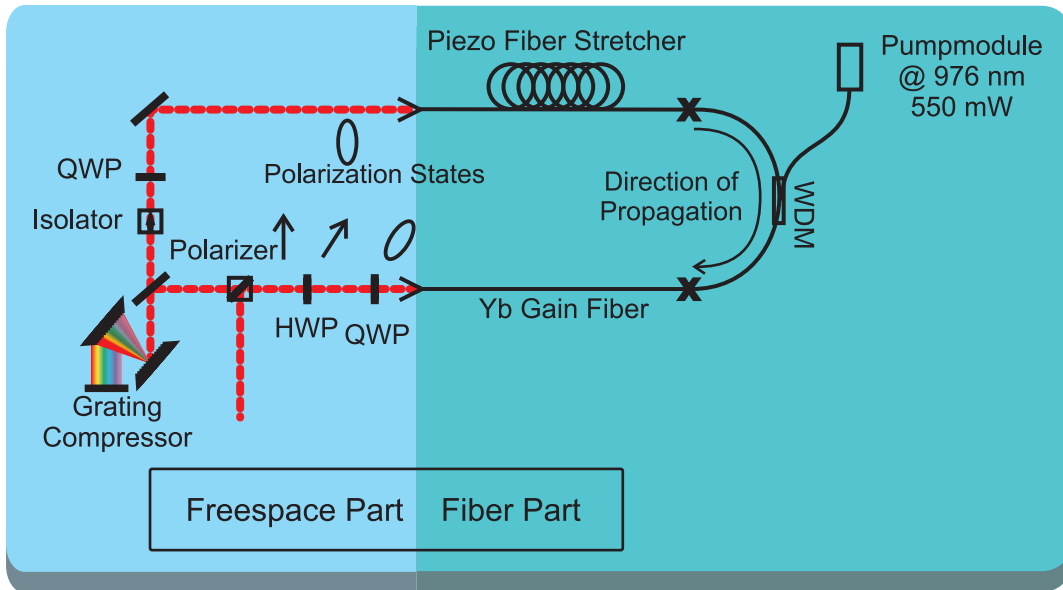


**Figure 5.1:** Schematic drawing of the free-space and fiber part of the laser oscillator. Courtesy of F. Müller [27].

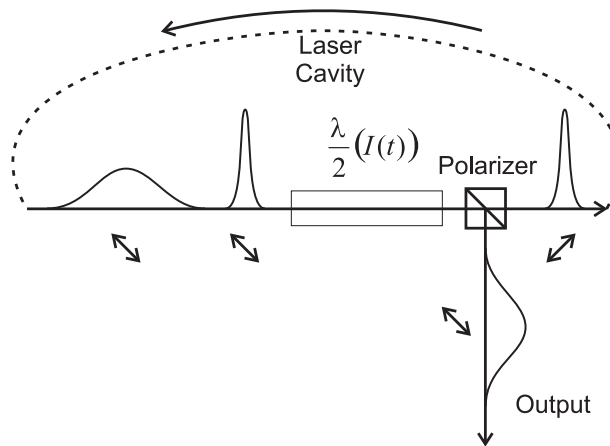


**Figure 5.2:** Schematic drawing of NPE which acts like an intensity dependent HWP inside a laser resonator which is set up with a polarizing beam splitter in a way that only pulses with a high peak intensity are kept inside the laser cavity. F. Müller [27]

The grating compressor is required to partly compensate the positive dispersion (i. e. shorter wavelength components travel slower through a medium than longer wavelength components) which occurs inside the fiber part of the oscillator which has a length of a few meters shown in Fig. 5.1. Our grating compressor consists of two parallel gratings and a roof top mirror for deflection. The incoming beam is dispersed by the first grating and then the parts with different wavelengths travel parallel to each other (horizontal displacement) after the second grating. They are then deflected by a roof top mirror which not only deflects the beam but also moves it parallel in vertical direction to allow for an easy out-coupling of the beam with a D-shaped mirror after it has passed the two gratings again (otherwise the incoming and outgoing beam would travel right on top of each other). Light components with a longer wavelength travel a longer distance than light with a shorter wavelength thus introducing negative dispersion in dependence of the



distance between the gratings (a larger distance, generates a larger negative dispersion). This negative dispersion can - to some extent (in first order) - compensate the positive dispersion inside material such as glass fibers.

The grating compressor is set up to have a slightly positive net dispersion, leading to self similar pulses which have been proven most suitable for the subsequent amplification (see p. 76 ff for more details [27]). A typical spectrum of those self-similar pulses inside the oscillator recorded with an Optical Spectrum Analyzer (OSA) - a fiber-coupled spectrum analyzer for light - can be seen in Fig. 5.3.

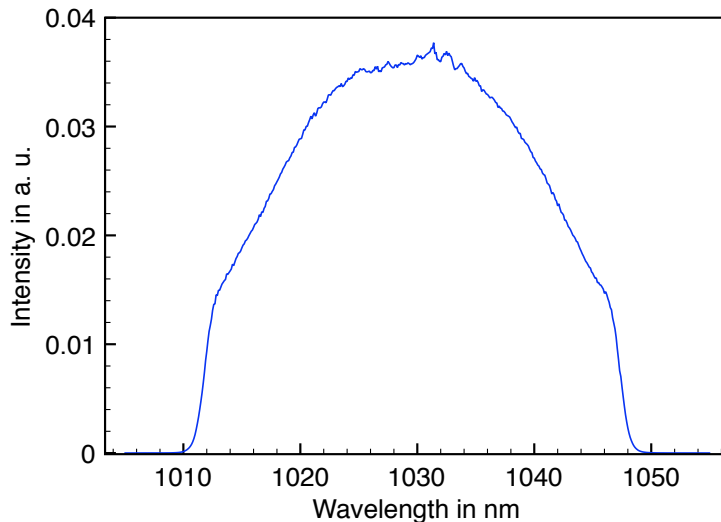


**Figure 5.3:** Typical spectral distribution inside the laser oscillator for self similar pulses.

### 5.2.2 Synchronization Unit

In order to achieve temporal overlap between the laser pulse and the electric field of the electron bunch inside the EO crystal, the laser system needs to be actively synchronized to the revolution frequency of the electron bunches (2.7 MHz for ANKA) with a sub-ps accuracy. To achieve such an accurate synchronization, not the revolution frequency but the storage ring RF of 500 MHz is used for the phase comparison.

For an active synchronization between the laser pulses and the electron bunches a correction signal from a phase-locked loop (PLL) is used as feedback for a piezo stretcher inside the fiber part of the oscillator. When a voltage is applied to this piezo stretcher it mechanically stretches the fiber which is wrapped around it by a few  $\mu\text{m}$ .

The PLL mixes a laser repetition frequency signal from a fast photodiode - filtered around 500 MHz - with the 500 MHz RF signal from the storage ring. If the repetition frequency of the laser is slightly different from the RF reference signal, then an amplified DC correction signal is applied to the piezo stretchers acting as feedback inside the laser oscillator by changing the total length of the optical beam path.

This means the oscillator repetition frequency needs to be a subharmonic of 500 MHz, but also an harmonic of 2.7 MHz (which is 500 MHz divided by the harmonic number of ANKA: 184). The original design repetition rate of the laser system was 50 MHz, so it could be easily synchronized to the 10th subharmonic of the 500 MHz RF system of the Swiss Light Source (SLS) [72].

For operation at ANKA the constraints upon the oscillator repetition rate are then given by the dividers of the harmonic number which factorizes into  $23 \times 8$ . So the options are rather limited with  $500 \text{ MHz} / 8 = 62.5 \text{ MHz}$  or its multiples and  $500 \text{ MHz} / 23 = 21.7 \text{ MHz}$ . As the original PSI system is optimized for  $50 \text{ MHz}$ , the two options either meant to decrease the oscillator length by a free-space-equivalent of  $1.2 \text{ m}$  or increase it by  $6.7 \text{ m}$ . After careful consideration of the required fiber and free-space lengths<sup>2</sup> in the oscillator, the first option with  $62.5 \text{ MHz}$  was chosen and the reduction was achieved entirely by making the fiber part shorter by about  $80 \text{ cm}$ .

As the piezo stretcher stretches or compresses the fiber by a total length of about  $5 \mu\text{m}$  it can only compensate small frequency mismatches in the order of  $500 \text{ Hz}$  for a frequency of  $500 \text{ MHz}$ . The RF frequency at ANKA is not exactly  $500 \text{ MHz}$ , but is usually varied between  $499.69$  to  $499.73 \text{ MHz}$ , depending on the machine settings. Also temperature and humidity dependent drifts inside the laser itself can make it necessary to vary the oscillator length in larger steps. For this, the roof top mirror in the grating compressor inside the laser oscillator is mounted on a motorized linear stage (changing the distance of the roof top mirror from the gratings does not influence the dispersion). Its position can be changed by a total of about  $25 \text{ mm}$  in small steps ( $\Delta x = 1.25 \mu\text{m}$ ) leading to a twice as long change in oscillator length. So, in addition to the relatively fast feedback with the piezo stretcher (bandwidth about  $1 \text{ kHz}$ ), a slow (bandwidth below  $5 \text{ Hz}$ ) software feedback loop monitors the voltage of the piezo stretcher and moves the mirror if necessary. Figure 5.4 shows the laser synchronization following a change in RF frequency.

Measurements at PSI with the original system have shown that the integrated phase noise above the loop bandwidth of about  $1 \text{ kHz}$  up to a frequency of  $25 \text{ MHz}$  is as low as  $50 \text{ fs}$  (p. 82 ff [27]). A cross-correlation measurement between the fiber laser system and a Ti:Sa system - both synchronized to the RF clock - has resulted in a jitter as low as  $125 \text{ fs}$  FWHM ( $\approx 52 \text{ fs}$  RMS) (see p. 82 ff in [27]).

In order to ensure a reproducible, absolute synchronization to the revolution frequency of  $2.7 \text{ MHz}$ , a coincidence detector is included in the synchronization unit which compares the coincidence between the laser signal and the revolution clock while the delay of the laser is scanned by changing the phase of the RF signal with a vector modulator (VM). This method is accurate to within about  $5 \text{ ps}$  and allows one to find the temporal overlap quickly again even after re-synchronization (see p. 85 ff in [27]).

### 5.2.3 Amplifier System

The amplification unit consists of a grating compressor (GC1) at the end of the oscillator, then a pulse picker to lower the repetition frequency and finally a single pass fiber amplifier. The whole setup can be seen in Fig. 5.5.

The grating compressor at the end of the laser oscillator (GC1) is used to pre-compensate dispersion inside the fiber amplifier.

---

<sup>2</sup>Light propagation in fiber is about 1.5 times slower than in free space



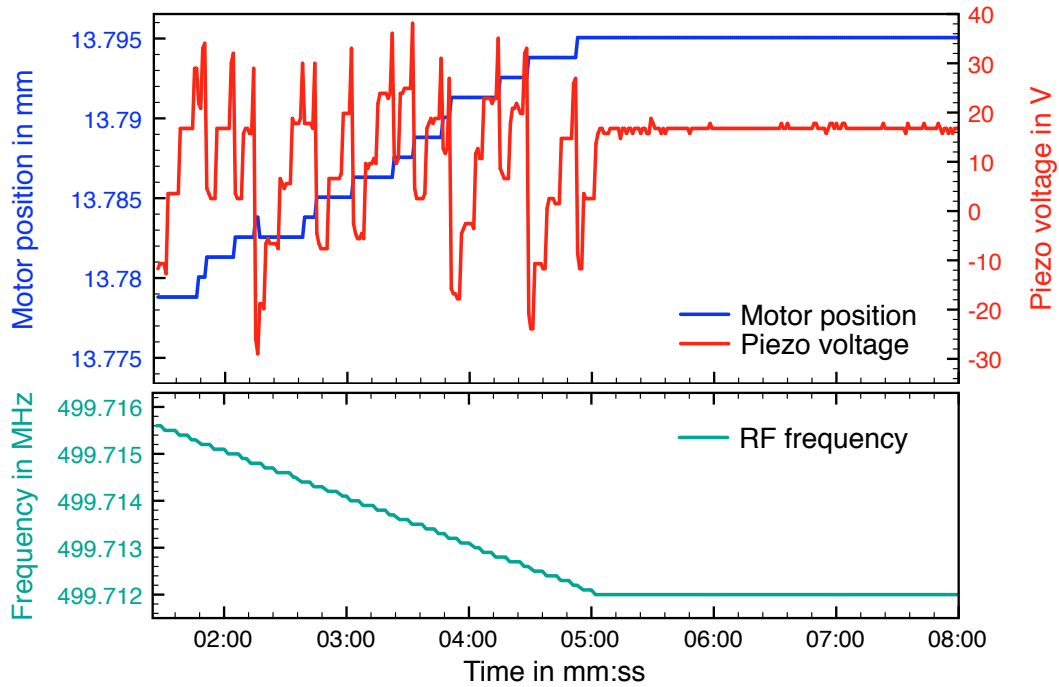


**Figure 5.4:** Showing the laser synchronization following a change in RF frequency (100 Hz step-size). Small changes (up to 500 Hz) can be corrected with the piezo voltage, but as soon as it reaches its limits, the motor is moved, compensating an equivalent change of about 300-350 Hz in RF frequency.

The pulse picker which lowers the repetition rate of the laser pulses is controlled by an acousto-optic modulator (AOM) which can be gated. In our case, for the gating a programmable pulse counter is used which counts at the third harmonic of the laser oscillator repetition rate (around 187 MHz). Its high- and low-times can be controlled in steps of the count rate. The laser pulses are then combined with the pump light by a wave division multiplexer (WDM) inside a polarization maintaining (PM) fiber where the laser light and the pump light are counter propagating.

The laser pulses of the oscillator have a pulse energy in the order of 1 nJ (at 62.5 MHz). After amplification by the polarization maintaining single-pass fiber amplifier their energy is increased to about 10 nJ (at 0.9 MHz repetition rate). The pulses are then delivered to

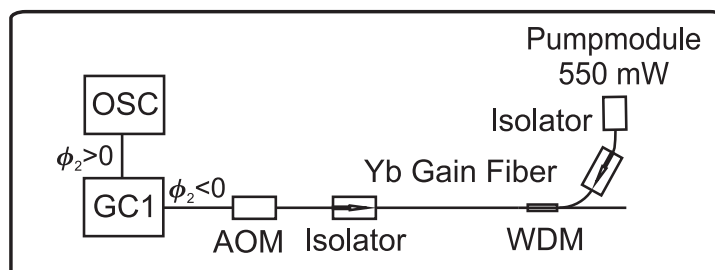


**Figure 5.5:** The setup of the laser amplification unit consisting of GC1 at the end of the oscillator and an AOM to reduce the repetition rate. The laser and the pump light are then combined by a WDM inside a PM fiber. Courtesy of F. Müller [27].

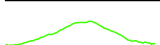
the EO-monitor (see Section 5.3), for which the increased pulse energy is needed to ensure that the laser signal for nearly crossed polarizer settings (see Section 3.3) is still single-shot detectable at about 20 pJ.

While the repetition rate of a fiber laser is most stable when the oscillator is tuned to a repetition rate in the higher MHz range (typically 50 - 100 MHz), one then wants a lower overall repetition rate of the system to match the revolution frequency of 2.7 MHz for the actual EO measurements. For single-shot EOSD measurements we choose an even lower repetition rate of only one third of the revolution frequency to avoid the need for additional gating of the detection unit. Another advantage of the fiber amplifier is that it can broaden the spectral width of the laser pulses due to self-phase modulation inside the amplifier if the pulses reach a sufficiently high peak intensity. The spectral broadening can be controlled by changing the settings of a grating compressor (GC1) at the exit of the laser oscillator which is used to pre-compensate the dispersion the laser undergoes within the fiber of the amplifier. Figure 5.6 shows the temporal intensity and phase of oscillator pulses which have passed through 5 m of fiber for different settings of GC1 (lower values mean the gratings are closer together i. e. less compression). The measurements have been performed with a Frequency Resolved Optical Gating (FROG) device which allows to characterize a laser pulse in time- and frequency-domain and also includes the corresponding phase [74]. One can clearly see that if a low value is chosen for GC1 a), the laser pulses which already are positively chirped with a length of about 2 ps FWHM when they exit the oscillator, are still relatively long, but when the gratings are moved further apart (higher values of the GC1 position, b), the laser pulses are further compressed and the phase over the center region of the pulse becomes 0, which means that there is no chirp. In c), for an even higher setting of GC1, the pulses already start to increase in length again. The best settings for GC1 are determined experimentally by checking not only the spectral width, but also the shot-to-shot stability. For our measurements a setting of 15.6 mm has proven to be most suitable.

#### 5.2.4 Control System

The laser is controlled via an Experimental Physics and Industrial Control System (EPICS) [75] running on a standard Linux PC which gives access to remotely controllable components of the system. Those include: Ten individual motors to move/rotate the various translation stages and rotation mounts both inside the laser system itself and on the EO-Monitor. A compact I/O unit which is used to monitor signals, such as the voltage applied to the piezo stretcher and a “lock signal” which is positive while the synchronization loop is running. In addition to that, the I/O unit controls a relay which can open the PLL in case the piezo voltage rises above a certain threshold to prevent damage to the piezo stretchers. The interface between the PC and motor controller cards is directly done via ethernet while the I/O controller and the programmable counter have a serial connection which is ported to ethernet with a serial-to-ethernet module.

A graphical user interface (GUI) has been built with Control System Studio (CSS) to allow for an easy online-monitoring and operation of the laser system, including the settings of the VM and the programmable pulse counter.



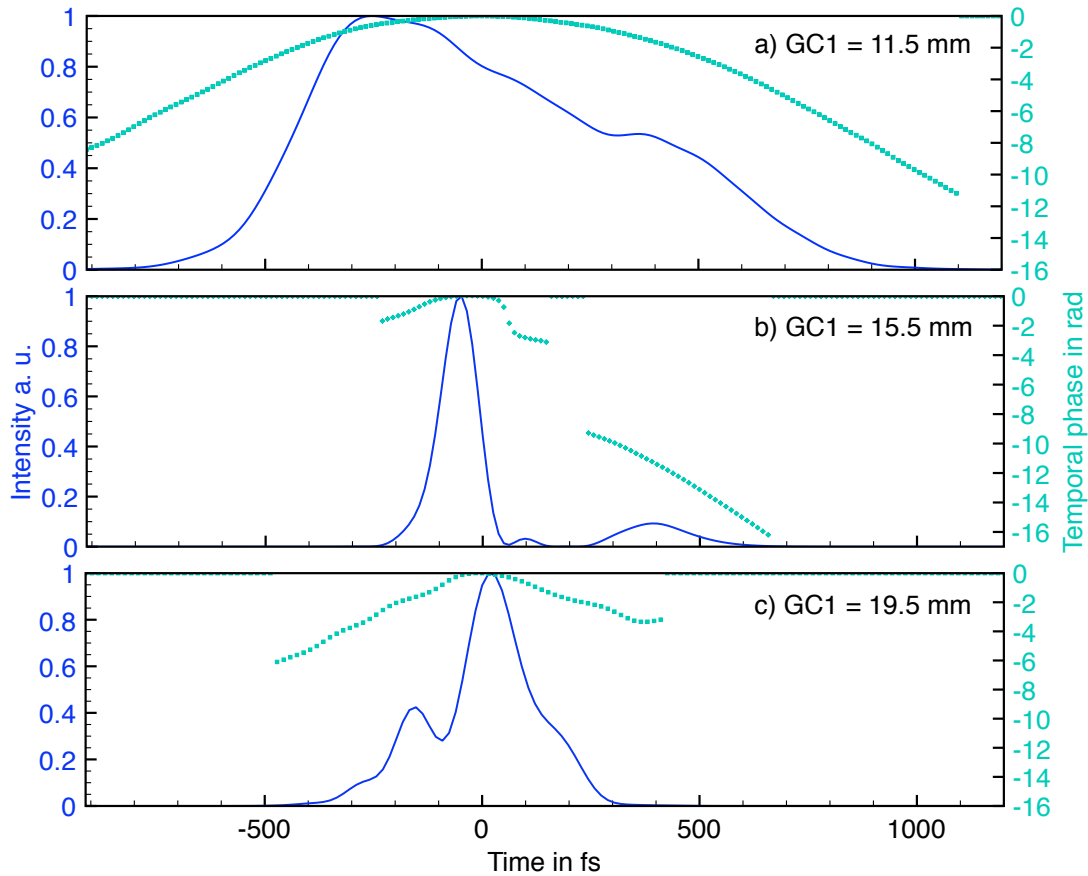


**Figure 5.6:** Temporal intensity and phase of the oscillator pulses for different settings of the grating compressor (GC1) at the end of the oscillator output. Lower values for GC1 mean that the gratings are closer together, so there is less total negative dispersion introduced to pre-compensate the subsequent fiber. All traces are measured with a FROG device. The discontinuity in the phase in b) at a time of around 200 fs is caused by the lack of intensity for this region.

While the systems at PSI and DESY are being further developed to become completely remote controllable to allow for access-free operation within the accelerator tunnel(s), our system at ANKA requires manual access to the laser unit itself for switching on and off and starting the PLL as, for example, the pump diode controllers and the proportional–integral controller (PI) which controls the PLL are not remote controlled. This, however is not an issue for the present placement at ANKA which will be explained further down in Fig. 5.9, as the laser system itself is placed in a laser hutch outside of the radiation protection wall and fully accessible during machine operation.

The laser system is designed to work stably in an accelerator environment (no clean room required) and can conveniently be mounted inside a 19" rack together with all the accompanying electronics. Figure 5.7 shows the customized board on which the laser oscillator is mounted. Figure 5.8 shows an image of the whole laser system mounted inside a rack table. It is placed in a provisional laser hutch which used to be a storage area between two beam lines and operates very stable there.

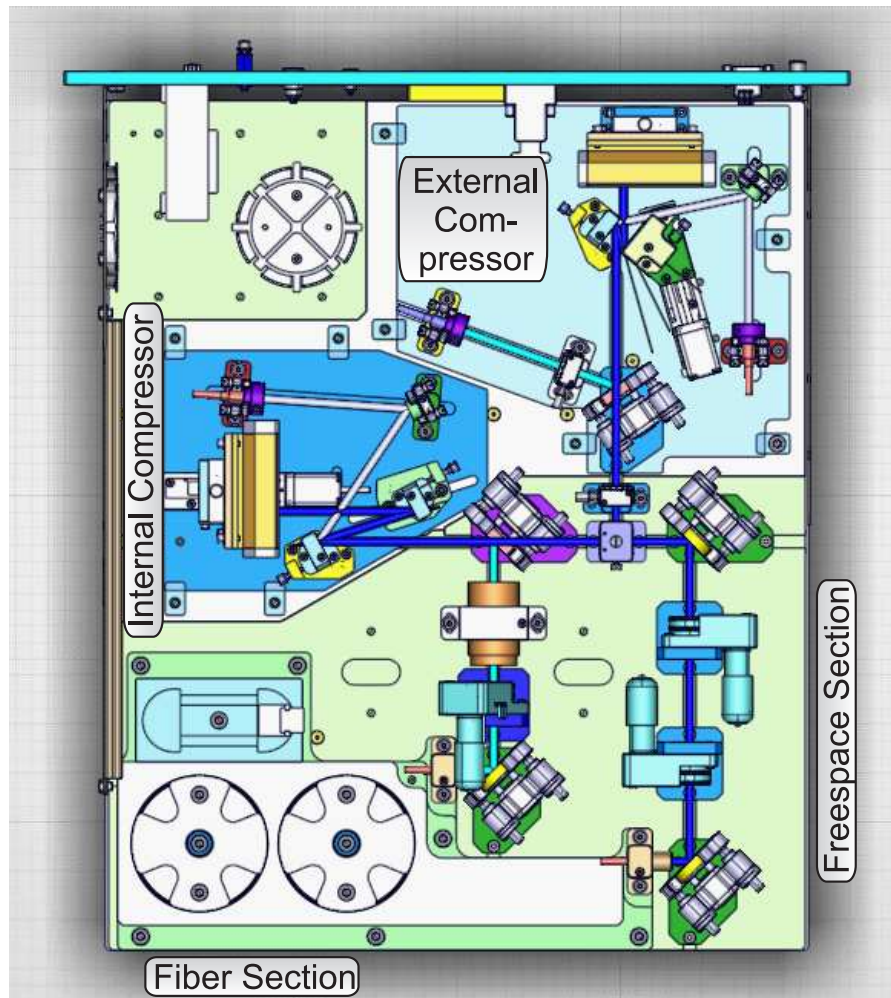


Figure 5.7: Drawing of the compact laser packaging fitting inside a 19" rack F. Müller [27].

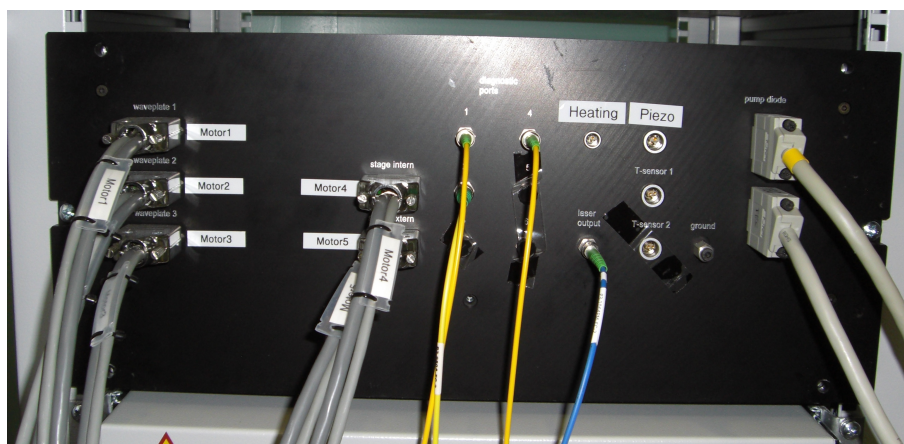
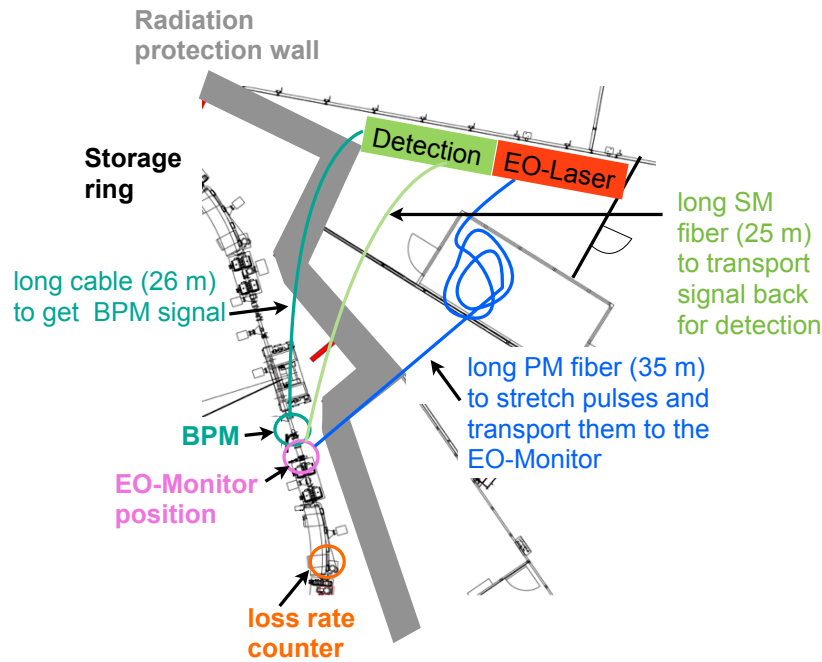


Figure 5.8: Photograph of the laser mounted inside a 19" rack at ANKA.

## 5.3 Near-Field Setup



**Figure 5.9:** Schematic drawing of the placement of the different components of the near-field EO setup at ANKA. Both the laser itself and the detection unit are placed outside of the radiation protection wall, so they are freely accessible at all times. The laser signal is transported through a PM fiber to the inside of the ring where the EO-Monitor is placed. It is then coupled back out through a SM fiber to the detection unit. The signal from a nearby BPM which is used to find temporal overlap, is coupled out via a long cable.

The near-field setup at ANKA consists of the compact fiber-coupled EO-Monitor, the signal from a beam position monitor (BPM) to check the temporal overlap, and a loss rate counter to ensure that the electron beam life time is not significantly decreased and the crystal is not damaged. For the placement of the components it was most convenient to place both the detection unit and the laser system outside of the radiation protection wall, so they are freely accessible at all times. The transport of the laser signal to the inside of the ring, where the EO-Monitor is placed is achieved with a 35 m long PM fiber, which is also used to stretch the laser pulses in the time domain (long laser pulses are required for the EOSD measurements). To transport the laser signal back out to the detection unit, a 25 m long single-mode (SM) fiber is used (this is the minimum length possible due to the distance). The signal from the BPM is transported to the laser hutch via a 26 m long RF cable.

Figure 5.9 shows the placement of the different components of the setup. The individual components are described in more detail in the following subsections.

### 5.3.1 EO-Monitor

The compact fiber-coupled EO-Monitor allows us to couple the laser into the UHV-system of the storage ring where the field induced laser modulation occurs inside an EO crystal.

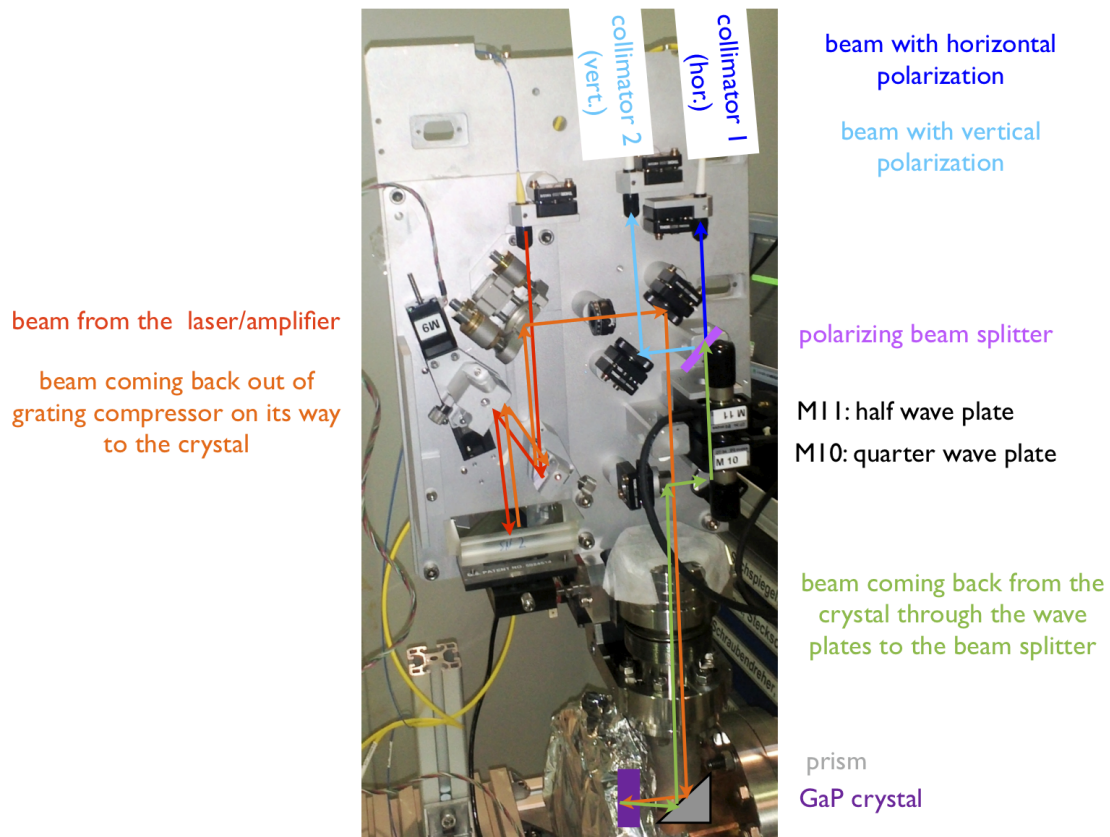


**Figure 5.10:** Photograph of the far-field setup at ANKA with the beam path highlighted. See text for a more detailed description of the beam path.

The modulated laser pulses are then also coupled back out through the same vacuum viewport and can be transported back to the detection unit via a SM fiber. A photograph of the setup before installation into the storage ring can be seen in Fig. 5.10. The beam path is highlighted and goes the following way: The laser beam (shown in red) is coupled in via a PM fiber collimator in the top left, from where it passes through a grating compressor in which the laser pulse length can be adjusted by changing the position of the second grating (via M9) thus increasing or decreasing the distance between the two gratings to control the dispersion. To separate the ingoing (red) and outgoing (orange) beams in vertical direction, a roof top mirror is used inside the grating compressor which does not only reflect the beam, but also displaces it vertically. From there the compressed beam (orange) is sent towards the EO crystal (5 mm thick Gallium phosphide) inside the vacuum. On its way to the viewport it passes a polarizer to ensure that the polarization at the crystal is as linear as possible. The viewport is anti-reflective (AR) coated for a wave length of  $1064 \text{ nm}^3$ . Inside the vacuum, the beam is deflected  $45^\circ$  by a silver-coated glass prism. The crystal's front side is AR coated and its back side is highly-reflective (HR) coated with a narrow-band (FWHM  $\approx 250 \text{ nm}$ ) dielectric coating centered around  $1050 \text{ nm}$  (this is to ensure that mostly the laser is reflected and not the electric field of the electron bunch). The direction of polarization of the Coulomb field of the electron bunch is radial, so at the position of the laser spot inside the crystal, it can be treated as vertical polarization.

<sup>3</sup>commercial solution, to couple in Nd:YAG lasers



The polarization of the laser pulse is also vertical to ensure maximum modulation (see Ch. 3.3.1). The modulation of the laser by the electric field of a bypassing electron bunch happens mostly when the laser pulse and electron bunch are co-propagating after the laser has been reflected at the HR side of the crystal [76].

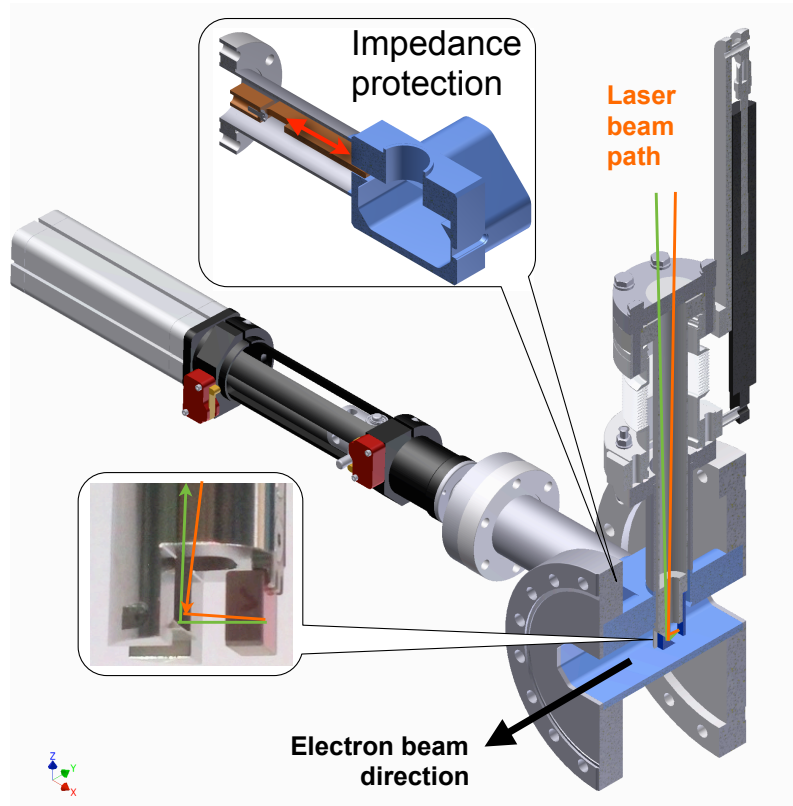


**Figure 5.11:** Detailed drawing of the in-vacuum parts of the EO-Monitor showing a zoom into the impedance protection slider that can fully cover the beam pipe when the crystal is retracted (top) and the crystal mounting (bottom).

A detailed view of the in-vacuum part can be seen in Fig. 5.11. The laser is sent towards the crystal under a small angle, so it can be coupled out separately (shown in green) and sent towards the wave plates (QWP and HWP) which are required to turn the polarization modulation into an intensity modulation (see Ch. 3.3.2). Back to Fig. 5.10, the beam is then split by a polarizing beam splitter and both the horizontal (dark blue) and the vertical (light blue) polarization can be coupled out separately via SM fiber collimators. The whole setup including the optics plate and the crystal holder can be retracted fully from the electron beam pipe which can then be sealed off with an impedance protection slider (see Fig. 5.11 top zoom). This impedance protection was installed in order to ensure that the normal user operation at ANKA would not be influenced by any impedance changes introduced by the setup. It also protects the crystal mount from heating up during multi-bunch operation.

Our near-field setup is based on the design for a compact EO-Monitor in use at the SwissFEL injector test facility at PSI [76], but the in-vacuum part has been extended with the impedance protection slider for the use at a storage ring and on the optics plate a grating compressor for direct pulse length control has been added.

It has been installed at the end of the long straight section in sector 3. Right between a stripline<sup>4</sup> and a vacuum valve which is followed by a quadrupole magnet. For the installation a 12 cm long section of the ANKA beam pipe had to be replaced. For laser protection reasons, the EO-Monitor has been sealed off with a metal cover. An image of the EO-Monitor after its installation can be seen in Fig. 5.12.



**Figure 5.12:** Photograph of the EO-Monitor after installation. It is located in Sector 3 between a stripline at the end of a long straight section (left) and a vacuum valve which is followed by a quadrupole (right).

### 5.3.2 Temporal overlap

To find initial temporal overlap between the laser pulses and the electron bunches when both pass the EO crystal without scanning over a full ANKA revolution of 368 ns which would take too long, the signal of one of the buttons from a BPM in sector 3 (BPM S3.10) which is 70 cm upstream of the EO setup is measured relative to the signal from the laser coming back from the EO-Monitor. Given the uncertainties on some of the delays involved this narrows down the search interval to a few nanoseconds. Figure 5.13 shows the cable and fiber sections the two different signals pass until they are detected by an oscilloscope. The delay in the 25 m long cable was measured with a Network Analyzer. The delay inside the 25 m long fiber was measured by attaching an additional 25 m long fiber and checking

<sup>4</sup>The time domain signal from the stripline is used to monitor the filling pattern in real-time in the control room.



the delay this introduced. From this it was estimated what the delay in 1 m additional fiber would be. The additional 2 m of cable for both setups should cancel out. The geometrical distance between the BPM and the EO-Monitor was measured to be 70 cm and should not be off by more than a few centimeters. The length of the laser beam path was measured from the CAD drawing and should be accurate to within a centimeter. So the temporal overlap was estimated to be found for a delay of 6 ns between BPM signal and the laser signal. Figure 5.14 shows the first successful temporal overlap measurement at ANKA. The experimentally determined value was found to be at a delay of 11.988 ns between the negative peak of the BPM signal and the positive peak of the photodiode signal, which is about 6 ns more than we expected from measurements and calculations. This discrepancy is most likely caused by a mix of different effects. For one, the reaction time of the fast photodiode is unknown as only the rise time is specified to be  $< 225$  ps<sup>5</sup>. The delay inside the 25 m fiber was not measured for the fiber which is installed but for a spare one which should have exactly the same length ( $\pm 1\%$  specifications). The delay difference between the two ports from the EO-Monitor which use two separate but equal fibers was found to be about 800 ps (corresponds to 24 cm in free-space) which is already significantly more than the sheer optical path difference of less than 10 cm.

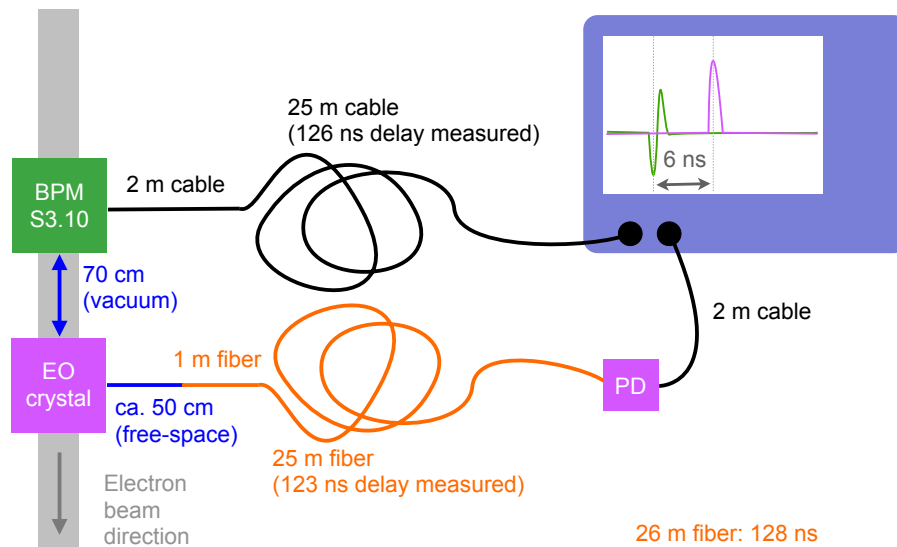


**Figure 5.13:** Sketch of the free-space, cable and fiber delays for the signal from the BPM and the laser. 26 m of fiber should introduce a delay of 128 ns (2 ns longer than 25 m cable), so the total delay should be 6 ns (the equivalent of 120 cm free-space, which is 4 ns plus 2 ns from the fiber-cable-difference). The experimental value however is about 12 ns.

### 5.3.3 Loss Rate Monitor

For the actual EO measurements, the movable arm of the EO-Monitor needs to be moved close to the electron beam, so the electric field strength from the bypassing electron bunches is strong enough to cause a detectable modulation<sup>6</sup>. When doing so, however, one does not

<sup>5</sup>ET-3010 from Electro-Optics Technology, Inc.

<sup>6</sup>The peak electric field decays with  $1/r$ .





**Figure 5.14:** Screenshot of the first temporal overlap seen with an infinite persistence scan. The oscilloscope was triggered on the BPM signal. The laser delay was scanned while keeping infinite persistence switched on for the photodiode signal. This superimposes multiple wave forms in the same view, drawing the most recent one in a brighter color. This allows us to spot an EO signal directly on the screen without having to read out every single wave form for every delay and analyzing it.

want to influence the beam or damage the crystal by a too high radiation load. As means of detection, a lead glass loss counter which is a few meters further downstream of the EO setup in a highly dispersive section of the ring has proven to be a very sensitive tool. It detects Cherenkov radiation which is generated by lost electrons which create a shower of secondary particles inside the lead glass block. It was used for an energy calibration measurement and the detailed setup is described in [77, Chapter 3.2.1]. For all the EO measurements, the crystal arm is only moved in so far that the count rate does not increase significantly, this is usually the case for a minimum distance of about 5 mm between the bottom edge of the crystal and the geometrical center of the beam pipe.

## 5.4 Laser Detection System

The laser signal returning from the EO-Monitor via the SM fibers can be detected both temporally - by a fast fiber-coupled photodiode - and spectrally - by a single-shot grating spectrometer with a line-array. Whereas the temporal detection is required to find the initial overlap and for EOS measurements, the spectral detection is required for all EOSD measurements.

### 5.4.1 Temporal Detection for EOS

The fast fiber-coupled PD<sup>7</sup> is used to detect the peak signal of the laser pulses. This detection method is firstly used to find temporal overlap between the laser and electron bunch for subsequent EOSD measurements. Multi-shot EOS measurements, however, also offer the possibility to study wake-fields which trail a bypassing electron bunch. For EOS measurements the averaged peak signal of the photodiode (averaged over 50 sweeps) is recorded with an oscilloscope<sup>8</sup> in dependence of the relative time delay between laser and electron bunch which is changed with a VM. Both the readout of the oscilloscope and the VM are controlled by a MATLAB script that has direct access to the oscilloscope and can access the channels of EPICS.

### 5.4.2 Spectral Detection for EOSD

For EOSD measurements a spectral detection of the laser pulses is required. This is realized with a single-shot grating spectrometer which is equipped with a 512-pixel line-array of PDs<sup>9</sup>. The single-shot spectrometer was set up during the scope of the bachelor thesis of Sophie Walther [78] and has since been slightly altered to increase its spectral resolution.

The laser signal is coupled in via a SM fiber collimator and then propagates in free-space towards a reflective grating<sup>10</sup> with 300 grooves per mm and a blazing angle of  $8^\circ 36'$ . The angle of incidence for our setup is about  $15^\circ$  and the reflected intensity for the first order lies at around 70 % [78]. As the angle under which the laser light is dispersed is only about  $2^\circ$ , a relatively long beam path is required to achieve sufficient dispersion and then focus the dispersed beam onto the line array which has a dimension of  $12.8 \times 0.5$  mm [78].

The line array is integrated into EPICS and receives an external trigger signal (with the revolution frequency of 2.7 MHz) which is generated by the ANKA timing system. The maximum acquisition speed of the detector is 193 spectra per second, but the fastest stable readout we can achieve with a MATLAB script via EPICS is in the order of 7 Hz.

In order to determine the resolution of the spectrometer the laser was used in continuous wave (CW) operation to achieve a very narrow-band spectrum ( $\text{FWHM} > 1$  nm). For this, the current supply of the pump diode for the laser oscillator was tuned down to 83 mA (typically it is set to 420 mA during mode-locked operation), which is right around the lasing threshold. Figure 5.15 shows the measured spectrum (blue, primary Y-axis) and

<sup>7</sup>ET-3010 from Electro-Optics Technology, Inc.

<sup>8</sup>LeCroy 600 MHz WaveRunner 64Xi with 10Gs/s.

<sup>9</sup>iDus A-DU490A-1.7 from Andor Technologies

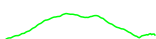
<sup>10</sup>Thorlabs GR13-0310



for better comparison also an amplified mode-locked spectrum which passes through the whole EO-Monitor. At the bottom a precise measurement of the CW spectrum with an OSA is shown, revealing that it consists of two very narrow peaks close to each other. From the FWHM of the CW spectrum measured with our spectrometer, the resolution of the spectrometer was determined to be 9 pixels.

With the current alignment, only about one third of the 512 pixels of the spectrometer are illuminated and the signal on 140 of them can be used for spectral decoding measurements (pixels 170 to 310, marked as “range used for analysis”). For the future, it is foreseen to enhance the optical beam path with a different grating and lens to make better use of the full amount of pixels.

A detailed report on further characterization studies can be found in Chapter 6.



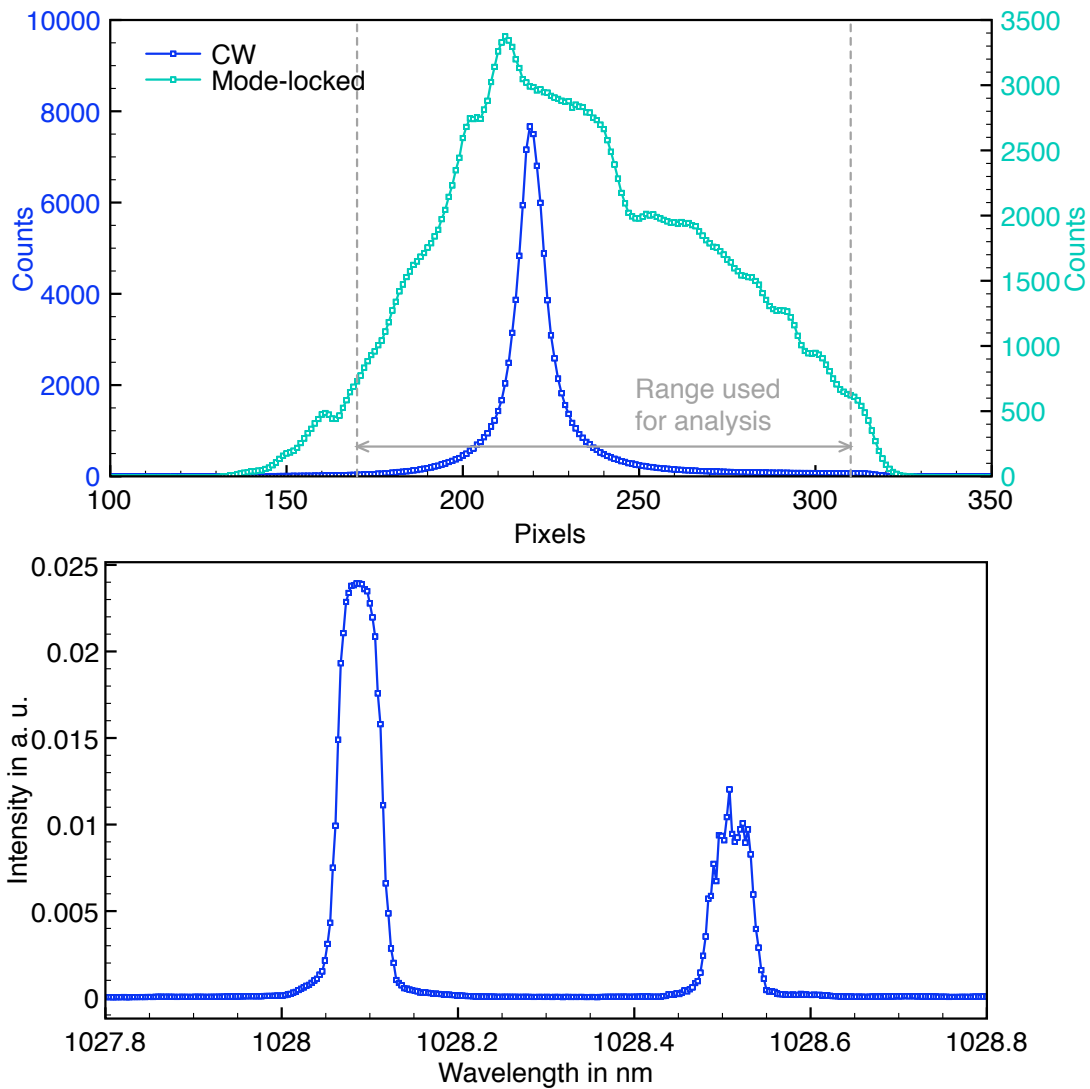


**Figure 5.15:** Top: Plot showing an averaged spectrum (100 shots) of an amplified, mode-locked pulse which passes through the EO-Monitor and is then detected by the spectrometer and the very narrow spectrum of non-amplified CW radiation (coming directly from the laser oscillator) for which the pump power of the laser was tuned down so much that it would not start mode-locking and not saturate the detector. The FWHM of the CW-pulse is 9 pixels which is taken to be the resolution of the spectrometer. Bottom: CW radiation recorded with an OSA showing that it consists of two very narrow band lines.





## 6. Systematic Studies with the EO Setup at ANKA

This chapter presents the measurement results of systematic studies with the near-field EO setup at ANKA.

The first two sections present the results of thorough characterization measurements with the setup and describe the read out and data processing for EOS - in Section 6.1 - and for EOSD in Section 6.2. Section 6.3 ends the chapter with the discussion of wake-field induced heat problems which were experienced during multi-bunch operation.

### 6.1 Characterization of the Electro-Optical Sampling (EOS) Setup

In order to study longitudinal beam dynamics with EOS- and EOSD-measurements, the characteristics of the experimental setup need to be fully understood. This chapter explains the data readout and analysis for EOS-measurements with the setup at ANKA.

For EOS, the electric field is sampled by a stepwise change in delay between the laser pulse and the electron bunch. The returning laser pulse is then analyzed as a whole with a fast PD and only its peak value is recorded.

When EOS measurements are used to determine the electron bunch length, their resolution depends on the length of the laser pulses which are used to sample the electric field, the size of the delay steps, and the jitter between electron bunch and laser. For an ideal measurement, one wants all of those limiting factors to be much smaller than the bunch length.

This means:

- Very short laser pulses, which need to be compressed to their Fourier limit, typically  $< 200$  fs FWHM.
- Very precise and small delay steps:  $< 100$  fs can be achieved with an optical delay line.



- The synchronization of the laser system to the RF system also needs to have a very low jitter ( $< 200$  fs integrated).
- Very low jitter on the electron bunch arrival time relative to the RF system: For this some kind of longitudinal feedback system for the accelerator is required.
- The temporal shape of the electron bunches should not change during the scope of one measurement which typically takes a few minutes, depending on the amount of delay steps.

As there was no longitudinal beam feedback system in operation at ANKA when the studies were performed<sup>1</sup>, previous measurements with the SC had shown that, especially during the low- $\alpha_c$ -operation, the bunches can oscillate longitudinally with amplitudes up to a few picoseconds (see Fig. 4.3 for an image of the synchrotron oscillations recorded with the SC). These synchrotron oscillations, of course, also smear out any EOS measurement, but fortunately they are not such a big problem for single-shot EOSD measurements, because for those, the whole bunch profile is recorded in one shot and synchrotron oscillations will just show up as arrival time fluctuations.

The dynamic changes in bunch deformation or substructure on the electron bunches, which we were expecting to see because of the bursting behavior of the CSR (see Ch. 2.3) would therefor not be detectable with EOS measurements.

Because of those limiting factors of the EOS technique, the main focus of our EO system is to achieve a sub-ps time resolution for single-shot EOSD measurements, for which the bunch shape is encoded into the spectrum of the laser pulse. For this measurement technique, however, the laser pulses need to be stretched to lengths longer than that of the electron bunches.

It is very hard to accomplish both extremes of very short (sub-ps) and rather long ( $\approx 50$  ps FWHM) laser pulses with one experimental setup without putting a lot of effort into the dispersion control which is required for compressing the laser pulses after they have passed dispersive elements such as fibers and other optical media.

The focus for our setup was laid upon the EOSD measurements and the fact that the laser pulses could only be compressed down to about 20 ps FWHM was accepted.

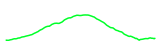
To sum this up, EOS measurements are a convenient way to scan for temporal overlap between the laser pulses and the electron bunch and their experimental setup is less demanding than the one for EOSD, because only a temporal detection of the whole laser pulse is required. Because of this, they even work at very low laser and beam intensities and pose as a great tool to measure the long-range wake-fields which trail the electron bunch for which a sub-ps resolution is not required.

### 6.1.1 Data Readout for EOS

Data readout for EOS measurements is done with a MATLAB script that reads the peak value of the PD signal from an oscilloscope via a direct connection and then changes the delay between the laser pulses and the RF clock in steps and records the peak value again

---

<sup>1</sup>In October 2013 a longitudinal feedback system has been installed at ANKA.



until the desired delay range is covered. Experimentally the change in delay is achieved with a VM inside the laser synchronization unit, which allows us to change the phase of the 500 MHz RF signal in steps of 488 fs<sup>2</sup>. This VM is controlled via EPICS. The main measurement data is peak value versus time delay. The beam current is recorded for every data point because, especially the long range EOS scans which cover a range of about 3 ns with a step width of usually 5 ps, take a few minutes (< 10 min) during which the beam current will have decayed slightly. For very high bunch currents above 2 mA and very compressed bunches the beam life time can drop down to values as low as about 45 min<sup>3</sup>. Other beam parameters, such as the orbit, energy, RF voltage and frequency are only recorded at the start of the measurement. The laser settings (positions of all linear motors and rotation mounts) are recorded at the start as well. The time base and sensitivity settings of the oscilloscope are also recorded at the start of the measurement.

### 6.1.2 Data Processing for EOS

Data processing is rather simple for EOS measurements in comparison to EOSD measurements. The peak voltage of the photodiode is recorded in dependence of the VM steps, so the time axis can easily be calculated by multiplying the steps with -488 fs (the minus comes from the fact that a positive VM step decreases the delay between laser and electron bunch). For the Y-axis there are several possibilities. A few examples of these can be seen in Fig. 6.1: The raw signal from the photodiode already gives a rough measure of the electric field for a certain delay (top image), the relative modulation is just the PD signal divided by the unmodulated signal (average value of the flat region without any modulation where the delay is set in a way that the laser pulse passes the EO crystal before the electron bunch) - this is most suitable when current dependent effects want to be studied and raw modulation strengths want to be compared.

The relation between phase retardation and relative modulation is fairly linear for small phase retardations between -5° and 5°. This can be seen in Fig. 6.2, where a calibration measurement to give the relation between phase retardation and relative modulation is shown. The phase retardation for this measurement was not induced by the birefringence inside the EO crystal, but by rotating the HWP. Here a rotation by 1° gives a phase retardation of 4°. The relative modulation is the PD signal relative to that at an angle of 4.6°, which we chose as standard angle for our measurements. In the top image the whole measurement range is shown and the rather large changes of phase retardation clearly show the cosine behavior, which is represented very accurately by the following fit:

$$y = \frac{A}{2} \cdot \left( 1 - \cos \left( (x + C) \frac{\pi}{180^\circ} \right) \right) + B \quad (6.1)$$

with  $y$  being the relative modulation and  $x$  being the phase retardation  $\Gamma$  introduced by the HWP angle  $\Theta$ . A, B and C are fit coefficients. The plot at the bottom of Fig. 6.2 shows a zoom into the range of typical phase retardations induced inside the EO crystal from the field of the bypassing electron bunch at ANKA. Typical EOS measurements with our system have shown relative modulations between 0.8 and 1.2, for cases with a

<sup>2</sup>360°  $\hat{=}$  2 ns  $\hat{=}$  4096 steps

<sup>3</sup>With a life time of 45 min the beam will have decayed by 20% over the course of 10 min.

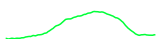
very high beam current even as high as 1.3. Over this range, the relation between relative modulation and phase retardation is nearly linear and the relative modulation is already a good measure of the electric field strength. The phase retardation is only used when absolute electric field strengths want to be calculated.

Most suitable for EOS measurements which want to compare the shape of the wake-fields independently of the beam current, is to show the current normalized modulation, for which the relative modulation is also normalized to the beam current for every measurement point an example of this can be seen in the middle graph in Fig. 6.1. This gives a measure of modulation per mA of beam current. When comparing the intensity of wake-fields present in different measurements it makes sometimes sense to normalize the curves, so the height of the first peak, which is caused by the Coulomb field of the electron bunch, is normalized. As the systematic studies for different distances from the electron beam and for different beam currents are also interesting beam studies, their results are shown in Chapter 7.2 rather than here.

### 6.1.3 Wave Plate Settings

Wave plate settings play a key role in the measurement optimization process. We chose a near-crossed polarizer setup in order to achieve a nearly linearly dependent response which has already been shown in the previous paragraph. For this a small angle in the order of  $5^\circ$  (relative to the angle of maximum signal suppression) is set with the HWP on the EO-Monitor. The optimum setting for the QWP which is used to compensate for any intrinsic birefringence, the EO crystal has, is determined experimentally - to have maximum signal suppression.

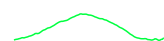
Figure 6.1 shows EOS traces recorded with our initial wave plate settings in February 2013 and traces recorded for optimized wave plate settings from March 2013. While for the initial settings, a crossing angle of  $4^\circ$  was chosen, for the final settings, we used  $4.6^\circ$ , but also rotated the QWP by  $8.7^\circ$  relative to its original settings. The image in the top shows the raw signals recorded with the PD. For the initial settings the absolute voltage of the PD signal has decreased by about a factor of three for the new settings, which is mostly due to the optimized settings of the QWP (for a larger HWP angle it will increase slightly), but also partly because of non-recoverable misalignment of the EO-Monitor, which will be discussed in Section 6.3 and could be improved again by optimizing the coupling into the fiber collimator on the EO-Monitor. With the optimized wave plate settings, the overall modulation could be increased and the negative ringing after the first peak which would result in shorter measured bunch lengths could be minimized. Also the peak height of the wake-field induced peaks in comparison to the Coulomb peak (first peak) could be slightly decreased, so the main peak is now always the highest one. The effect that the baseline for the data set with the initial settings is increasing slightly towards larger delays is probably due to the fact that it was the first scan, right after moving the crystal close to a single bunch with a beam current of nearly 3 mA, which led to a slight misalignment due to heating up of the crystal and its holder. For clarification: The scan is done from right to left, because positive steps with the VM decrease the delay of the laser pulses. For later



measurements a thermal equilibrium is reached.

Once those optimized settings were found, we kept the QWP fixed and performed studies with different angles of the HWP, their results are shown in Fig. 6.3. Here both plots show the current normalized modulations for different angles of the HWP. While the graph in the top shows the curves for positive angles and for  $-0.4^\circ$ , the one at the bottom shows the curves for negative angles which lead to a change in sign of the modulation. For ideal wave plates one would expect to see no modulations smaller than 1 for a measurement with crossed angles ( $0^\circ$ ), because the starting point should be completely in the minimum of the cosine curve, so both negative and positive electric-field strengths would lead to an increase in signal. In our case, however, even for the measurement with an angle of  $-0.4^\circ$  the relative modulations still went slightly into the region below 1.

Further systematic studies will be required to fully understand the effect the QWP angle has on the shape of the measured trailing wake-fields. To keep all later measurements comparable, we chose fixed settings of the QWP and kept the HWP also constant when comparing different measurements.



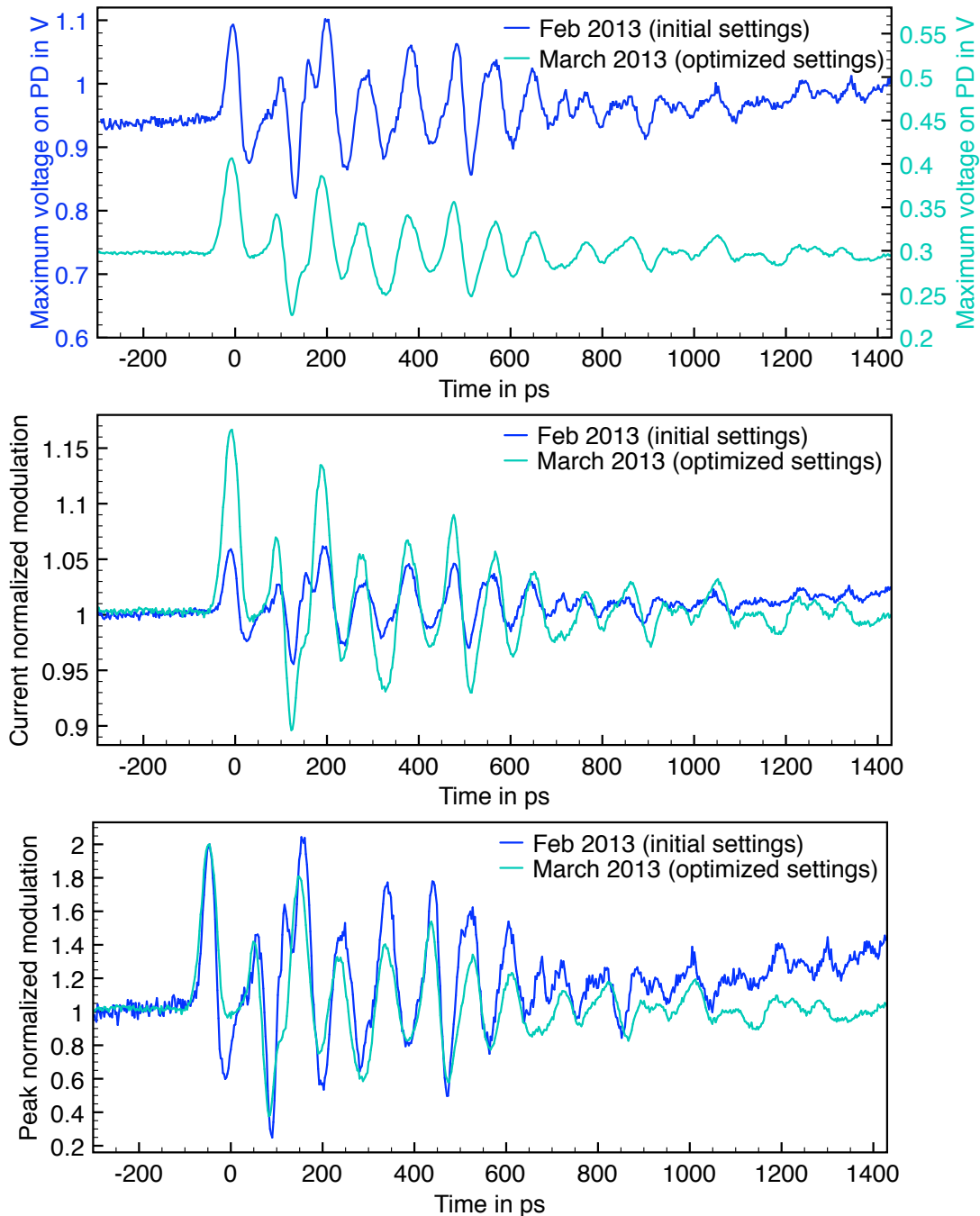


**Figure 6.1:** Three different displays of EOS traces recorded with our initial wave plate settings in February 2013 and traces recorded for optimized wave plate settings from March 2013. Top: Absolute peak signals of the PD. Middle: Current normalized modulation - peak signal of the PD divided by the the unmodulated signal (average of signal before the first peak) and the beam current (current measured for every measurement point). Bottom: Peak normalized modulation - relative modulation normalized to the intensity of the first peak. For all measurements: Identical electron beam parameters: 1.3 GeV,  $f_s = 13$  kHz, 450 kV RF voltage per cavity. Feb 2013:  $4^\circ$  HWP angle; 5.3 mm crystal distance, 2.95 mA beam current. March 2013: 5.6 mm crystal distance,  $4.6^\circ$  HWP angle, QWP rotated by  $6^\circ$  in comparison to the old settings, 2.34 mA beam current.

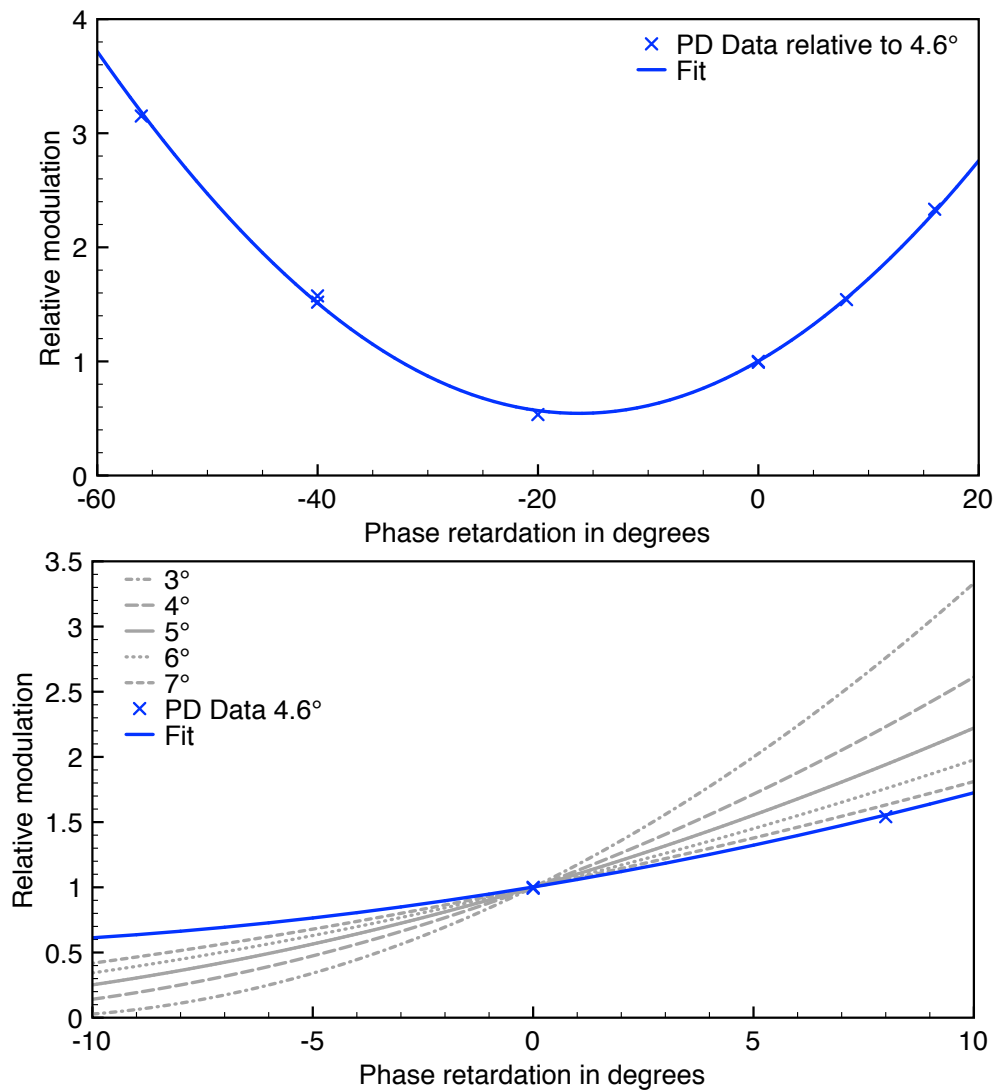


**Figure 6.2:** Top: Showing the peak signal of the PD relative to that at  $4.6^\circ$  in dependence of the phase retardation (achieved by rotating the HWP). Due to the fact that even for crossed angles, there is a non-zero transmission, the slope is not as high as expected for an ideal HWP (see bottom). A fit (see Eq. 6.3) to these curves gives the conversion between relative modulation and phase retardation (see text for details). Bottom: Comparing the measurement data with the theoretical predictions for ideal wave plates.

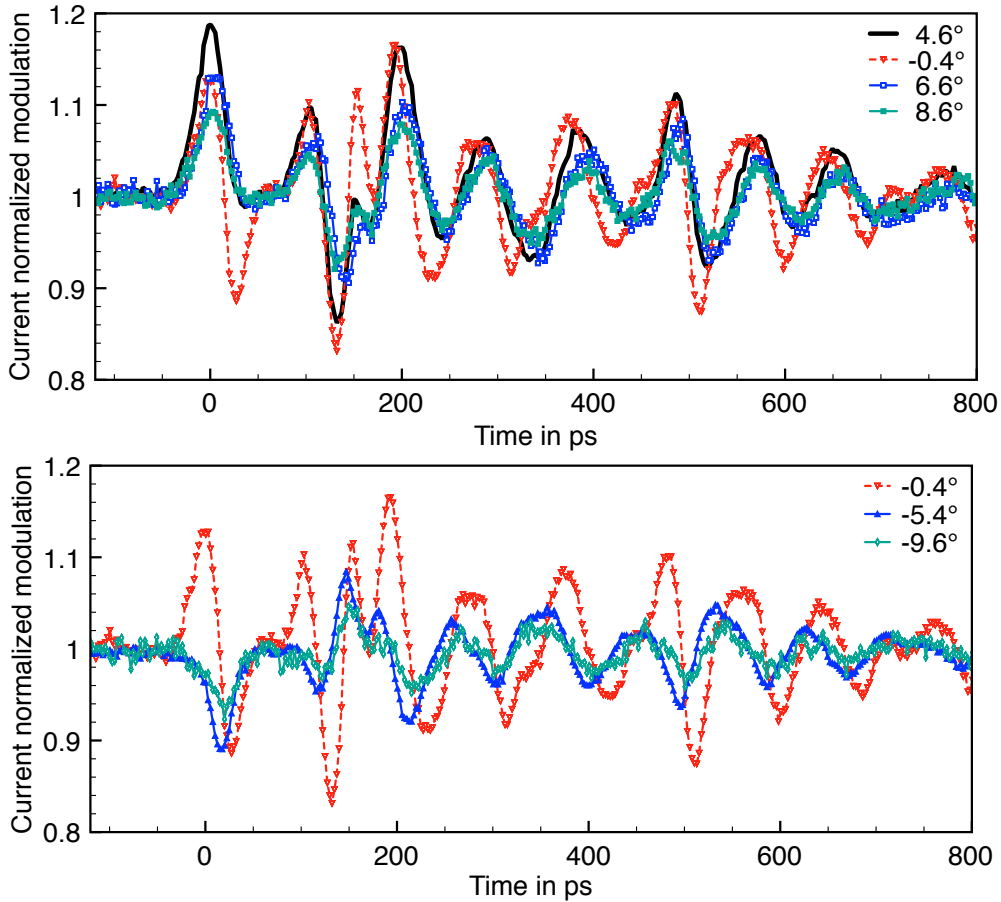


**Figure 6.3:** Top: EOS scans for different positive angles of the HWP and for  $-0.4^\circ$ . For  $4.6^\circ$ , the current normalized modulation of the first peak is largest. Bottom: EOS scans for different negative angles of the HWP, while for  $-0.4^\circ$ , the first peak still shows a modulation  $> 1$ , for the larger negative angles, the signal is flipped.

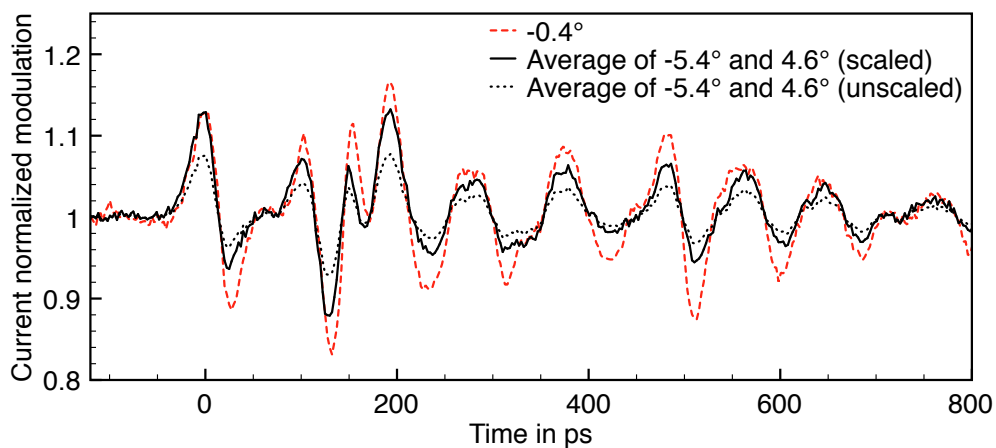


**Figure 6.4:** Comparing the EOS scan for  $-0.4^\circ$  with the average of the scans for  $-5.4^\circ$  and  $4.6^\circ$ . For the scaled data set, the data has been scaled in  $y$ -direction to match the amplitude of the first peak. The agreement of the peak positions is very good, just the amplitudes of most of the peaks and dips of the trailing wake-fields are slightly lower for the averaged signal than for the measurement at  $-0.4^\circ$ .



## 6.2 Characterization of Electro-Optical Spectral Decoding (EOSD) Measurements

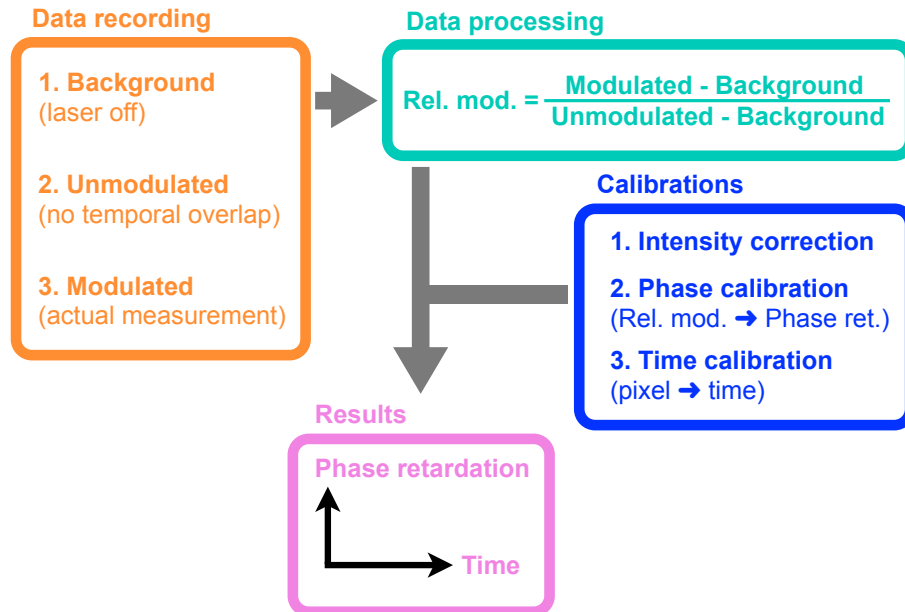


**Figure 6.5:** Schematic of the measurement steps for EOSD bunch profile measurements.

For the more complex EOSD-measurements a schematic drawing of the measurement process is depicted in Fig. 6.5. This following section goes into detail of which steps need to be performed to do actual single-shot bunch profile measurements with EOSD. The steps are grouped in: data recording, data processing and calibration measurements, all together, leading to the final measurement results. In Section 6.2.4 the fully processed measurement data is analyzed regarding the sensitivity and the resolution of the whole setup.

### 6.2.1 Data Recording for EOSD

The data recording is all done with the 512-pixel line detector which is part of the spectrometer discussed in Section 5.4.2. Besides measuring the actual modulated spectra, a background spectrum and an unmodulated spectrum need to be recorded.

The background spectrum, for which an example can be seen in the top of Fig. 6.6, is recorded without the presence of any laser light. For better statistics, the average over 100 consecutive measurements, each with the same exposure time as the actual later measurements is recorded. It gives the noise level of every pixel in the detector. The whole spectrometer is covered with a dark card box to avoid stray light. Even though the averaged background values for different pixels can differ by more than 10 %, they are inherent to those pixels. The absolute values do not change significantly from one measurement to the other even though there might be days between different measurements. The bottom of Fig. 6.6 shows the difference in averaged counts between two background spectra recorded on different days, showing that the mean fluctuation is as low as 0.12 % and no pixels show a larger difference than -2 or +4 counts. From any measurements done with

the laser illuminating the detector, a background spectrum - usually measured at the start of a measurement shift - is deducted.

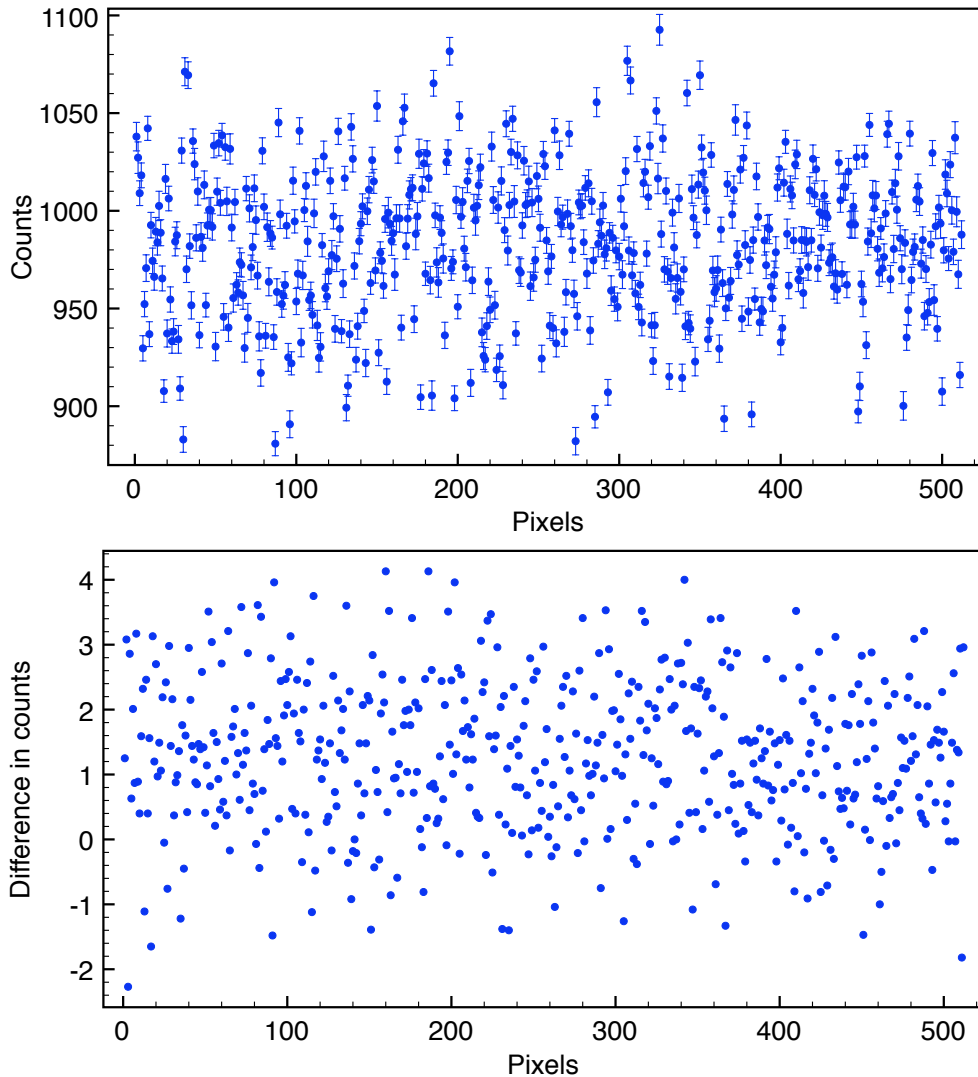


**Figure 6.6:** Top: Averaged background spectrum recorded without any laser light. Error bars are standard deviation of 100 shots. Bottom: Difference in counts for two different background spectra recorded on different days. The mean difference is less than 1.3 pixels which is a fluctuation of just 0.12%.

The unmodulated spectrum is recorded when there is no temporal overlap between the laser pulse and the electric field from a bypassing electron bunch inside the EO-crystal. This is achieved by shifting the delay of the laser pulse in a way that it passes the crystal well before the electron bunch (usually in the order of 300-500 ps earlier). For this, the crystal is ideally already moved in close to the electron beam, so thermal equilibrium is reached and intensity drifts due to thermal expansion are minimized. As it is crucial for single-shot EOSD-measurements to have a high shot-to-shot stability of the laser spectrum, the unmodulated spectra were analyzed thoroughly. The standard deviation, shown as error bars in Fig. 6.7 of the counts for 100 consecutive unmodulated spectra seem to be very high at first glance (in the order of up to 10%), this however seems to be caused by intensity

fluctuations of the signal recorded with the detector which leave the overall shape of the spectrum unchanged. This means that if the spectrum of the laser would change from shot to shot, then the shape of the relative modulation, which is the spectrum divided by the averaged spectrum, would fluctuate highly from shot to shot. If just the intensity of the recorded signal changes from shot to shot, then the relative modulation would just be horizontal lines displaced in y-direction. The top of Fig. 6.8 which shows 10 unmodulated spectra divided by an averaged unmodulated spectrum, strengthens the assumption that the biggest contribution of the fluctuations comes from the overall intensity change, rather than laser spectrum fluctuations. Even though the relative modulation averaged over the whole spectrum seems to vary from shot to shot, the deviations from this constant value seem to be rather small, which can be seen better at the bottom of Fig. 6.8 where 100 of those relative modulations were averaged after their mean value (average over all pixels) was shifted to 1. For better visibility the standard deviation is additionally shown on the second y-axis. The standard deviation is in the order of 1 to 1.5% over the analysis range. This gives an idea how far the data can be trusted and to which extent small changes in relative modulation are really signal which could be caused by substructure of the electron bunch.

As the fast photodiode does not record very large shot-to-shot intensity fluctuations, we assume that the intensity fluctuating effect is mostly caused by the fact that even though the camera is triggered externally, the exposure time does not start right when the trigger-signal reaches the camera, but only at the next clock-cycle of the internal readout clock of the camera, thus leading to significant phase jitter of the exposure gating with respect to the laser pulse. This would not be a problem if the gate pulse controlling the exposure time would be perfectly rectangular, because the laser pulse length, even after all the propagation through fiber should still be well below 500 ps FWHM which is short in respect to the exposure time of 1.4  $\mu$ s which we picked to ensure that only one laser pulse at a time illuminates the detector. This exposure time, however, is the smallest possible setting for the detector, so the gate will be not very rectangular but more a rather smeared out pulse, which can, together with the internal clock of the detector explain these rather large intensity fluctuations. For now, those fluctuations will be corrected for with the data processing algorithm explained in Section 6.2.2.

The dip in standard deviation over counts around pixels 205 and 180 in Fig. 6.7 could be caused by the fact that some part of the laser spectrum in those regions is not only inside the short laser pulse, but a CW contribution, thus being not so much affected by jitter in the exposure timing. In the future, this should be further investigated, for now, ideally a measurement range is chosen which has the main signal start after pixel 220.



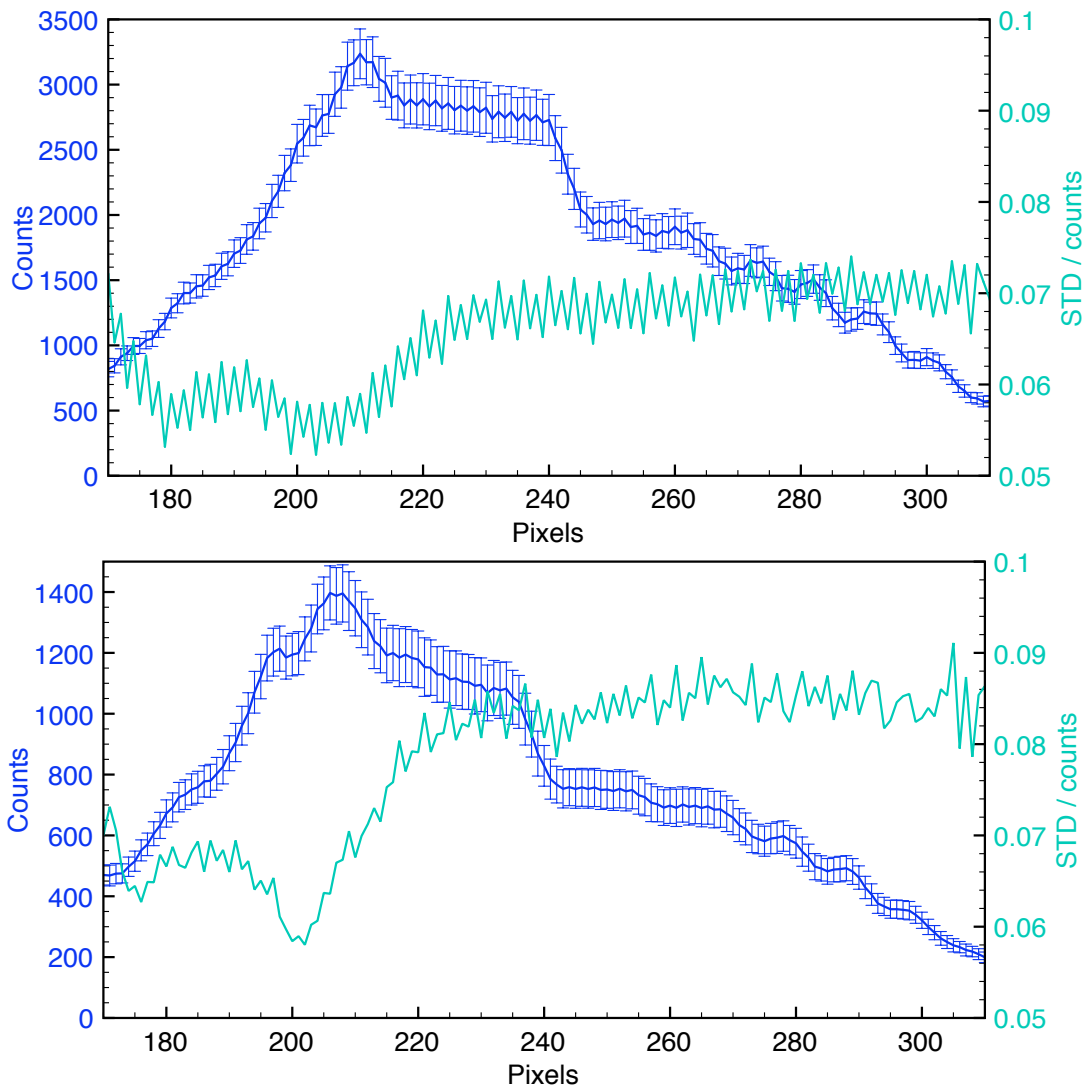


**Figure 6.7:** Two averaged unmodulated spectra for different laser pulse lengths. In addition to that as second Y-axes the standard deviations divided by the averaged counts are shown for every pixel within the analysis range from pixel 170 to 310. Top: Longer laser pulses (compressor: 15 mm) recorded on 2013-04-11. Bottom: Slightly shorter laser pulses (compressor: 25 mm) recorded on 2013-05-08.

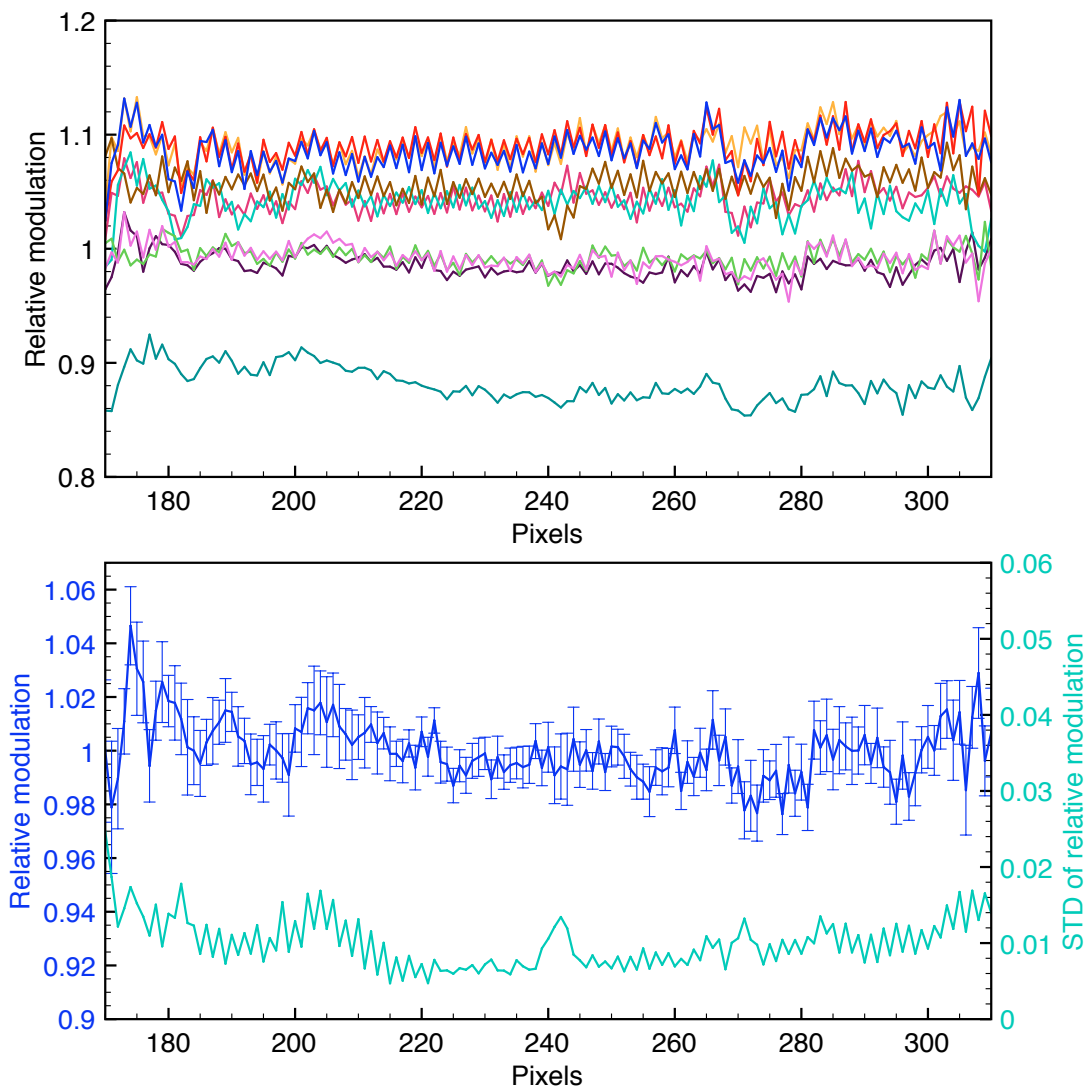


**Figure 6.8:** Top: 10 unmodulated spectra divided by an averaged unmodulated spectrum. The shift in baseline comes from the intensity fluctuations of the unmodulated signal due to the camera gate jitter and can be corrected by subtracting the average modulation. (The 10 shots are from a different dataset than the averaged unmodulated is; 20 min time in between). Bottom: Left axis: Showing the averaged intensity corrected relative modulation with the standard deviation over 100 shots as error bars. Right axis: Showing just the standard deviation.

### 6.2.2 Data Processing for EOSD

Once the data recording is done, the spectra need to be processed. For this, first the averaged background spectrum is deducted from both the unmodulated and modulated spectra. Figure 6.9 shows examples of those background deducted spectra for different measurements. Finally, the modulated spectra are divided by the averaged unmodulated spectrum to give the relative modulation which is shown in Fig. 6.10, to avoid any divisions “by zero”, a suitable analysis range has to be picked which, for our case, is the range between pixel 170 and 310.

Some of the relative modulations in Fig. 6.10 show strong ripples all over the spectrum (e. g. Shot 999 in the top of the figure), as this is usually not present for all 1000 shots of a typical measurement sequence, but appears for some shots and then vanishes for some shots again, we assume that it is caused by the fact that the camera’s odd and even pixels are read out by different ADCs. Those ripples definitely are an artifact on some bunch profile measurements especially as such small substructures on the electron bunch could not be resolved by the spectrometer (see Section 5.4.2 for details about the resolution). As those ripples tend to mislead the eye when looking at bunch profiles, we remove them for the display by forming a moving average over two neighboring pixels.

The processed data - now in the shape of relative modulation versus pixel - is then transformed into phase retardation (directly proportional to the electric field strength) versus time, for which several calibration measurements are required. They are discussed in the following section.



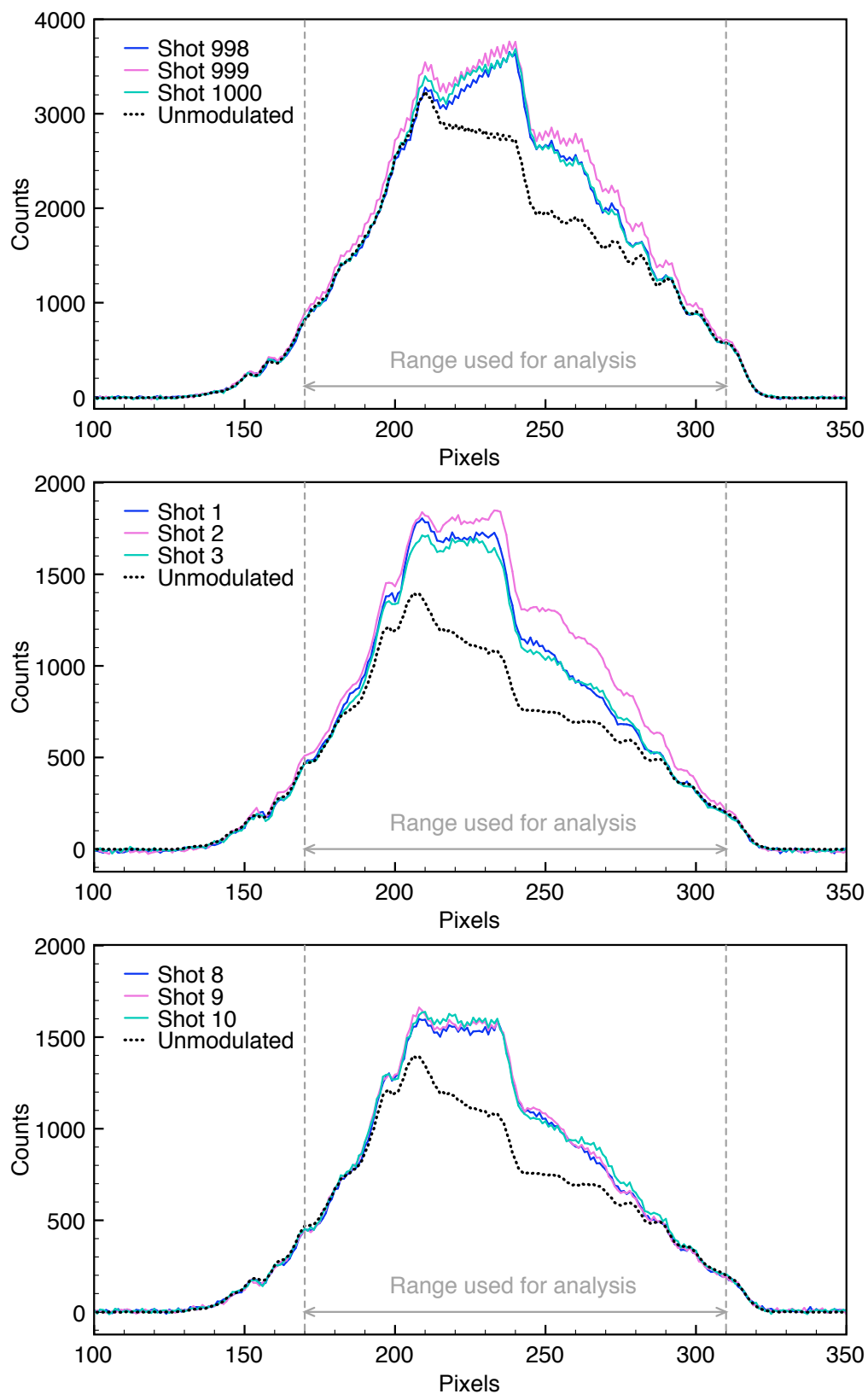


**Figure 6.9:** Each image shows 3 background subtracted modulated spectra and an averaged unmodulated spectrum. Top: 2013-04-11 with longer laser pulses (compressor: 15 mm) Middle & Bottom: 2013-05-08 with slightly shorter laser pulses (compressor: 25 mm).

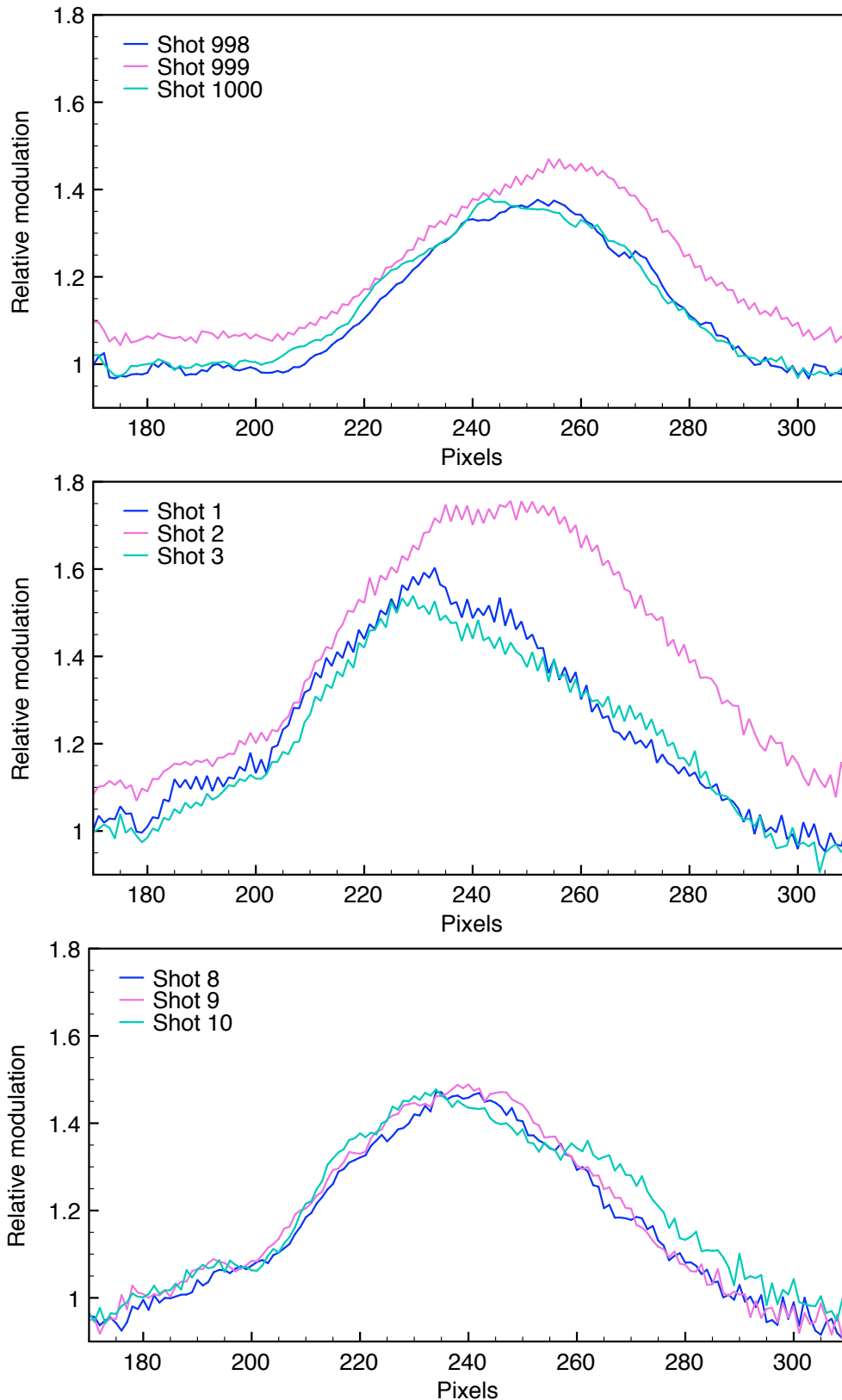


**Figure 6.10:** Relative spectrum modulations for 3 shots for different data sets. The off-set in relative modulation caused by fluctuations of the total intensity of the modulated spectra is strongly visible for Shots 2 and 999. Top: 2013-04-11 with longer laser pulses (compressor: 15 mm) Middle & Bottom: 2013-05-08 with slightly shorter laser pulses (compressor: 25 mm).



### 6.2.3 Calibration Measurements for EOSD

Starting out with the processed data in the shape of relative spectrum modulation versus pixel several further steps need to be performed in order to obtain actual longitudinal bunch profiles. Besides the correction for any intensity fluctuations that would shift the base line of the relative modulation, there are two main calibration measurements which need to be performed for EOSD-measurements, a phase calibration, to calculate the phase retardation from the relative modulation, and a time calibration, to convert the pixel axis of the spectrometer into a time axis. Those three steps are discussed in more detail below.

#### 6.2.3.1 Intensity correction

The intensity correction is performed by taking the relative modulations and doing a Gaussian fit with the following shape to them:

$$y = a \cdot e^{-\left(\frac{x-b}{c}\right)^2} + d \quad (6.2)$$

with  $a, b, c$  and  $d$  being fit parameters. The fit parameter  $d$  gives a measure of the baseline which will fluctuate by a maximum of about  $\pm 0.1$  around a relative modulation of 1. This is due to the before mentioned trigger fluctuations of the camera. In order to get an “intensity fluctuation corrected relative modulation”,  $d-1$  is subtracted from the relative modulation for every pixel. An example of such an intensity correction can be seen in Fig. 6.11.



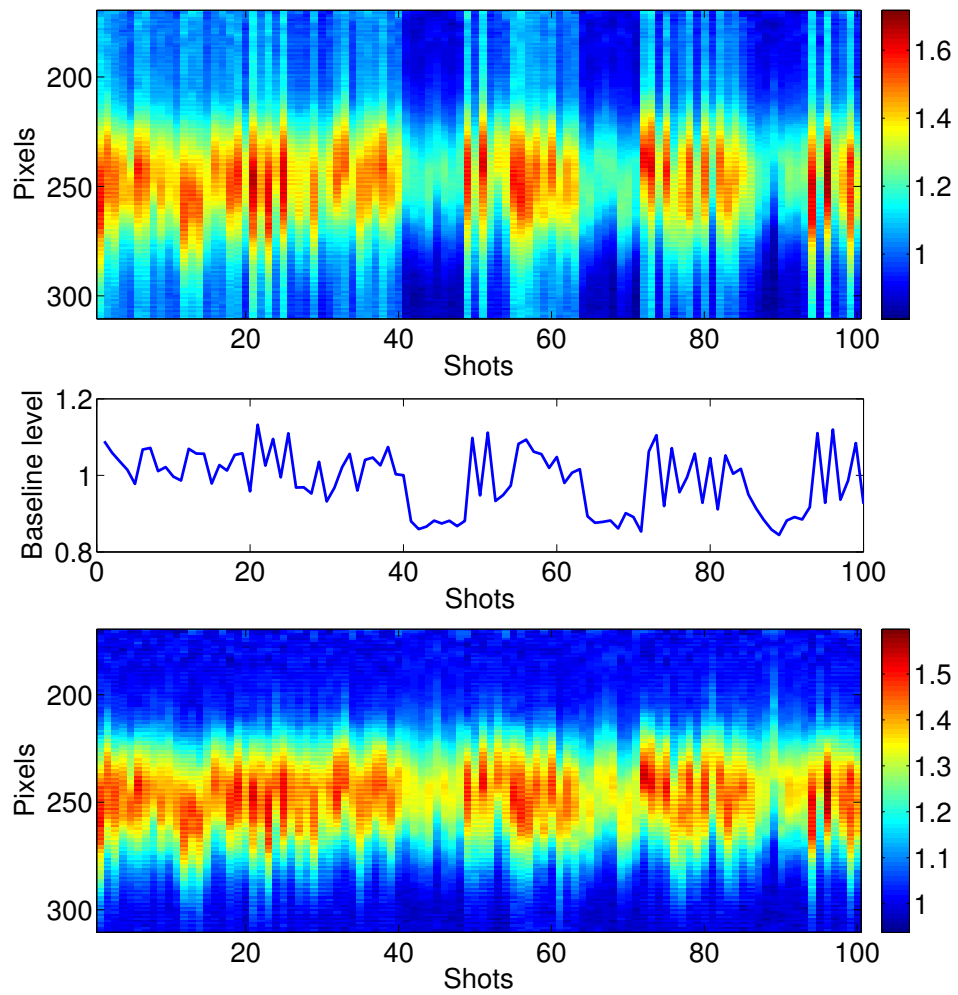


**Figure 6.11:** Example for an intensity correction. Top: Relative modulation raw data for 100 consecutive shots showing intensity fluctuations. Middle: Showing the fitted baseline level of the above data sets. Bottom: Intensity corrected relative modulations for which the baseline -1 has been subtracted.

### 6.2.3.2 Phase calibration

The phase calibration is the next step in the measurement chain. It will convert the relative modulation to a phase retardation which is proportional to the charge density of the electron bunch.

The phase calibration for the signal from the PD, previously depicted in Fig. 6.2, showed a rather linear relation between relative modulation and phase retardation, as predicted by calculations shown in Fig. 3.5 in Ch. 3.3.2. When repeating this measurement with the spectrometer, however, we experienced a pixel dependence of the slope, which required a calibration on a per-pixel basis to avoid signal distortions. As this behavior had not been observed at PSI, where the same laser system and a very similar optical setup were used [27], we believe it to be caused by chromatic effects of the wave plates in our setup and plan to replace them with higher quality ones. The first part of this subsection will discuss the actual phase calibration measurement and the second part will cover a systematic analysis of the obtained results and how they will affect EOSD measurements.

#### 6.2.3.2.1 Phase Calibration Measurement

The relationship between relative modulation and phase retardation can be calibrated by rotating the HWP on the EO-Monitor which introduces a known phase retardation of  $\Gamma = 4 \cdot \Theta$ , where  $\Theta$  is the rotation angle (see Eq. 3.2 on p. 31). The top part of Fig. 6.12 shows unmodulated spectra for different settings of the HWP angle, where  $0^\circ$  is chosen as angle for minimum spectral transmission through the optical setup.

For a setup with only ideal wave plates which do not exhibit any kind wave length dependence, the change in HWP angle should only change the intensity of the spectrum. It is easily seen that the intensity varies less for lower pixels than it does for higher pixels, this can be seen in more detail in the plot at the bottom where the relative modulation with respect to the a reference spectrum at  $4.6^\circ$  is shown. This angle is chosen as reference because it has been found to be very suitable for measurements, giving a good balance between a linear response and a decent signal to noise level.

The approximation of a perfect HWP does not seem to be valid for our wave plate, even though it is supposed to be achromatic. With the laser spectrum having a spectral width in the order of 100 nm, this effect could be caused by a poor quality of the HWP, as the measurements at PSI [27] did not show such a behavior. We plan to replace all our wave plates in the setup with ones of higher quality within the next longer shutdown period. For now, we can only cope with the effect by doing a calibration measurement for every pixel.

As the effect seems to increase gradually for higher pixel numbers, fits to the relative modulation in dependence of the phase retardation have been done for every pixel within the analysis range. The fits are of the following type (see Eq. 6.1):

$$y = \frac{A}{2} \cdot \left( 1 - \cos \left( (x + C) \frac{\pi}{180^\circ} \right) \right) + B \quad (6.3)$$

with  $y$  being the relative modulation and  $x$  being the phase retardation  $\Gamma$  introduced by the HWP angle  $\Theta$ .  $A$ ,  $B$  and  $C$  are fit coefficients which will then be used as calibration coefficients.



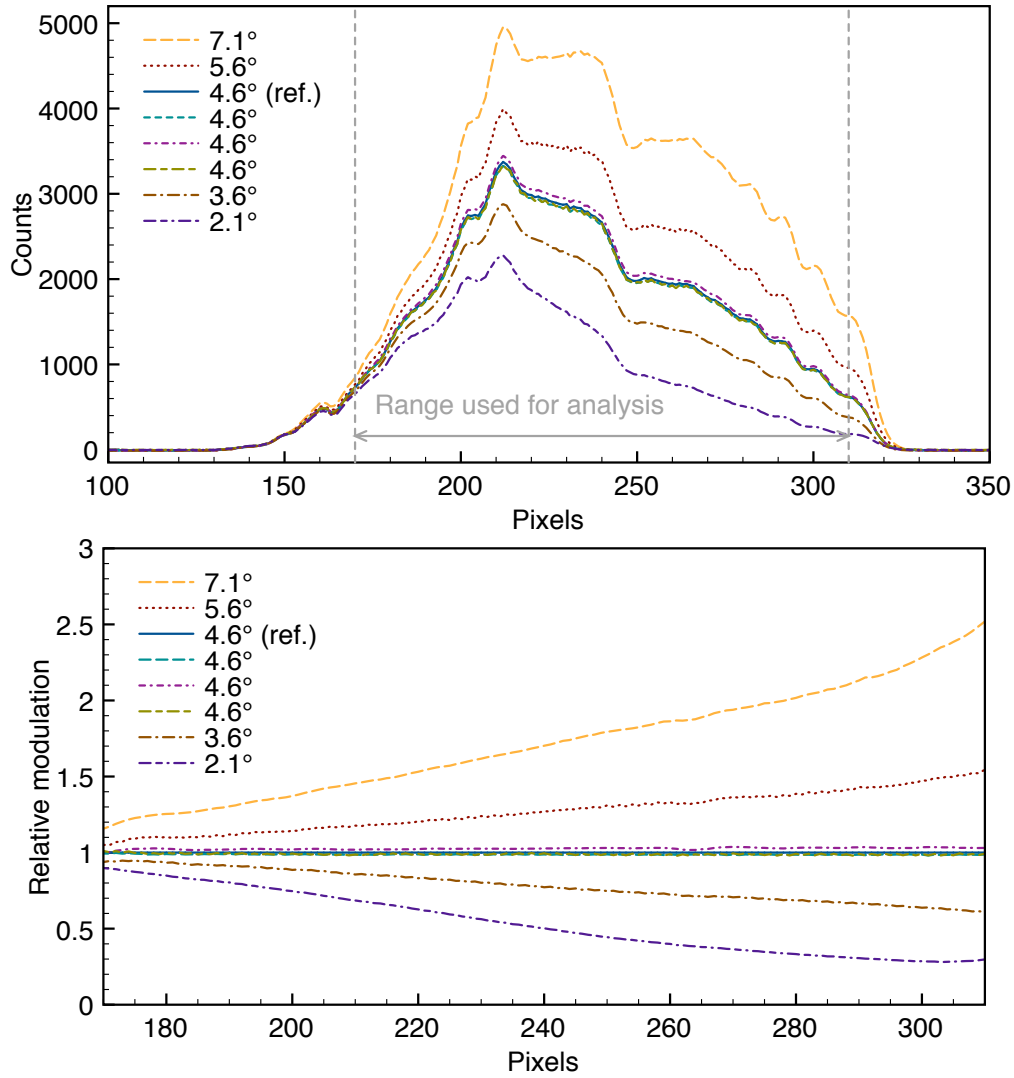


**Figure 6.12:** Top: Background subtracted laser spectra for different angles of the HWP in degrees, where  $0^\circ$  has been chosen to be the angle for minimum transmission. Bottom: Displaying the spectrum modulations relative to the one for an HWP angle of  $4.6^\circ$ . If the HWP had no wavelength dependence, then this would be horizontal, parallel lines with a constant relative modulation for each angle.

The top of Fig. 6.13 shows the data points with the corresponding fits for every 20th pixel. The behavior for lower pixel numbers is more linear and has a smaller slope, as one would expect for larger crossing angles in the near-crossed polarizer setup (compare with Fig. 6.2 on p. 71).

In contrast to this stand the results for larger pixel numbers for which the cosine behavior is clearly visible as one would expect for smaller crossing angles.

With the results from the fits, the phase retardations of the initial relative modulation measurements in Fig. 6.12 (bottom) have been calculated and are shown at the bottom of Fig. 6.13. The different measurements at  $4.6^\circ$  show small off-sets which can be most likely explained by a slight backlash when changing the direction of rotation of the HWP. The scans were done in an order such that the starting position was  $4.6^\circ$ , then we would move step-wise to  $7.1^\circ$ , then go back to  $4.6^\circ$  and then move step-wise to  $2.1^\circ$  and then finally

back to  $4.6^\circ$  again. The calibration works very well, just for for pixels at the lower edge of the analysis range, small deviations can be seen, they however do not play a big role as the the main region of interest for the actual bunch profile measurements lies between pixels 190 and 300. Unfortunately this means that random spectrum fluctuations for lower pixels will get amplified more, as for those pixels, even small intensity fluctuations correspond to rather significant phase retardations, an effect that will be shown in more detail at the end of this chapter in Section 6.2.4.



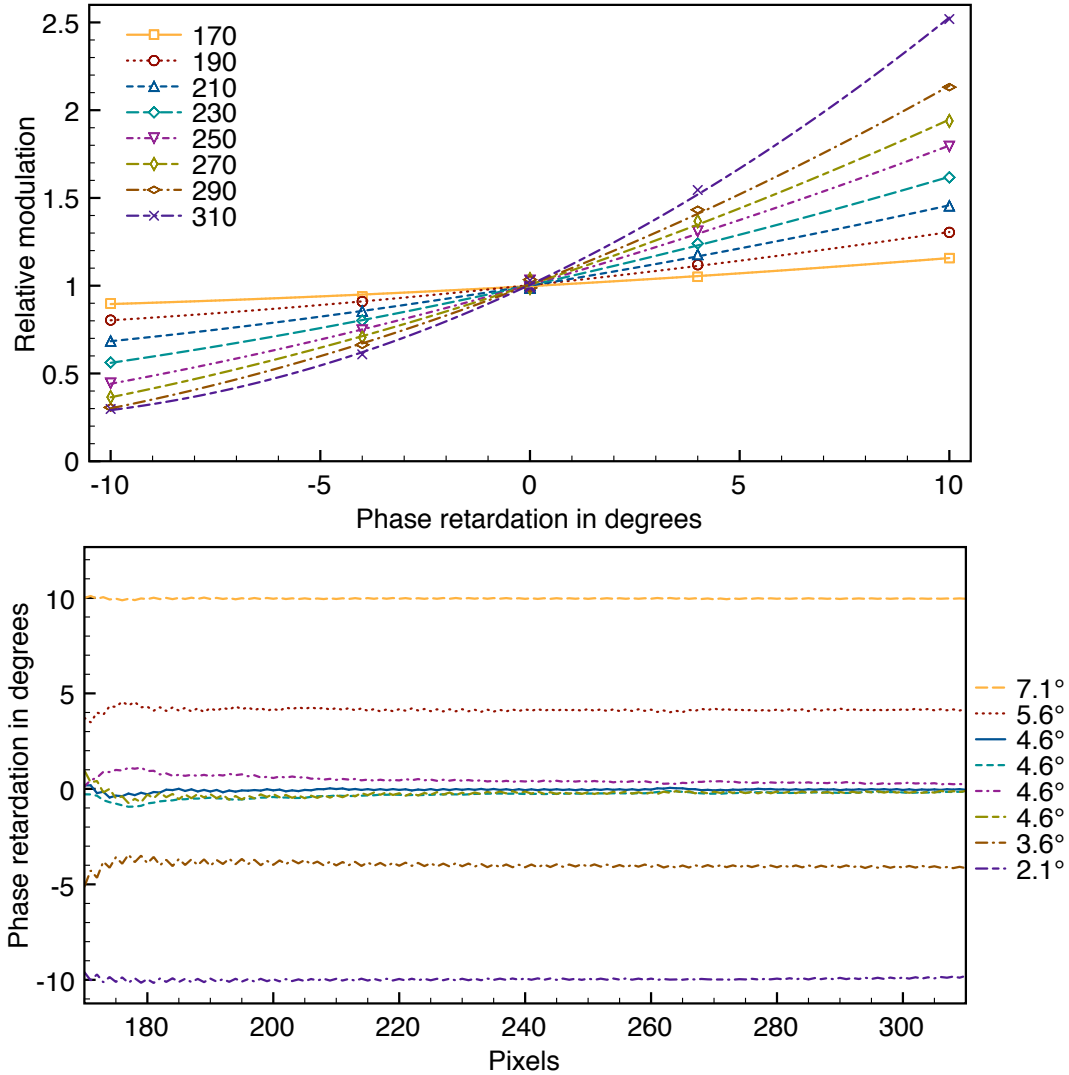


**Figure 6.13:** Top: Spectrum modulation relative to the one for an HWP angle of  $4.6^\circ$  in dependence of phase retardation relative to  $4.6^\circ$  for selected pixels within the analysis range (pixel 170 to 310).  $1^\circ$  in change of HWP angle gives  $4^\circ$  of phase retardation. The curves are fits to the data points following equation 6.3. Bottom: Showing the phase retardation computed from the calibration measurement for different HWP angles (see text for more details about the calibration measurement). For a perfect calibration one would expect horizontal lines with their y-values being 4 times the difference between the HWP angle and the reference angle of  $4.6^\circ$  (e. g.  $0^\circ$  phase retardation for an angle of  $4.6^\circ$  and  $-10^\circ$  for an angle of  $2.1^\circ$ ).

### 6.2.3.2.2 Systematic Studies for the Phase Calibration

In order to understand the effects of the phase calibration on the measured bunch profiles, studies have been done with generated Gaussian shaped phase retardation profiles for different delays<sup>4</sup>.

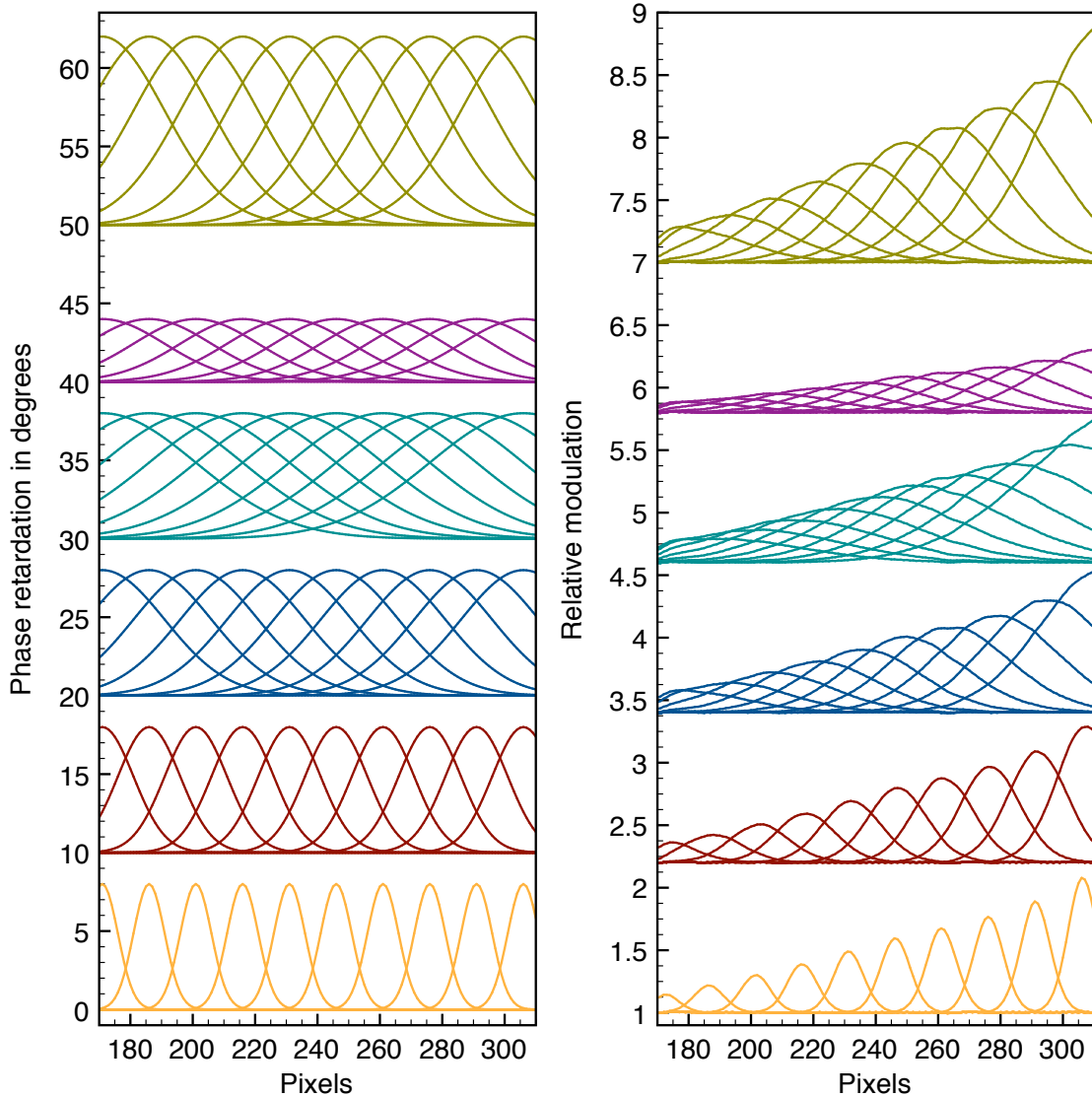


**Figure 6.14:** Left: Generated Gaussian shaped phase retardation for different delays. For better visibility the different data sets have been shifted in y-direction. The parameters of the generated Gaussians are from bottom to top:  $\sigma = 5$  pixels, 10 pixels, 20 pixels, 30 pixels, 20 pixels (with a lower amplitude), 20 pixels (with a higher amplitude). Right: Relative modulation computed from the phase retardation data on the left with the calibration coefficients obtained from the fits shown in Fig. 6.13.

Figure 6.14 shows in the left those Gaussian profiles for different amplitudes and widths. In the right the corresponding relative modulations are shown (computed with the measured calibration coefficients). Then Gaussian fits like in Equation 6.2 were used to retrieve the centroid position and the pulse length. The results can be seen in Fig. 6.15, the top

<sup>4</sup>This is how we would expect real bunch profiles, which are proportional to the phase retardations, to behave. A change in delay of the laser pulse should only shift the centroid position of the retrieved profile, but not alter its length or shape.

graph shows the centroid pixels retrieved from the fits to the relative modulations over the centroid position of the original phase retardation profiles.

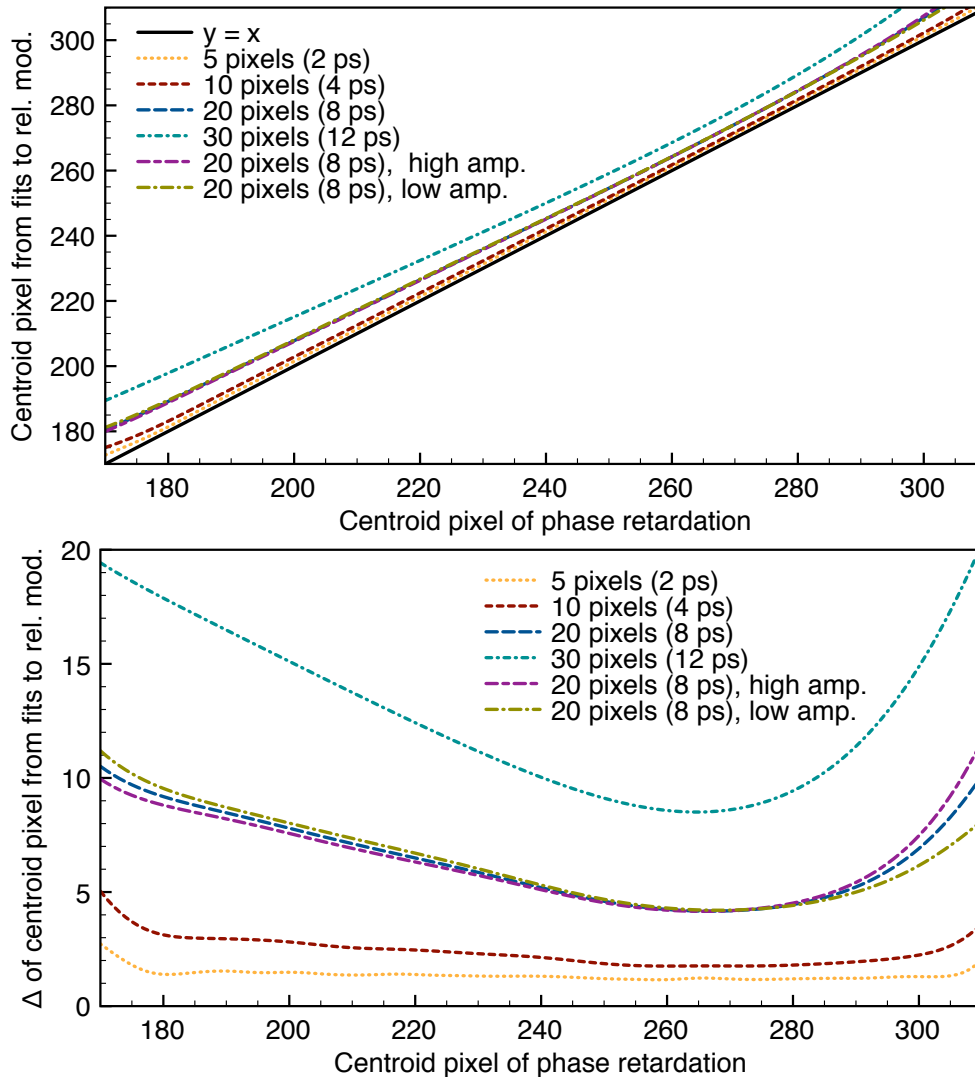


**Figure 6.15:** Analysis of the centroid position of the relative modulation profiles from the rhs of Fig. 6.14, the bunch lengths in ps (written in brackets) correspond to a linear conversion of 0.4 ps per pixel (typical value for certain laser settings to give a rough estimate of the relevance for bunch length measurements). Top: Comparison of the centroid position from fits to the relative modulation profiles over the actual centroid position from the original phase retardation profiles (lhs of Fig. 6.14). The main effect seems to be a shift of the centroid position. Bottom: Difference of the centroid fitted to the relative modulations to the original centroid of the phase retardation profiles over the original centroid pixels. Here it can be seen that especially for longer bunch lengths, the shift is not constant for every pixel.

The main effect seems to be a slight shift in centroid position towards higher values, which is especially dominant for higher widths of the Gaussians. The graph at the bottom shows the difference in pixels from the fitted centroid to the original centroid of the phase retardation profiles, here it can be seen more clearly, for profiles wider than 10 pixels the shift is stronger for lower pixels, then becomes smaller by about a factor of 2 for pixels between 260 and 280 and then increases again. The differences for different amplitudes of



the original profiles cause only a small extra shift compared to the effect of the pulse width and are visible mostly for very low and very high pixel numbers. The non-linear centroid shifting effect plays a role for the time calibration measurements which will be discussed in the next paragraph.

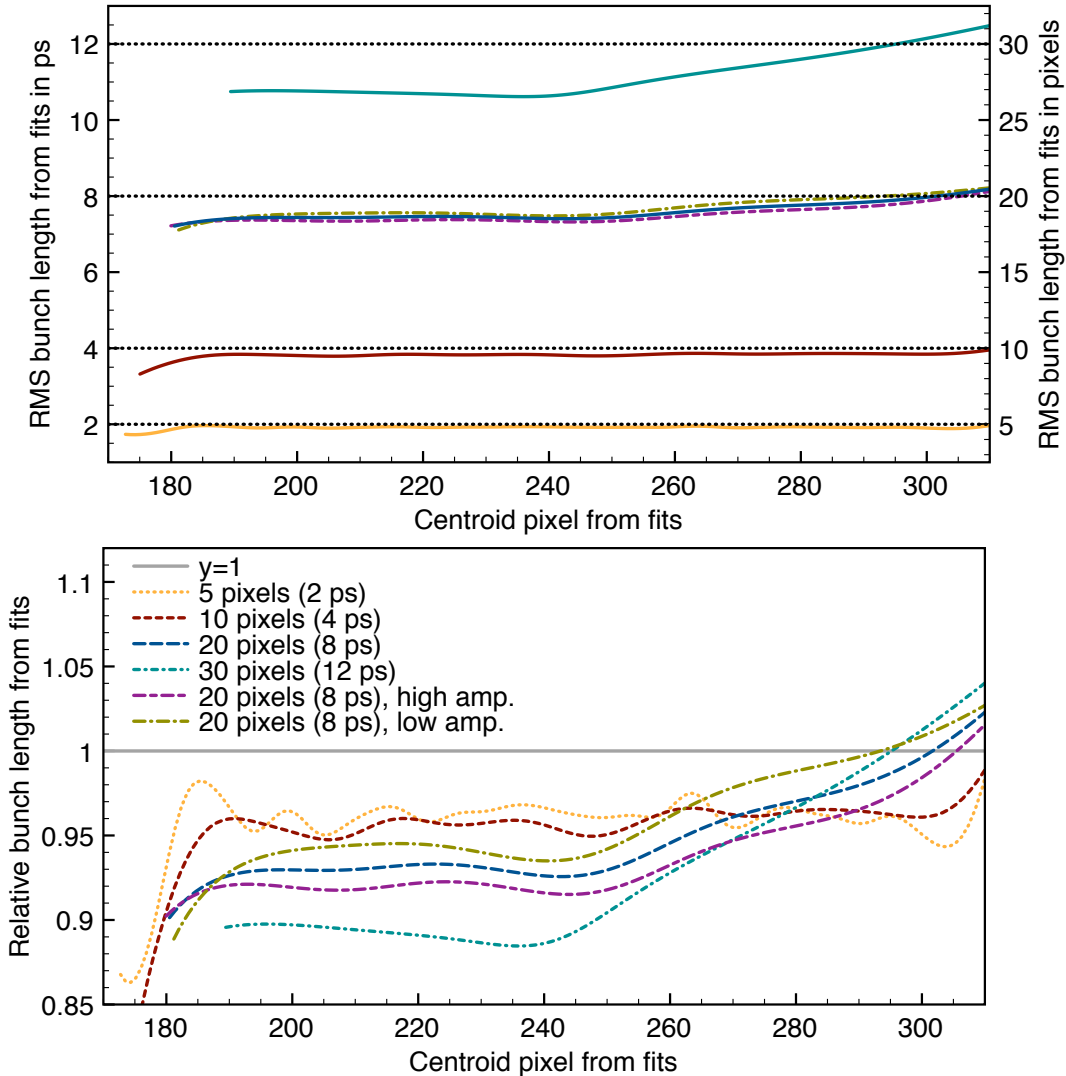


**Figure 6.16:** Fit results for the bunch length of the profiles in the rhs of Fig. 6.14. Top: Absolute bunch lengths retrieved to the fits for the different data sets with the black dotted lines showing the original bunch length of the phase retardation profiles (lhs of Fig. 6.14). Bottom: Relative bunch lengths for the above data, showing that the effect that lets the bunch length from the fits appear to be shorter is more pronounced for longer bunch lengths and also not constant for every pixel. Even the amplitude of the phase retardation has an effect, being more prominent for a higher amplitude than for a lower one.

In Fig. 6.16 the effects on the retrieved bunch lengths are shown. In the top, the bunch lengths retrieved from fits to the relative modulations are shown for the different original bunch lengths (depicted as black dotted lines). At first glance the fits to the relative modulations seem to produce a systematically shorter result than the width of the original profiles. At the bottom the width is shown relative to the original profile width. Here it

can be seen more clearly, how the effect depends on the different parameters. Whereas for an original width of 5 and 10 pixels, the shortening is about 5% and relatively constant over the whole pixel range (excluding pixels below 190 and above 300 which typically do not play a significant role, as for measurements a delay is chosen, so the centroid position lies roughly between pixels 210 and 280). For an original width of 20 or even 30 pixels, the shortening is more pronounced (but rather constant) for pixels up to 240, it then gradually decreases. The initial amplitude of the phase retardation seems to cause mostly a shift with a higher relative bunch length for lower amplitudes and a lower relative bunch length for higher amplitudes.

**A comparison with measurement data** for different time delays has been recorded and the results have been analyzed analogously to the generated profiles, the results are presented and discussed below. Figure 6.17 depicts the phase retardation and relative modulation profiles for three different measurements. The relative modulations are the actual measurements and the phase retardation data is computed from them with the above mentioned measured phase calibration coefficients. A full list of measurement parameters can be found in Tab. 6.1.

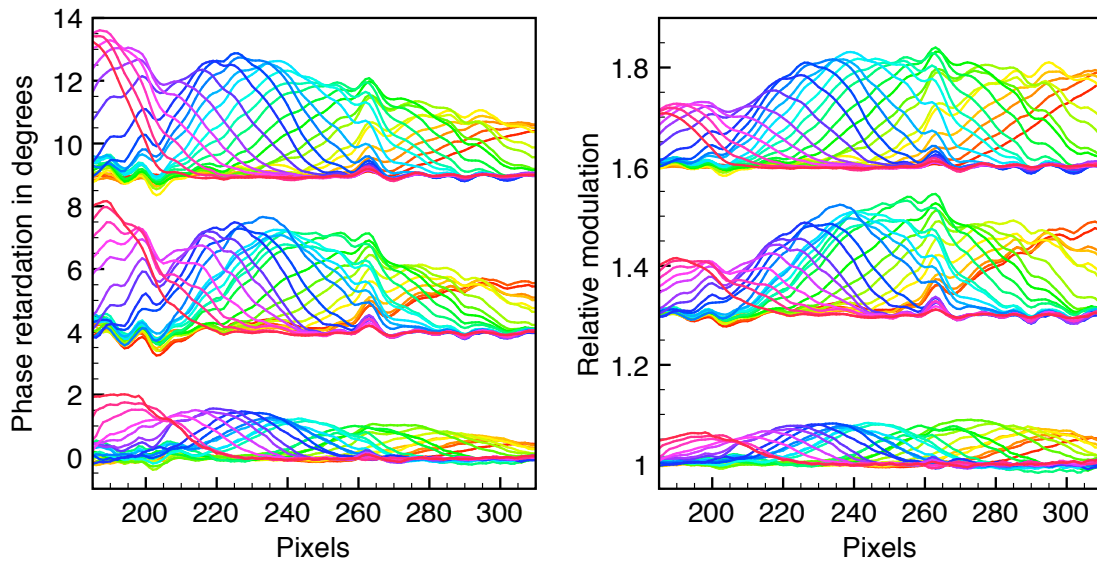


**Figure 6.17:** Phase retardation and relative modulation averaged profiles for three real measurements. Data 1 (top, 50 shot average) and 2 (middle, 20 shot average) were recorded right after each other (0.53 and 0.45 mA) and Data 3 (bottom, 20 shot average) about an hour later when the beam current had decayed to 0.16 mA. A comprehensive list of electron beam and measurement parameters can be found in Tab. 6.1. For better visibility the data sets are shifted in y-direction.

Like previously for the generated Gaussian profiles, Gaussian fits have been performed to both the phase retardation, and the relative modulation profiles and the parameters have been compared. Figure 6.18 shows in the top the centroid positions retrieved from fits to the relative modulation over the centroid positions from the fits to the phase retardation profiles. As expected a small shift is observed. The bottom of Fig. 6.18 shows the differential shift for the data (for a better comparison with the expected results from Fig.

6.15 some curves are shown again in grey). The expected shift can be clearly seen for the data sets. Data set 3 has a lower bunch length and here the shift is smaller than for data sets 1 and 2 which were recorded right after each other and show very similar results.

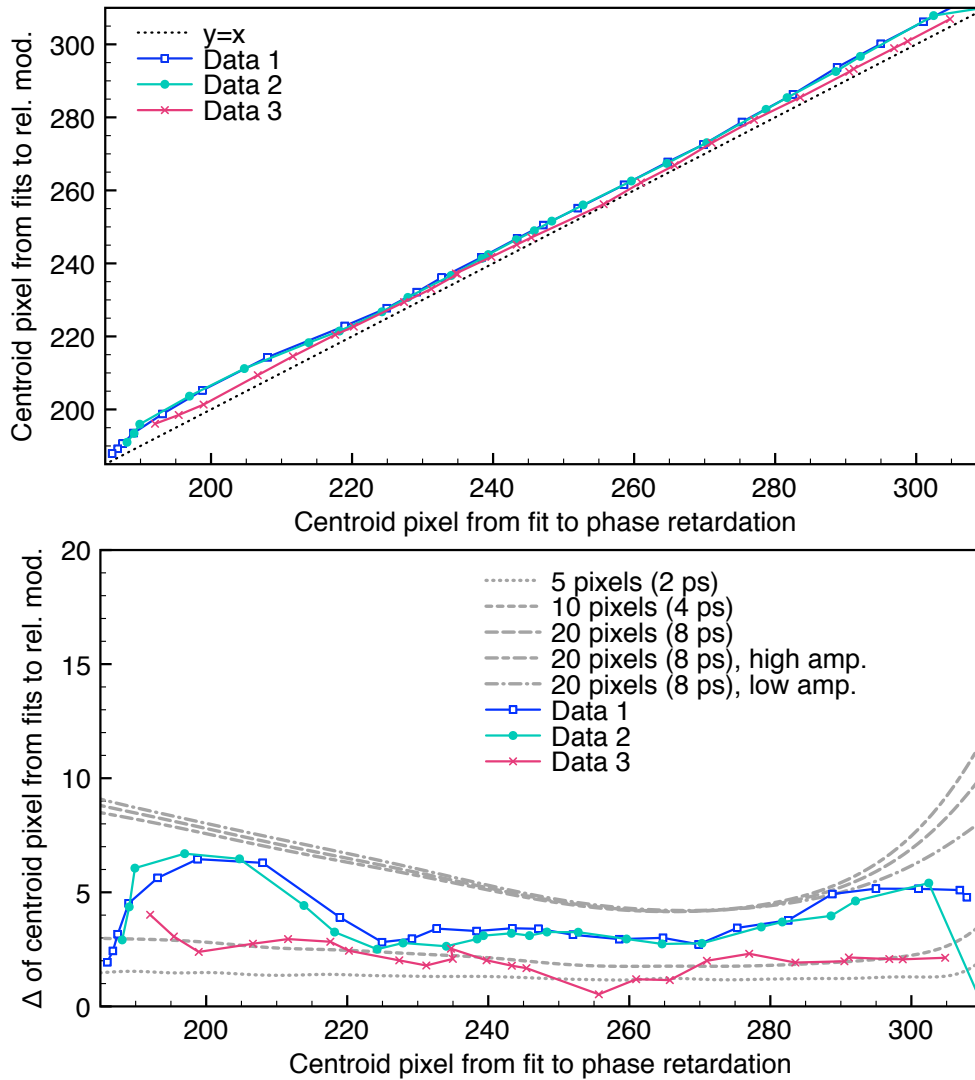
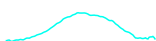


**Figure 6.18:** Analysis of the centroid positions of the relative modulation and phase retardation profiles from Fig. 6.17, Top: Comparison of the centroid position from fits to the relative modulation profiles over the centroid position from fits to the phase retardation profiles (lhs of Fig. 6.17). As expected from Fig. 6.15, the main effect seems to be a shift of the centroid position. Bottom: Difference of the centroid fitted to the relative modulations to the centroid fitted to the phase retardation profiles over the centroid from the phase retardation profiles. For better comparison, some results from Fig. 6.15 (bottom) are shown again.

When looking at the bunch lengths observed for the data sets from the relative modulation and phase retardation profiles, as it is done in the top of Fig. 6.19, one can easily see that there is another effect altering them, as the measured bunch length for the phase retardations is not constant for different centroid pixels. This effect is most likely caused by a mixture of nonlinearities in the phase of the laser pulse and an additional amplitude modulation from the wavelength dependence of the EO-effect and will be analyzed in more detail further down. For now, only the effect of the phase calibration is of interest. There-

fore, at the bottom of Fig. 6.19, the bunch length retrieved from the relative modulation profiles is shown relative to the one retrieved from the phase retardation profiles. For better comparison with the expected results, the results for the generated Gaussian profiles are also shown again in grey. The variations of relative bunch lengths for data sets 1 to 3 are roughly in the order of what is expected, however the larger dip around pixel 210-220 seems to be systematic. When looking back at the raw profiles in Fig. 6.17, one can see that all profiles show a dip around pixel 205. This can have two origins: Either that this part of the spectrum does not get modulated by the bypassing electron bunch as much as neighboring parts which could be explained by the fact that a certain percentage of photons from this part of the spectrum, do not pass the EO crystal at the same time as the others (bad spectral phase for this region). The second possible explanation would be that the laser spectrum has changed for this region since the unmodulated spectrum has been recorded. This then would not be a rapid fluctuation of the shape of the laser spectrum, but a more long term change (as this dip remains there for the whole measurement which takes about 7-8 minutes depending on the number of images that are recorded with a speed of roughly 7 Hz).

For the future one could think about recording more unmodulated spectra during long “normal” measurements by adapting the measurement script in a way that it changes the delay to the position for unmodulated spectra in regular time intervals and then continues with the actual measurement to see if the laser spectrum itself is changing.



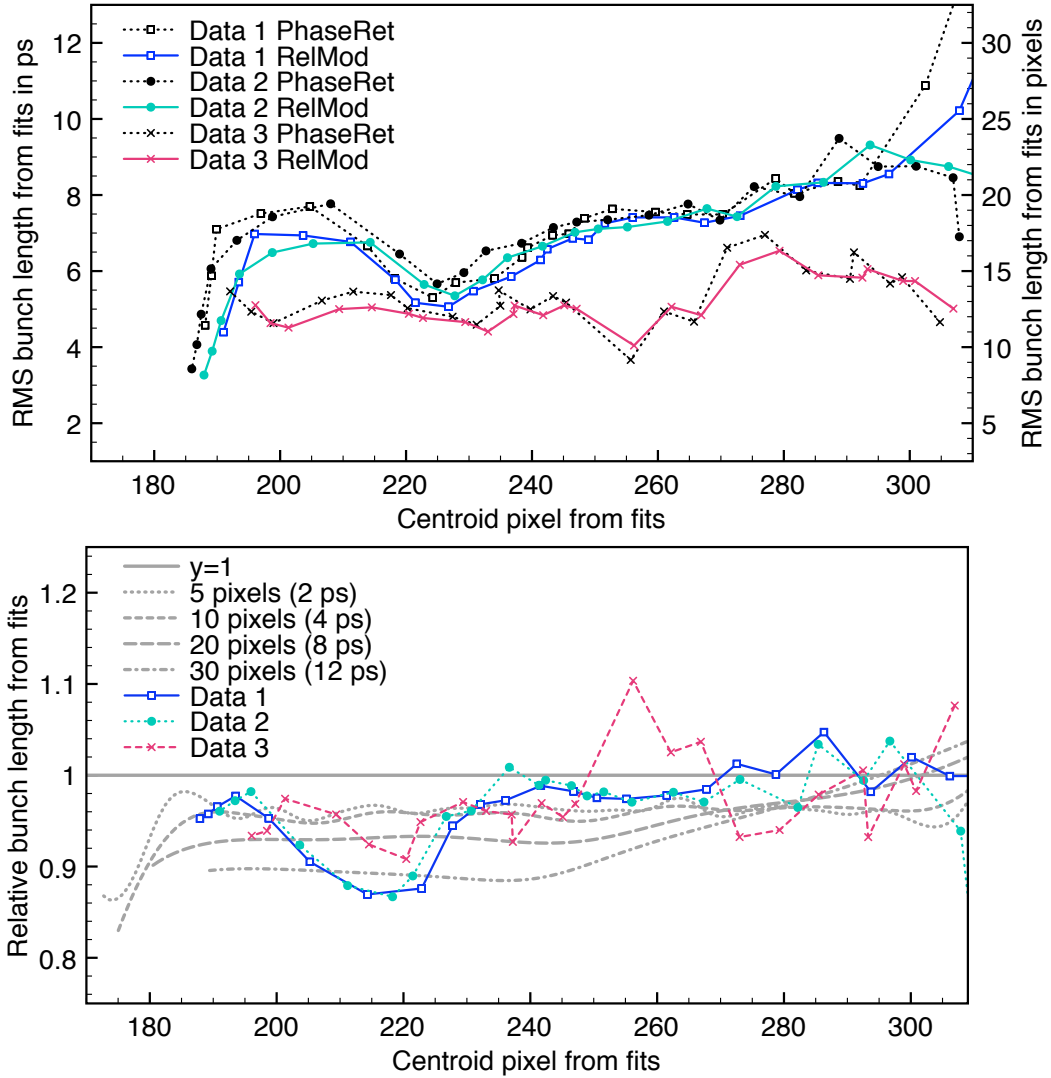


**Figure 6.19:** Fit results of for the bunch length of real data profiles. Data 1 and 2 were recorded right after each other (0.53 and 0.45 mA) and Data 3 about an hour later when the beam current had decayed to 0.16 mA. For a full list of measurement parameters, see Tab. 6.1. Top: Absolute bunch lengths retrieved to the fits for the relative modulations and phase retardations. The data already shows that another effect must be causing even larger shifts of the measured bunch length in dependence of the centroid pixel. Bottom: Bunch length from the fits to the relative modulations relative to the bunch length from the corresponding fits to the phase retardation. The X-axis shows the centroid pixels retrieved from the fits to the phase retardation.

The laser wave-length dependence of the EO effect is given by the following equation (see Ch. 3.3.1):

$$\Gamma = \frac{\omega d}{c} n^3 r_{41} E \quad (6.4)$$

Where  $\Gamma$  is the phase retardation,  $\omega$  the laser frequency (not repetition rate),  $c$  the speed of light,  $n$  the refractive index of the material (GaP in our case),  $r_{41}$  the electro-optical coefficient of the material and  $E$  the electric-field strength of the modulating field.

To get an estimate on the effects of this relation on the actual measurement, the simulation with Gaussian phase retardation profiles from Fig. 6.13 was adapted to include the wavelength dependency. As the pixel axis is not precisely calibrated to a wavelength axis, but the laser spectrum had been measured previously with a calibrated spectrometer to have a width of about 100 nm FWHM, this width and a center wavelength of 1050 nm have been assumed for the simulation. This leads to an increase of phase retardation by about 5% for the lowest pixel and a decrease by about 5% for the highest pixel. In Fig. 6.20 the modified and unmodified phase retardation and relative modulation profiles are shown. The effect of the wavelength dependence on the profiles is rather small and slightly counteracts the nonlinearity of the HWP which lets the relative modulation increase strongly for larger pixels. When analyzing the simulated profiles, no significant effect on the observed centroids and widths is observed hence the plots are not shown. If the absolute electric field strength is to be calculated, however, this effect can be taken into consideration to improve the results.

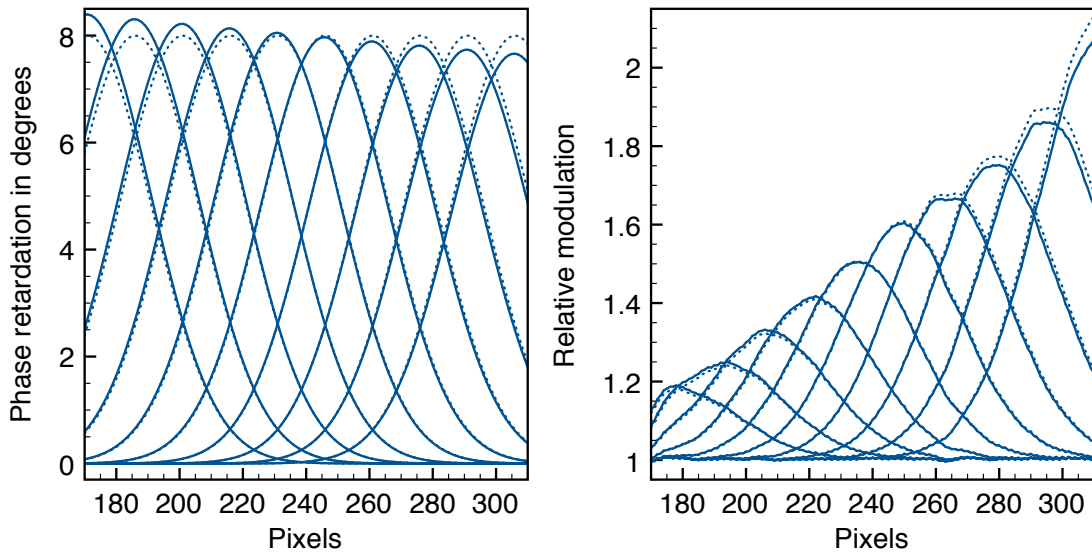


**Figure 6.20:** Left: Generated Gaussian shaped phase retardation for different delays. Dotted profiles:  $\sigma = 20$  pixels; solid profiles: same width, but the laser wavelength dependence of the phase retardation caused inside the EO crystal has been taken into account (assuming a center wavelength of 1050 nm and a total spectral width of 100 nm over the depicted pixel range, which leads to an amplitude change by +5% for the low pixel numbers and -5% for higher pixel numbers). Right: Relative modulation computed from the phase retardation data on the left with the calibration coefficients obtained from the fits shown in Fig. 6.13. It can be seen that the laser wavelength dependence of the phase retardation slightly mitigates the stronger effect of the nonlinearity of the wave plates.

Comparing those results to the amplitudes for real measurements like in Fig. 6.17, one easily sees that the decrease in amplitude over the pixel range seems to be larger for real data. Which had already been hinted in the discussion of Fig. 6.19 earlier on. Figure 6.21 shows the fit amplitudes for fits to the phase retardation profiles relative to the amplitudes around pixel 230 over the centroid position (also retrieved from those fits). Even though there are some variations for the different measurements, the general behavior seems to be the same for all 11 data sets: Between pixels 200 and 230 there is a small plateau of constant amplitude and when ignoring this region the expected nearly linear behavior is observed. A polynomial fit of ninth degrees has been added to guide the eye.

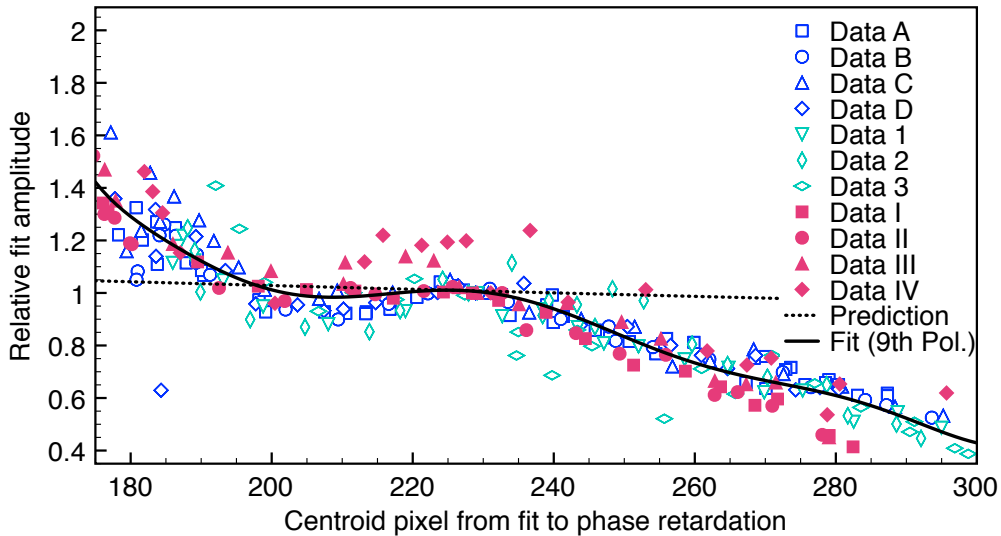


**Figure 6.21:** Amplitude of the fits to the phase retardation profiles over the centroid pixel (also obtained from the fits). The amplitude is shown relative to the value for pixel 230 for the different data sets. A list of all laser and measurement parameters for the different data sets can be found in Tab. 6.1. The drop in amplitude seems to be mostly independent of laser and beam parameters, but is stronger than predicted from the laser wavelength (see dashed line corresponding to data in Fig. 6.20). A plateau can be seen between pixels 200 and 230 for all data sets, ignoring these areas the behavior is rather linear as expected from theory.

Further simulations have then been performed modulating the amplitude of the Gaussian phase retardation profiles with the polynomial fit of ninth degree from Fig. 6.21, to see if this effect can explain the change in measured bunch length. Figure 6.22 shows the simulated Gaussian phase retardation profiles (width 20 pixels) with the new amplitude modulation. They now look more like the ones from the real measurement shown in the left of Fig. 6.17, but because the dip in the measured profiles around pixel 205 is much shorter than the length of the profiles, it cannot be reproduced with this approach. At the bottom of Fig. 6.22 the results of the fits to retrieve the bunch length are shown relative to the expected width from the Gaussian distributions. To see the influence of the profile width more clearly, an additional simulation set for a smaller width with just 10 pixels has also been added. For a shorter width the effect is not as pronounced and only affects the

measured bunch lengths in the order of  $\pm 2\%$  in the region of interest<sup>5</sup>, for a pulse width of 20 pixels, the effect increases up to  $\pm 5\%$  around the center region.

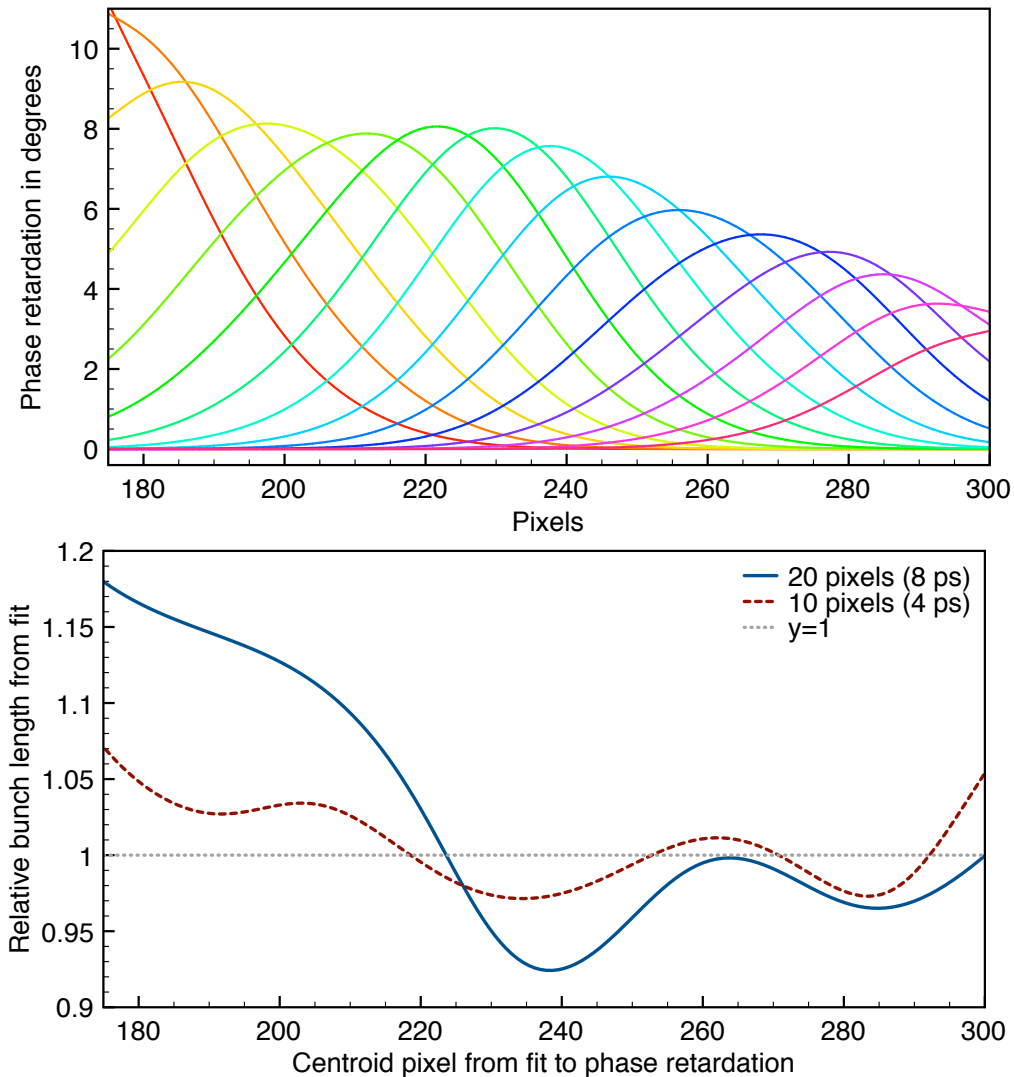


**Figure 6.22:** Top: Simulated Gaussian phase retardation profiles for different delays with a width of 20 pixels which have been amplitude modulated by the polynomial fit shown in Fig. 6.21. Bottom: Bunch length relative to the initial width of the Gaussian profiles for the above shown profiles and also for profiles with a reduced width of 10 pixels. For a shorter width the effect is not as pronounced and only affects the measured bunch lengths in the order of  $\pm 2\%$  in the region of interest, for a pulse width of 20 pixels, the effect increases up to  $\pm 5\%$  around the center region.

These simulation results are then compared with data sets from different time calibration measurements which are shown in Fig. 6.23. In the top the absolute bunch lengths are shown over the centroid pixels (one should keep in mind that for Data I-IV the laser pulses were shorter because of a different setting of the grating compressor). At the bottom, the bunch length is shown relative to the one around pixel 230. For better comparison the simulation results from the bottom of Fig. 6.22 are shown again. The change in bunch length of the real data is stronger than expected from the simulations (about 10-15% for

<sup>5</sup>For normal bunch length measurements, the centroid is chosen to lie between pixels 220 to 260.



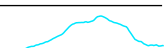
pixel 220 and then increasing to +15% for pixel 260 with even larger changes for data sets 3 and IV which were recorded at very low currents). While the agreement for the different data sets is rather good between pixels 200 to 300, the large discrepancy for pixel numbers below 200 is most likely not very significant because a very large part of the profiles lies outside of the analysis range and cannot be represented by the fit adequately. As for typical measurements a range is chosen, so that the centroid of the bunch profiles lies above pixel 220, ideally between pixels 240 and 260.

Figure 6.23 gives rise to the assumption that the amplitude modulation alone does not explain the change in measured bunch length for different centroid pixels to its full extent. A possible explanation could lie within the phase of the laser pulse: If the relation between time and spectrum within the laser pulse is not linear, but has some inhomogeneities. This could, for example, be that some wavelength components are smeared out over a longer temporal range inside the laser pulse, so for certain areas in the laser spectrum, the relative modulation would not be continuous. When thinking back to Fig. 6.17, where the phase retardation profiles were shown for different delays, there was a dip visible around Pixel 205, which could shorten the results of Gaussian fits to the profiles. Further studies will be required in the future to see if this effect can be minimized by adjusting certain laser settings.

As this effect is not fully understood at the moment, any correlations between arrival time of the bunches, which might hold interesting beam dynamics information, and the bunch length should be carefully compared to time calibration measurements before drawing any conclusions.

For the evaluation of those systematic studies, averaged bunch profiles have been used. The averaging of the different profiles for one delay was done directly without the correction of any arrival time fluctuations. When just the mean arrival time is of interest, this is perfectly fine, but the measured bunch length will be slightly longer than the average of the single measurements due to fluctuation in arrival times of the different profiles which are being averaged. Figure 6.24 illustrates this effect by showing the fit results for the bunch lengths of the single profiles and the averaged profiles. The overall trend of the change in bunch length shows for the averaged and the single profiles equally.

For completeness, Fig. B.3 in the Appendix B on p. 151 shows all correlations between different fit parameters.



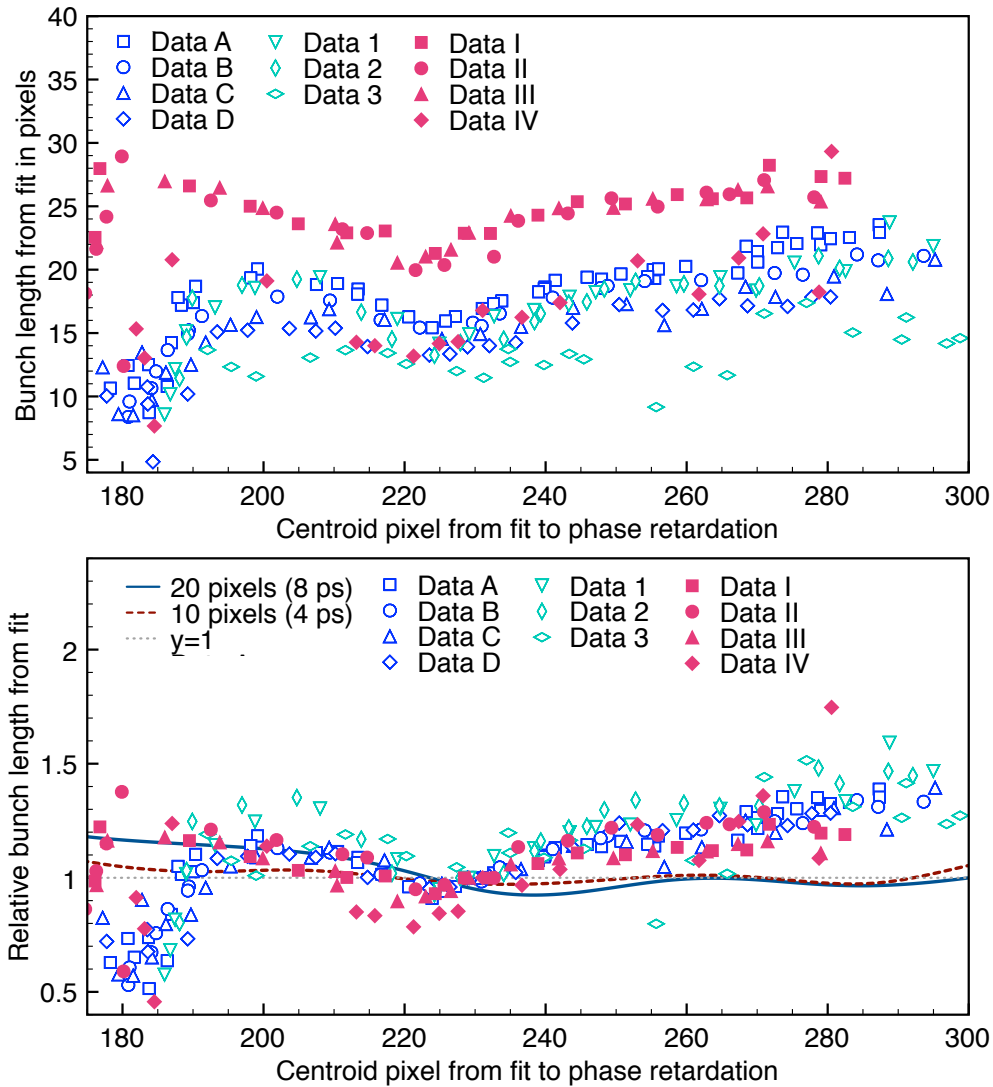


**Figure 6.23:** Top: RMS bunch lengths retrieved from fits to the averaged phase retardation profiles in dependence of centroid pixel (also determined by fits) for different data sets. See Tab. 6.1 for a detailed list of measurement parameters. Bottom: Bunch lengths relative to the lengths around a centroid pixel of 230 shown for the same data sets. In addition to that the curves from the bottom of Fig. 6.22 are shown again as comparison. The observed change in measured bunch length cannot be fully explained by the amplitude modulation.

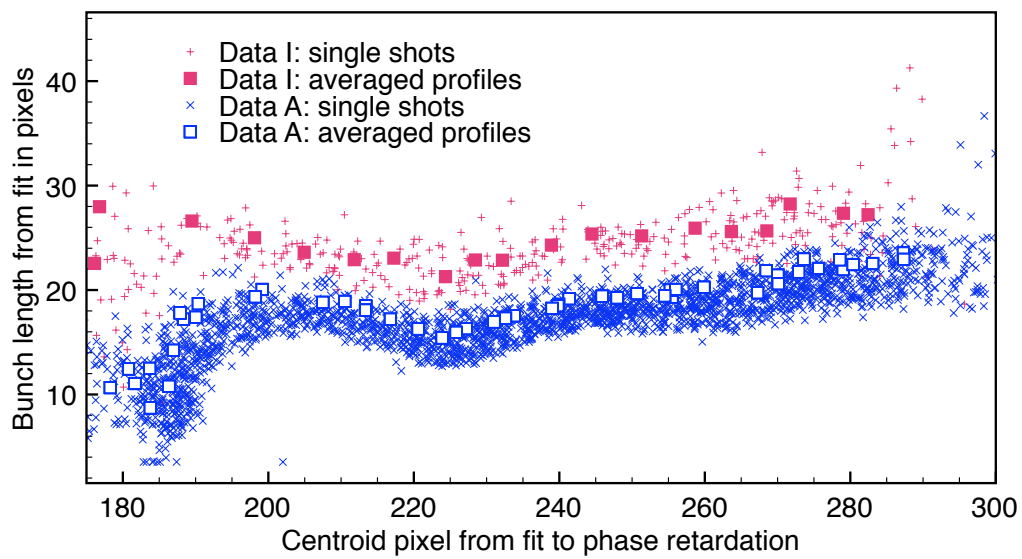


**Figure 6.24:** Scatter plot showing the bunch length retrieved from the fits to phase retardation profiles in dependence of the centroid pixel (also retrieved from the fits) for single shots and the averaged profiles from Data set I and A. It can be seen easily that the results for the bunch length from the averaged profiles lie slightly above the average of the single shots which are not broadened by time of arrival fluctuations.

### 6.2.3.3 Time calibration

Time calibration measurements are required to convert the pixel axis into a time axis. For this, the delay of the laser pulses is changed by moving a certain amount of steps with the VM and measuring the change in centroid pixel position of the phase retardation. A sketch to illustrate the whole measurement and calibration process is shown in Fig. 6.25.

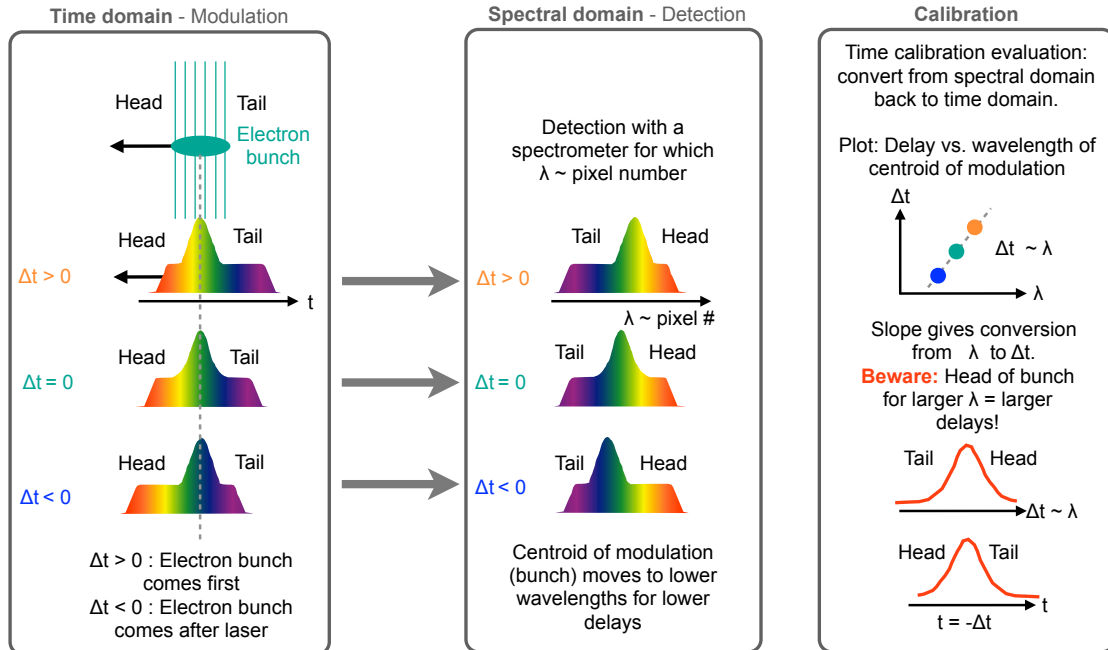


**Figure 6.25:** Illustration of the time calibration measurement. The left block shows what is happening in the time domain for 3 selected delays. The electron bunch modulates the laser pulse in the time domain. For larger delays ( $\Delta t > 0$ ), the arrival time of the laser pulse is slightly later than that of the electron bunch, for lower delays, the laser arrives earlier than the bunch. The block in the middle shows the spectral detection of the bunch profiles for the different delays. Here it can be seen that the centroid of the modulation (bunchprofile) moves towards lower wavelengths for lower delays, while the head of the bunch is always at higher wavelengths than the centroid. The block to the right shows the data processing which is required to convert from the spectral domain (wavelength axis) into the time domain (time axis). For this, the delay is plotted versus the wavelength of the centroid of the modulation and a fit to this gives the relation between  $\Delta t$  and  $\lambda$ . With this relation, the wavelength axis is converted into a delay time axis, this however leaves the head of the bunch at larger delays, so the delay axis needs to have its sign inverted to turn it into a time axis for the bunchprofile.

As it was illustrated in Fig. 6.25, the bunch orientation within the laser spectrum is such that the delay axis needs to have its sign inverted to become a time axis, which might seem a bit counter-intuitive because for the EOS scans discussed in Section 6.1, a larger delay really meant that we were looking at what is happening at later times.

With EOS we are taking snapshots of the bunch profile and its trailing wake-fields at certain times relative to the bunch, but with EOSD we have a fixed time window with a fixed bunch orientation within it and we can only change the time relative to the bunch at

which our time window starts, but the orientation of the time axis within our time window always stays the same.

Lets imagine we are doing an EOS scan in one direction of time, e. g. we start at a large delay this means that the laser comes a long time after the electron bunch, so while we decrease the delay we will first see all the trailing wake-fields, then the tail of the bunch and then the head of the bunch. Now imagine we are reversing the direction of the scan, starting at smaller delays, we would first see the head of the bunch, then the center of the bunch, then the tail and then the trailing wake-fields and so on. Doing the same with EOSD would of course have the same effect, but not alter the fact that within our EOSD time window, we always see the head of the bunch first, as we cannot reverse the time axis, the laser pulse is dictating us, we can only change its delay.

Figure 6.26 shows the averaged phase retardations recorded during such a time calibration measurement.

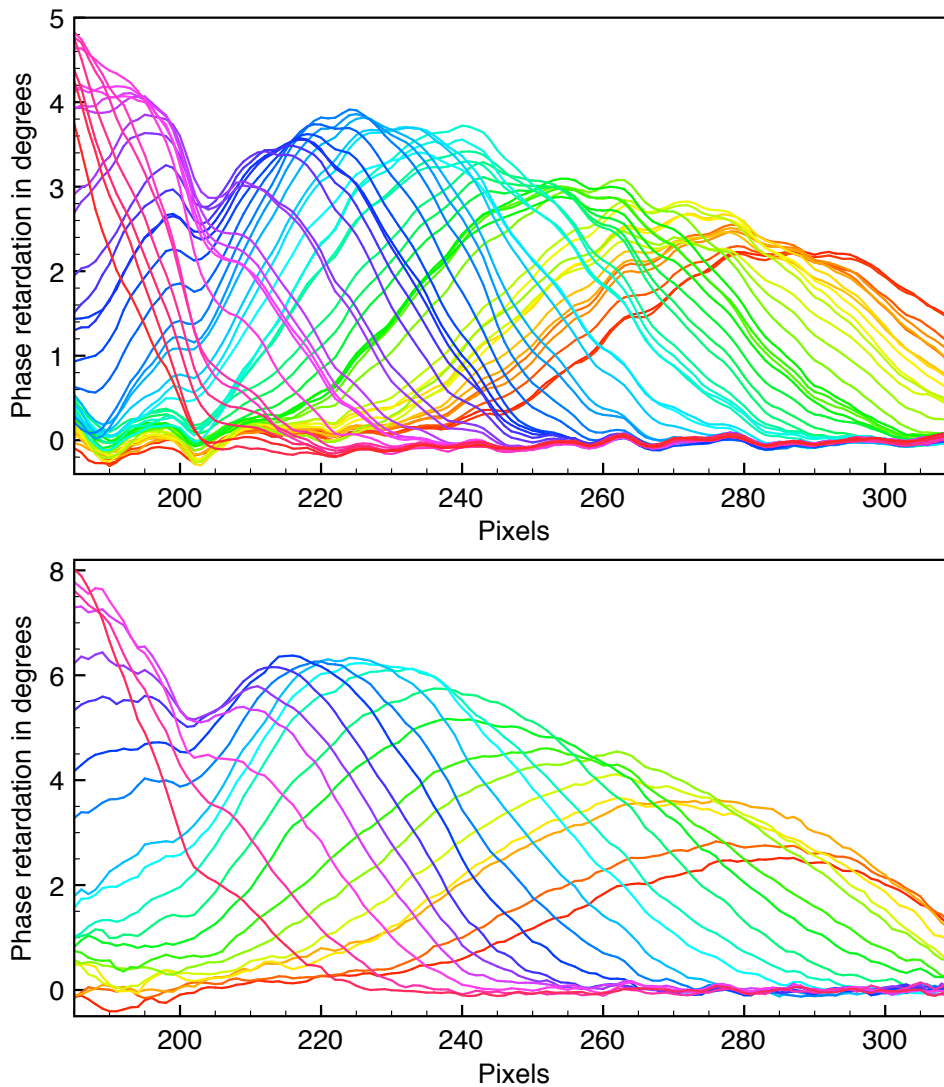


**Figure 6.26:** Showing averaged phase retardation profiles (Top: 50 shot average, Bottom: 20 shot average) for different time delays recorded during two different time calibration measurements with different laser pulse lengths (Top: Data A with slightly longer laser pulses and a current of 0.6 mA, Bottom: Data I with shorter laser pulses and a current of 0.96 mA, see Tab. 6.1 for a detailed list of parameters).

The centroid position is then retrieved by Gaussian fits. For the data sets in Fig. 6.26 it can be seen that the region around pixel 200-205 does not seem to get modulated as much as the remaining pixels leading to a dip in the profiles. Thinking back to Fig. 6.7 where a dip in the standard deviation of the spectral fluctuations was observed at exactly this region, it is best to avoid this region for bunch profile measurements. So for normal EOSD measurements, the signal is shifted in time, so it starts after pixel 210.

For the evaluation of the time calibration measurement, the known time delay<sup>6</sup> introduced by the VM is plotted versus the centroid positions from the Gaussian fits and a linear fit is done to the data to achieve the conversion from pixel number to delay time. The slope is the main parameter which we want to extract from this, the offset is rather arbitrary because it depends on the starting delay and definitely changes when the laser needs to be resynchronized to the RF clock. Figure 6.27 shows the results of several such time calibration measurements. A detailed list of beam and measurement parameters can be found in Tab. 6.1. In the top, Data A to D are shown for Fill 4623. All four data sets have been recorded with short breaks in between during which normal measurements have been performed. All measurements were done with heavy averaging of the profiles (50-100 shots), so one measurement took in the order of 6 - 7 minutes. The slopes seem to fluctuate quite a bit from measurement to measurement, leading to an average slope of  $(0.396 \pm 0.029)$  ps/pixel with a standard deviation for the slope of about 7%. Giving a total time window of about 45 ps over the pixel range from 180 to 300. This could be caused by fluctuations of the water loop cooling ANKA's RF cavities (which has a period length in the order of 5 minutes), rather than fluctuations of the laser system itself, which generally runs very stable due to the phase lock to the RF clock, which had already been shown at PSI to achieve a very high accuracy (p. 82 in [27]). More information on any machine drifts which can be observed with the EOSD measurements can be found later on in Chapter 7.4 where we used EOSD as arrival time monitor.

In the middle plot Data 1 to 3 are shown which have been recorded about two months later with the same laser settings (ANKA was tuned to a slightly lower bunch compression setting). Data 1 and 2 have been recorded right after each other and Data 3 about an hour later for a very low beam current leading to a very weak signal. For every data point the average profile over 50 consecutive shots was taken. The averaged value for the slope of  $(0.384 \pm 0.03)$  ps/pixel which agrees very well to the previously obtained results.

For Data sets I to IV, the laser compressor was moved to 25 mm which decreased the laser pulse length further to increase the temporal resolution of the measurement (unfortunately this will also decrease the time window). The ANKA machine settings are equal to the ones for Data sets A to D. For Data sets I to III the bunch current was quite high with 0.96 to 0.87 mA. Because the problem of machine drifts influencing the measurement had already been seen on previous fills, for those measurements the approach for time calibration measurements was slightly different. Instead of averaging heavily and taking many data points for only slightly different delays, the averaging was cut down 20 shots per profile and the time delay step size was slightly increased thus cutting down the acquisition time for a whole measurement to 65 s (from previously about 6 - 7 minutes). The average

---

<sup>6</sup>A larger delay means the laser arrives at a larger later delay with respect to the electron bunch.

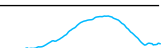


slope for those four measurements decreased to  $(0.330 \pm 0.009)$  ps/pixel. The general decrease in slope of about 15 % comes from the different laser compressor setting making the laser pulses shorter, this also narrows down the overall time window to a bit less than 40 ps. What should also be noted is the fact that the standard deviation of the slope value decreased from previously 7 % to just under 3 %.

For the future it is planned to investigate a more complex algorithm for changing the time delay to always have a reference measurement with “zero-delay” between steps rather than just moving in one direction, which would then allow for higher averaging without the downside of machine drifts due to the long acquisition time of the whole measurement.

**Table 6.1:** Electron beam and measurement parameters for the different data sets shown in various plots throughout this chapter

2013-04-11 Fill 4623:			
$f_s = 7.7$ kHz; bunch compression: 27k steps; $V_{RF} = 450$ kV / cavity			
laser compressor: 15 mm; HWP angle = $4.6^\circ$			
Data set	Time	bunch current in mA (bunch charge in pC)	# of shots per average
A	22:01	0.60 (222)	50
B	22:11	0.47 (174)	100
C	22:33	0.31 (115)	100
D	22:44	0.26 (96)	100
2013-06-07 Fill 4708:			
$f_s = 9.1$ kHz; bunch compression: 26k steps; $V_{RF} = 450$ kV / cavity			
laser compressor: 15 mm; HWP angle = $4.6^\circ$			
Data set	Time	bunch current in mA (bunch charge in pC)	# of shots per average
1	3:20	0.56 (207)	50
2	3:28	0.45 (167)	50
3	4:30	0.16 (59)	50
2013-05-08 Fill 4666:			
$f_s = 7.5$ kHz; bunch compression: 27k steps; $V_{RF} = 450$ kV / cavity			
laser compressor: 25 mm; HWP angle = $4.6^\circ$			
Data set	Time	bunch current in mA (bunch charge in pC)	# of shots per average
I	13:22	0.96 (355)	20
II	13:24	0.91 (337)	20
III	13:25	0.87 (322)	20
IV	14:18	0.29 (107)	20



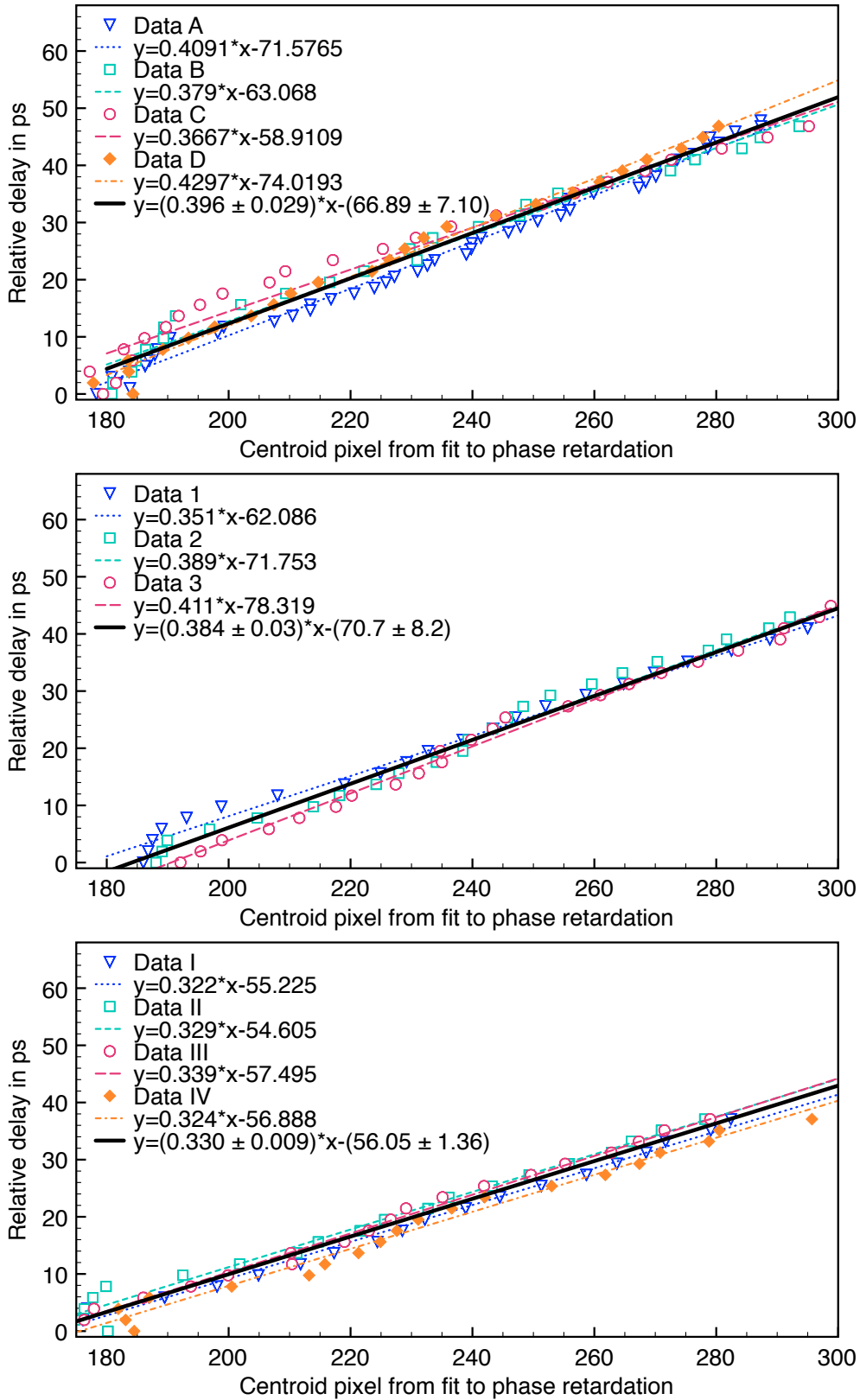


**Figure 6.27:** Comparison of different time calibration measurements. Top and Middle were recorded for the same laser settings but during different fills. Bottom has been recorded during a third fill, but also with shorter laser pulses to increase the resolution by about 15%. A detailed list of beam and laser parameters can be found in Tab. 6.1. The dashed lines are fits to a single data set and the solid black lines are calculated from the average of the slopes and offsets from the single fits with the standard deviations shown as uncertainties. See text for more details.



### 6.2.4 Resolution and Sensitivity of EOSD Measurements

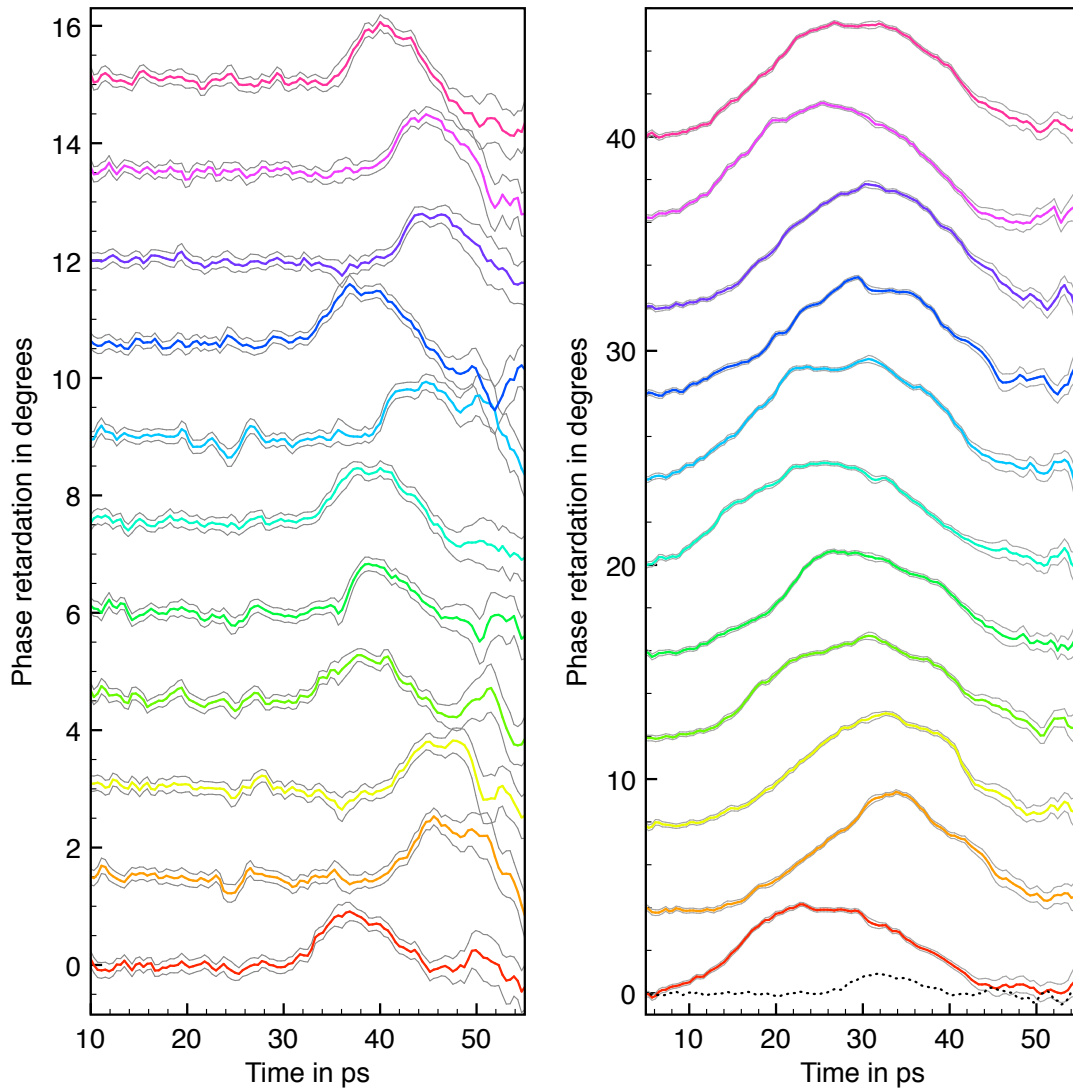
The resolution and sensitivity of the EOSD setup are of key interest when comparing the technique with other longitudinal bunch profile measurement techniques such as the SC setup at ANKA. With the above mentioned calibration measurements the raw measurement data of relative modulation as function of pixel can be turned into phase retardation as function of time allowing for single-shot measurements of the longitudinal bunch profile with a resolution as low as 0.330 ps/pixel and a point spread function of 9 pixels FWHM which equals 3.0 ps FWHM (1.3 ps RMS) for the settings with the shortest laser pulses (see Fig. 5.15).

The point spread function (PSF) gives a measure of the time scales of single structures which can be resolved. For example, if we assume a Gaussian electron bunch of length  $\sigma_{bunch} = 5.0$  ps and an also Gaussian point spread function of  $\sigma_{PSF} = 1.3$  ps, then we would measure a bunch profile that is the convolution of the two profiles. In the case of Gaussians, this simplifies to  $\sigma_{meas} = \sqrt{\sigma_{bunch}^2 + \sigma_{PSF}^2} = 5.17$  ps, if we would now measure the length of a bunch which is 5.5 ps long, we would obtain 5.65 ps. Because the difference between the two measured results is greater than our resolution of 0.4 ps, we would be able to resolve the fact that the second bunch is longer than the first one.

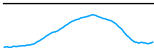
The setup is sensitive enough to measure down to bunch charges in the range of 28 pC (0.08 mA) and an example for single shot bunch profiles recorded at such a low charge can be seen in the left of Fig. 6.28. For higher bunch charges, some single-shot EOSD profiles are depicted in the right of Fig. 6.28. Those profiles were then compared with very good agreement to the averaged result, the SC yields which is shown in Fig. 6.29 for single-shot profiles and profiles for single images from the SC and the corresponding averaged profiles are compared in Fig. 6.30. While the overall agreement between the profiles is good, some systematic differences are visible, especially when comparing the averaged profiles. The SC profiles lean more to the front (towards the head of the bunch), as we would expect, while the EOSD profile does not show this behavior.

It was depicted in Fig. 5.11 on p. 57 that with the compact geometry of the EO-Monitor, the laser pulse is sent towards the EO crystal where it is reflected at the backside of the crystal. This means that the laser pulse will first counter-propagate with the electron bunch and then after its reflexion it will co-propagate with the bunch. When the laser pulses are stretched greatly, it can happen that the electric-field will modulate not only the head of the laser pulse which is already on its way back to the prism, but also the tail of the laser pulse which is still on its way to the reflective backside of the crystal. This will lead to a slight signal distortion. Brief simulations for our laser and electron beam parameters have been carried out with an EO simulation code written by B. Steffen to see if this effect would distort our measured profiles significantly [79]. Figure 6.31 shows the result of such a simulation: While the head of the signal does not undergo significant alterations, the tail of the measured phase retardation profile is expected to stay at a slightly heightened baseline. The simulated EOSD response is compared to an averaged measured EOSD signal and the agreement is rather good, also hinting a slight increase in baseline after the bunch.





**Figure 6.28:** Single-shot EOSD measurements. For all data sets: The head of the bunch is in the left (for lower times). Left: Showing 11 single shot EOSD measurements for a very low bunch current of just 0.08 mA (28 pC). For better visibility, the different profiles have been shifted in y-direction. Their average bunch length was found to be  $(3.31 \pm 0.45 \pm 0.24)$  ps (RMS) with the first uncertainty coming from the statistical fluctuations of fits to the 11 shots and the second uncertainty coming from the fluctuation of the time calibration measurements for this fill. The measurement was recorded during Fill 4623 (see Tab. 6.1 for measurement parameters). Right: Measurement recorded during the same fill but for a higher bunch current of 1.13 mA (418 pC), for better comparison of the total amplitude one curve from the lhs is shown again with a dotted line. The 11 shots have a bunch length of  $(9.11 \pm 0.57 \pm 0.24)$  ps.



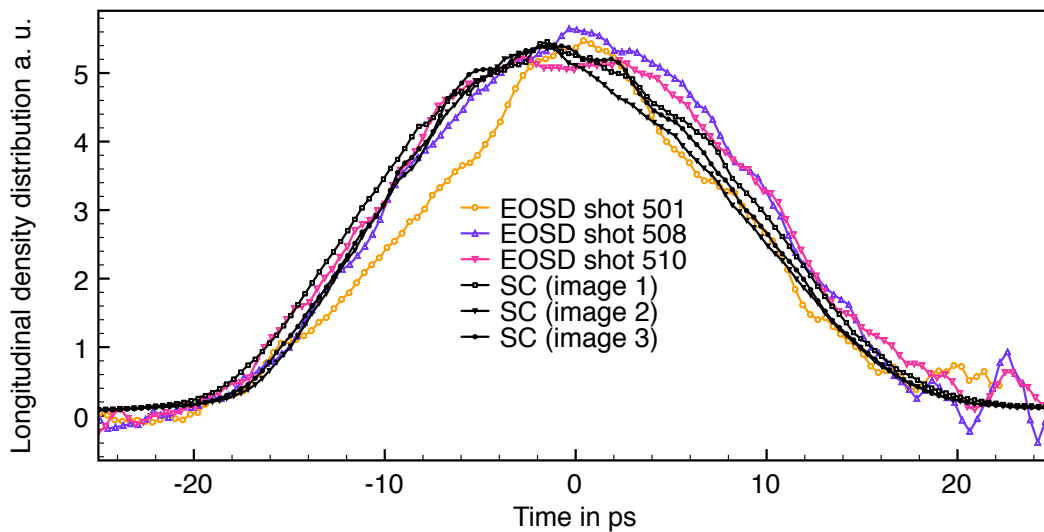


**Figure 6.29:** Three of the single shot EOSD profiles from the right of Fig. 6.28 compared to 3 profiles of single images of the SC (1 image covers a time of 1 ms). The SC profiles have been scaled in Y-direction to match the amplitude of the EOSD profiles which in turn have been aligned (not scaled) in X-direction. For better visibility, the error bands are not shown.

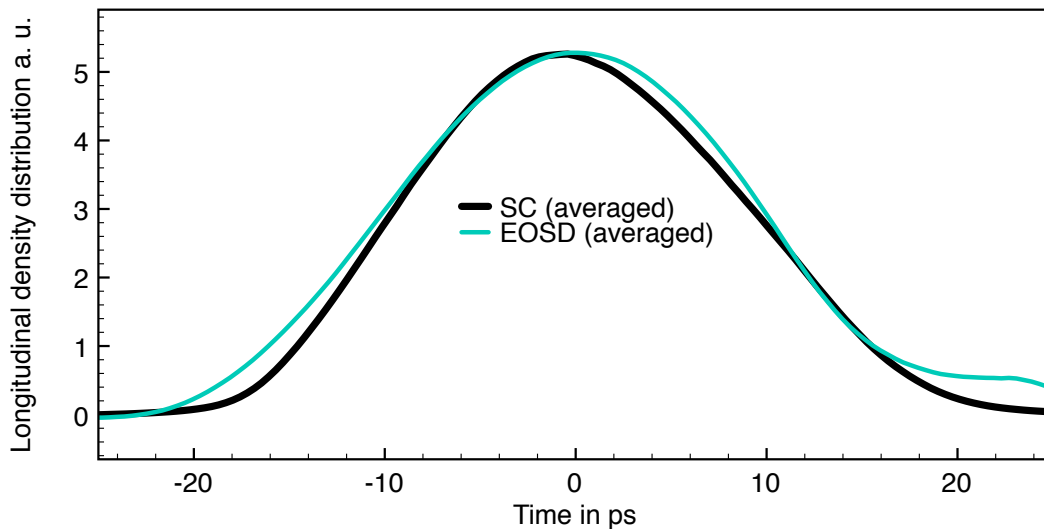


**Figure 6.30:** Comparing an arrival time corrected averaged EOSD profile (averaged over all 1000 shots) compared to an averaged profile (averaged over 100 images, each spanning 1 ms) recorded with the SC at the same time. The SC profile has been scaled in Y-direction to match the amplitude of the EOSD profile which in turn has been aligned (not scaled) in X-direction. For better visibility, the error bands are not shown. The averaged profiles seem to have slight systematic differences, the SC profile leans forward more than the averaged EOSD profile.

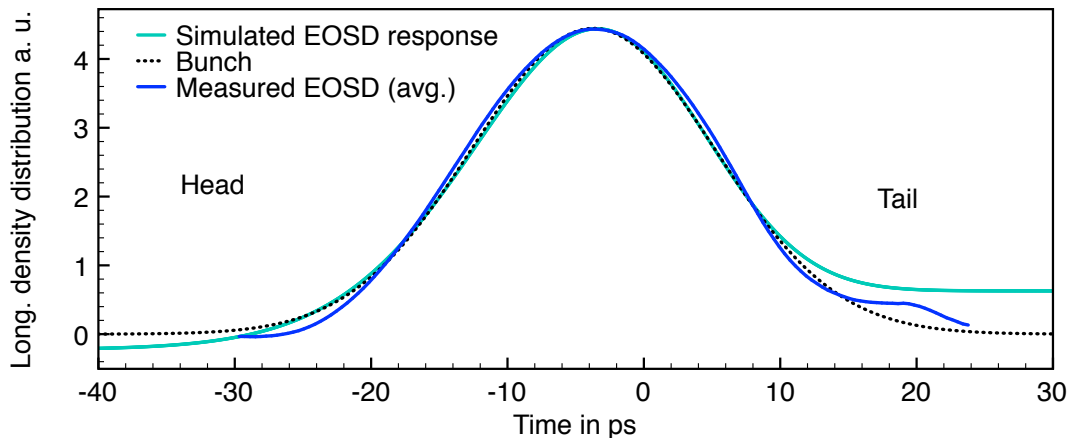


**Figure 6.31:** Comparison of the measured EOSD signal (averaged signal from Fig. 6.29) with the simulated response to a Gaussian electron bunch with a length of 8.9 ps RMS. The slight decrease in baseline before the bunch and the plateau behind the bunch are caused by the fact that the laser first counter-propagates (with respect to the electron bunch) inside the the EO crystal and is then reflected at the back surface, to co-propagate with the electron bunch. Especially the tail of the laser pulse is affected by this, because during its counter-propagation through the crystal, the electron bunch will have traveled far enough to modulate it. The curves have been scaled in y-direction to have the same amplitude for better comparison. Simulation code courtesy of B. Steffen [79].

The fact that for lower pixel numbers even small changes in relative modulation lead to a significant phase retardation has the result that noise for pixels below pixel number 220 gets amplified more by the conversion. This effect is not very desirable for measurements. Thinking back to the background studies shown in Fig. 6.8, the Figure 6.32 shows two sets of averaged phase retardation backgrounds and their standard deviations (both as error bars and separately on the second y-axis). When searching for the expected substructure on electron bunches, this noise level should be kept in mind, so especially any peaks for pixels below 220 will most likely be noise whereas for higher pixel numbers, the standard deviations decrease to values around 0.1 to 0.2°.

To give an indication of this noise level, all plots showing single-shot EOSD profiles have  $1\sigma$  error bands drawn. The error bands are computed by measuring the standard deviations of the relative modulations (background fluctuation measurements like the ones shown in Fig. 6.32) and then adding and subtracting them to the data before the phase retardation is computed.

For the future it is planned to exchange the wave plates for the setup by very broadband, high quality ones to remove the strong wavelength dependence, the current wave plates introduce.

It was already shown in Section 6.2.3.2.2 that the measured bunch length from EOSD seems to depend slightly upon the position of the centroid pixel of the measured signal. When comparing the measured bunch lengths to those measured by the SC, we observe a slight systematic off-set shown in Fig. 6.33. If the centroid is at larger pixels, we tend to measure slightly longer than the SC, for a centroid position around pixel 240, the agree-

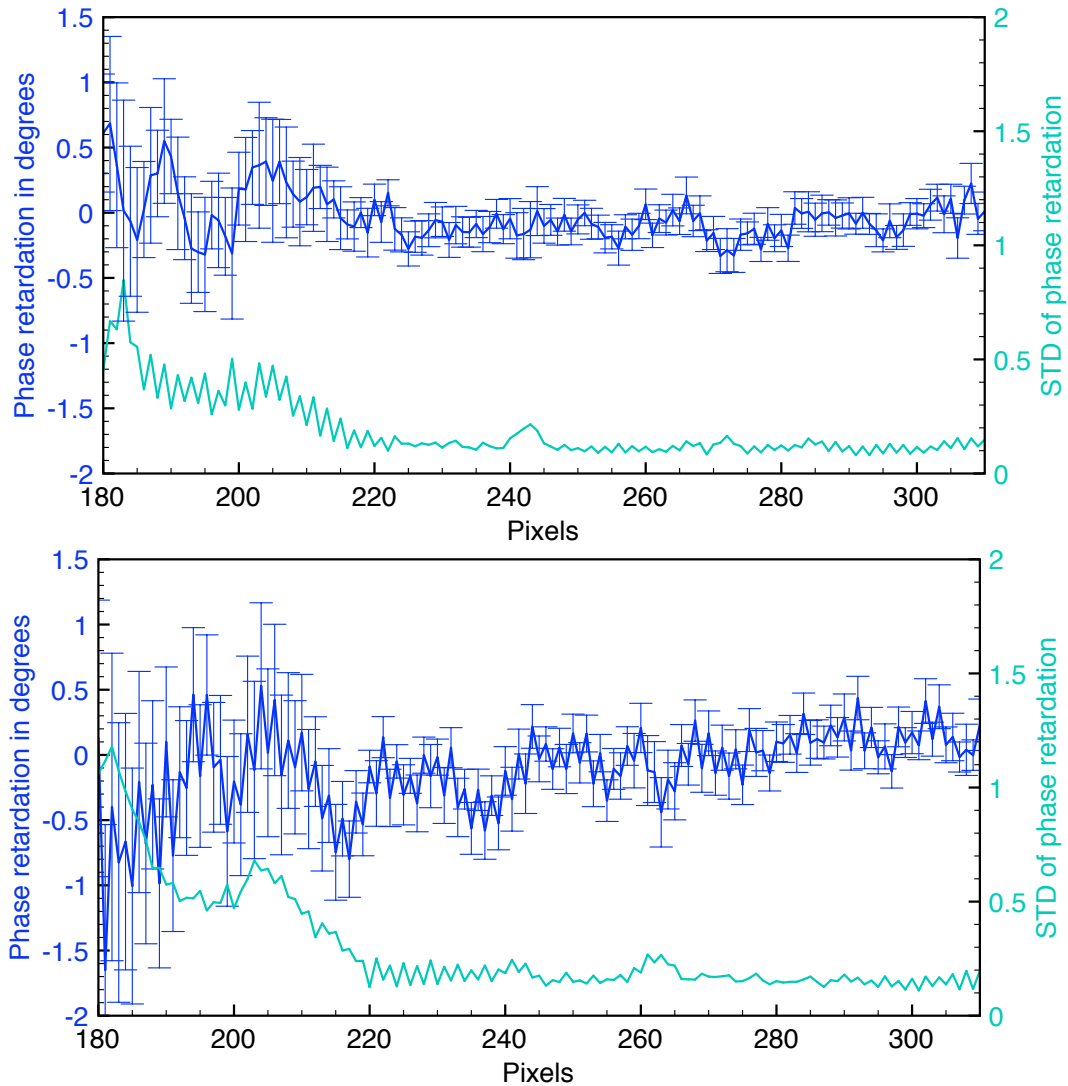


**Figure 6.32:** Showing two sets of averaged phase retardation backgrounds and their standard deviations (both as error bars and separately on the second y-axis) Top: The same measurements for which the relative modulation was shown at the bottom of Fig. 6.8 (2013-04-11 Fill 4623). Bottom: Data from measurements during another fill (2013-06-07 Fill 4708).

ment between the measurements is best. Figure 6.34 shows again the measured bunch length dependence with relation to the centroid pixel. The exact cause of this effect is currently not fully understood. Because it has not been observed at PSI, where measurements with the same setup - with better wave plates - have been carried out [27], we hope to decrease it with an upgrade of our wave plates.

The resolution of the EOSD measurements can be increased further if the laser pulses were to be compressed more. The easiest way for this will be to decrease the length of the fiber leading the amplified laser pulses to the EO-Monitor, currently its length is 35 m, but 25 m would also be sufficient to cover the distance and decrease the fiber length by nearly 30%<sup>7</sup>. With this, the time delay per pixel could be decreased further, this should,

<sup>7</sup>In first approximation the dispersion introduced by a glass fiber is  $200 \text{ fs}^2/\text{cm}$

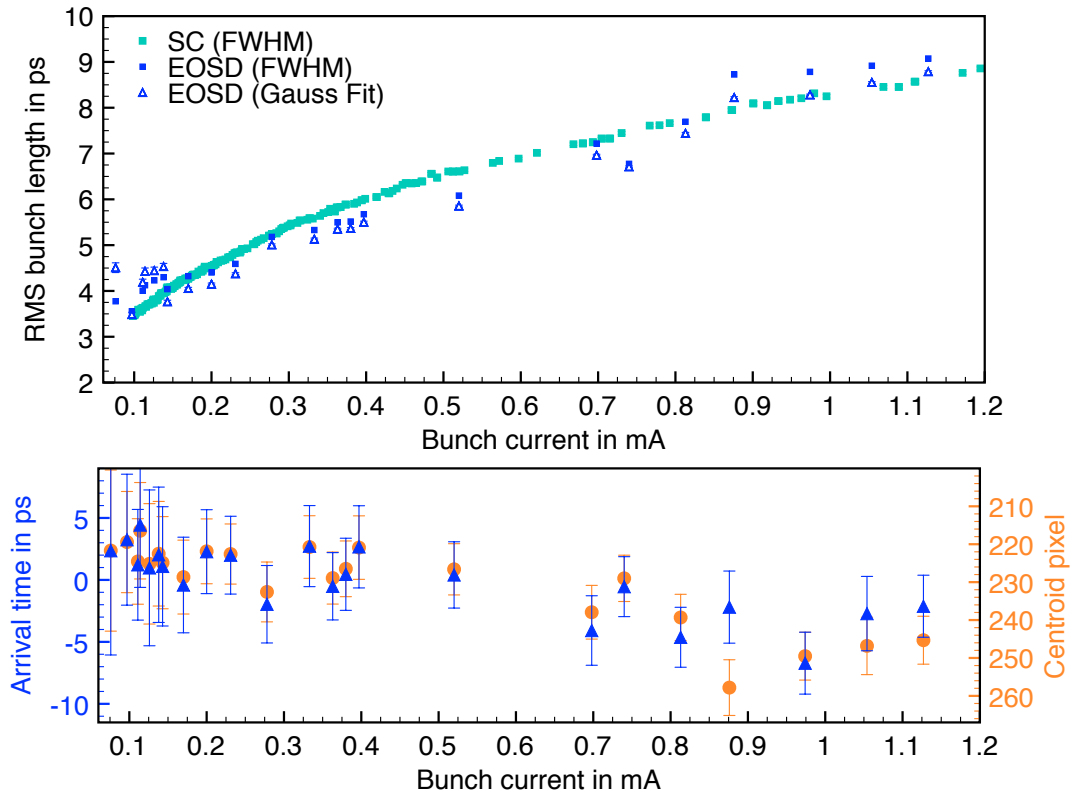


**Figure 6.33:** Top: Showing the RMS bunch length for different currents during Fill 4623 (see Tab. 6.1 for more beam parameters) recorded with the SC and EOSD. While the SC data comes from the average of the FWHM/2.35 for 100 images per data point, two options for the EOSD bunch length values are shown. Firstly, the FWHM/2.35 of an averaged phase retardation profile (before averaging, the individual profiles have been corrected for their different arrival times) and secondly the average of the fit values of Gaussian fits to every one of the 1000 single shots per data point. The very small error bars are not the fluctuations, but the standard error which is the standard deviation divided by  $\sqrt{(n)}$  with  $n$  being the amount of measurements (1000 for EOSD, 100 for the SC). The mismatch in measured bunch lengths for some data points is not within the statistical fluctuations, but has a systematic origin which was already pointed out in Fig. 6.23. It can be explained, by the different centroid positions for the EOSD measurements (see bottom). Bottom: Showing the averaged absolute arrival times (left y-axis and triangular, blue data points) and the centroid positions (right y-axis and round, orange data points) retrieved from the fits to the EOSD data. During the course of the measurement, the delay was slightly adjusted with the VM, which is taken into account for the calculation of the arrival time. The slight trend of the arrival time towards lower later times for lower currents is most likely caused by the synchronous phase shift. It can be seen that for the data points for which the centroid pixels is at rather low pixel values, the results for the bunch length measurements are significantly shorter than the SC results which is believed to be a detector systematic of the EO setup rather than a real change in bunch length (see Fig. 6.34 for more details).

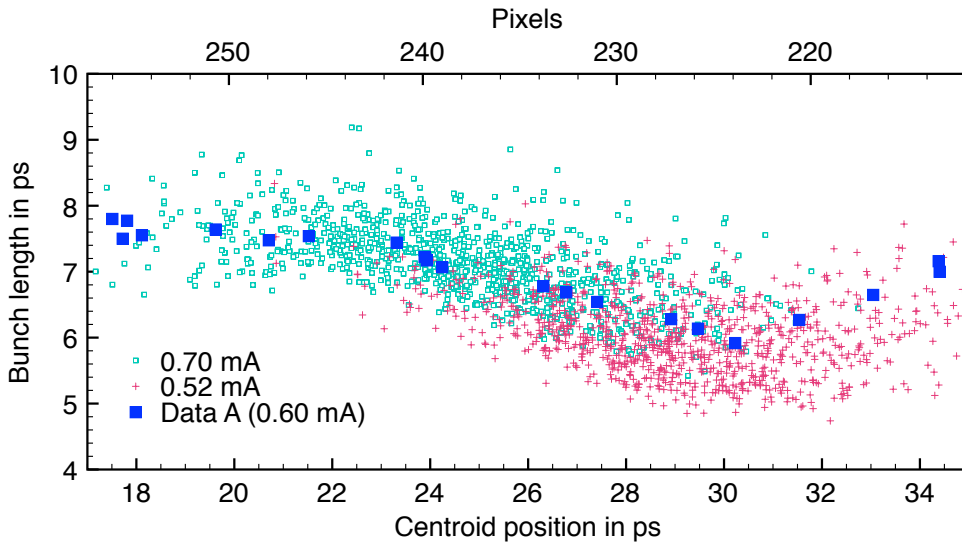


**Figure 6.34:** Showing bunch length data from averaged phase retardation profiles (Data A from the top of Fig. 6.23) which was recorded during a time calibration measurement for 0.6 mA during Fill 4623 versus the centroid position (for better comparison, the second x-axis in the top also shows the pixel scale). In addition to that the data sets recorded before and after the time calibration measurement for the currents of 0.70 and 0.52 mA are shown. This plot strengthens the assumption that the mismatch in measured bunch length for the SC and EOSD from Fig. 6.33 can be explained by the arrival time dependent characteristic behavior of the EOSD setup rather than any beam dynamics.

however, go hand in hand with an increase of the resolution of the spectrometer, which can be achieved by better focusing onto the detector and using more than the current 141 out of the total 512 pixels. This should make it possible to increase the overall resolution by at least a factor of two.

Our overall acquisition speed for single shot EOSD measurements lies at about 7 Hz, a value that we would like to increase up to the kHz-range in the near future and to a maximum of 2.7 MHz - the revolution frequency of ANKA, on the long run. This would enable us to have a turn by turn analysis of the longitudinal bunch profile, which in turn, combined with simulations of the longitudinal bunch profile on a turn by turn basis would allow a deeper understanding of the bursting mechanisms which lead to the formation of substructure on the electron bunches.

The availability of the EO setup at ANKA paves the way for many new interesting beam dynamics studies allowing single shot EOSD longitudinal bunch profile measurements during the low- $\alpha_c$ -operation which previously had not been possible.

### 6.3 Wake-Field Induced Heat Load

After the first installation of the EO-Monitor into the UHV system of the storage ring in October 2012, no temporal overlap was found. Instead it was recorded that the laser intensity (peak signal of the fast photodiode) decreased dramatically over time when the crystal was brought closer to the multi-bunch electron beam, even though there was no temporal overlap between laser and electron bunches (the laser was synchronized to an external free-running 500 MHz clock).

Figure 6.35 shows the results from three different measurements for which we moved the crystal closer to the electron beam. For each plot, the peak voltage of the signal from the PD - which detects the laser pulses that have pass through the whole EO-Monitor - and the position of the crystal from the center of the beam pipe were recorded over the course of several minutes. During this time, the position the crystal was moved closer to the beam and then retracted again.

The three measurements were done for different electron beam conditions. For the image in the top, the electron beam conditions were an unsqueezed (uncompressed) multi-bunch fill at the standard low- $\alpha_c$ -operation energy of 1.3 GeV with an averaged beam current of 36 mA during the experiment. As soon as the crystal enters the electron beam pipe (from 16 mm onwards), the signal decreases rapidly until the crystal is retracted again, it then slowly seems to recover to its original value, but repetitive measurements have left the signal slightly lower than before. The middle part of Fig. 6.35 shows the same measurement for a squeezed (compressed) single-bunch with a much lower total current just below 1 mA. Here the signal decreases only very slightly and fully recovers.

The bottom of Fig. 6.35 shows the effect of solely opening and closing of the impedance protection slider (shutter) for an even higher beam current of nearly 60 mA during a squeezed multi-bunch operation. The signal decreased dramatically to less than half of its original value.

The exponential decrease of signal and the time scales on which the decrease and the recovery occurred gave rise to the assumption that the crystal and the arm it is mounted on heat up due to wake-fields generated by the structure. The temperature increase then leads to a slight misalignment of the laser's beam path which can easily affect the very delicate coupling of the laser beam into the SM collimator<sup>8</sup> on the EO-Monitor. Numerical wake-field simulations to estimate the power loss due to wake-fields have been carried out by my colleague B. Kehrer and lead to the conclusion that for a multi-bunch beam current of 31 mA the lost power can well be around 10 W [80], which could explain the strong effect we observe. This, for now, confines the use of the EO setup to single-bunch operation (studies with 2 or more bunches and a total beam current below 3-4 mA are, of course, also possible).

The 2 mm thick GaP crystal was then replaced during a shutdown period in January 2013 by a 5 mm thick one. Figure 6.36 shows a microscopic image of the 2 mm crystal after it has been removed from the ring. It shows clear signs of damage on its HR coated side which is facing the electron beam. Altechna, the company we bought the crystals from,

---

<sup>8</sup>The diameter of the core of the fiber is only 6  $\mu\text{m}$ .





suggested that the cracks in the coating could be caused by thermal expansion and rapid cooling afterwards. The melting point of the dielectric coatings is above  $1000^{\circ}\text{C}$ , so it is unlikely that they have melted. As GaP is an anisotropic material, it has different thermal expansion coefficients in different directions, the coating materials however are isotropic, so rapid heating and cooling rates could easily lead to cracks in the coating material [81].



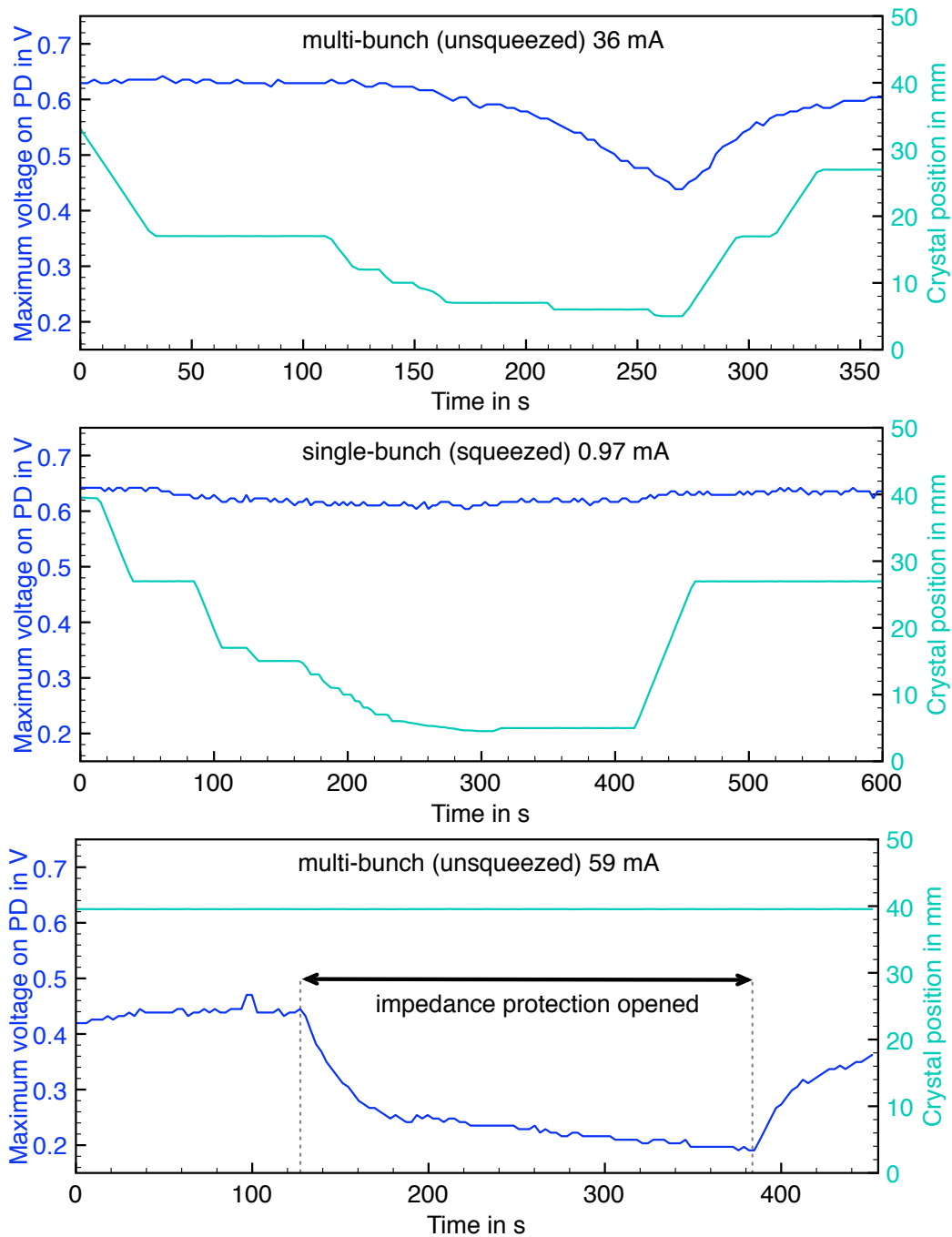


**Figure 6.35:** All three plots show the peak signal recorded with the PD (blue curve and left y-axis) and the crystal position relative to the center of the vacuum beam pipe (light blue curve and right y-axis) over the course of several minutes. The electron beam energy was 1.3 GeV for all measurements, but the filling pattern and bunch compression were varied for the different measurements: Top: Multi-bunch fill with uncompressed (unsqueezed) bunches and a total current of 36 mA. Middle: A compressed single-bunch with a current of 0.97 mA. Bottom: Uncompressed multi-bunch with a rather high current of 59 mA for which solely the the opening and closing of the impedance protection slider (shutter) has a noticeable effect.

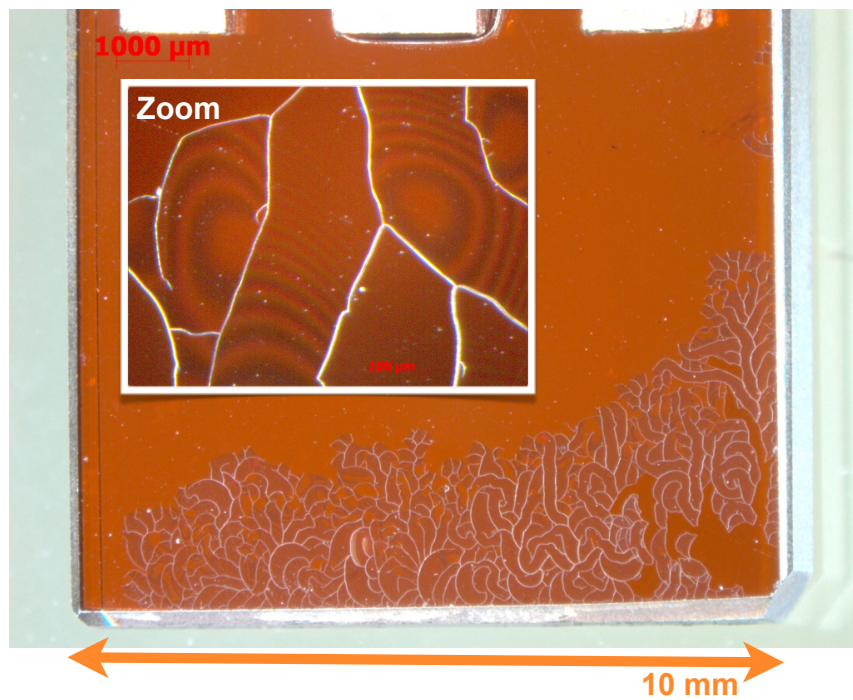


**Figure 6.36:** Microscopic image of the 2 mm thick GaP crystal which had been installed into the ring between October 2012 and January 2013. The image shows the crystals HR coated side which is facing the electron beam. The coating shows cracks at the bottom edge which could be caused by rapid cooling.



# 7. Beam Studies with Longitudinal Diagnostics at ANKA

With the SC being the main tool for bunch length measurements until EO-techniques became available, an extensive characterization of ANKA's low- $\alpha_c$ -mode has been undertaken to gain more insight of bunch lengthening effects, which do play a significant role during any short-bunch operation in storage rings. The new results obtained with the EO setup just give a glimpse of the new possibilities which have opened up for longitudinal diagnostics. By no means is the characterization of the low- $\alpha_c$ -operation is finished and fully understood. Most results are mere first observations of aspects of longitudinal beam dynamics, which have not been visible previously and will require extensive further studies before all the effects can be explained.

The chapter starts off with Section 7.1 by giving an overview of characterization measurements of the low- $\alpha_c$ -mode at ANKA for which measurements of bunch length and shape have been carried out with the SC for many different machine conditions. The results are then extended with previously unavailable measurements that the EO setup has now allowed us to do. Then Section 7.2 follows with studies of the long range wake-fields that also only now are possible due to the EO setup. After that, Section 7.3 shows some measurements of the bunch length during the energy ramp which reveal strong longitudinal instabilities at the injection energy of 500 MeV. Section 7.4 shows an example of how arrival time measurements with EOSD have allowed us to notice problems with the cooling loop of one of our cavities.

## 7.1 Low- $\alpha_c$ -Mode Characterization

The characterization of the low- $\alpha_c$ -mode is grouped in different topics. First I show studies of the averaged bunch length, which - due to the microbunching instability - increases quite dramatically for higher currents during the low- $\alpha_c$ -operation. The bunch lengthening is studied for different values of  $\alpha_c$  and for different RF voltages.



Then a glimpse of bunch length fluctuation studies - another topic presently under study at ANKA - is given where single-shot EOSD data is compared with SC data.

This is followed by the comparison of averaged longitudinal bunch profiles for different currents and machine settings, which reveals a bunch asymmetry towards the head of the bunch for higher bunch currents and more compressed bunches.

Finally, a selection of bunch profiles recorded with single-shot EOSD are shown which reveal not only a strong bunch deformation, but also the theoretically predicted formation of time dependent sub-structures which form ripples on the compressed bunches.

### 7.1.1 Bunch Length in Dependence of Current for Different Values of the Momentum Compaction Factor $\alpha_c$

The momentum compaction factor  $\alpha_c$  of the ANKA optics can be varied gradually during low- $\alpha_c$ -operation. To monitor the change in  $\alpha_c$  it is sufficient to measure the synchrotron frequency  $f_s$  which is proportional to  $\sqrt{\alpha_c}$  (see Ch. 2.1.2 on p. 12).

For the standard low- $\alpha_c$ -mode at a beam energy of 1.3 GeV and a total RF voltage of 0.6 MV (evenly divided over 4 cavities),  $f_s$  can be decreased stepwise from about 31 kHz down to around 4 kHz, so the zero current bunch length<sup>1</sup> ( $\sigma_{z,0}$ ) is typically reduced by a factor of up to 10. The current dependent bunch length behavior of a single bunch for various optics settings between  $f_s = 30.8$  kHz and 5.6 kHz can be seen in Fig. 7.1. The SC measurements show clearly that for uncompressed bunches (i. e.  $f_s = 30.8$  kHz), the bunch length barely changes with beam current, but for more compressed bunches (lower values of  $f_s$ ), the bunch length strives towards a constant value ( $\sigma_{z,0}$ ) only for very low currents, but for higher currents, their length follows the dotted line which is  $\sigma_z = (10.33 \pm 0.23) ps \times (mA)^{-3/7} \times I_{bunch}^{3/7}$ . The fits shown in the plot are empirical to guide the eye. For  $I_{bunch}$  reaching towards 0, they strive towards a constant value which allows for the extraction of a value for  $\sigma_{z,0}$  and for large values of  $I_{bunch}$  they are  $\propto k \cdot I_{bunch}^{3/7}$ . The scaling of the bursting threshold with  $I_{bunch}^{3/7}$  has been predicted by the theory of Stupakov and Heifets [20].

For the bursting threshold data shown in Fig. 7.1 the bunch current at which the bursting behavior of the CSR stopped during a beam decay for a certain  $f_s$  has been determined with THz-detectors [82]. Namely a Si bolometer which has a rather slow response time, but is very sensitive and a hot electron bolometer (HEB), which is a very fast THz detector allowing for the detection of the signals from single bunches [83]. The corresponding zero current bunch length to that value of  $f_s$  has been extracted from the linear extrapolation shown in Fig. 7.2, where the measured zero current bunch length (for a fixed RF voltage) is shown in dependence of the  $\alpha_c$ -dependent  $f_s$ . Both, the SC and the THz-detector data show a behavior to follow the  $k \cdot I^{3/7}$  trend, but with a slightly lower value for  $k$  for the data from the THz-detectors  $k_{THz} = (9.38 \pm 0.27) ps \times (mA)^{7/3}$  than for the SC data  $k_{SC} = (10.33 \pm 0.27) ps \times (mA)^{7/3}$ .

<sup>1</sup>While the actual bunch length increases with current, the zero current bunch length states the asymptotic lower limit for infinitesimally low currents.



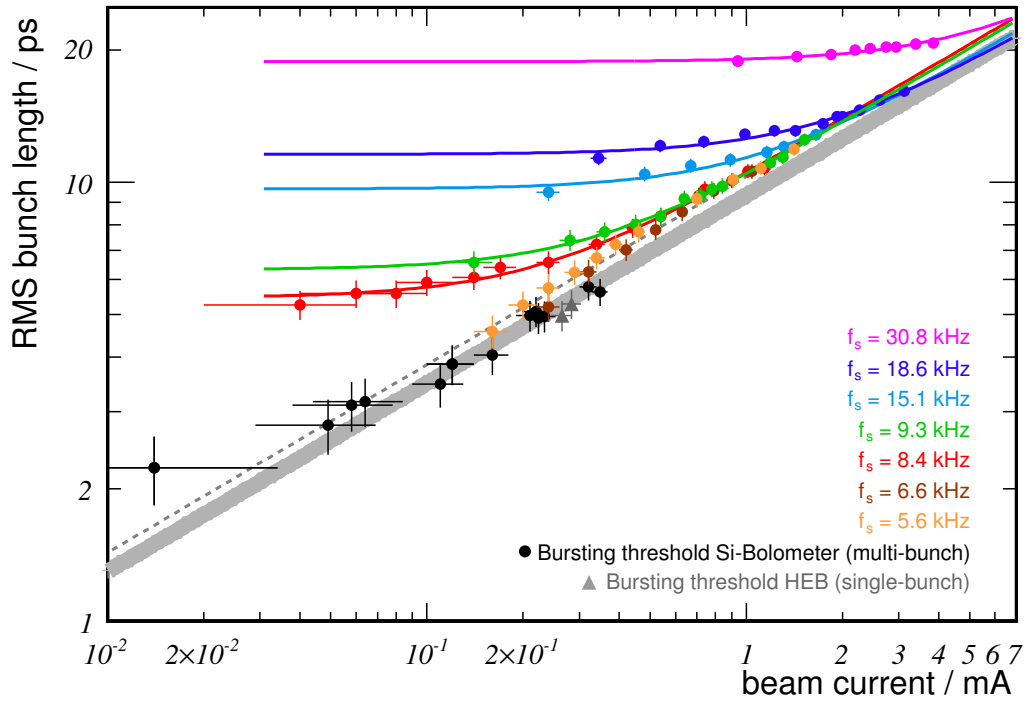


**Figure 7.1:** Comparison of various bunch lengthening and bursting threshold measurements for different momentum compaction factors (proportional to the synchrotron frequency  $f_s$ ) at a fixed RF voltage of 0.6 MV (equally distributed over 4 cavities). The bunch length measurements were done with the SC and bursting threshold measurements with THz-detectors (HEB data courtesy of V. Judin). The fits to the SC data are empirical to guide the eye and allow for the extracting of  $\sigma_{z,0}$ . Published in [70].

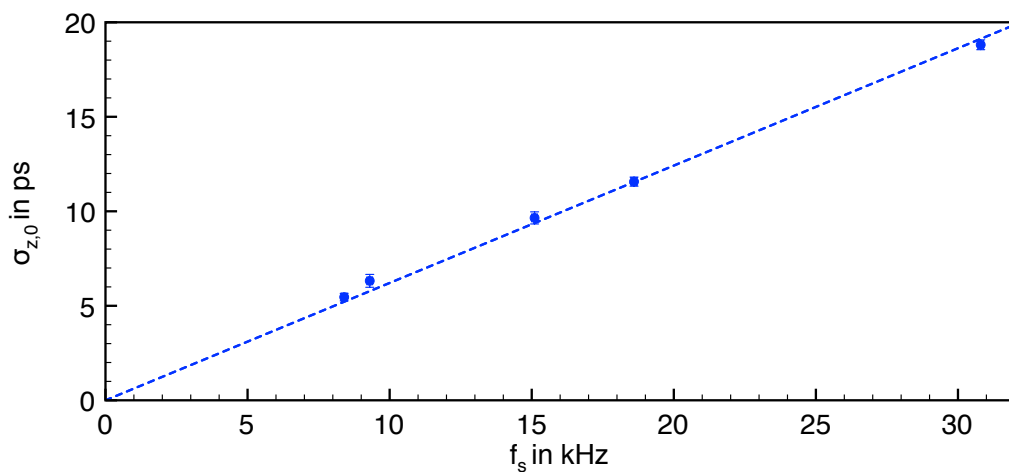


**Figure 7.2:** Zero current bunch length  $\sigma_{z,0}$  retrieved from the fits in Fig. 7.1 for a total RF voltage of 0.6 MV versus synchrotron frequency  $f_s$  measured with a spectrum analyzer. The behavior is described reasonably well with a linear fit according to  $\sigma_{z,0} = (0.6209 \pm 0.006)$  ps/kHz  $\cdot f_s$ .

### 7.1.2 Bunch Length in Dependence of Current for Different RF Values

To study the effect of the RF voltage on the bunch compression, the bunch length was measured during a single bunch decay for a fixed low- $\alpha_c$ -optic while changing the RF voltage between 0.2 and 1.8 MV (equally distributed over 4 cavities). The results are shown in Fig. 7.3. A higher RF voltage leads to a bunch compression for all current ranges in contrast to a change in  $\alpha_c$  (see Fig. 7.1) only leading to a decrease of  $\sigma_{z,0}$ . Also a shift of the bursting current towards lower values is observed.

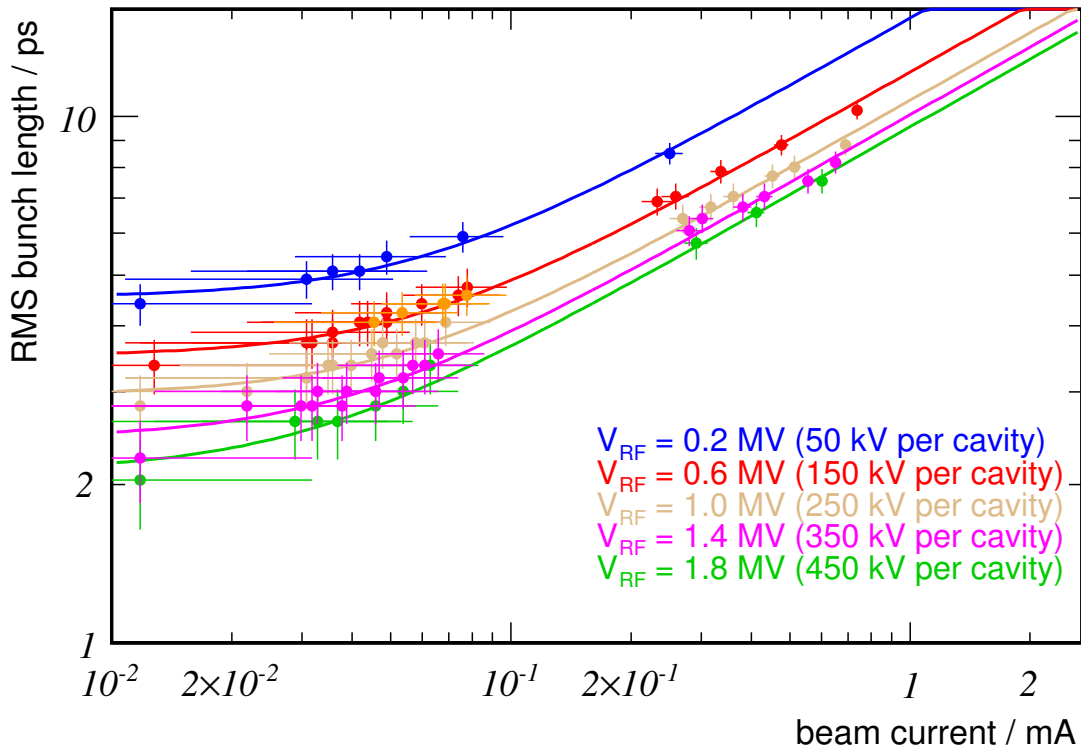


**Figure 7.3:** Comparison of bunch length values for different RF voltages during one fully compressed fill (4274). The synchrotron frequency was 4.17 kHz at 0.6 MV. The fits are empirical to guide the eye.



### 7.1.3 Studies of Bunch Length Fluctuations

Extensive studies of bunch length fluctuations recorded with the SC have been undertaken by P. Schönfeldt [71]. He performed wide-ranging studies with our SC system, greatly increased the data processing and increased the frequency of measurements. While previous bunch profiles were recorded sporadically during one single-bunch decay for a few different currents only, now the acquisition of bunch profiles is nearly continuous and the analysis quasi-real-time. This allows to link changes in the fluctuations of bunch length measurements to changes in the bursting behavior recorded with THz detectors. A short summary of his work can also be found in [69].

In this work, a first comparison of bunch length distributions measured with the SC and with single-shot EOSD are shown, pointing out the many opportunities the EO system is opening up for longitudinal diagnostics.

For this, the distribution of bunch lengths for one series of measurements is analyzed. Figure 7.4 shows the results. For the SC, sequences of 100 images<sup>2</sup> are recorded and the bunch length is evaluated separately for every image. Even though the SC does not measure single-shot bunch profiles, the amount of consecutive bunch revolutions which are shown for a single image, is about 2700 (1 ms). As the time scale over which CSR bursts occur changes for different currents and machine settings, the SC is sensitive to detect some changes in modes. Typically the burst duration is below 1 ms for lower currents, but can increase to durations above 1 ms for higher currents.

The bunch lengths of those 100 measurements are then filled into a histogram, to see what kind of distribution we obtain. For the EOSD data, sequences of 1000 single-shot measurements are analyzed and their individual bunch length results (obtained by Gaussian fits to the longitudinal profiles) are also filled into a histogram<sup>3</sup>. Those histograms are then compared for different currents. Unfortunately, for the EO-data the density of measurements is not yet as high as for the SC, where a slight change in shape of the histograms is visible for currents around 0.5 mA and below, when the distribution starts to become asymmetric, favoring shorter bunch lengths rather than longer ones. The EO-data also seems to confirm this behavior, but for currents below 0.15 mA, the single-shot detection becomes very noisy, leading to a broadening of the histogram which is not observed for the SC data.

Further studies will be required to make any clear statements about the observed behavior and to explain and understand the effect in detail, but the first results do look promising to hold interesting beam dynamics and bursting behavior information.

---

<sup>2</sup>The image acquisition frequency is about 10 Hz.

<sup>3</sup>The image acquisition frequency is about 7 Hz.



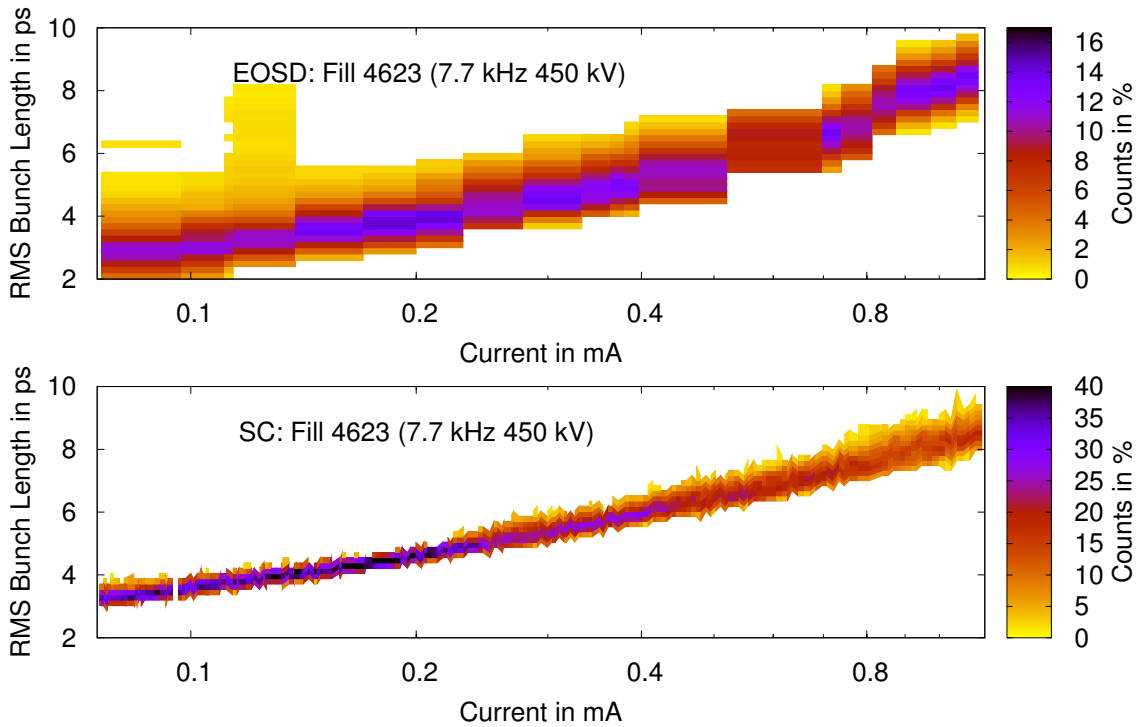
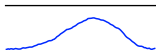


**Figure 7.4:** Comparing bunch length histograms for different currents for EOSD (top) and the SC (bottom). For EOSD, the bunch length is measured by Gaussian fits to the phase retardation for 1000 single-shot measurements and for the SC, the data comes from computing the FWHM and dividing it by 2.35 for 100 consecutive images where every image covers several hundred revolutions. Both data sets show a slight asymmetry towards shorter bunch lengths for currents between 0.5 and 0.25 mA. For currents below 0.15 mA the spread in measured bunch lengths increases drastically for the EOSD data which is caused by a very low signal to noise ratio rather than actual bunch length fluctuations. For the EOSD data, the current at which the measurement took place is at the right edge of the histograms. SC data courtesy of P. Schönfeldt.



### 7.1.4 Average Bunch Shapes for Different Currents

The SC allows for the evaluation of very precise averaged bunch profiles. During the low- $\alpha_c$ -operation, not only the bunch length changes, but also the shape of the longitudinal bunch profiles. For high bunch charges, the profiles distort towards the head of the distribution - they lean forward - this is believed to be caused by the CSR impedance [32].

Figure 7.5 shows averaged bunch profiles for different bunch currents during one single-bunch fill. For better comparison, the profiles are normalized to have the same area, otherwise their integral would be proportional to the bunch charge unless any SC settings like the gain are changed between different measurements. In addition, the distributions are aligned to have their center of mass at zero. It shows clearly that for high currents, the bunch profiles do not only get longer (by about a factor of two), but also lean forward a bit more (the maximum shifts to the left). Even for very low currents, the distribution does not become perfectly symmetrical.

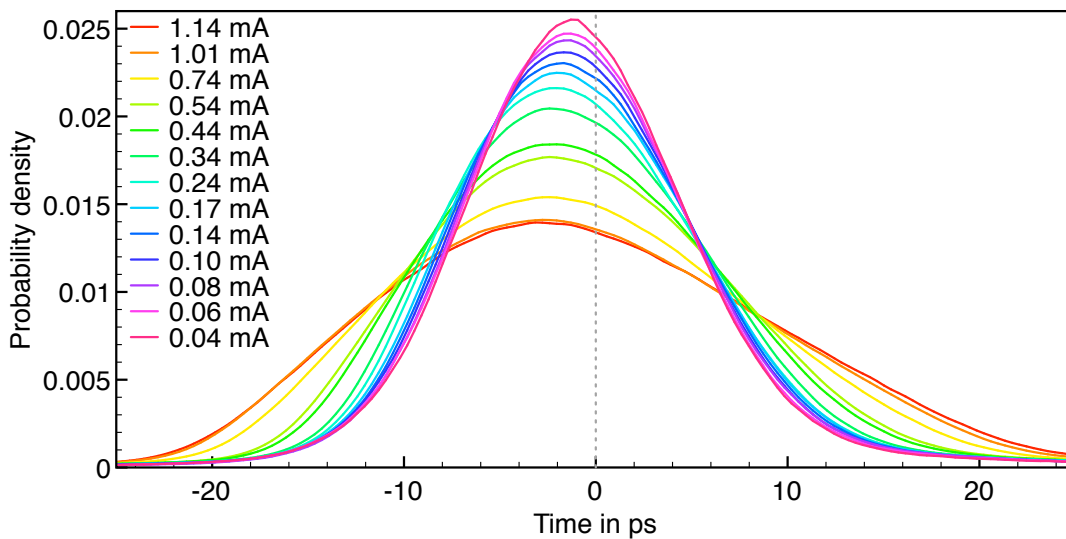


**Figure 7.5:** Averaged bunch profiles recorded with the SC for different bunch currents during the compressed Fill 3517 (beam energy 1.3 GeV). For better comparison of the bunch shapes, the profiles have been normalized to have the same area. The head of the distribution is to the left and the tail to the right. It shows clearly that for higher currents the profiles do not solely increase in length, but also seem to deform more with their heads leaning further to the left. The beam parameters were:  $f_s = 8.4$  kHz, 23k steps, RF voltage 150 kV / cavity. The bunch currents for the different profiles can be found in the legend. The bunch lengths range from 10.8 ps down to 5.2 ps.

In Fig. 7.6 additional bunch profiles are shown for very compressed bunches (left) for which the effect is more visible and for only slightly compressed bunches (right) where the bunch profiles do not change as much over a comparable current range.

Figure 7.7 shows bunch profiles recorded during ANKA's standard user operation at 2.5 GeV for rather long ( $\sigma_z \approx 44$  ps RMS), uncompressed bunches. Here the bunch distribution is perfectly Gaussian and nearly independent of current. To get an impression on the compression during the low- $\alpha_c$ -operation, the shortest profile from the left hand side (lhs) of Fig. 7.6 (scaled down to have the same amplitude as the long profiles) is shown again (grey dashed curve).

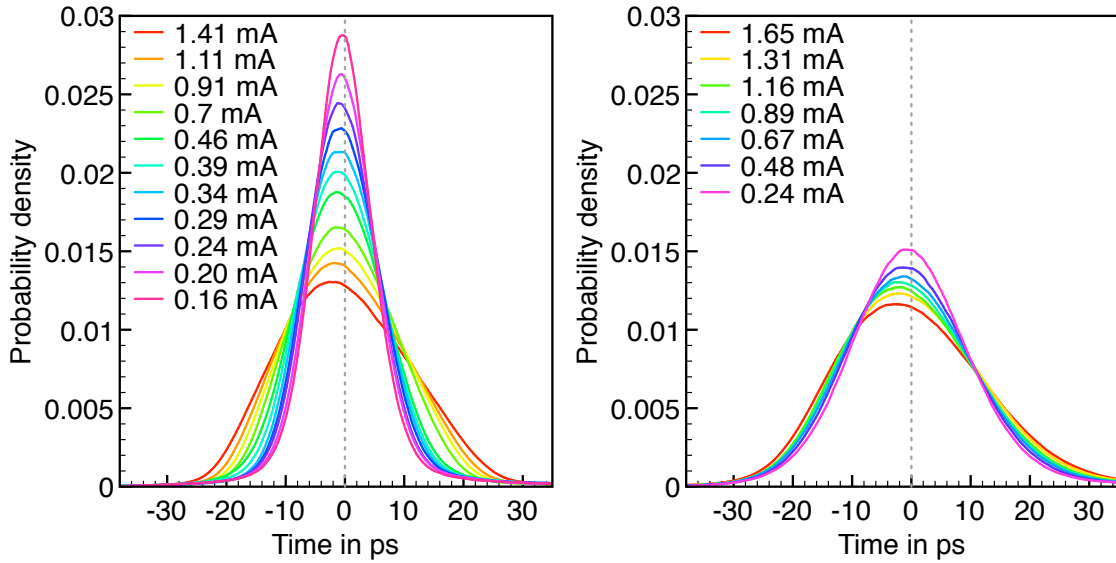


**Figure 7.6:** Two sets of normalized (area = 1) averaged bunch profiles (recorded with the SC) for different currents during two compressed fills (beam energy 1.3 GeV). Left: The bunches were fully squeezed (Fill 3185, 27k steps,  $f_s = 5.6$  kHz, RF 150 kV / cavity), the bunch lengths range from 11.9 ps down to 4.6 ps. Right: The bunches were only slightly compressed (Fill 3186, 19k steps,  $f_s = 15.1$  kHz, RF 150 kV / cavity), the bunch lengths range from 12.8 ps down to 9.5 ps.

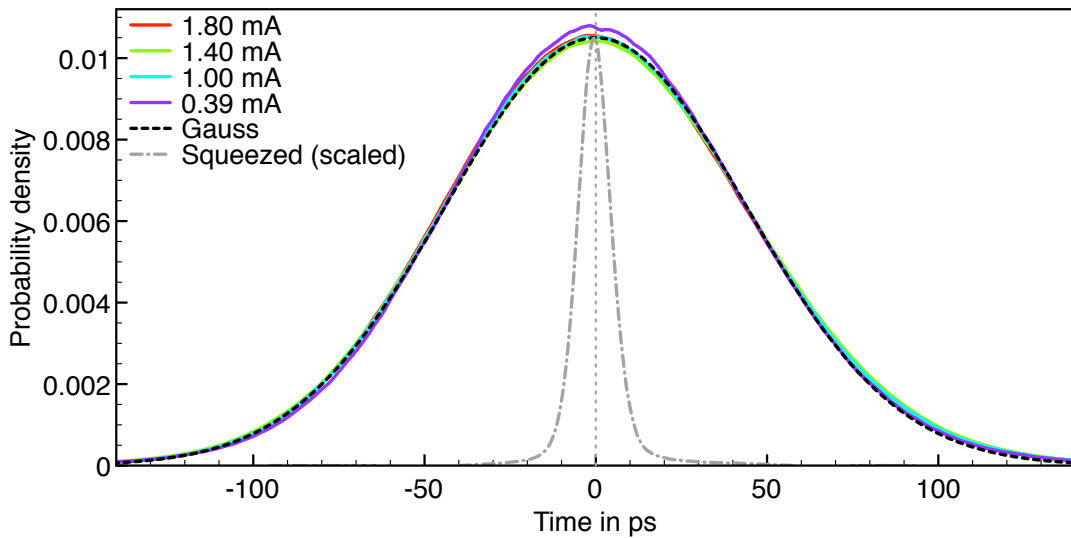


**Figure 7.7:** Normalized bunch profiles for different currents recorded during a single bunch fill at a beam energy of 2.5 GeV with the standard user optics. For better comparison a Gaussian with the same width as the profiles is also drawn. To show how much the bunches are longer than during the low- $\alpha_c$ -operation, the shortest profile from the lhs of Fig. 7.6, scaled down to have the same amplitude, is shown again (grey dashed curve).



### 7.1.5 Single-Shot Bunch Length and Shape Measurements

With EOSD near-field measurements, the longitudinal bunch shape and length can be measured for a single electron-bunch revolution within the storage ring. In contrast to the SC, which measures the longitudinal profile of the incoherent synchrotron radiation pulses, our EO-setup measures the electric field of the electron bunch passing by an EO crystal.

The relatively high resolution and sensitivity of the measurement setup (see Chapter 6.2.4) allows us to measure the longitudinal bunch profile with a sub-ps resolution down to bunch lengths as low as 1.5 ps RMS<sup>4</sup> for bunch currents down to about 0.15 mA (56 pC), for lower currents, the measurements become rather noisy and averaging is required. This enables us to detect time dependent substructures on the electron bunches down to a length in the order of the point-spread function of 1.5 ps RMS. A detailed discussion of the resolution of the system can be found in Chapter 6.2.4.

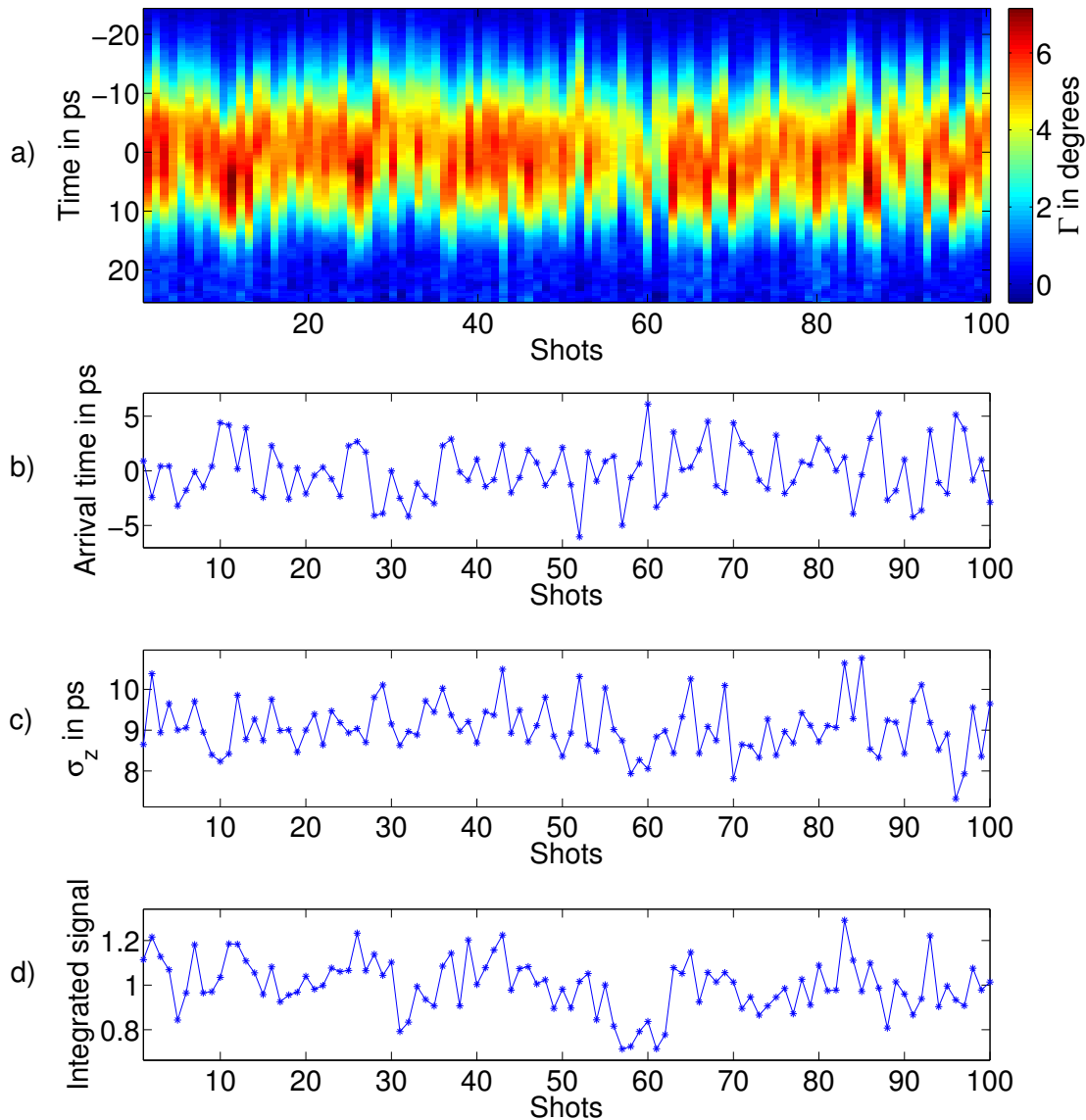
Unfortunately, the dead time between two consecutive measurements is currently rather high, with the acquisition speed being in the order of 6-7 Hz. This does not allow us to see the temporal evolution of CSR bursts, but only to picture them at different snapshots in time. This is a limitation we are trying to overcome in the future by increasing the readout speed of the photodiode array within the EOSD setup. The measurements, however, still offer great insight into longitudinal beam dynamics.

Figure 7.8 shows 100 consecutive single-shot EOSD bunch profiles. In the sub-plots below, the arrival time (centroid position) of the different profiles and the bunch lengths, both retrieved from Gaussian fits to the profiles, are shown. The signal intensity fluctuations which can be seen in top image could be caused by transverse, betatron oscillations of the bunches, which would change the geometric distance between the electron bunch and the laser spot inside the crystal. For the future, it is foreseen to perform a frequency analysis of these fluctuations, currently we are lacking precise enough time stamps for the single measurements.

---

<sup>4</sup>While one pixel corresponds to time steps between 360 and 400 fs, the point spread function of the spectrometer itself - the response to monochromatic light - is 9 pixels FWHM which corresponds to 1.4 - 1.5 ps RMS depending on the time resolution per pixel.





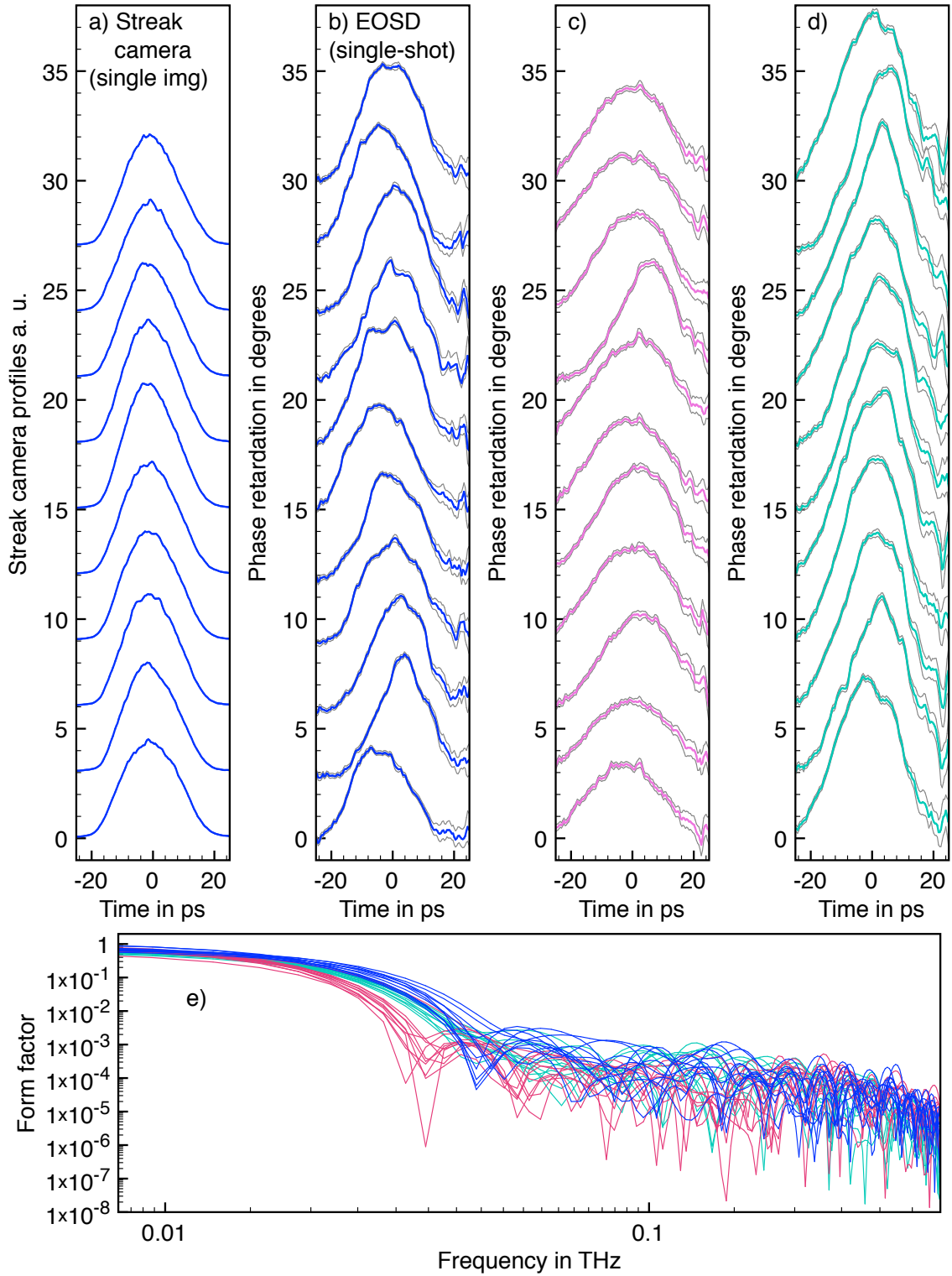
**Figure 7.8:** a) Showing 100 consecutive single-shot EOSD phase retardation ( $\Gamma$ ) bunch profiles out of a 1000 shot sequence. The shots are recorded at about 7 Hz, so the 100 shots show snapshots over a total time of about 15 s. b) Depicting the arrival time for every shot. c) Resolution corrected RMS bunch length from Gaussian fits to the profiles. d) Showing the integrated signal, which is computed from the Gaussian fit parameters and normalized to its mean value. The standard deviation of the fluctuations shown is 12%. The beam parameters were: Fully compressed beam during Fill 4623 (450 kV / cavity; 27k steps,  $f_s = 7.7$  kHz) with 1.13 mA (418 pC) bunch current, average bunch length over the whole sequence:  $8.79 \pm 0.63$  ps.



Figure 7.9 takes a closer look at bunch profiles for different machine parameters during the low- $\alpha_c$ -operation. There, for three different machine settings, bunch profiles are shown. While plots b), c) and d) show single-shot EOSD profiles, plot a shows bunch profiles recorded with the SC taken at the same time as the profiles shown in b). All the profiles have been displaced in  $y$ -direction for better visibility. The profiles recorded with the SC (plot a) are not single-shot, but only averaged over one image, which spans a time of 1 ms. The acquisition over such a time span will most likely lead to the averaging out of any kind of dynamic substructure. The error bands for the EOSD profiles in the plots give a measure of the one- $\sigma$ -fluctuation retrieved from background measurements (see Chapter 6.2.4). They confirm that the bunch deformations and the substructures in the order of a few picoseconds are highly significant. While the data set in b) shows more substructures on an otherwise rather rounded profile, the data set in d) shows rather triangular bunch shapes. For the data set in c), the bunch compression was not as high and deformations and substructure do not seem to occur as strongly and frequently. In the bottom, the normalized form factors of the different profiles are shown[84]. They give an idea what the spectrum of the CSR emitted from bunches with the above profiles would look like. This also explains the observed fluctuations of integrated power in the CSR, which is observed in the THz frequency range (“bursting”).

In the future, those measurements can be compared to measurements of the CSR in the spectral domain to gain deeper insights into the temporal behavior of the bursts detected with THz detectors.





**Figure 7.9:** Bunch profiles for for different machine parameters. The curves have been displaced vertically for better visibility. a) Streak camera profiles for single images (Courtesy of P. Schönfeldt). b) Single-shot EOSD profiles recorded around the same time. Beam parameters for a) and b): Fully compressed beam (Fill 4623; 450 kV / cavity; 27k steps,  $f_s = 7.7$  kHz) with 1.13 mA (418 pC) bunch current, average bunch length  $8.79 \pm 0.63$  ps. c) Single-shot EOSD profiles for a slightly compressed beam (Fill 4627; 180 kV / cavity; 23k steps,  $f_s = 8.3$  kHz) with 1.14 mA (422 pC) bunch current, average bunch length  $13.56 \pm 1.26$  ps. d) Single-shot EOSD profiles for a heavily compressed beam (Fill 4656; 450 kV / cavity; 25.3k steps,  $f_s = 10.4$  kHz) with a high beam current of 1.75 mA (648 pC), average bunch length  $7.97 \pm 0.81$  ps. e) Computed form factors for the EOSD profiles (Courtesy of M. Schwarz).



In Figures 7.10 and 7.11 single-shot bunch profiles are shown for different currents during the decays of single bunches. The decays are for the profiles shown in b) and d) of Fig. 7.9.

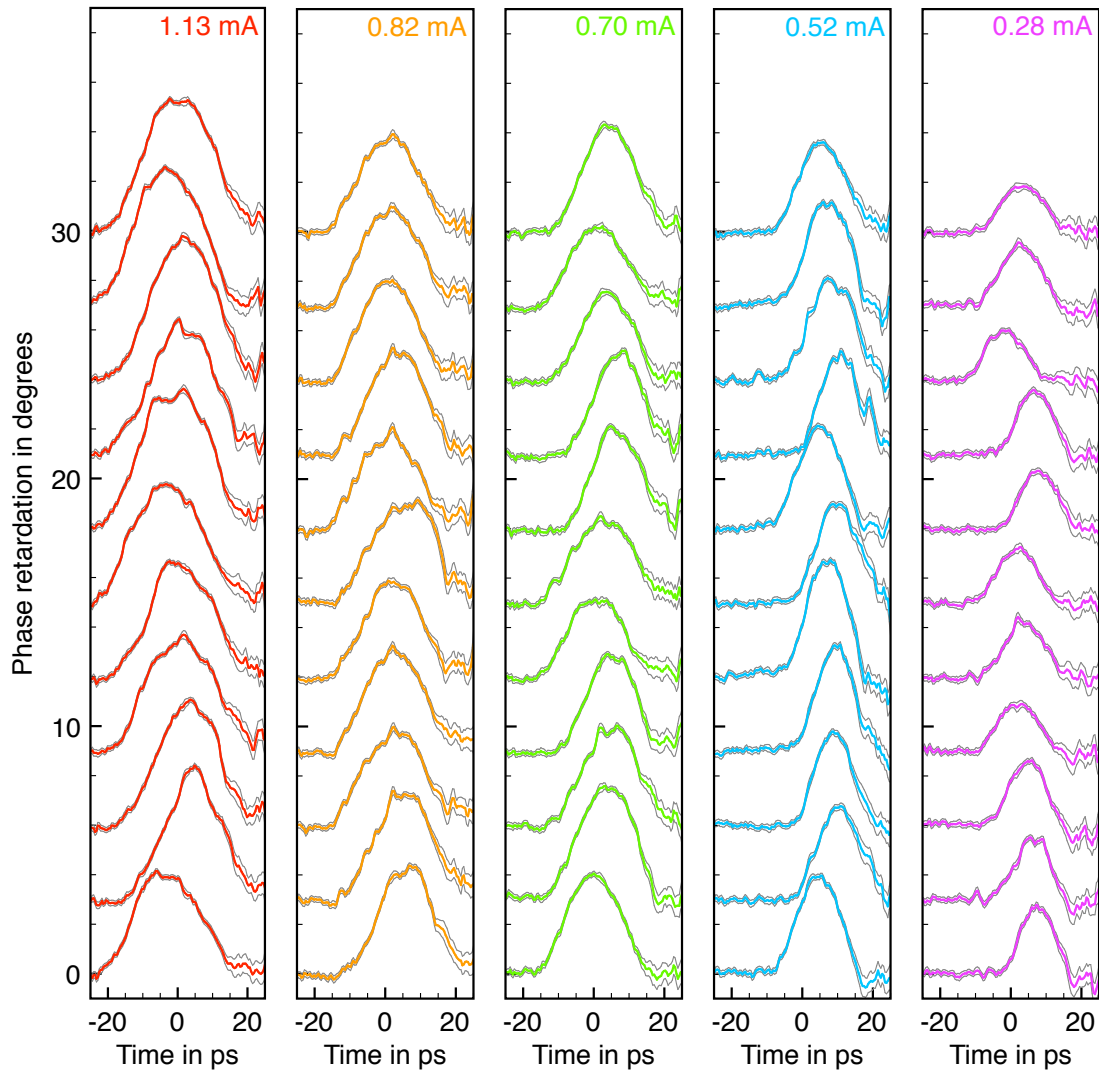


**Figure 7.10:** Showing 5 sets of 11 consecutive single-shot EOSD bunch profiles for different currents recorded during the fully compressed Fill 4623. The curves have been displaced vertically for better visibility. The beam parameters are the following: 450 kV / cavity; 27k steps,  $f_s = 7.7$  kHz.

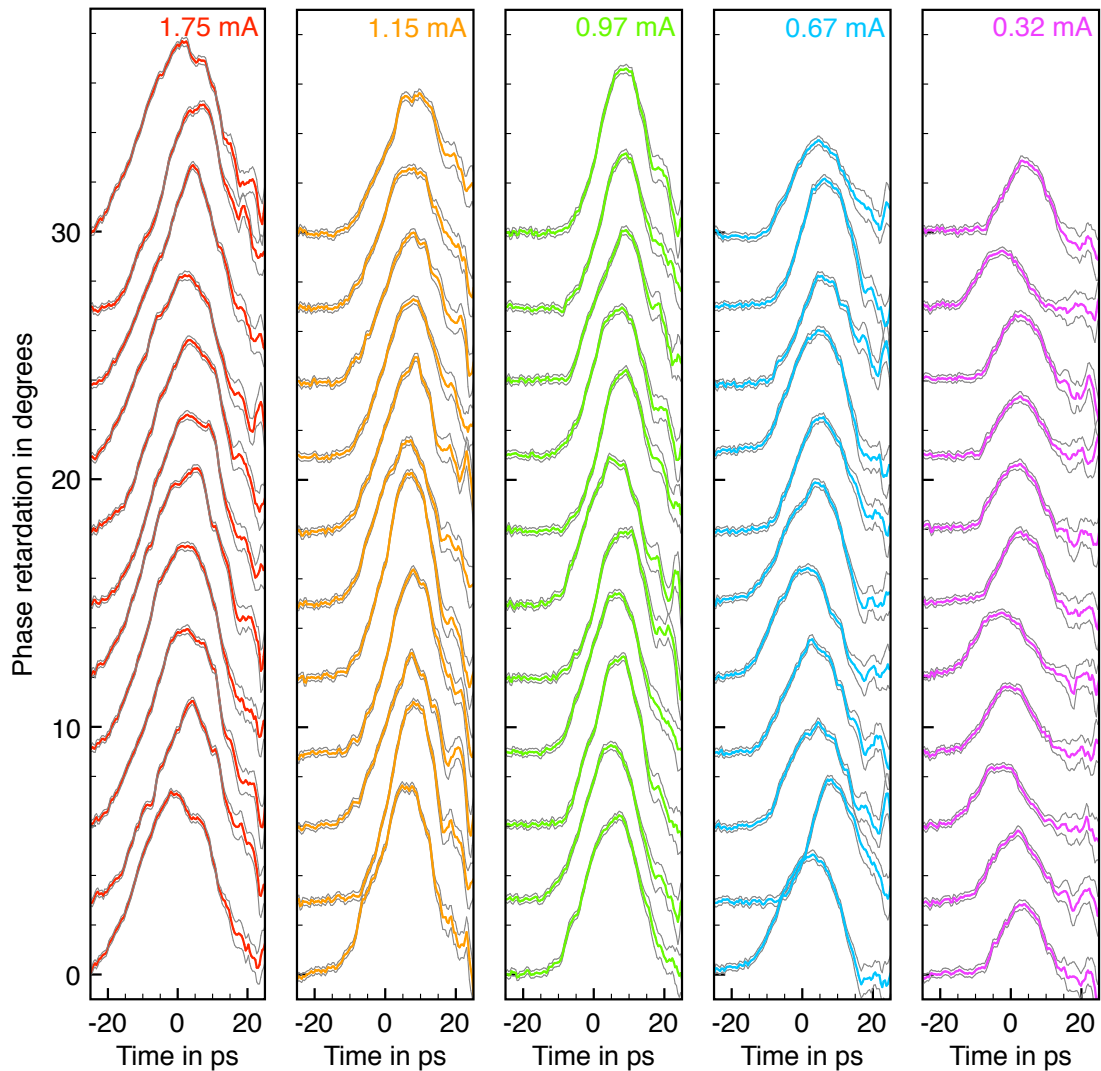


**Figure 7.11:** Showing 5 sets of 11 consecutive single-shot E OSD bunch profiles for different currents recorded during the heavily compressed Fill 4656. The curves have been displaced vertically for better visibility. The beam parameters are the following: 450 kV / cavity; 25.3k steps,  $f_s = 10.4$  kHz.

## 7.2 Studies of Long Range Wake-Fields

The EO measurements allow us to study not only the bunch length and longitudinal profile, but also the temporal characteristics of the vertically polarized field component of wake-fields that trail the electron bunch. Here the geometrical structure of the in-vacuum parts of the EO-Monitor, which holds the EO crystal, plays a strong role on the exact shape of the wake-fields. Simulations of the predicted wake-fields are being carried out by B. Kehrer, and first results showing very good agreement with the measured curves, have recently been published [80].

However, these EOS scans do not have a sub-ps resolution, because for our setup the laser pulse length cannot be compressed below values in the order of 20 ps FWHM which will inevitably broaden any shorter structures (see Chapter 6.1).

Results for different measurement series, studying the current, distance, and optics dependent shape of the wake-fields are shown. And at the end of the section, it is shown that the induced wake-fields are long enough to influence a following electron bunch.

### 7.2.1 Current Dependence of Wake-Fields

Figure 7.12 shows long range EOS scans which show not only the Coulomb field of the electron bunch (first peak at a time around 0), but also a significant amount of wake-fields that follow the bunch. While the image in the top shows the relative modulations for different currents, the image in the bottom shows the same curves, but every data point is additionally scaled down by the current for that data point. This is done for every data point separately, because the measurements take about 10 minutes, a time during which the beam current will have already slightly decayed. The signal of the main peak which is proportional to the longitudinal charge distribution inside the electron bunch is expected to scale linearly with the bunch current (for constant bunch lengths), which can be seen rather nicely by the scaled peaks overlapping perfectly. The comparably flat region to the left of the main peak gives an idea of the measurement fluctuations because the electric field before the bunch passes the crystal should be zero (relative modulation of 1) unless there are still any wake-fields from the previous revolution left (368 ns revolution time for ANKA).



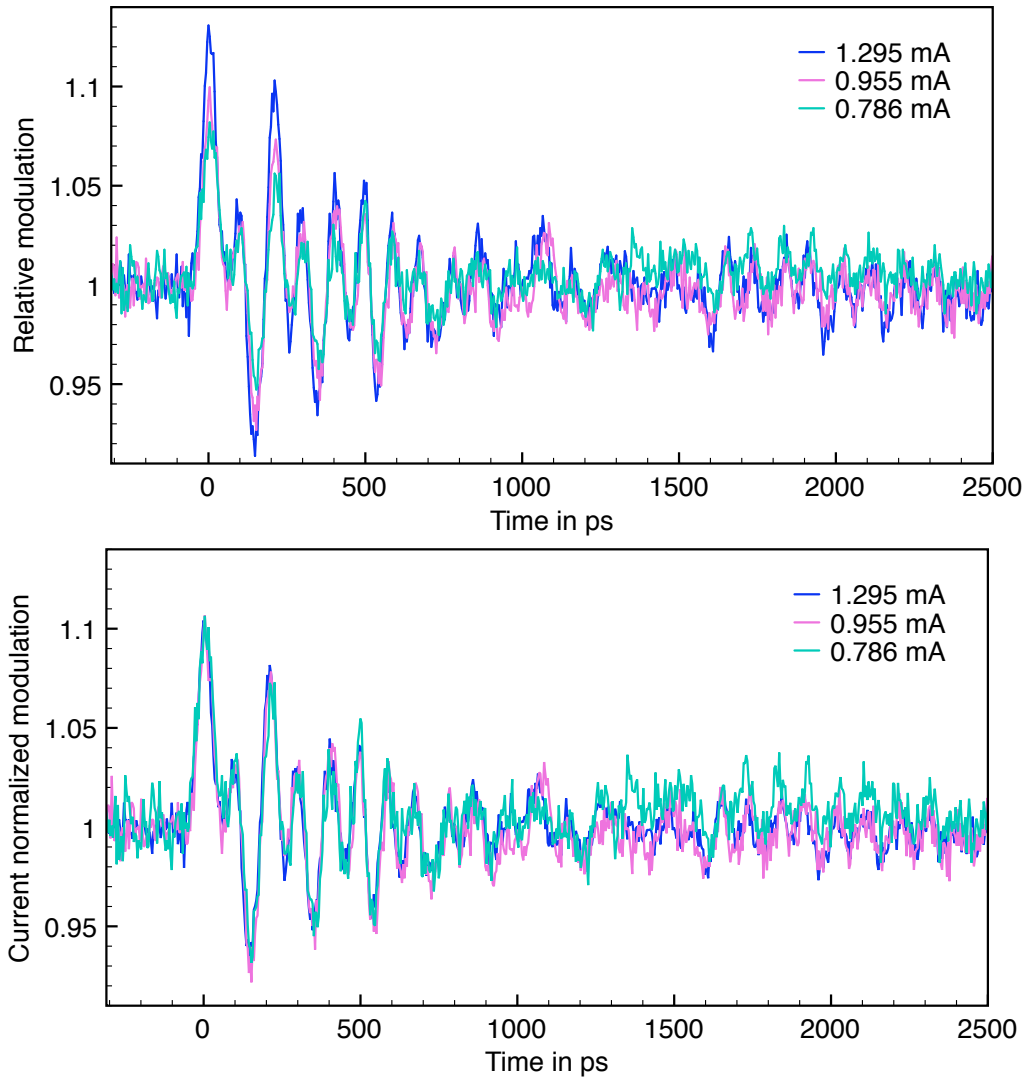


**Figure 7.12:** Top: Relative modulation of EOS scans for different beam currents. Bottom: Same data as in the top image, but with the Y-axis normalized to the beam current. All measurements were done with an unsqueezed electron beam at 1.3 GeV and an RF voltage of 180 kV / cavity. For this current range and these machine settings, the bunch length remains constant. The signal fluctuations at times before the first peak, where we would not expect to see any modulation, give a measure of the noise level for this measurement.

### 7.2.2 Distance Dependence of Wake-Fields

In Fig. 7.13 two sets of EOS measurements for different distances of the EO crystal from the electron beam are shown. Here, it should be mentioned again that the total height of the ANKA beam chamber is 32 mm, so a crystal position of 15.3 mm from the center of the beam pipe will have nearly fully retracted the crystal. As previously, the data is normalized by the beam current, to allow for the comparison of the different measurements during which the beam current has decreased slightly. While the data set in the top was recorded for an unsqueezed electron bunch which had a rather high bunch current (hence the seemingly lower noise level), the data set in the middle was recorded for a slightly compressed bunch, but here the beam current changed only slightly, because the beam life time at lower currents increases. In the bottom of the figure, the amplitudes of the first peaks (retrieved by fits to the areas around the peaks) are shown in dependence of the crystal distance from the center of the beam pipe. The expected decrease of the electric field strength with  $\frac{1}{x}$  can be seen nicely. The peaks of the wake-fields, however, seem to be rather persistent, and especially the peak around a time of 660 ps seems to remain unchanged.



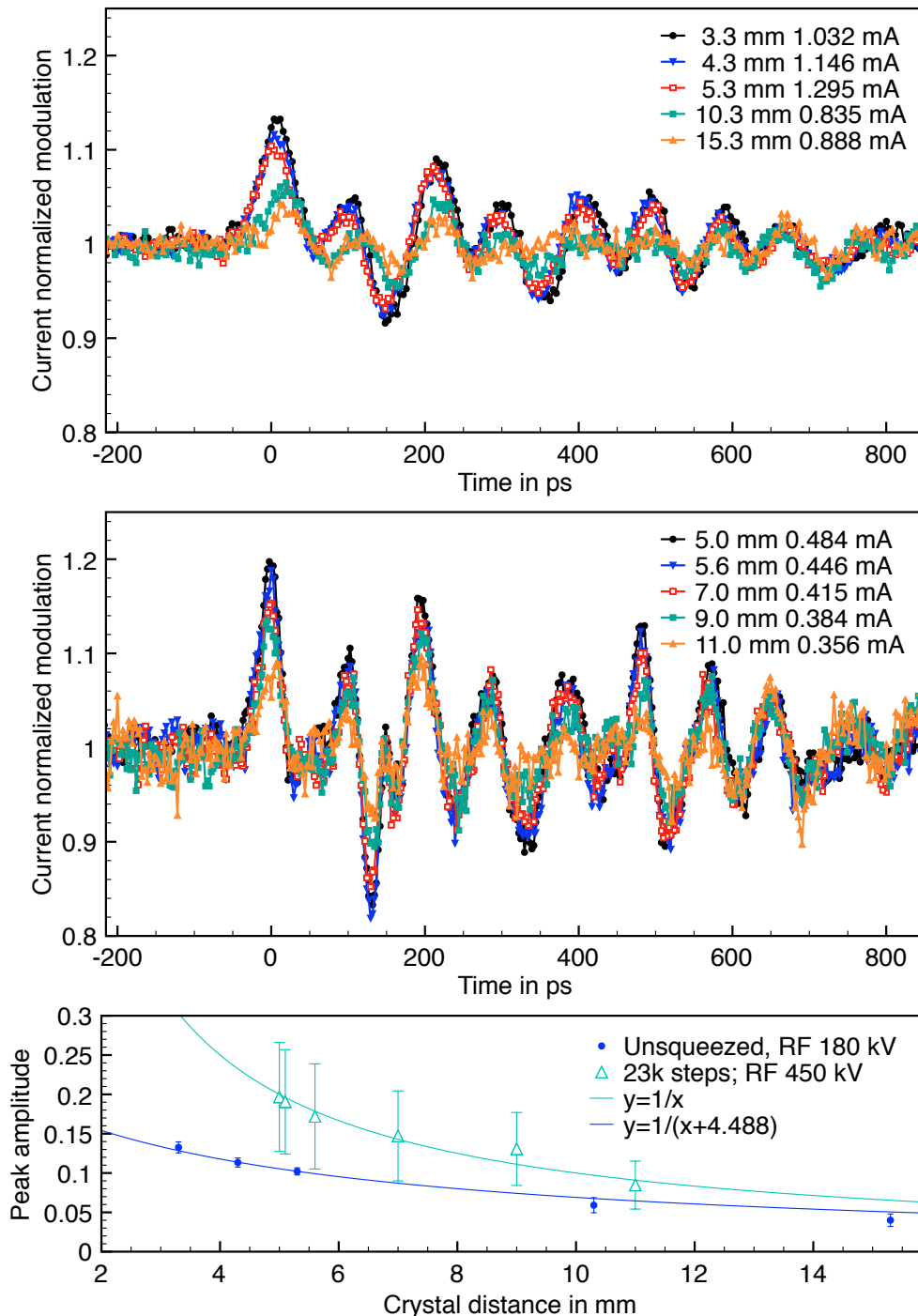


**Figure 7.13:** Top: Current normalized relative modulations for different distances of the crystal from the center of the beam pipe, which has a full standard height of 32 mm. The measurements were done for an unsqueezed electron beam at 1.3 GeV and an RF voltage of 180 kV / cavity and a bunch length of about 20 ps. The laser repetition rate was 0.9 MHz. Middle: Same measurement as above for slightly different distances, a squeezed beam (23k steps,  $f_s = 13.0$  kHz) and a higher RF voltage of 450 kV / cavity. For these settings, the bunch length was around 11 ps. The laser repetition rate was 2.7 MHz. The higher noise level most likely comes from the lower current. Both measurements show that the main peak is strongly influenced by change in distance, but the peak at 660 ps seems to be nearly unaffected. Bottom: Showing the peak amplitude of the first peak (obtained by a fit) in dependence of the distance, with  $(x - a)^{-1}$  curve fits. The error bars show the standard deviations of the data points obtained from measuring the fluctuation of the background signals.

### 7.2.3 Maschine Parameter Dependence of Wake-Fields

The shape of the wake-fields has also been studied for different machine parameters. Figure 7.14 shows EOS profiles for different bunch compression settings, all normalized to the corresponding bunch currents. Because the electron beam orbits were slightly different, the signal was additionally scaled down according to the following equation, which takes the distances between crystal and beam orbit in x and y direction into account [26]<sup>5</sup>:

$$\Gamma(\Delta x, \Delta y) \propto \frac{1}{\sqrt{\Delta x^2 + \Delta y^2}} \sqrt{1 + 3 \frac{\Delta y^2}{\Delta x^2 + \Delta y^2}} \quad (7.1)$$

Here  $\Delta x$  is the horizontal distance between the center of the EO crystal and the electron bunch and  $\Delta y$ , the vertical one. The values have been computed taking into account the information obtained from electron beam orbit data from a nearby beam position monitor for the different data sets. This, however, led to only very small adjustments and did not significantly alter the amplitudes of the peaks. The behavior for the first four data sets seems to be nearly identical. Just the third data set for a bunch length of 8.5 ps shows slightly higher amplitudes than the others, which we would expect for a shorter bunch length. The data set for a bunch length of 20.8 ps shows a broadening of the main peak and most of the following peaks leading to a slight decrease in peak-amplitude compared to the other data sets. The fact that the last data set, which has roughly the same bunch length as the first data set, shows a significantly lower amplitude than the first one, is currently not understood and further studies for the same machine conditions will have to be carried out to see if this is a reproducible effect.

---

<sup>5</sup>p. 147 ff.; bear in mind that, for our geometry x and y are swapped compared to the geometry present in the reference.



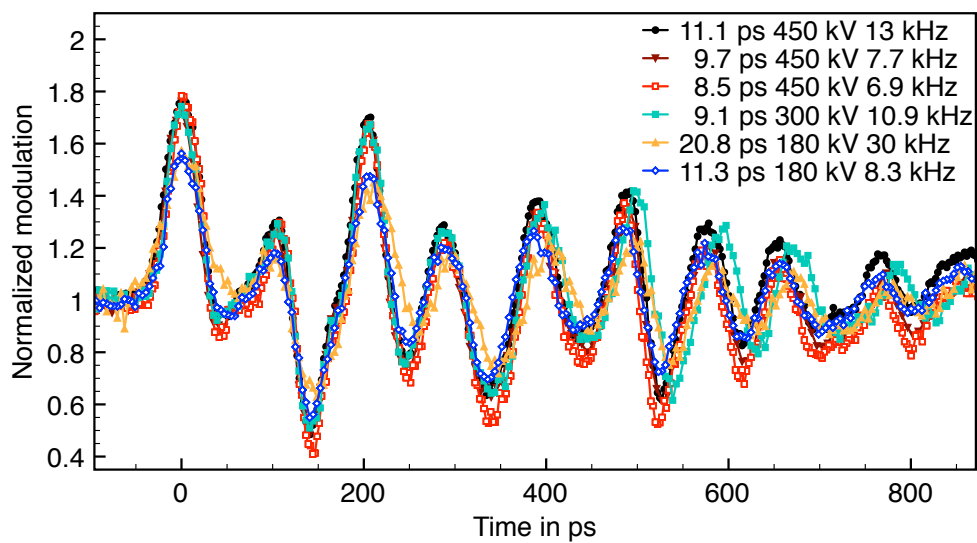
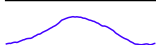


**Figure 7.14:** Current and distance normalized relative modulations for different machine parameters. The currents have been measured for every data point. Additionally, the different data sets are scaled according to Eq. 7.1 to take into account the different crystal and orbit positions, although this effect is rather small, leading to less than 6% difference in scaling for the different data sets. The two data sets for an RF voltage of 180 kV / cavity show a smaller amplitude and the peaks are wider for the bunches that are 20.8 ps long.





### 7.2.4 Wake-Fields Influencing Following Bunches

Clear indications of bunches influencing the bursting behavior of bunches following them has previously been observed at ANKA [70]. This influencing effect is believed to be caused by wake-fields.

Figure 7.15 shows EOS measurements for a single- and a double-bunch fill. The curves are normalized to the current in the first bunch. The image in the top shows the scans over a range of more than 2.5 ns behind the first bunch. For the first data set, only one bunch was in the machine, but the wake-fields show a non-vanishing component at a position of 2 ns where a second bunch was filled for the second data set. From the modulation it looks as if the current in the second bunch was slightly higher than the current in the first bunch, but filling pattern measurements with the TCSPC system have shown the bunch current of the second bunch to be lower than that of the first bunch. So for the figure in the bottom, the signal from the second bunch has been scaled by the bunch current of the second bunch and was displaced by 2 ns to the front for comparison with the signals for just one bunch and for the first bunch. A significant increase in peak amplitude can be seen for all positive wake-field peaks and also for the first peak, which is now, most likely not just caused by the Coulomb field any more, but by a superposition of Coulomb field and wake-field from the previous bunch. EOS mainly detects vertically polarized field components they, however, are linked to the longitudinal components (see Panofsky-Wenzel theorem [85, 86]). The results strengthen the assumption that wake-fields are causing neighboring bunch effects and further studies with simulations of the different electric-field components are foreseen.

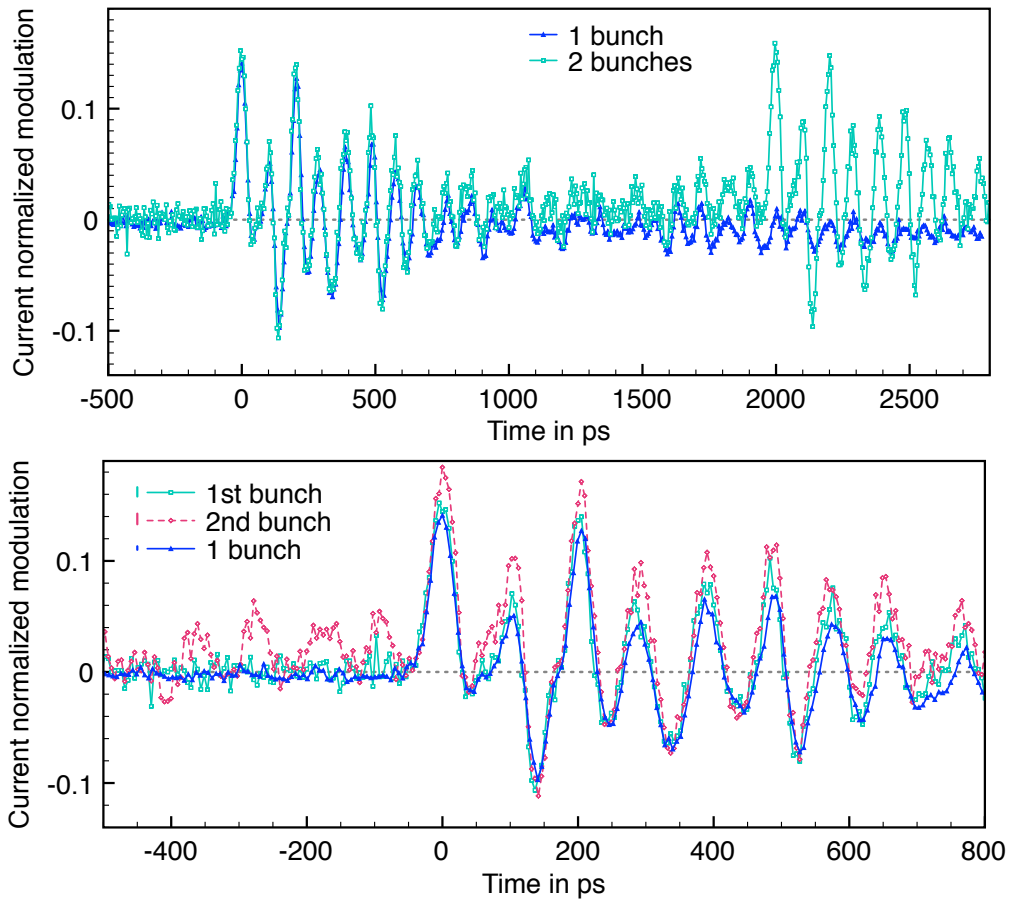


**Figure 7.15:** Top: Two EOS scans over a time range of 3 ns. For the first one, only one bunch was filled, but for the second one, two consecutive bunches were filled (2 ns bunch spacing at ANKA). The modulations have been normalized to the corresponding bunch currents which have been obtained by TCSPC measurements. For the first data set this is 98.4% of the total current and for the second data set this is 53.1% of the total current and the total currents were measured for every data point separately. It can clearly be seen that at a delay of 2000 ps (where a second bunch would be), the measured electric field of the trailing wake-fields is non-zero. Bottom: Comparison of the signals from the first and second bunch for which the data of the second bunch has been normalized by the bunch current of the second bunch (45.8%) and shifted in time, to overlap with that of the first bunch. In addition to that, the signal from the fill with just one bunch is also shown again. To give a feeling for the noise level, sticks with a length of  $2\sigma$  are shown next to the legend. The signals for the 1st bunch and for 1 bunch look nearly identical apart from the noise level, of the 1st bunch being higher because its absolute current was lower (we normalize by the current), but the signal of the 2nd bunch is clearly higher than what would be expected from its bunch current.

### 7.3 Bunch Length Measurements During the Energy Ramp

For any low- $\alpha_c$ -operation at storage rings, the main goal is to reduce the bunch length. As the zero current bunch length increases with the beam energy, a preferably low beam energy would be favorable (see Ch. 2.1.2). For ANKA the range of available beam energies lies between 0.5 and 2.5 GeV. The low- $\alpha_c$ -operation at ANKA was introduced before a single-bunch operation [87, 88] and even the SC became available [14], but it had been known from indirect bunch length measurements via the spectrum of the signal from an annular electrode that there were longitudinal instabilities below 1.3 GeV [89]. 1.3 GeV was chosen for the “standard” low- $\alpha_c$ -operation [70] with the possibility to go to slightly higher energies (e.g. 1.6 or 1.8 GeV) for users who are interested in short X-ray pulses [90, 91].

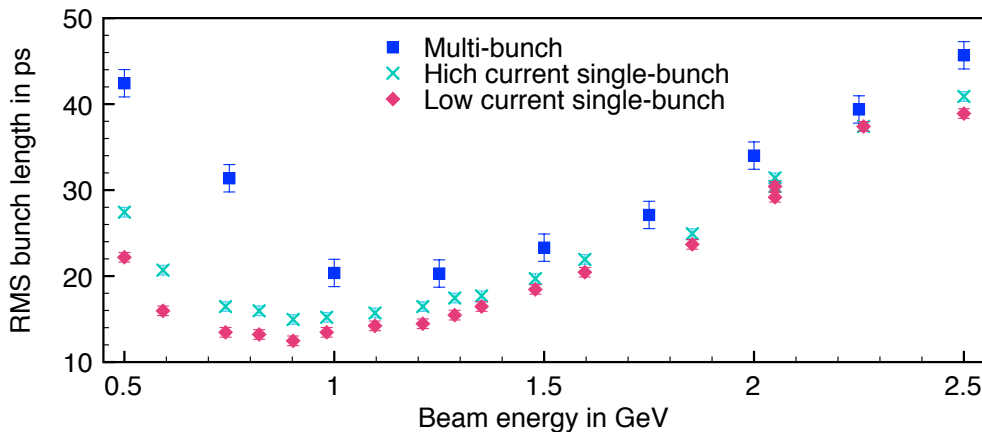


**Figure 7.16:** SC measurement of bunch length over beam energy for a constant  $f_s$  (adjusted by increasing the RF voltage with energy). For low energies (0.5 to 1 GeV) the bunch length is dominated by instabilities blowing up the bunches longitudinally, especially visible for the multi-bunch data, whereas for higher energies (above 1 GeV), the bunch length increases due to the increase in energy as expected. Published in [70].

When the SC first became available at ANKA in 2007, the bunch length was measured in dependence of beam energy during multi-bunch-mode. There it was verified that below 1.0-1.3 GeV the bunch length was severely increased due to longitudinal instabilities. When single-bunch operation and the visible light diagnostics beam port became available, this measurement was repeated as shown in Fig. 7.16. For the old multi-bunch measurement the synchrotron frequency changed between 30.3 and 37.0 kHz during the energy ramp, but for the single-bunch measurements  $f_s$  was kept constant between  $33.5 \pm 0.1$  kHz by slightly increasing the RF voltage during the energy ramp. For better comparison, a scaling to a frequency of 33.5 kHz was applied to the multi-bunch data. The single bunch measurements were performed for two different bunch currents of about 1.13 mA (high current single bunch) and 0.38 mA (low current single bunch) to estimate the effect of the current dependent bunch lengthening. For the multi-bunch measurement, the average bunch current was about 0.85 mA. For the injection energy of 0.5 GeV the increase in bunch length is quite tremendous, especially for the multi-bunch operation, but also for the single-bunch operation. For an energy of about 0.9 GeV, the minimum bunch length is reached for single bunch operation, whereas for multi-bunch operation, the minimum seems to lie at slightly higher energies around 1.3 GeV.

## 7.4 Influences of the Cavity Cooling Loop on the Bunch Arrival Time

During one measurement shift with EOSD, we observed sinusoidal changes in the bunch arrival time in the order of nearly 10 ps peak-to-peak with a period length in the order of 5 minutes. These arrival time fluctuations could be correlated to changes in the readback voltage and the reflected power from Cavity 2 in sector 4, which seemed to be having problems with its cooling loop regulation during that day. During this measurement EOSD has proven to be a very sensitive bunch arrival monitoring tool for machine diagnostics.

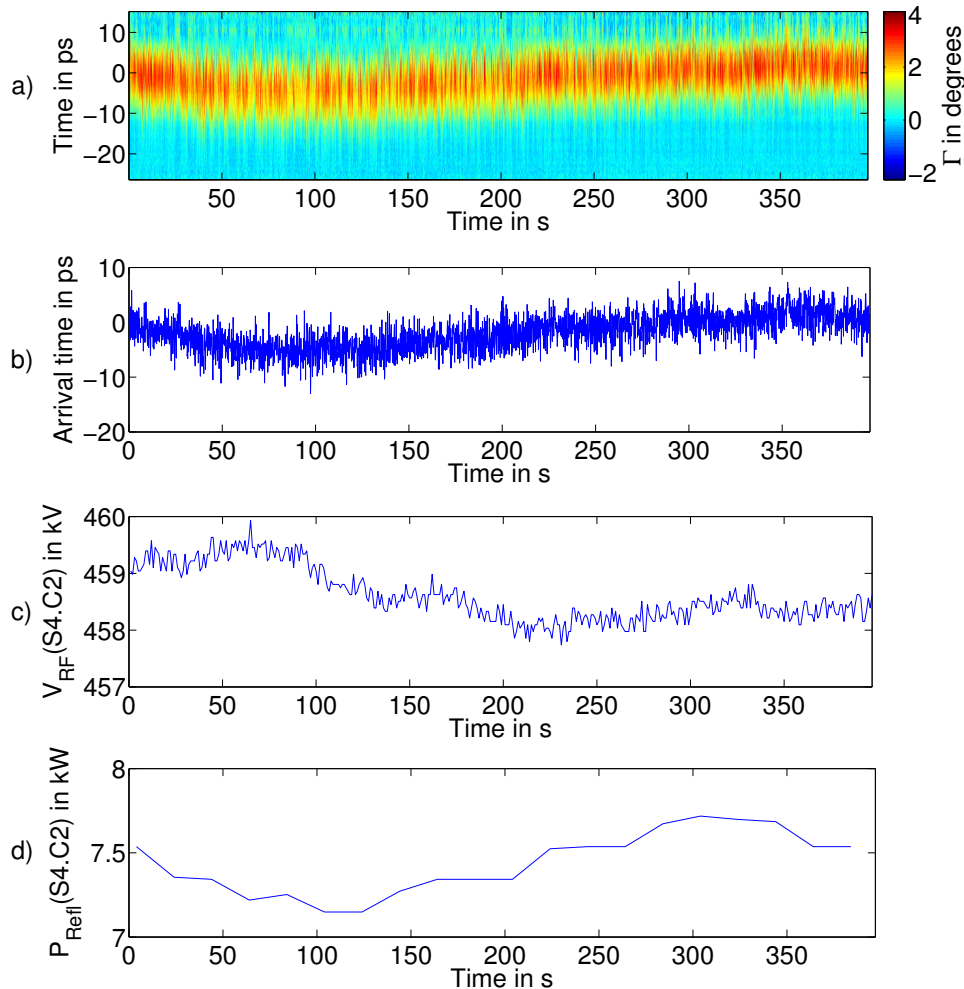


**Figure 7.17:** During a long 3000 shot EOSD sequence (about 400 s long) a drift in arrival time in the order of 5 ps was observed. The change in arrival time of the EOSD data can be correlated to the readback value of the voltage and the reflected power of Cavity 2 in Sector 4, which seemed to have extraordinary drifts during this measurement. a) 3000 consecutive EOSD bunch profiles, this time, the x-axis has been converted into seconds (linear approximation between start- and end-time of the measurement) to allow for a comparison with the readback values of the RF voltage which is logged every second. b) Bunch arrival time, extracted from fits to the EOSD profiles. c) Readback values of the RF voltage of Cavity 2 in Sector 4. d) Reflected power of Cavity 2 in Sector 4.



## 8. Summary

ANKA is the storage ring based synchrotron radiation facility of the KIT. In its evacuated beam pipe, highly relativistic electron bunches are deflected in a magnetic field to emit synchrotron radiation (SR). The spectrum of the emitted SR covers a large wavelength range from the far-infrared into the hard X-ray range, allowing for many user experiments to take place at the various measurement stations around the ring.

During ANKA's low- $\alpha_c$ -operation, the length of the electron bunches is reduced drastically to generate coherent synchrotron radiation (CSR). Unlike normal synchrotron radiation, whose spectrum is independent of the bunch shape, CSR is emitted only for wavelengths that are longer than the length of the electron bunches.

When the bunch length is reduced to lengths of a few picoseconds, the emission of the highly amplified CSR can be moved into the THz range, a frequency range heavily demanded by some users. The compression of the bunches is limited by the so-called microbunching instability. In the microbunching model, the electron bunch interacts with its own radiation leading to the formation of substructures in the longitudinal density profile of the bunch. The microbunching then amplifies itself via the emission of CSR. Due to the fact that the spectrum of the CSR is linked to the longitudinal bunch profile, even small changes of the charge density profile can result in large changes of the emitted CSR power. The growth and decay of the microbunches then causes a series of quasi-periodic bursts of CSR, making the emission unstable and resulting in a fluctuating intensity. In addition to that, the overall bunch length increases with increasing bunch charge, thus limiting the maximum achievable longitudinal compression of the bunches. This poses not only problems for existing storage rings with a short-bunch-operation (low- $\alpha_c$ ), but also for next generation machines aiming at the generation of synchrotron radiation with an even higher brilliance (e. g. ultra-low emittance rings) and even for machines for high energy physics (e. g. damping rings), because all of them operate with electron beam optics that highly compress the electron bunches in all directions, leading to very high charge densities.

A deeper understanding of the microbunching instability is desired to improve the modeling, and find ways to control the emission of CSR to make it more applicable to user



experiments.

The dynamic changes of the longitudinal charge density happen on a short time scale and can change from one bunch revolution to the next, making them only detectable with single-shot measurements that have a sub-ps resolution.

In the framework of this thesis, a setup for single-shot bunch profile measurements was designed and successfully installed into the vacuum chamber of the ANKA storage ring. The setup is based on the method of electro-optical spectral decoding (EOSD), using the Pockels effect inside an EO crystal. The electric near-field of the electron bunch induces a birefringence inside the EO crystal that is brought close to the electron bunch. This birefringence is then probed by a laser pulse passing through the crystal. If a femtosecond laser pulse is stretched in the time domain with a known relation between laser wavelength and time delay within the pulse, the whole temporal profile of a single electron bunch can be encoded as intensity modulation onto a single laser pulse and, subsequently, be detected with a single-shot spectrometer. From the known relation between wavelength and time delay, the spectral profile can be transformed back into a temporal profile, yielding a single-shot measurement of the longitudinal bunch profile.

ANKA is now the first storage ring in the world with a near-field EOSD single-shot setup. For the setup, an Yb-doped fiber laser system, developed at PSI, specifically for the purpose of EO measurements, has been adapted to meet the requirements for operation at ANKA. The compact near-field setup to hold the crystal and couple the laser beam into the UHV system of the storage ring is based on a design by a collaboration between PSI and DESY. It has been extended with an impedance protection slider to protect the delicate setup from radiation damage during ANKA's normal user operation, and to ensure that the normal user operation is not influenced by a change of vacuum chamber geometry.

I have performed extensive characterization measurements of the complex setup revealing many detector systematics that can mostly be removed with calibration measurements. The system has a resolution (granularity) of 0.4 ps and can measure bunch lengths and substructures down to its resolution limit of 1.5 ps RMS. Its high sensitivity allows for single-shot measurements down to bunch charges slightly below 30 pC. Some systematic effects, however, persist and might be caused by poor quality components in the optical setup that are going to be replaced in the future. The method of EOSD has shown great potential to become a reliable standard diagnosis tool during the low- $\alpha_c$ -operation.

To cross-check the new method of EOSD with existing techniques, a streak camera (SC) has been used for comparative measurements, showing good agreement of the measured longitudinal bunch lengths. The bunch profiles measured with the two techniques show slight systematic differences. While the streak camera allows for very precise measurements of the averaged longitudinal bunch profile, its single-shot capabilities are limited. To increase the availability of the streak camera, which detects the length of the synchrotron radiation pulses in the visible range of the spectrum, I collaborated with the ANKA-Team



---

in the planning and commissioning of a visible light diagnostics beamline at ANKA. At this new beamline, the photon flux in the visible range is greatly increased in comparison to the IR1 beamline at ANKA, where prior streak camera measurements were conducted. This allows us to measure averaged bunch profiles down to very low bunch charges. I did characterization studies with the streak camera that included the determination of the exact resolution limit of the streak camera by measuring femtosecond laser pulses with it. In addition to that, the data analysis of the streak camera data was improved to correct for longitudinal bunch oscillations that would lead to lengthened measurement results.

Wide-ranging accelerator characterization measurements of the bunch lengthening caused by the microbunching instability were performed with the streak camera. A theoretically predicted scaling of the threshold current for the bursting behavior of the CSR could be identified by observing the changes in bunch length. Studies of the current-depending bunch-lengthening effect have been performed for various states of bunch compression achieved by different machine optics and amplitudes of the field inside the RF cavities, which compensate for the energy loss of the bunches. The measured averaged profiles of the compressed bunches are not Gaussian any more as they are for uncompressed bunches, but lean slightly forward towards the head of the bunch. This is a predicted effect to compensate for the energy loss due to the emission of CSR.

Measurements with the EO setup showed indications of the expected substructures on the electron bunches. In addition to that, strong bunch deformations were observed for high bunch charges at high bunch compression settings.

The EO setup also allowed us to study the long-ranged wake-fields trailing the electron bunch. While the exact shape of those wake-fields is mainly caused by the geometry of the in-vacuum parts of the setup, and only slightly changes for different beam parameters, many structures inside the electron beam pipe can cause similar fields. Wake-fields are believed to be the cause for bunch-bunch interactions that had recently been observed at ANKA. The EO measurements strengthen this assumption by showing that the wake-fields ranging long enough to influence a consecutive bunch traveling 2 ns behind the first bunch.

To summarize, the adaption of the EOSD technique for operation in a storage ring environment was highly successful and first results are very promising, revealing the much sought after substructure on the bunches, which theories predict. This allows, for the first time, to benchmark those theories. The measured wake-fields allow for the comparison with numerical simulation codes that will aid in the development of geometries suppressing those long ranging wake-fields. There is of course still plenty of room for improvements of the complex setup, for example, to decrease the impact of systematic effects and to improve the resolution, all planned for the future. A proposal to increase the acquisition speed, to allow for the recording of every single bunch revolution has been approved and is currently under development with a joint collaboration with the institute for data processing and electronics (IPE) within the KIT.







## 9. Appendix

### A Mathematical Description of the Pockels Effect

The following deduction of the formulae for the description of the Pockels effect follow the treatment in [26, 92].

Birefringence occurs inside optically anisotropic materials. For an optically isotropic material, the polarization  $\mathbf{P}$  induced by an electric field  $\mathbf{E}$  is always parallel to the electric field vector. It is related to the field by a scalar factor, the susceptibility  $\chi$ .

$$\mathbf{P} = \epsilon_0 \chi \mathbf{E} \quad (9.1)$$

Here  $\epsilon_0$  is the vacuum permittivity. For an optically anisotropic material, however, the induced polarization is not per se parallel to the electric field, so the susceptibility becomes a tensor.

$$P_i = \epsilon_0 \sum_j \chi_{ij} E_j \quad (9.2)$$

It means that, for a light pulse propagating through the material, the refractive index is dependent upon the direction of propagation. The coefficients of  $\chi_{ij}$  depend upon the choice of the coordinate system relative to the crystal lattice. There exists always a coordinate system in which  $\chi_{ij}$  becomes a diagonal matrix with just the three entries  $\chi_{ii}$ . This coordinate system is then along the so called principal axes of the crystal. If at least two of the  $\chi_{ij}$  have different values, the crystal will exhibit birefringence.

The dielectric permittivity tensor is defined by the following equation:

$$\epsilon_{ij} = 1 + \chi_{ij} \quad (9.3)$$

With this definition and Eq. 9.2, the polarization in the following definition of the electric displacement field  $\mathbf{D}$

$$\mathbf{D} \equiv \epsilon_0 \mathbf{E} + \mathbf{P} \quad (9.4)$$

can be rewritten into:

$$\mathbf{D}_i = \epsilon_0 \sum_j \epsilon_{ij} E_j \quad (9.5)$$



Assuming that there is no magnetic permeability, the phase velocity  $v_p$  of a plane wave in an anisotropic medium

$$v_p = \frac{c}{\sqrt{\epsilon}} = \frac{c}{n} \quad (9.6)$$

depends upon its direction of propagation and its polarization. For a given direction of propagation, two perpendicular optical axes  $\mathbf{u}_s$  and  $\mathbf{u}_f$  exist which have different phase velocities (the “slow” and the “fast” axis) and thus different indices of refraction,  $n_s$  and  $n_f$ . If the polarization of an incident light wave is parallel to one of these optical axes, its polarization state will remain unaltered. For arbitrary directions of polarization, the electric field vector can be split into two components parallel to  $\mathbf{u}_s$  and  $\mathbf{u}_f$ . Because the two components have different phase velocities, a phase shift between them occurs, which leads to a change of polarization of the exiting wave.

To determine  $n_s$  and  $n_f$ , it is helpful to look at the index ellipsoid. The index ellipsoid can be deduced from the relation of the energy density  $w$

$$w = \frac{1}{2} \mathbf{E} \cdot \mathbf{D} = \frac{1}{2} \sum_{i,j} E_i \epsilon_{ij} E_j \quad (9.7)$$

by changing to a coordinate system in which the dielectric tensor  $\epsilon_{ij}$  is diagonal, so Eq. 9.7 is rewritten to

$$2w = \frac{D_1^2}{\epsilon_1} + \frac{D_2^2}{\epsilon_2} + \frac{D_3^2}{\epsilon_3}. \quad (9.8)$$

If we now introduce a dimensionless vector  $\mathbf{u}$

$$\mathbf{u} = \begin{pmatrix} u_1 \\ u_2 \\ u_3 \end{pmatrix} = \frac{\mathbf{D}}{\sqrt{2\epsilon_0 w}} \quad (9.9)$$

and the main indices of refraction  $n_i$

$$n_i = \sqrt{\epsilon_i}, \quad i = 1, 2, 3 \quad (9.10)$$

Eq. 9.8 simplifies to

$$1 = \frac{u_1^2}{n_1^2} + \frac{u_2^2}{n_2^2} + \frac{u_3^2}{n_3^2} \quad (9.11)$$

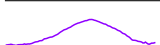
the index ellipsoid. Its main axes, have a length of  $2n_i$  and are parallel to the optical axes of the crystal.

By defining the permeability tensor  $\boldsymbol{\eta} = \boldsymbol{\epsilon}^{-1}$  which, in the principal coordinate system of the crystal is given by

$$\boldsymbol{\eta} = \boldsymbol{\epsilon}^{-1} = \begin{pmatrix} \frac{1}{n_1^2} & 0 & 0 \\ 0 & \frac{1}{n_2^2} & 0 \\ 0 & 0 & \frac{1}{n_3^2} \end{pmatrix} \quad (9.12)$$

we can further simplify the equation for the index ellipsoid (Eq. 9.11) to

$$1 = \mathbf{u}^T \cdot \boldsymbol{\eta} \cdot \mathbf{u} \quad (9.13)$$



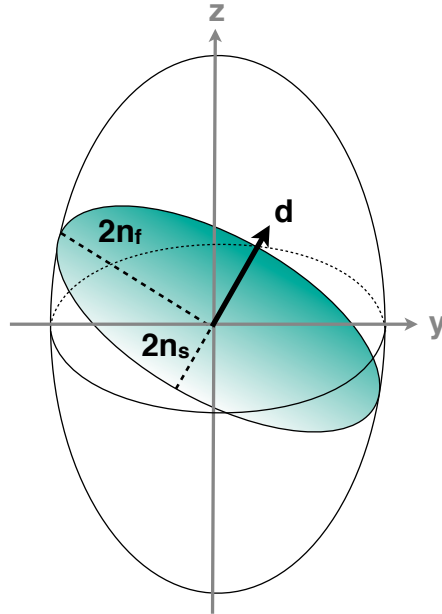


**Figure A.1:** The green ellipse marks the intersection of the index ellipsoid with the original plane normal to the direction of incidence  $\mathbf{d}$ . Its major and minor axes have the lengths of  $2n_s$  and  $2n_f$ . With  $n_s$  and  $n_f$  being the indices of refraction of the material for light traveling along  $\mathbf{d}$ .

Figure A.1 shows a graphical interpretation of the index ellipsoid and how  $n_s$  and  $n_f$  are related to it, for a wave propagating along  $\mathbf{d}$ .

Coming back to the Pockels effect: For strong electric fields there are also higher orders of susceptibility, which play a role, and a Taylor series expansion of Eq. 9.2 leads to an approximation:

$$\mathbf{P} \approx \epsilon_0 \left( \chi^{(0)} \mathbf{E} + \chi^{(1)} \mathbf{E}^2 + \chi^{(2)} \mathbf{E}^3 + \dots \right) \quad (9.14)$$

While  $\chi^{(0)}$  is the linear susceptibility,  $\chi^{(1)}$  is the second order susceptibility, which induces the Pockels effect. The next higher order,  $\chi^{(2)}$  induces a non-linear effect, called the Kerr effect which plays a role in many non-linear phenomena used in optics, e. g. Kerr lensing.

The fact that the Pockels effect induces a linear change in refractive index depending upon an external electric field, is due to the fact that  $\chi$  and  $\eta$  are related by equations 9.3 and 9.12. In the presence of an electric field,  $\eta$  becomes  $\eta(\mathbf{E})$ , which can then in turn be expanded into a Taylor series around  $\mathbf{E} = 0$ :

$$\eta_{ij} = \eta_{ij}(0) + \sum_k r_{ijk} E_k + \sum_{k,l} s_{ijkl} E_k E_l + \dots \quad (9.15)$$

$r_{ijk}$  holds the Pockels coefficients and  $s_{ijkl}$ , the Kerr coefficients. For gallium phosphide (GaP), the material we use for the EO measurements, their order of magnitudes is [26]:

$$r_{ijk} \approx 10^{-12} \frac{\text{m}}{\text{V}} \quad (9.16)$$

$$s_{ijkl} \approx 10^{-21} \frac{\text{m}^2}{\text{V}^2} \quad (9.17)$$

The Pockels effect, which we want to utilize for EO measurements, is clearly dominating for the fields in the order of  $< 10^7 \frac{V}{m}$  and the Kerr effect can be neglected for the following description. The components of the tensor  $r_{ijk}$  have the symmetry  $r_{ijk} = r_{jik}$  because of the fact that  $n_{ij} = n_{ji}$ , and a matrix representation, which groups  $i$  and  $j$  into a new index varying from 1 to 6, is more convenient. The following table 9.1 shows the conversion.

**Table 9.1:** Mapping of the coefficients of  $r_{ijk}$  to a  $(6 \times 3)$  matrix.

(1,1) $\mapsto$ 1	$r_{11k} \mapsto r_{1k}$
(2,2) $\mapsto$ 2	$r_{22k} \mapsto r_{2k}$
(3,3) $\mapsto$ 3	$r_{33k} \mapsto r_{3k}$
(2,3) $\mapsto$ 4	$r_{23k} = r_{32k} \mapsto r_{4k}$
(1,3) $\mapsto$ 5	$r_{13k} = r_{31k} \mapsto r_{5k}$
(1,2) $\mapsto$ 6	$r_{12k} = r_{21k} \mapsto r_{6k}$

With this new convention of  $r_{ik}$ , we write the field-induced part of the refractive index  $\Delta\eta_{ij}$  as

$$\Delta\eta_{ij} = \Delta \left( \frac{1}{n_i^2} \right) = \sum_k r_{ik} E_k \quad (9.18)$$

Gallium phosphide (GaP) has a zincblende crystalline structure and is initially isotropic, which means it only exhibits birefringence in the presence of an electric field, so for  $E = 0$  the refractive index is constant in all directions  $n_i = n_0$ . The matrix  $\mathbf{r}$  has only one independent entry  $r_{41} = r_{52} = r_{63}$ , referred to as the Pockels coefficient of GaP[26]. This greatly simplifies Eq. 9.13 to

$$1 = \frac{1}{n_0^2} (u_1^2 + u_2^2 + u_3^2) + 2r_{41} (E_1 u_2 u_3 + E_2 u_3 u_1 + E_3 u_1 u_2) \quad (9.19)$$

The GaP crystal in use for the EO measurements is cut along the (110)-plane which can be seen in Fig. A.2. For normal incidence, the electric field lies also within the (110)-plane. It is convenient to change to a new coordinate system spanned by X and Y within the (110)-plane (see rhs of Fig. A.2).

$$X = \frac{1}{\sqrt{2}} \begin{pmatrix} -1 \\ 1 \\ 0 \end{pmatrix} \quad (9.20)$$

$$Y = \begin{pmatrix} 0 \\ 0 \\ 1 \end{pmatrix} \quad (9.21)$$

It can be deduced that if the field is polarized along the X axis, the Pockels effect reaches its maximum [26]. Here just the simplified approach is shown, where the polarization is already assumed along the X axis[27]. For this, the components of the electric field vector are inserted into Eq. 9.19. The equation can then be solved by identifying the new principle



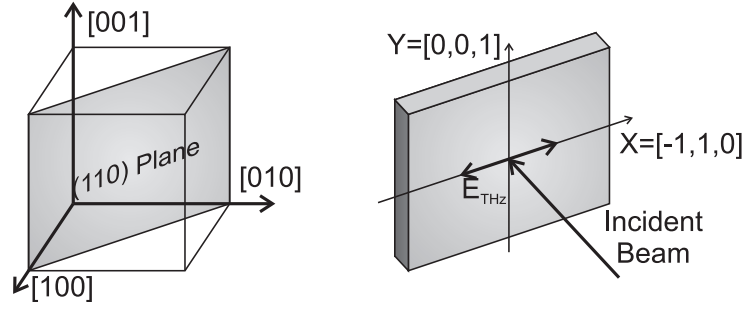


**Figure A.2:** Left: The GaP crystals in use for EO bunch length measurements are cut in the (110)-plane. Right: The variation of the refractive index reaches a maximum if the incident electric field which causes the birefringence is polarized along the X axis. Courtesy of F. Müller [27].

axes and their corresponding indices of refraction. This can be computed by determining the eigenvalues and their corresponding eigenvectors. The assumption  $n_0^2 r_{41} E \ll 1$  will need to be made to obtain the main refractive indices:

$$n_1 \approx n_0 + \frac{1}{2} n_0^3 r_{41} E \quad (9.22)$$

$$n_2 \approx n_0 - \frac{1}{2} n_0^3 r_{41} E \quad (9.23)$$

$$n_3 = n_0 \quad (9.24)$$

And their corresponding normalized eigenvectors:

$$\mathbf{u}_1 = \frac{1}{2} \begin{pmatrix} -1 \\ 1 \\ \sqrt{2} \end{pmatrix} \quad (9.25)$$

$$\mathbf{u}_2 = \frac{1}{2} \begin{pmatrix} 1 \\ -1 \\ \sqrt{2} \end{pmatrix} \quad (9.26)$$

$$\mathbf{u}_3 = \frac{1}{\sqrt{2}} \begin{pmatrix} -1 \\ -1 \\ 0 \end{pmatrix} \quad (9.27)$$

Now we would like to compute the induced phase shift  $\Gamma$  - also called phase retardation - a laser pulse experiences when it travels along the same direction as the electric field. It is assumed that the laser pulse's initial polarization also along the X axis. The phase retardation is caused by the difference in refractive indices  $\Delta n$ , which results in

$$\Delta n = n_1 - n_2 = n_0^3 r_{41} E. \quad (9.28)$$

Please bear in mind that  $E$  is the electric field strength of the modulating field and not that of the laser.

For a crystal of thickness  $d$  and a given frequency of the propagating light wave  $\omega$  the phase retardation  $\Gamma$  is

$$\Gamma = \frac{\omega d}{c} n_0^3 r_{41} E. \quad (9.29)$$

For the more general treatment, shown in [26] for which the polarization of the modulating electric field can be tilted by an angle of  $\alpha$  with respect to X within the X-Y plane, the result is the following:

$$\Gamma(\alpha) = \frac{\omega d}{c} n_0^3 r_{41} E \sqrt{1 + 3 \cos^2(\alpha)}. \quad (9.30)$$



## B Correlations Between Fit Parameters

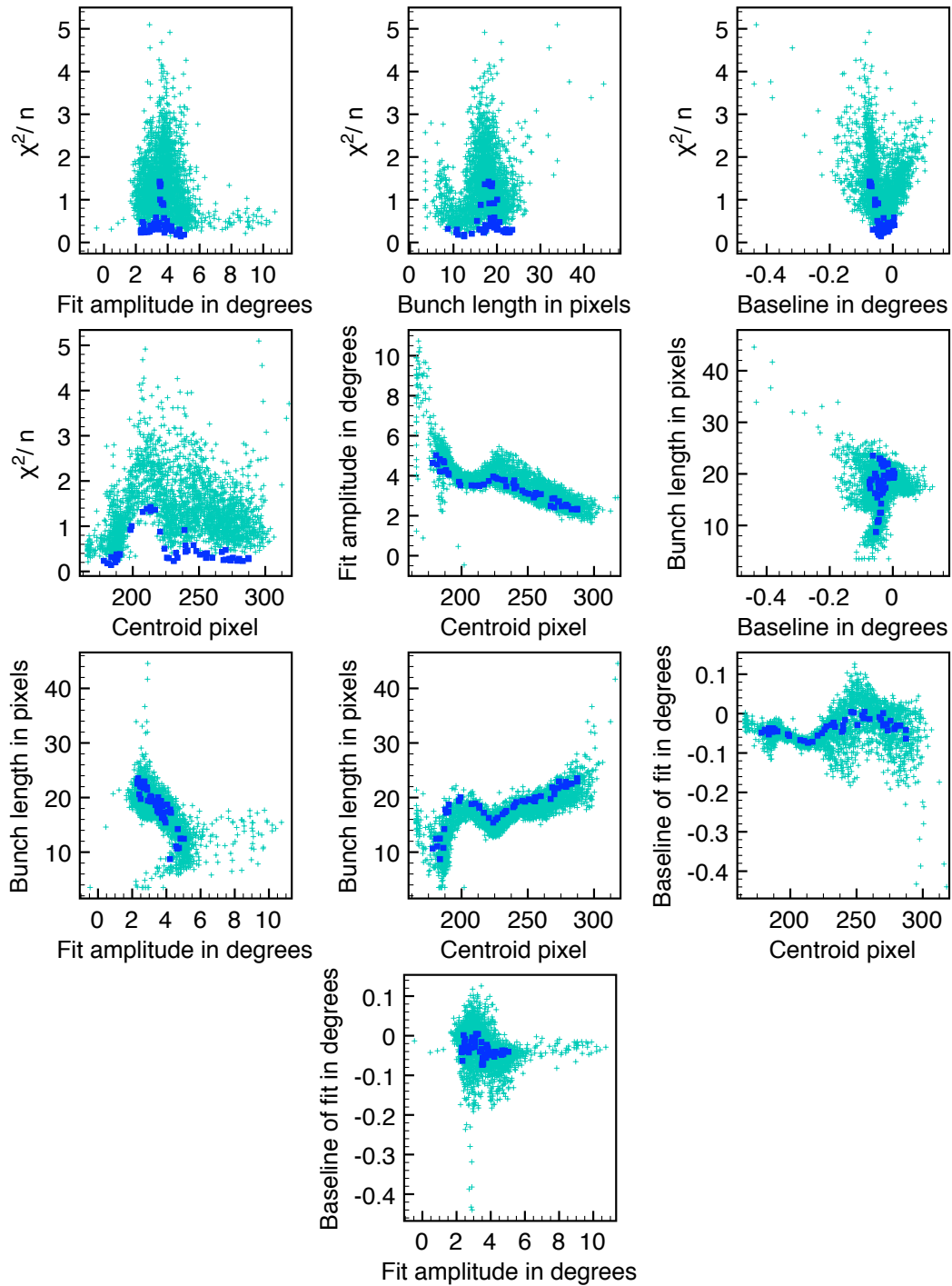


**Figure B.3:** Various correlations between the fit parameters to the phase retardation profiles recorded during a time calibration measurement (Data A see Tab. 6.1 on p. 103) and  $\chi^2/n$ , which has been computed afterwards for the fits, taking into account the standard deviations of the phase retardation for every pixel separately. The dark blue data points are from the averaged profiles and the teal data points for the individual single-shots.





# Acronyms

**ADC** analog digital converter

**AR** anti-reflective

**AOM** acousto-optic modulator

**ANKA** Ångström Source Karlsruhe

**BPM** beam position monitor

**CAD** computer-aided design

**CCD** charge-coupled device

**CoM** center of mass

**CSS** Control System Studio

**CSR** coherent synchrotron radiation

**CTR** coherent transition radiation

**CW** continuous wave

**DC** direct current

**DESY** Deutsches Elektronen-Synchrotron

**EO** electro-optical

**EOS** electro-optical sampling

**EOSD** electro-optical spectral decoding

**EPICS** Experimental Physics and Industrial Control System

**FLUTE** Ferninfrarot Linac- Und Test-Experiment

**FROG** Frequency Resolved Optical Gating

**FWHM** full width at half maximum

**GUI** graphical user interface

**HEB** hot electron bolometer



**HR** highly-reflective

**HWP** half-wave plate

**IMS** Institute of Micro- und Nanoelectronic Systems

**IPE** institute for data processing and electronics

**IR** infrared

**KIT** Karlsruhe Institute of Technology

**lhs** left hand side

**NPE** non-linear polarization evolution

**OSA** Optical Spectrum Analyzer

**PD** photodiode

**PI** proportional–integral controller

**PLL** phase-locked loop

**PM** polarization maintaining

**PSF** point spread function

**PSI** Paul Scherrer Institute

**QWP** quarter-wave plate

**RF** radio frequency

**rhs** right hand side

**RMS** root mean square

**SC** streak camera

**SLS** Swiss Light Source

**SM** single-mode

**SR** synchrotron radiation

**SRW** Synchrotron Radiation Workshop

**TCSPC** time-correlated single photon counting

**Ti:Sa** titanium-sapphire

**UHV** ultra-high vacuum

**VM** vector modulator

**WDM** wave division multiplexer


---




# Bibliography

- [1] F. R. Elder, A. M. Gurewitsch, R. V. Langmuir, and H. C. Pollock. Radiation from electrons in a synchrotron. *Physical Review*, 71(11):829–830, June 1947. doi: 10.1103/PhysRev.71.829.5. URL <http://link.aps.org/doi/10.1103/PhysRev.71.829.5>.
- [2] J. Schwinger. On radiation by electrons in a betatron. transcribed by M. A. Furman, 1945. URL <http://cosmology.princeton.edu/~mcdonald/accel/schwinger.pdf>.
- [3] D. Iwanenko and I. Pomeranchuk. On the maximal energy attainable in a betatron. *Physical Review*, 65(11-12):343–343, June 1944. doi: 10.1103/PhysRev.65.343. URL <http://link.aps.org/doi/10.1103/PhysRev.65.343>.
- [4] J. Blewett. Radiation losses in the induction electron accelerator. *Physical Review*, 69(3-4):87–95, February 1946. ISSN 0031-899X, 1536-6065. doi: 10.1103/PhysRev.69.87. URL <http://adsabs.harvard.edu/abs/1946PhRv...69...87B>.
- [5] L. I. Schiff. Production of particle energies beyond 200 mev. *Review of Scientific Instruments*, 17(1):6, 1946. ISSN 00346748. doi: 10.1063/1.1770395. URL <http://scitation.aip.org/content/aip/journal/rsi/17/1/10.1063/1.1770395>.
- [6] A. L. Robinson. History of synchrotron radiation sources. URL [http://xdb.lbl.gov/Section2/Sec\\_2-2.html](http://xdb.lbl.gov/Section2/Sec_2-2.html).
- [7] E. M. Rowe and Frederick E. Mills. Tantalus I: A dedicated storage ring synchrotron radiation source. Technical report, 1973. URL <http://cds.cern.ch/record/1107919>.
- [8] Lightsources.org. URL <http://www.lightsources.org>.
- [9] J. S. Nodvick and D. S. Saxon. Suppression of coherent radiation by electrons in a synchrotron. *Physical Review*, 96(1):180–184, October 1954. doi: 10.1103/PhysRev.96.180. URL <http://link.aps.org/doi/10.1103/PhysRev.96.180>.
- [10] J. Yarwood, T. Shuttleworth, J. B. Hasted, and T. Nanba. A new radiation source for the infrared region. *Nature*, 312(5996):742–744, December 1984. doi: 10.1038/312742a0. URL <http://www.nature.com/nature/journal/v312/n5996/abs/312742a0.html>.
- [11] T. Nakazato, M. Oyamada, N. Niimura, S. Urasawa, O. Konno, A. Kagaya, R. Kato, T. Kamiyama, Y. Torizuka, T. Nanba, Y. Kondo, Y. Shibata, K. Ishi, T. Ohsaka, and M. Ikezawa. Observation of coherent synchrotron radiation. *Physical Review*



- Letters*, 63(12):1245–1248, September 1989. doi: 10.1103/PhysRevLett.63.1245. URL <http://link.aps.org/doi/10.1103/PhysRevLett.63.1245>.
- [12] E.B. Blum, U. Happek, and A.J. Sievers. Observation of coherent synchrotron radiation at the Cornell linac. *Nuclear Instruments and Methods in Physics Research Section A: Accelerators, Spectrometers, Detectors and Associated Equipment*, 307(2–3): 568–576, October 1991. ISSN 0168-9002. doi: 10.1016/0168-9002(91)90232-F. URL <http://www.sciencedirect.com/science/article/pii/016890029190232F>.
- [13] R. Kato, T. Nakazato, M. Oyamada, S. Urasawa, T. Yamakawa, M. Yoshioka, M. Ikezawa, K. Ishi, T. Kanai, and Y. Shibata. Suppression and enhancement of coherent synchrotron radiation in the presence of two parallel conducting plates. *Physical Review E*, 57(3):3454, 1998. URL [http://pre.aps.org/abstract/PRE/v57/i3/p3454\\_1](http://pre.aps.org/abstract/PRE/v57/i3/p3454_1).
- [14] A.-S. Müller, I. Birkel, B. Gasharova, E. Huttel, R. Kubat, Y.-L. Mathis, D. A. Moss, W. Mexner, R. Rossmannith, M. Wuensch, P. Wesolowski, F. Perez, M. Pont, and C. J. Hirschmugl. Far infrared coherent synchrotron edge radiation at ANKA. In *Proceedings of PAC'05*, Knoxville, Tennessee, USA, 2005. URL <http://accelconf.web.cern.ch/AccelConf/p05/PAPERS/RPAE038.PDF>.
- [15] U. Arp, G. T. Fraser, A. R. Hight Walker, T. B. Lucatorto, K. K. Lehmann, K. Harkay, N. Sereno, and K.-J. Kim. Spontaneous coherent microwave emission and the sawtooth instability in a compact storage ring. *Physical Review Special Topics - Accelerators and Beams*, 4(5):054401, May 2001. doi: 10.1103/PhysRevSTAB.4.054401. URL <http://link.aps.org/doi/10.1103/PhysRevSTAB.4.054401>.
- [16] A. Andersson, M. S. Johnson, and B. Nelander. Observation of coherent synchrotron radiation from a 1-mm electron bunch at the MAX-I storage ring. pages 77–87, October 1999. doi: 10.1117/12.366631. URL [http://spie.org/x648.html?product\\_id=366631](http://spie.org/x648.html?product_id=366631).
- [17] M. Abo-Bakr, J. Feikes, K. Holldack, D. Ponwitz, G. Wüstefeld, and H. W. Hübers. Coherent mm-radiation experiments at the BESSY II storage ring. In *Proceedings of PAC'00*, pages 720–722, Vienna, Austria, 2000. URL <https://accelconf.web.cern.ch/accelconf/e00/PAPERS/WEP3A11.pdf>.
- [18] B. Podobedov, G. L. Carr, S. L. Kramer, and J. B. Murphy. Longitudinal density modulation of unstable bunches emitting coherent IR. In *Proceedings of PAC'01*, page 1921–1923, Chicago, USA, 2001. URL [http://ieeexplore.ieee.org/xpls/abs\\_all.jsp?arnumber=987228](http://ieeexplore.ieee.org/xpls/abs_all.jsp?arnumber=987228).
- [19] G. L. Carr, S. L. Kramer, J. B. Murphy, RPSM Lobo, and D. B. Tanner. Observation of coherent synchrotron radiation from the NSLS VUV ring. *Nuclear Instruments and Methods in Physics Research Section A: Accelerators, Spectrometers, Detectors and Associated Equipment*, 463(1):387–392, 2001. URL <http://www.sciencedirect.com/science/article/pii/S0168900201005216>.
- 
- 


- [20] G. Stupakov and S. Heifets. Beam instability and microbunching due to coherent synchrotron radiation. *Physical Review Special Topics - Accelerators and Beams*, 5(5):054402, May 2002. doi: 10.1103/PhysRevSTAB.5.054402. URL <http://link.aps.org/doi/10.1103/PhysRevSTAB.5.054402>.
- [21] M. Venturini and R. Warnock. Bursts of coherent synchrotron radiation in electron storage rings: A dynamical model. *Physical Review Letters*, 89(22):224802, November 2002. doi: 10.1103/PhysRevLett.89.224802. URL <http://link.aps.org/doi/10.1103/PhysRevLett.89.224802>.
- [22] J. M. Byrd, W. P. Leemans, A. Loftsdottir, B. Marcelis, Michael C. Martin, W. R. McKinney, F. Sannibale, T. Scarvie, and C. Steier. Observation of broadband self-amplified spontaneous coherent terahertz synchrotron radiation in a storage ring. *Physical Review Letters*, 89(22):224801, November 2002. doi: 10.1103/PhysRevLett.89.224801. URL <http://link.aps.org/doi/10.1103/PhysRevLett.89.224801>.
- [23] X. Yan, A. M. MacLeod, W. A. Gillespie, G. M. H. Knippels, D. Oepts, A. F. G. van der Meer, and W. Seidel. Subpicosecond electro-optic measurement of relativistic electron pulses. *Physical Review Letters*, 85(16):3404–3407, October 2000. doi: 10.1103/PhysRevLett.85.3404. URL <http://link.aps.org/doi/10.1103/PhysRevLett.85.3404>.
- [24] I. Wilke, A. M. MacLeod, W. A. Gillespie, G. Berden, G. M. H. Knippels, and A. F. G. Van Der Meer. Single-shot electron-beam bunch length measurements. *Physical review letters*, 88(12):124801, 2002. URL <http://link.aps.org/doi/10.1103/PhysRevLett.88.124801>.
- [25] A. L. Cavalieri, D. M. Fritz, S. H. Lee, P. H. Bucksbaum, D. A. Reis, J. Rudati, D. M. Mills, P. H. Fuoss, G. B. Stephenson, and C. C. Kao. Clocking femtosecond x rays. *Physical review letters*, 94(11):114801, 2005. URL <http://link.aps.org/doi/10.1103/PhysRevLett.94.114801>.
- [26] B. Steffen. *Electro-Optic Methods for Longitudinal Bunch Diagnostics at FLASH*. Ph. d. thesis, University of Hamburg, Hamburg, Germany, 2007.
- [27] F. L. Müller. *Electro-Optical Bunch Length Measurements at the Swiss Light Source*. Ph. d. thesis, University of Bern, Bern, Switzerland, 2011.
- [28] H. Wiedemann. *Particle Accelerator Physics I*. Springer, 1999.
- [29] K. Wille. *Physik der Teilchenbeschleuniger und Synchrotronstrahlungsquellen*. Teubner Studienbücher, 1992.
- [30] J. Liouville. Note sur la théorie de la variation des constantes arbitraires. *Journal de mathématiques pures et appliquées 1re série*, 3:342–349, 1838.
- [31] A.-S. Müller. *Beschleunigerphysik 1: Teilchenbeschleuniger*; Lecture, Karlsruhe Institute of Technology, 2013.
- 
- 


- [32] M. Klein. *Optics Calculations and Simulations of Longitudinal Beam Dynamics for the Low-alpha Mode at ANKA*. Ph. d. thesis, Faculty of Physics, Karlsruhe Institute of Technology, Karlsruhe, Germany, 2012.
- [33] F. Zimmermann M. G. Minty. *Measurement and Control of Charged Particle Beams*. Springer, 2003.
- [34] M. Klein, N. Hiller, A. Hofmann, E. Huttel, V. Judin, B. Kehrer, S. Marsching, A.-S. Müller, and K. G. Sonnad. Modeling the low-alpha mode at ANKA with the accelerator toolbox. In *Proceedings of PAC'11*, New York, NY, USA, 2011. URL <http://epaper.kek.jp/pac2011/papers/wep005.pdf>.
- [35] J. D. Jackson. *Classical Electrodynamics*. John Wiley & Sons, 3rd edition, 1998.
- [36] H. Wiedemann. *Particle Accelerator Physics II*. Springer, 1999.
- [37] A.-S. Müller. Accelerator-based sources of infrared and terahertz radiation. *Reviews of Accelerator Science and Technology*, 03(01):165–183, January 2010. ISSN 1793-6268, 1793-8058. doi: 10.1142/S1793626810000427. URL <http://www.worldscientific.com/doi/abs/10.1142/S1793626810000427>.
- [38] V. Judin. *Untersuchung von Bunch-Bunch-Wechselwirkungen und des Einflusses der geometrischen Impedanz bei der Erzeugung kohärenter THz-Strahlung*. Ph. d. thesis, Faculty of Physics, Karlsruhe Institute of Technology, Karlsruhe, Germany, November 2013.
- [39] V. Judin, S. Hillenbrand, N. Hiller, A. Hofmann, E. Huttel, M. Klein, S. Marsching, A. S. Müller, N. Smale, and K. G. Sonnad. Observation of bursting behavior using multiturn measurements at ANKA. In *Proceedings of IPAC'10*, page 2526–2528, Kyoto, Japan, 2010. URL <http://epaper.kek.jp/ipac10/papers/wepea021.pdf>.
- [40] P. Kuske. CSR-Driven longitudinal single bunch instability thresholds. In *Proceedings of IPAC'13*, pages 2041–2043, Shanghai, China, 2013. ISBN ISBN 978-3-95450-122-9. URL <http://accelconf.web.cern.ch/AccelConf/IPAC2013/papers/weoab102.pdf>.
- [41] C. Evain, J. Barros, A. Loulergue, M. A. Tordeux, R. Nagaoka, M. Labat, L. Cassinari, G. Creff, L. Manceron, J. B. Brubach, P. Roy, and M. E. Couprie. Spatio-temporal dynamics of relativistic electron bunches during the micro-bunching instability in storage rings. *EPL (Europhysics Letters)*, 98(4):40006, May 2012. ISSN 0295-5075, 1286-4854. doi: 10.1209/0295-5075/98/40006. URL <http://stacks.iop.org/0295-5075/98/i=4/a=40006?key=crossref.c70d1cecf6dcff571c4ea35949b8584c>.
- [42] K. L. F. Bane, Y. Cai, and G. Stupakov. Comparison of simulation codes for microwave instability in bunched beams. In *Proceedings of IPAC'10*, page 2096–2098, Kyoto, Japan, 2010. URL <http://epaper.kek.jp/IPAC10/papers/tupd078.pdf>.
- [43] K. Scheidt. Review of streak cameras for accelerators: features, applications and results. In *Proceedings of EPAC'00*, page 182–186, Vienna, Austria, 2000. URL <http://accelconf.web.cern.ch/Accelconf/e00/PAPERS/WEYF202.pdf>.

- [44] B. Kehrer. *Einzelphotonendiagnostik am ANKA-Speicherring*. Diploma thesis, Faculty of Physics, Karlsruhe Institute of Technology, Karlsruhe, Germany, May 2011.
- [45] P. Thoma, A. Scheuring, M. Hofherr, S. Wünsch, K. Il'in, N. Smale, V. Judin, N. Hiller, A.-S. Müller, A. Semenov, H.-W. Hübers, and M. Siegel. Real-time measurement of picosecond THz pulses by an ultra-fast  $\text{YBa}_2\text{Cu}_3\text{O}_{7-\delta}$  detection system. *Applied Physics Letters*, 101(14):142601, 2012. doi: 10.1063/1.4756905. URL <http://link.aip.org/link/?APL/101/142601/1>.
- [46] Schematic drawing of the streak camera working principle. URL <http://www.mpg.de/495195/pressRelease200402241>.
- [47] A. Plech, S. Casalbuoni, B. Gasharova, E. Huttel, Y. L. Mathis, A.-S. Müller, K. Sonnad, A. Bartels, and R. Weigel. Electro-optical sampling of terahertz radiation emitted by short bunches in the ANKA synchrotron. In *Proceedings of PAC'09*, Vancouver, Canada, 2009. URL <http://accelconf.web.cern.ch/AccelConf/PAC2009/papers/tu5rfp026.pdf>.
- [48] A. Yariv and P. Yeh. *Optical Waves in Crystals: Propagation and Control of Laser Radiation*. Number 54 in Wiley Series in Pure and Applied Optics. John Wiley & Sons, 1st edition, 2002. ISBN 0471430811.
- [49] S. P. Jamison, G. Berden, W. A. Gillespie, P. J. Phillips, and A. M. MacLeod. Limitations of electro-optic measurements of electron bunch longitudinal profile. In *Proceedings of EPAC'08*, Genoa, Italy, 2008. URL <http://accelconf.web.cern.ch/Accelconf/e08/papers/tupc042.pdf>.
- [50] J. A. Valdmanis, G.A. Mourou, and C. W. Gabel. Picosecond electro-optic sampling system. *Applied Physics Letters*, 41(3):211, 1982. ISSN 00036951. doi: 10.1063/1.93485. URL <http://scitation.aip.org/content/aip/journal/apl/41/3/10.1063/1.93485>.
- [51] J. Valdmanis, G.A. Mourou, and C. W. Gabel. Subpicosecond electrical sampling. *IEEE Journal of Quantum Electronics*, 19(4):664–667, 1983. ISSN 0018-9197. doi: 10.1109/JQE.1983.1071915.
- [52] Z. Jiang and X.-C. Zhang. Electro-optic measurement of THz field pulses with a chirped optical beam. *Applied Physics Letters*, 72(16):1945–1947, 1998. URL [http://ieeexplore.ieee.org/xpls/abs\\_all.jsp?arnumber=4897918](http://ieeexplore.ieee.org/xpls/abs_all.jsp?arnumber=4897918).
- [53] T. Tsang, V. Castillo, R. Larsen, D. M. Lazarus, D. Nikas, C. Ozben, Y. K. Semertzidis, T. Srinivasan-Rao, and L. Kowalski. Electro-optical measurements of picosecond bunch length of a 45 MeV electron beam. *Journal of Applied Physics*, 89(9):4921–4926, 2001. URL [http://ieeexplore.ieee.org/xpls/abs\\_all.jsp?arnumber=5029632](http://ieeexplore.ieee.org/xpls/abs_all.jsp?arnumber=5029632).
- [54] M. J. Fitch, A. C. Melissinos, P. L. Colestock, J.-P. Carneiro, H. T. Edwards, and W. H. Hartung. Electro-optic measurement of the wake fields of a relativistic electron beam. *Physical Review Letters*, 87(3):034801, June 2001. doi: 10.1103/PhysRevLett.87.034801. URL <http://link.aps.org/doi/10.1103/PhysRevLett.87.034801>.
-

- [55] H. Loos, A. Doyuran, J. B. Murphy, J. Rose, T. Shaftan, B. Sheehy, Y. Shen, J. Skaritka, X. J. Wang, and Z. Wu. Electro-optic longitudinal electron beam diagnostic at SDL. In *Proceeding of PAC'03*, volume 4, page 2455–2457, Portland, Oregon, USA, 2003. URL [http://ieeexplore.ieee.org/xpls/abs\\_all.jsp?arnumber=1289152](http://ieeexplore.ieee.org/xpls/abs_all.jsp?arnumber=1289152).
- [56] A. Winter, M. Tonutti, S. Casalbuoni, P. Schmüser, S. Simrock, B. Steffen, T. Korhonen, T. Schilcher, V. Schlott, and H. Sigg. Bunch length measurements at the SLS linac using electro-optical techniques. In *Proceedings of PAC'04*, Lucerne, Switzerland, 2004. URL <https://accelconf.web.cern.ch/accelconf/e04/PAPERS/THOALH01.PDF>.
- [57] B. Steffen, S. Casalbuoni, E.-A. Knabbe, H. Schlarb, B. Schmidt, P. Schmüser, and A. Winter. Electro optic bunch length measurements at the VUV-FEL at DESY. In *Proceedings of PAC'05*, page 3111–3113, Knoxville, Tennessee, USA, 2005. URL [http://ieeexplore.ieee.org/xpls/abs\\_all.jsp?arnumber=1591381](http://ieeexplore.ieee.org/xpls/abs_all.jsp?arnumber=1591381).
- [58] I. Katayama, H. Shimosato, M. Bito, K. Furusawa, M. Adachi, M. Shimada, Heishun Zen, S.-i. Kimura, N. Yamamoto, M. Hosaka, M. Katoh, and M. Ashida. THz field detection of the coherent synchrotron radiation produced by laser bunch slicing. In *2010 Conference on Lasers and Electro-Optics (CLEO) and Quantum Electronics and Laser Science Conference (QELS)*, pages 1–2, 2010. doi: <http://dx.doi.org/10.1364/CLEO.2010.CMF6>.
- [59] C. Kaya, C. Schneider, A. Al-Shemmary, W. Seidel, M. Kuntzsch, J. Bhattacharyya, M. Mittendorff, P. Evtushenko, S. Winnerl, and G. Staats. Phase sensitive monitoring of electron bunch form and arrival time in superconducting linear accelerators. *Applied Physics Letters*, 100(14):141103–141103, 2012. URL [http://ieeexplore.ieee.org/xpls/abs\\_all.jsp?arnumber=6178152](http://ieeexplore.ieee.org/xpls/abs_all.jsp?arnumber=6178152).
- [60] Y. Okayasu, S. Matsubara, H. Tomizawa, K. Ogawa, T. Matsukawa, and H. Minamide. Progress report of the spectral decoding based eos with organic poekels EO crystals. In *Proceedings of IBIC'13*, Oxford, UK, 2013. URL <http://ibic2013.org/prepress/papers/wepc35.pdf>.
- [61] X. Wang, H. Zhai, and L. Li. Real-time measurement of the full spatiotemporal field of a single terahertz pulse by pulsed digital holography. volume 7851, pages 78510J–78510J–6, 2010. doi: [10.1117/12.872482](http://dx.doi.org/10.1117/12.872482). URL <http://dx.doi.org/10.1117/12.872482>.
- [62] J. van Tilborg, N. H. Matlis, G. R. Plateau, W. P. Leemans, Steven H. Gold, and G. S. Nusinovich. Optical sideband generation: a longitudinal electron beam diagnostic beyond the laser bandwidth resolution limit. In *AIP Conference Proceedings 1299*, pages 565–569, 2010. doi: <http://dx.doi.org/10.1063/1.3520387>. URL <http://scitation.aip.org/content/aip/proceeding/aipcp/10.1063/1.3520387>.
- [63] M. J. Nasse, M. Schuh, S. Naknaimueang, M. Schwarz, A. Plech, Y.-L. Mathis, R. Rossmannith, P. Wesolowski, E. Huttel, M. Schmelling, and A.-S. Müller. FLUTE: a versatile linac-based THz source. *Review of Scientific Instruments*, 84(2):022705,



2013. ISSN 00346748. doi: 10.1063/1.4790431. URL <http://link.aip.org/link/RSINAK/v84/i2/p022705/s1&Agg=doi>.
- [64] Y.-L. Mathis, H. O. Moser, and R. Steininger. Status of and research opportunities at anka synchrotron radiation facility under construction. *Ferroelectrics*, 249(1):11–20, 2001. ISSN 0015-0193. doi: 10.1080/00150190108214961. URL <http://www.tandfonline.com/doi/abs/10.1080/00150190108214961>.
- [65] Y.-L. Mathis, B. Gasharova, and D. Moss. Terahertz radiation at ANKA, the new synchrotron light source in karlsruhe. *Journal of biological physics*, 29(2-3):313–318, June 2003. ISSN 0092-0606. doi: 10.1023/A:1024429801191. PMID: 23345850.
- [66] N. Hiller, S. Hillenbrand, A. Hofmann, E. Huttel, V. Judin, B. Kehrer, M. Klein, S. Marsching, A.-S. Müller, and A. Plech. Observation of bunch deformation at the ANKA storage ring. In *Proceedings of IPAC'10*, Kyoto, Japan, 2010. URL <http://accelconf.web.cern.ch/AccelConf/IPAC10/papers/wepea020.pdf>.
- [67] B. Kehrer, N. Hiller, A. Hofmann, E. Huttel, V. Judin, M. Klein, S. Marsching, A.-S. Müller, and N. Smale. Filling pattern measurements at the ANKA storage ring. In *Proceedings of IPAC'11*, San Sebastian, Spain, 2011. URL <https://accelconf.web.cern.ch/accelconf/IPAC2011/papers/tupc087.pdf>.
- [68] O. Chubar and P. Elleaume. Accurate and efficient computation of synchrotron radiation in the near field region. In *Proceedings of EPAC'98*, Stockholm, Sweden, 1998. URL <https://accelconf.web.cern.ch/AccelConf/e98/PAPERS/THP01G.PDF>.
- [69] P. Schönfeldt, N. Hiller, V. Judin, A.-S. Müller, M. Schwarz, and J. Steinmann. Comparison of different approaches to determine the bursting threshold at ANKA. In *Proceedings of IPAC'13*, Shanghai, China, 2013. URL <http://accelconf.web.cern.ch/AccelConf/IPAC2013/papers/mopea020.pdf>.
- [70] A.-S. Müller, N. Hiller, A. Hofmann, E. Huttel, K. Il'in, V. Judin, B. Kehrer, M. Klein, S. Marsching, C. Meuter, S. Naknaimueang, M.J. Nasse, A. Plech, P. Probst, A. Scheuring, M. Schuh, M. Schwarz, M. Siegel, N. J. Smale, M. Streichert, F. Caspers, A. Semenov, H.-W. Hübers, and E. Bründermann. Experimental Aspects of CSR in the ANKA Storage Ring. In *ICFA Beam Dynamics Newsletter No. 57*, pages 154–165, April 2012. URL [http://icfa-usa.jlab.org/archive/newsletter/icfa\\_bd\\_nl57.pdf](http://icfa-usa.jlab.org/archive/newsletter/icfa_bd_nl57.pdf).
- [71] P. Schönfeldt. *Systematische Untersuchungen der Bestimmung von Burstingschwellen*. Diploma thesis, Faculty of Physics, Karlsruhe Institute of Technology, Karlsruhe, Germany, 2013.
- [72] F. Müller, S. Hunziker, V. Schlott, B. Steffen, D. Treyer, and T. Feuerer. Ytterbium fiber laser for electro-optical pulse length measurements at the SwissFEL. In *Proceedings of DIPAC'09*, Basel, Switzerland, 2009. URL <http://accelconf.web.cern.ch/AccelConf/d09/papers/tupd31.pdf>.
- [73] R. Paschotta. Encyclopedia of laser physics and technology, . URL [http://www.rp-photonics.com/mode\\_locking.html](http://www.rp-photonics.com/mode_locking.html).
- 
- 

- [74] R. Paschotta. Encyclopedia of laser physics and technology, . URL [http://www.rp-photonics.com/frequency\\_resolved\\_optical\\_gating.html](http://www.rp-photonics.com/frequency_resolved_optical_gating.html).
- [75] Experimental physics and industrial control system. URL <http://epics.org/>.
- [76] F. L. Müller, P. Peier, V. Schlott, and B. Steffen. A compact electro optical bunch length monitoring system-first results at PSI. In *Proceedings of FEL'10*, Malmoe, Sweden, 2010. URL <http://accelconf.web.cern.ch/AccelConf/FEL2010/papers/wepa09.pdf>.
- [77] T. Bückle. *Bestimmung der Strahlenergie des ANKA-Speicherring Mittels Resonanter Elektron-Spin-Depolarisation*. Diploma thesis, Faculty of Physics, University of Karlsruhe, Karlsruhe, Germany, 2008. URL [digbib.ubka.uni-karlsruhe.de/volltexte/documents/1608771](http://digbib.ubka.uni-karlsruhe.de/volltexte/documents/1608771).
- [78] S. Walther. *Aufbau und Test eines Einzelschuss-Spektrometers für elektro-optische Bunchlängenmessungen am ANKA Speicherring*. Bachelor thesis, Faculty of Physics, Karlsruhe Institute of Technology, Karlsruhe, Germany, 2013.
- [79] B. Steffen. Courteously allowed me to use his - at the time of this publication - unpublished code to simulate the EOSD response inside an EO crystal.
- [80] B. Kehrer, A. Borysenko, E. Hertle, N. Hiller, E. Huttel, V. Judin, S. Marsching, A.-S. Müller, M. J. Nasse, and M. Schuh. Numerical wakefield calculations for electro-optical measurements. In *Proceedings of IPAC'13*, Shanghai, China, 2013. URL <http://epaper.kek.jp/IPAC2013/papers/mopme015.pdf>.
- [81] R. Sliupas, 2013. e-Mail communication.
- [82] A. S. Müller, I. Birkel, S. Casalbuoni, B. Gasharova, E. Huttel, Y. L. Mathis, D. A. Moss, N. Smale, P. Wesolowski, and E. Bründermann. Characterizing THz coherent synchrotron radiation at the ANKA storage ring. In *Proceedings of EPAC'08*, page 2091–2093, Genoa, Italy, 2008. URL <https://accelconf.web.cern.ch/AccelConf/e08/papers/wepc046.pdf>.
- [83] A.-S. Müller, I. Birkel, E. Huttel, Y. L. Mathis, N. Smale, H. W. Hübers, A. Semenov, J. Feikes, M. v. Hartrott, G. Wüstefeld, R. Klein, R. Müller, G. Ulm, E. Bründermann, T. Bückle, M. Fitterer, S. Hillenbrand, N. Hiller, A. Hofmann, V. Judin, M. Klein, S. Marsching, and K. Sonnad. Observation of coherent THz radiation from the ANKA and MLS storage rings with a hot electron bolometer. In *Proceedings of PAC'09*, Vancouver, Canada, 2009. URL <http://accelconf.web.cern.ch/accelconf/PAC2009/papers/tu5rfp027.pdf>.
- [84] P. Basler, M. v. Borstel, and M. Schwarz. Analytic calculation of the electric field of a coherent THz pulse. to be published, 2013.
- [85] W. K. H. Panofsky and W. A. Wenzel. Some considerations concerning the transverse deflection of charged particles in radio-frequency fields. *Review of Scientific Instruments*, 27(11):967–967, 1956. ISSN 0034-6748, 1089-7623. doi: 10.1063/1.1715427. URL <http://scitation.aip.org/content/aip/journal/rsi/27/11/10.1063/1.1715427>.
- 
- 

- [86] S. Vaganian and H. Henke. The Panofsky-Wenzel theorem and general relations for the wake potential. *Particle Accelerators*, 48:239–242, 1995. URL <http://cds.cern.ch/record/1108316>.
- [87] A. Hofmann, M. Fitterer, M. Klein, S. Marsching, A.-S. Müller, K. Sonnad, T. Weis, E. Huttel, R. Weigel, G. Blokesch, and C. Piel. A single bunch electron gun for the ANKA injector. In *Proceedings of PAC'09*, Vancouver, Canada, 2009. URL <http://accelconf.web.cern.ch/AccelConf/PAC2009/papers/mo6rfrp099.pdf>.
- [88] A. Hofmann, I. Birkel, M. Fitterer, S. Hillenbrand, N. Hiller, E. Huttel, V. Judin, M. Klein, S. Marsching, and A.-S. Müller. Single bunch operation at ANKA: gun performance, timing and first results. In *Proceedings of IPAC'10*, Kyoto, Japan, 2010. URL <https://accelconf.web.cern.ch/accelconf/IPAC10/papers/mopd094.pdf>.
- [89] F. Perez, I. Birkel, E. Huttel, A.-S. Müller, and M. Pont. Beam size and bunch length measurements at the ANKA storage ring. In *Proceedings of PAC'03*, Portland, Oregon, USA, 2003. URL <http://accelconf.web.cern.ch/accelconf/p03/PAPERS/RPPG044.pdf>.
- [90] S. Ibrahimkutty, D. Issenmann, S. Schlee, A.-S. Müller, Y.-L. Mathis, B. Gasharova, E. Huttel, R. Steininger, J. Göttlicher, T. Baumbach, A. Bartels, C. Janke, and A. Plech. Asynchronous sampling for ultrafast experiments with low momentum compaction at the ANKA ring. *Journal of Synchrotron Radiation*, 18(4):539–545, July 2011. doi: 10.1107/S0909049511018267. URL <http://dx.doi.org/10.1107/S0909049511018267>.
- [91] D. Issenmann, S. Ibrahimkutty, R. Steininger, J. Göttlicher, T. Baumbach, N. Hiller, A.-S. Müller, and A. Plech. Ultrafast laser pump x-ray probe experiments by means of asynchronous sampling. *Journal of Physics: Conference Series*, 425(9):092007, 2013.
- [92] S. Casalbuoni, H. Schlarb, B. Schmidt, B. Steffen, P. Schmuser, and A. Winter. Numerical studies on the electro-optic sampling of relativistic electron bunches. TESLA Report 2005-01, 2005. URL [http://tesla.desy.de/new\\_pages/TESLA\\_Reports/2005/pdf\\_files/tesla2005-01.pdf](http://tesla.desy.de/new_pages/TESLA_Reports/2005/pdf_files/tesla2005-01.pdf).





# Acknowledgments

First of all, I would like to thank Prof. Anke-Susanne Müller, Prof. Tilo Baumbach and Prof. Günter Quast for giving me the possibility to write this thesis.

Special thanks go to Anke-Susanne for supervising me for the past years, bringing the whole project to life, and also for the trust she put into me to get this ambitious project done, I wholeheartedly enjoyed being one of her PhD students.

The project was funded by the BMBF, the Karlsruhe House of Young Scientists (KHYS) made my 3-month-stay at PSI possible and the “Landesgraduiertenförderung” financed me for two years and I am very grateful for their support.

I wish to thank the whole ANKA-IPS-LAS-Team for providing such a fun and productive working environment and making me feel really at home. They shielded me from any daily business as best as they could while I was writing up. Special thanks go to Michael Nasse - “my postdoc” - for the countless SAP orders, he processed for me and for his wisdom on numerous topics be they work- or life-related. Also great thanks go to Marcel Schuh, who I also harassed with many SAP orders, who has been my “favorite ANKA-operator” (a title shared with Eddy) during the many measurement shifts, and who also provided me with great advice on numerous topics. I am deeply indebted to Sebastian Marsching and Edmund Hertle who not only got the laser control system and the hardware-control of the whole EO system implemented, but also been good friends over the past years. Then, of course, fine thanks go to Benjamin Kehrer and Andrii Borysenko who have both spent numerous first unsuccessful and then finally successful night- and even some day-shifts together with me in the laser hutch. Benjamin, our MATLAB-, CST- and train-expert, constantly helped to improve and extend our readout scripts and ensured that the coffee kept flowing. Andrii showed great mental arithmetic skills even in the middle of the night and found his passion for highly sophisticated word games with Benjamin. Together, we have become an excellent measurement trio who had fun times during the measurement shifts and kept the spirits high. Without you two I surely would’ve given up long before we saw first results! Special thanks also go to Patrik Schönfeldt, who inherited the SC and ended up being begged to do many many measurements for comparison with my EO results. Markus Schwarz, I want to thank for many interesting discussions, the tutoring on particle physics, for being “the theorist I can run to if I have a mathematical problem” and for being a very worthy opponent in Starcraft II. I also want to thank Somprasong Nakneimueang who also was one of the regular late-shift operators during our EO measurements and for the many cooking tips she has given me. Special thanks belong to Vitali Judin, for being



the best office room neighbor there is. We had many great discussions about work, life, the universe and everything. He and Sophie Walther were also great helps when aligning the EO-Monitor before its installation into the ring. I would also like to thank Marit Klein for the fruitful discussions about beam dynamics and the enjoyable atmosphere.

Great thanks also go to Anton Plech who has counseled me on many laser- and EO-related topics over the past years and helped me out with optics and optomechanics from his “magic cupboard” numerous times. I want to thank Erhard Huttel for making the whole installation of the EO-Monitor at ANKA possible in the first place. Special thanks also go to Nigel Smale who not only taught me how to get things done, but also supplied me with a plethora of tips on all kinds of topics while ensuring that I practiced my English skills. I want to thank Andreas Böhm and Richard Stricker for the help with numerous RF components and cables, Steffen Schott for the CAD drawings and making sure that the EO-Monitor physically fit into ANKA, the vacuum group (Thomas Fischböck and Andreas Völker) for their aid in the installation and prior leak-tests. I also want to thank Daniel Ritz, Uwe Werdin and the whole technical team at ANKA. Furthermore, thanks go to the IR group (especially Yves-Laurent Mathis, Biliana Gasharova and Michael Süpfle) and Jörg Göttlicher. I would also like to thank the excellent administrative team at ANKA, especially Margit Helma, Margit Costarelli and Anne Stößer, who were all very helpful.

Great thanks also go to the whole LAS-Team at Campus South, especially to Axel Bernhard, Christina Widmann and Klaus Eichhorn.

I would also like to thank Erik Bründermann for the many tips I have received from him throughout my scientific career. Also, my gratitude belongs to Shaukat Khan for many interesting and fruitful discussions.

It is time to thank my colleagues at PSI: In particular I want to thank Felix Müller for developing the special fiber-laser system for EO measurements that has made my measurements possible, Volker Schlott for offering us the possibility to get such a laser system at ANKA, inviting me to PSI for the assembly and commissioning and for motivating me again when I was about to give up hope. Especially, I want to thank Peter Peier for putting up with me during my stay at PSI, he gave me a crash-course in laser physics, shared his vast knowledge and experience about EO measurements with me, counseled me so many times during measurement shifts and ensured that I now understand Bärndütsch. Many thanks also go to all the other colleagues who I met during my stay at PSI, among them: Stephan Hunziker, Patrick Pollet, Daniel Treyer, Pavel Chevtsov, Dirk & Elke Zimoch and Rasmus Ischebek who made my stay there so enjoyable, productive and educating. Each of you contributed to the success of the project, I really learned a lot from you and it was great to get to see how things work at other accelerators.

Special thanks also goes to the EO team at DESY: Bernd Steffen and Christopher Gerth. With his thesis, Bernd laid the foundation for including EO measurements into regular longitudinal diagnostics at accelerators. Additionally, he counseled me together with Peter on so many aspects of EO measurements and lasers, and kindly let me use his simulation



code. Many thanks go to Christopher for making the collaboration between KIT and DESY so uncomplicated and helping me out with replacement crystals when I needed them on a very short notice, without his quick help the installation of the EO-Monitor at ANKA would have been delayed by at least 4 months.

I want to thank again all my meticulous proof-readers, who have gone through great lengths to earn a bar of chocolate: Anton, Axel, Marcel, Michael, Johannes Steinmann, Paul Vincze, and Markus. I hope, I have not forgotten anyone, otherwise feel free to come by my office and claim your chocolate bar!

Furthermore, I want to thank all of my friends for making sure that my life did not solely consist of physics. I would like to specially thank Golo Fuchert for many thought provoking discussions and helpful tips while the two of us were writing up. Many thanks also go to Steffen Hillenbrand, who has been a great friend over the past years.

I also want to thank my boyfriend Stefan Ernst who has been supporting me unconditionally for more than a decade now, I cannot put in words, how grateful I am to have you!<sup>1</sup>

Am Ende möchte ich mich auch noch von ganzem Herzen bei meiner ganzen Familie bedanken. Meine Eltern haben mich die ganze Zeit über bedingungslos unterstützt, standen mir mit Rat und Tat zur Seite, aber haben gleichzeitig alle meine Entscheidungen vollends akzeptiert (ein Dickkopf war ich ja schon immer =p). Meine Geschwister Tanja und Michael waren jederzeit für mich da und haben dafür gesorgt, dass ich nicht den Bezug zum “normalen Leben” verliere.

Now I dearly hope that I have not forgotten anyone who feels I should have mentioned their name here. If it should be the case, however, please don't hold a grudge against me: I thank you all!

---

<sup>1</sup>He also helped me to implement the awesome rainbow-colored flip-book you see in the bottom corners of my thesis.

---

